Molecular Machines for Controlling Transmembrane Ion Transport

Toby G. Johnson

Supervisor: Matthew J. Langton

Exeter College, University of Oxford





A thesis for the degree of Doctor of Philosophy

Department of Inorganic Chemistry

Trinity Term 2023

Molecular Machines for Controlling Transmembrane Ion Transport

Toby G. Johnson, Exeter College, University of Oxford

Supervisor: Matthew J. Langton

Abstract of Thesis submitted for the degree of Doctor of Philosophy, Trinity Term, 2023

This thesis describes the design of molecular machines for the control of transmembrane ion transport. Employing a relay transport mechanism, halogen bonding transporters with high ion selectivity and azobenzene based transporters with photo-modulated activity are reported.

Chapter 1 introduces the field of transmembrane ion transport, highlighting key examples of synthetic ion channels, mobile carriers and anchored carriers which display stimuli-responsive behaviour.

Chapter 2 identifies the dependence of membrane thickness on the therapeutically important Cl^- > OH^- anion transport selectivity and describes a novel highly active and selective halogen bonding relay transporter.

Chapter 3 describes a unique photo-switchable relay transport system which regulates transport activity through control of the length of a telescopic carrier arm on the relay transporter, switching with visible light within the membrane in a fully reversible manner.

Chapter 4 expands on the photo-switchable relay transport system, introducing a new anchoring ammonium group delivers transporters to both leaflets of pre-formed bilayers.

Chapter 5 outlines the experimental procedures employed in this work.

Acknowledgements

It has been a long and tumultuous path that has finally lead to this – the submission of my thesis. Of course, I have a long list of people I would like to thank for their support and guidance, which has enabled me to get this far! Firstly, thank you Matt for your supportive, generous and patient mentorship throughout my DPhil and even a bit before! Your guidance throughout the years has helped to keep me level headed and on track to the end. You were always there to impart your wisdom, even throughout two paternity leaves and a pandemic. I have loved my time in the Langton group and it has been a privilege to be part of its founding years.

Of course, I would like to thank the wonderful members of the Langton and Beer groups who have been in the lab with me throughout the adventure. Thank you to Arya Arun for being a great friend from day one and for putting up with me in the office as your desk partner. Thank you Charlie Simms for putting up with me when I moved next to you, in the office and in the lab – you have been a real confidant. Special thanks to Euan Walkley and Amir Sadeghi-Kelishadi my two masters mentees for your hard work and dedication, you were both fantastic fun to work with and I hope some of my lessons were of help to you. Thank you Adam Sedgwick for our walks to and from work and for evenings in the Holly Bush. To Sam, Hudson, Isi, Maria, Elba, Dome, Laura, Aidan, Shaun, Kelly, Martin, Elin, Xiaobo, Aaron, Andrew, Manzoor, Hui, Jamie, Andrew, Zongyao, Edward 'TJ-2' Mitchell, Robert, George and Krzysztof, it has been a fantastic experience because of you all, thank you.

Without the guidance of Alyssa-Jennifer Avestro, Paul McGonigal and Chris Hunter I would not have conducted this DPhil. Thank you for each supporting me to work within your groups during my undergraduate studies and help shape me into the research scientist I am today –

and for completing all the reference requests which have propelled me on. Phil Hope, Andrew Turley, Promeet Saha, Abhijit Mallick, Istvan Kocsis, Filip Szczypiński and of course Aisha Bismillah were there in my more formative years to guide me and I will be forever grateful to each and everyone of them for their friendship and support.

My time in Oxford has been surreal. The opportunity to enjoy my postgraduate life in this historic city has been made by my friends from Exeter who I have been able to share it with. Special mentions to Nicholas Lim and Jack Peters for the creation of Lunch Squad who have been steady members from the beginning even with the gain and loss of so many others. Christy Kin Cleaves and Kate Dicker, who instilled in me a love of Oxford formals. Owen Crowther and Hamish Innes for being my squash opponents and thoroughly thrashing me, and to so many others that created such a friendly and fun MCR experience at Exeter College.

My DPhil has been a life's ambition and I am so grateful to the countless people who have been there to facilitate my pursuit of '*Molecular Machines for Controlling Transmembrane Ion Transport*.' None more so than my now wife Hannah. You have been there for me from the beginning. I never expected when I started my DPhil that when I came to write my acknowledgements, I would be celebrating my first 6 months of marriage. But, I am so relieved that you said yes and have been there for me for the past 8 years, and forever more. I wish my Aunty Sally, Nana and Pops could have been here to see me reach the fruition of this course. I have to thank my brothers Oliver and Henry for the way they moulded and nurtured me into the man I am today. Papa and Grandma for providing endless love. The Schofields for welcoming me and my rantings about chemistry into their family. Finally, thank you Mummy and Daddy for your unequivocal love and support, allowing me to pursue my dreams – one of them being this DPhil.

Previously Published Work

Some of the work described in this thesis has been published:

9. Xiangyu Chao,† **Toby G. Johnson**,† Maria-Carmen Temian, Andrew Docker, Antoine L. D. Wallabregue, Aaron Scott, Stuart J. Conway and Matthew J. Langton, 'Coupling photo-responsive transmembrane ion transport with transition metal catalysis,' *Under review at J. Am. Chem. Soc.*

8. **Toby G. Johnson** and Matthew J. Langton, 'Molecular Machines for the Control of Transmembrane Ion Transport,' *J. Am. Chem. Soc., 2023, DOI: 10.1021/jacs.3c08877*

7. Hui M. Tay, **Toby G. Johnson**, Andrew Docker, Matthew J. Langton and Paul D. Beer, 'Exploiting the Catenane Mechanical Bond Effect for Selective Halide Anion Transmembrane Transport,' *Angew. Chem. Int. Ed*., 2023, **62**, e2023127.

6. Shaun A. Gartland, **Toby G. Johnson**, Euan Walkley and Matthew J. Langton, 'Inter-Vesicle Signal Transduction Using a Photo-Responsive Zinc Ionophore,' *Angew. Chem. Int. Ed*., 2023, **62**, e202309080.

5. **Toby G. Johnson**,† Andrew Docker,† Amir Sadeghi-Kelishadi and Matthew J. Langton, 'Halogen Bonding Relay and Mobile Anion Transporters With Kinetically Controlled Chloride Selectivity,' *Chem. Sci.,* 2023, **14**, 5006-5013.

4. Aisha N. Bismillah, **Toby G. Johnson**, Burhan A. Hussein, Andrew T. Turley, Promeet K. Saha, Ho Chi Wong, Juan A. Aguilar, Dmitry S. Yufit and Paul R. McGonigal, 'Control of Dynamic sp^3-C Stereochemistry,' *Nature Chemistry,* 2023, **15**, 615-624.

3. Andrew Docker, **Toby G. Johnson**, Heiki Kuhn, Zongyao Zhang and Matthew J. Langton, 'Multistate Redox-Switchable Ion Transport Using Chalcogen-Bonding Anionophores,' *J. Am. Chem. Soc.,* 2023, **145**, 4, 2661–2668

2. **Toby G. Johnson**, Amir Sadeghi-Kelishadi and Matthew J. Langton, 'A Photo-Responsive Transmembrane Anion Transport Relay,' *J. Am. Chem. Soc.,* 2022, **144**, 23, 10455-10461.

1. Laura E. Bickerton,† **Toby G. Johnson**,† Aidan Kerckhoffs† and Matthew J. Langton, 'Supramolecular Chemistry in Lipid Bilayer Membranes,' *Chem. Sci*., 2021, **12**, 11252-11274.

(† denotes joint first-authorship)

Conferences and Symposia Attended

Talk | Gordon Research Conference: Artificial Molecular Switches and Motors, USA, 2023.

Poster Presentation | RSC Macrocyclic and Supramolecular Chemistry Meeting, UK, 2022.

Poster Presentation | RSC Organic Chemistry Poster Symposium 2022, 5th December 2022.

Attended | Sygnature Discovery's Medicinal Chemistry Workshop, 2nd – 3rd October 2022.

Talk | Early Career Researcher Macrocyclic and Supramolecular Chemistry Meeting, UK, 2022.

Talk | Virtual Macrocyclic and Supramolecular Chemistry Seminars, 21st July 2022.

Poster Presentation | RSC Macrocyclic and Supramolecular Chemistry Meeting, UK, 2021.

Abbreviations

16 : 1 PC: 1,2-Dipalmitoleoyl-*sn*-glycero-3-phosphocholine; **18 : 1 PC**: 1,2-Dioleoyl-*sn*-glycero-3-phosphocholine; **20 : 1 PC**: 1,2-Dieicosenoyl-*sn*-glycero-3-phosphocholine; **δ**: Chemical shift; **Δ**: Change in; **λ**: Wavelength; **μW**: Microwave; **ADP**: Adenosine diphosphate; **ATP**: Adenosine triphosphate; **BLM**: Black lipid membranes; **br.**: Broad; **CF**: 5(6)-Carboxyfluorescein; **CFTR**: Cystic fibrosis transmembrane conductance regulator; **ChB**: Chalcogen bonding; **CS_2**: Carbon disulfide; **DBU**: 1,8-Diazabicyclo(5.4.0)undec-7-ene; **DBTO**: Dibutyltin(IV) oxide; **DCC**: *N*,*N*'-Dicyclohexylcarbodiimide; **DIC**: *N*,*N*'-Diisopropylcarbodiimide; **DIPEA**: *N*,*N*-Diisopropylethylamine; **DMAP**: 4-Dimethylaminopyridine; **DPPC**: 1,2-Dipalmitoyl-*sn*-glycero-3-phosphocholine; **DTA**: Dithiane; **DTT**: Dithiothreitol; **EC_{50}**: Effective concentration to reach 50% of maximal activity in the transport assay; **EYPC**: Egg yolk L-α-phosphatidylcholine; **EYPG**: egg yolk L-α-phosphatidylglycerol; **FCCP**: cyanide-*p*-trifluoromethoxyphenylhydrazone; **FRT**: Fischer rat thyroid cells; **Fmoc-Cl**: 9-Fluorenylmethyl chloroformate; **GSH**: Glutathione; **GSSG**: Glutathione disulfide; ***Gt*ACR1**: *Guillardia theta* anion-conducting channelrhodopsin; **XB**: Halogen bonding; **HATU**: Hexafluorophosphate azabenzotriazoletetramethyluronium; **HEPES**: 4-(2-Hydroxyethyl)piperazine-1-ethanesulfonic acid; **HPTS**: 8-Hydroxypyrene-1,3,6-trisulfonic acid; **HB**: Hydrogen bond; **I_{rel}**: Fractional fluorescence intensity; **ISE**: Ion selective electrode; **JC-1**: 5,5',6,6'-tetrachloro-1,1',3,3'-tetraethyl-imidacarbocyanine iodide; **KcsA**: K^+ channel from *Streptomyces lividans*; **LUVs**: Large unilamellar vesicles; **ε**: molar extinction coefficient; **MTT**: 3-[4,5-Dimethylthiazol-2-yl]-2,5 diphenyl tetrazolium bromide; **Mtt-Cl**: 4-methyltrityl chloride; **MQAE**: *N*-(Ethoxycarbonylmethyl)-6-methoxyquinolinium bromide; ***n***: Hill coefficient; **NCS**: *N*-Chlorosuccinimide; **NEt_3**: Triethylamine; **NMDG-Cl**: *N*-Methyl-D-glucamine chloride; **NQO1**: NAD(P)H dehydrogenase quinone 1; **PnB**: pnictogen bonding; **PPG**: Photo-protecting group; **PSS**: Photo-stationary state; **POPG**: 1-palmitoyl-2-oleoyl-*sn*-glycero-3-phospho-(1'-*rac*-glycerol); **POPC**: 1-palmitoyl-2-oleoyl-*sn*-glycero-3-phosphocholine; **QSAR**: Quantitative structure–activity relationship; **ROS**: Reactive oxygen species; **rt**: Room temperature; **StClC**: *Salmonella typhimurium* chloride ion channel; **TBACl**: Tetrabutylammonium chloride; **TFA**: Trifluoroacetic acid; **YFP**: Yellow fluorescent protein.

Table of Contents

Acknowledgements ii

Previously Published Work iv

Conferences and Symposia Attended iv

Abbreviations v

Chapter 1: Introduction 1

1.1 Biological Significance of Compartmentalisation 1

1.1.1 Biological Membranes 1

1.1.2 Ion Transporters Found in Nature 2

1.2 Synthetic Ion Transporters Mimicking Biotic Mechanisms of Transport 6

1.2.1 Synthetic Unimolecular Ion Channels 6

1.2.2 Synthetic Self-Assembled Ion Channels 9

1.2.3 Synthetic Mobile Ion Carriers 12

1.2.4 Therapeutic Importance of Selective Anion Transporters 15

1.2.5 Sigma-Hole Based Mobile Carriers 18

1.2.6 Metal Coordination Facilitated Anion Transport 22

1.2.7 Stimuli-Responsive Behaviour in Synthetic Mobile Carriers 23

1.2.8 Stimuli-Responsive Behaviour in Synthetic Channels 30

1.3 Anchored Ion Carriers 32

1.3.1 Unimolecular Anchored Transporters 33

1.3.2 Relay Transporters 36

1.4 Project Aims 38

Chapter 2: Designing Selective Anion Transporters 39

2.1.1 Therapeutic Importance of Selective Anion Transporters 39

2.1.2 Halogen Bonding Anionophores 40

2.2 Synthesis of Mobile Carriers 43

2.2.1 Quantifying Anion Transport Activity 44

2.2.2 Determining Chloride Over Hydroxide Selectivity 51

2.2.3 Impact of Membrane Hydrophobic Thickness on Mobile Carrier Anion Selectivity 54

2.3.1 Anti-Hofmeister Selectivity in Halogen Bonding Relay Transporters 59

2.3.2 Synthesis of Relay Transporters 60

2.3.3 Relay Transport Activity in POPC LUVs 63

2.3.4 Activity of Relay Transporters with Asymmetric Bilayer Distributions 67

2.3.5 Investigating The Effect Of Membrane Fluidity On Relay Mediated Anion Transport 68

2.3.6 Determining the Ion Selectivity of Relay Transporters 69

2.3.7 Impact of Membrane Thickness on Relay Transporter Anion Selectivity 73

2.4 Conclusions of Chapter 2 and Future Work 75

Chapter 3: Photo-Responsive Relay Transporters 77

3.1 Therapeutic Importance of Stimuli-Responsive Anion Transporters 77

3.2.1 Synthesis of Photo-switchable Relay Transporters 82

3.2.2 Photophysical Analysis of The Azobenzene Derivatives in Solution 87

3.2.3 Photophysical Analysis of The Azobenzene Functionalised Lipids in The Membrane Environment 89

3.2.4 Confirming The Relay Transport Mechanism 92

3.2.5 Photo-switchable Relay Transport Activity 102

3.3 Chapter 3 Conclusions and Future Work 111

Chapter 4: Photo-Switching Between Unique Ion Transport Mechanisms 113

4.1 The Influence of Phospholipid Binding on Mobile Carrier Activity 113

4.2.1 Design and Synthesis of Photo-switchable Transporters Operating Via Relay and Carrier Mechanisms 116

4.2.2 Photophysical Studies 120

4.2.3 The Effect Of An Ammonium Group On Mobile Carrier Mediated Anion Transport 122

4.2.4 Transport Activity of Contracted Azobenzene Ammonium-Anchored Transporters. 124

4.2.5 Transport Activity of Extended Azobenzene Ammonium-Anchored Transporters 130

4.2.6 Photo-switching Transport Activity of Ammonium Anchored Transporters *in situ*... 142

4.3 Conclusions of Chapter 4 145

Chapter 5: Experimental Procedures 147

5.1 Materials and Methods 147

5.2 Anion Transport Experiments 148

5.2.1 Vesicle Preparation 148

5.2.2 Transport assays with HPTS 149

5.3 Photo-switching Experiments 152

5.4.1 Chapter 2 Synthetic Procedures 153

5.4.2 Chapter 2 ^{1}H NMR Titration Experiments 158

5.4.2 Chapter 2 UV-vis Characterisation 159

5.5.1 Chapter 3 Synthetic Procedures 160

5.5.2 Chapter 3 UV-vis Characterisation 171

5.5.3 Chapter 3 Photo-stationary State Determination 172

5.5.4 Chapter 3 ^{1}H NMR Titration Experiments 172

5.5.5 Chapter 3 Photo-switchable Relay Anion Transport Data 174

5.6.1 Chapter 4 Synthetic Procedures 175

5.6.2 Chapter 4 Transport Activity Data 191

References 192

Chapter 1: Introduction

1.1 Biological Significance of Compartmentalisation

The sophistication of life is epitomised by the interconnected biochemical pathways and the diverse functions of different organelles in a cell. This complexity is the direct result of compartmentalisation maintained by the cellular membrane, where the isolation of components under different conditions leads to unique reactivities. While membranes facilitate the separation or confinement of different components, it is the ability to regulate transport across these barriers which is key to maintaining life. Therefore, it is of fundamental importance to investigate and understand the chemical process of transmembrane transport, which has already proven to be vital to the effect of certain therapeutics,[1] in tools for chemical biology[2] and for controlling reactivity in artificial cells.[3]

1.1.1 Biological Membranes

Biomembranes are bilayers primarily composed of amphiphilic phospholipids which provide structural integrity to the supramolecular structure through hydrogen bonding (HB) and electrostatic interactions of the lipid headgroups and van der Waals interactions of the fatty acid tails.[4] A plethora of proteins, glycan, lipids and other molecules are bound within or at the surface of the cellular membrane which serves as a viscous phospholipid bilayer solvent described as a fluid mosaic.[5] The hydrophobic interior of the membrane restricts the movement of charged and polar molecules, due to the high dehydration penalty to partitioning into this non-polar environment. In order to enable the transport of such molecules across cellular membranes, small molecule ionophores or membrane spanning protein channels are employed in nature (**Figure 1.1**). These structures shield the charge of ions to facilitate their movement through the hydrophobic membrane interior, either

encapsulating the ion and translocating through the membrane (mobile carrier) or providing a pore through which the ion can travel (channel).[6]

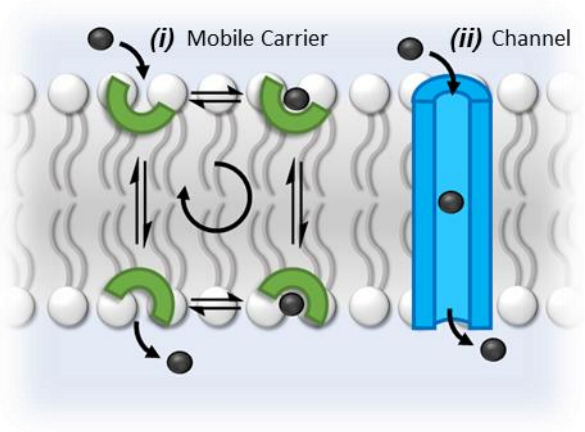

Figure 1.1 Schematic of the biotic mechanisms of ion transport. *(i) The mobile carrier mechanism depicts the cycle of binding, translocation of the ion-carrier complex, release of the ion and return of the carrier to the original position. (ii) The channel allows the flow of ions down a concentration gradient through the pore of the structure.*

1.1.2 Ion Transporters Found in Nature

Mobile carriers found in nature display high selectivity for a specific ion and enable the passive transport of this ion down a concentration gradient. Valinomycin is a natural product mobile carrier, with a high specificity for the transport of K^+ ions.[7,8] The dodecadepsipeptide has a neutral macrocyclic structure, with peripheral aliphatic side chains and an internal binding pocket of 6 convergently oriented carbonyls to bind a cation (**Figure 1.2A, C**). An intra-molecular hydrogen bonding framework between amide protons (donors) and carbonyls (acceptors) of alternating amino acids maintains the compact conformation ideal for the binding and electrogenic transport of K^+ (**Figure 1.2Bi**).[9] Secreted by the bacteria *Streptomyces fulvissimus*, valinomycin was the first natural product recognised as an ionophore with antibiotic activity and has since been shown to display a diverse range of biological activities including antibacterial, antifungal, antiviral and anticancer efficacy.[10]

Prodigiosin is a secondary metabolite produced by *Serratia marcescens* bacteria. The pyrrolylpyrromethene core is capable of binding the H^+/Cl^- ion pair and facilitating transport of the ions across lipid bilayers (**Figure 1.2A-B**).[11] The transport activity of prodigiosin has been employed to acidify the cytosol of cancer cells and induce apoptosis, demonstrating the application of ionophores as anticancer agents.[12] The H^+/Cl^- symport (co-transport) process is integral to the efficiency of the transporter since the disruption of pH homeostasis has been shown to initiate apoptosis. Studies of prodigiosin in model membranes have also demonstrated that the protonated species is capable of mediating a Cl^-/NO_3^- antiport process.[13]

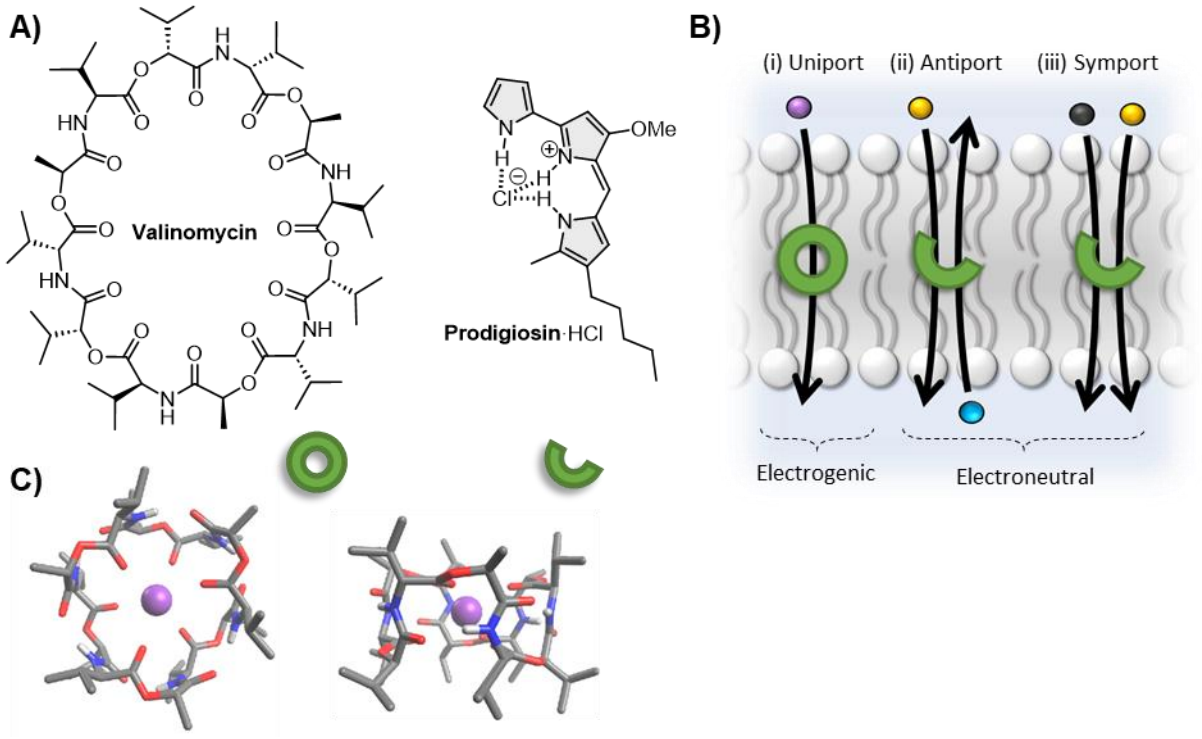

Figure 1.2 Mobile carriers found in nature and their ion exchange processes. *A) Structures of valinomycin and prodigiosin. B) Schematic of the uniport, antiport and symport ion exchange processes facilitated by ion transporters, which either change the net change across the membrane (electrogenic) or maintain the charge distribution (electroneutral). C) Top and side view of the K^+-valinomycin crystal structure.*[14]

Transmembrane protein channels, unlike natural product mobile carriers, can display stimuli-responsive behaviour in the form of gated-ion channels. In response to a stimulus (e.g. ligand binding, membrane potential, temperature, mechanical force and light), gated-channels undergo a conformational change to open the pore and allow the dissipation of ions down a concentration gradient.[6] Light-responsive channelrhodopsins employ the chromophore retinal as the light-sensitive molecule which switches conformation and induces a global change in conformation of the channel to regulate the opening and closing of the pore (**Figure 1.3A**).[15] The structure of the natural anion-conducting channelrhodopsin (*Gt*ACR1) has only recently been reported, discovered in the cryptophyte algae *Guillardia theta*.[16] The dimeric channel has a structure similar to previously reported cation-conducting channelrhodopsins, each monomer contains a retinal molecule bound through a lysine residue to form a Schiff base. The Schiff base region of *Gt*ACR1 is responsible for the anion selectivity and controlling the flow of anions, such that in the all-*trans*-retinal state there is a local positively charged region which inhibits the transport of anions, but in the 11-*cis*-retinal state the conformation of the pore adapts to allow ion flux.[17]

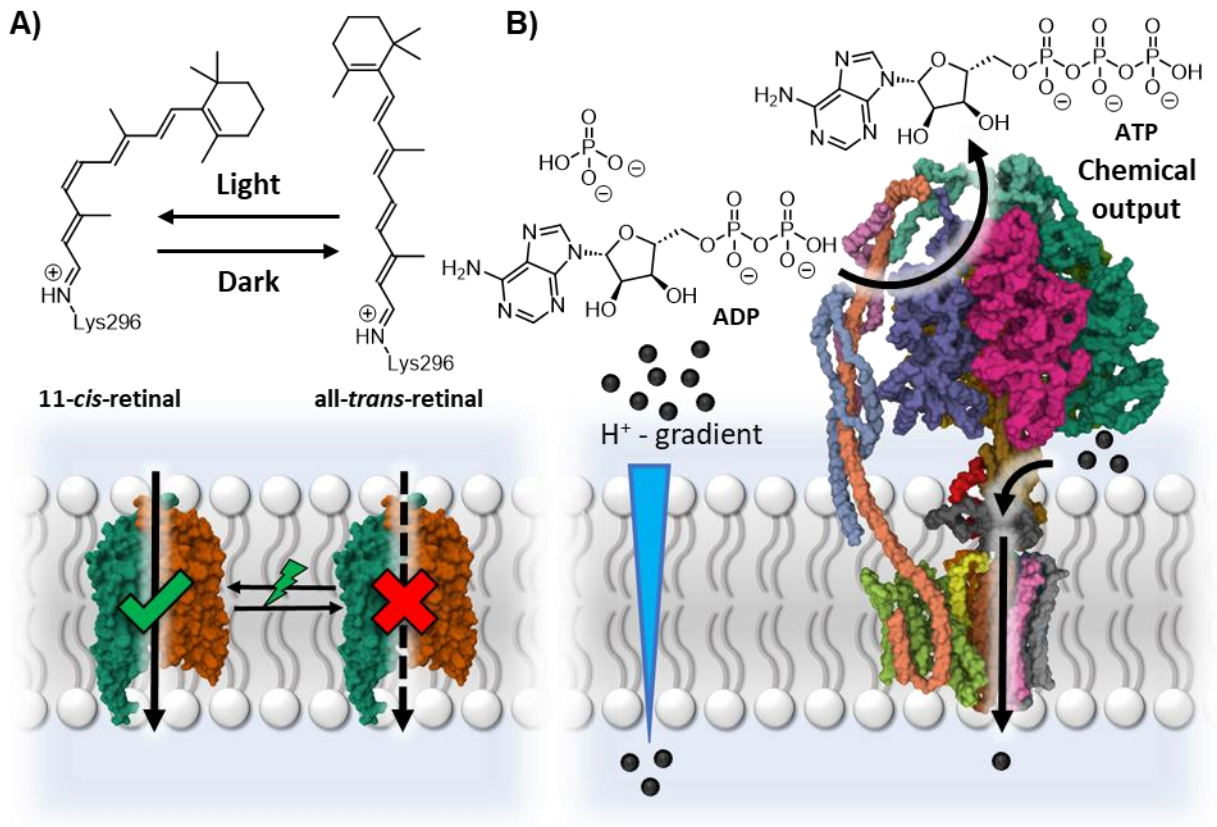

Figure 1.3 Gated-ion channel and biological molecular machine ion pump. *A) The anion-conducting channelrhodopsin GtACR1 (PDB ID: 6CSM)[16] responds to light through isomerisation of a double bond of retinal. 11-cis-retinal opens the pore of GtACR1 allowing chloride transport, while all-trans-retinal blocks the pore turning off anion transport. B) Dissipation of the proton gradient through ATP synthase (PDB ID: 5FIL)[18] leads to the chemical synthesis of ATP from ADP.*

Channels may also display the unique property of active transport, where transmembrane ion pumps drive the transport of ions against their concentration gradient perturbing the system from equilibrium. Perhaps the best-known active transporter is adenosine triphosphate (ATP) synthase (**Figure 1.3B**).[18] Typically, the transport of protons down a concentration gradient drives the rotation of the ATP synthase rotor subunit, which conformationally manipulates adenosine diphosphate (ADP) and an inorganic phosphate to lower the energy barrier to ATP synthesis.[19] The dissipation of the concentration gradient in this mode of operation drives the mechanical rotation of this biological molecular machine to synthesise ATP in a process called oxidative phosphorylation. The reverse operation is however also possible, where the release of energy from ATP hydrolysis drives the rotation of ATP synthase to facilitate the active transport of a proton against its concentration gradient. The ability of naturally occurring

protein channels capable of stimuli-responsive behaviour, and of ion pumps operating away from equilibrium has facilitated the evolution of life and these biological molecular machines continue to serve as a source of inspiration to supramolecular chemists.

1.2 Synthetic Ion Transporters Mimicking Biotic Mechanisms of Transport

Mimicking the operation of biological systems is a longstanding goal in supramolecular chemistry. The potential of synthetic analogues of mobile carriers and ion channels to serve as therapeutics, tools for chemical biology and to further the scientific understanding of biological processes are significant draws to the field of membrane supramolecular chemistry.[20,21]

1.2.1 Synthetic Unimolecular Ion Channels

Inspired by the hourglass-like shape of the selectivity filter located in the pore of the *Salmonella typhimurium* chloride ion channel (StClC), Wang and co-workers reported a highly Cl^- selective synthetic unimolecular ion channel.[22] The structure of channel **1a** contained a central electron-deficient tetraoxacalix[2]arene[2]triazines macrocycle with a persistent 1,3-alternating conformation. The four pendant arms of the central macrocycle therefore extend in alternate directions forming a saddle-shape mimetic of StClC (**Figure 1.4**). Channel **1a** conductance experiments were conducted in 1-palmitoyl-2-oleoyl-*sn*-glycero-3-phosphocholine (POPC) large unilamellar vesicles (LUVs) and in black lipid membranes (BLM). The transport activity of **1a** was shown to be strongly dependent on the anion present when tested in POPC LUVs with the halide responsive dye lucigenin encapsulated. Studies with LUVs prepared from dipalmitoylphosphatidylcholine (DPPC), a lipid with a gel-to-liquid crystalline phase transition at 41 °C, showed equivalent transport activity at 25 °C and 45 °C. The temperature-independent ion transport activity of **1a** in DPPC LUVs, and the observation of

square-like current signals in BLM experiments are characteristic of a channel mechanism. BLM experiments also allowed the quantification of the Cl^- > Br^- selectivity of channel **1a** to be measured by adding different anion containing buffer solutions on either side of the planar lipid bilayer (cis/trans = 1.0 M KCl/1.0 M KBr). Measuring the current of ion flow supported by channel **1a** at different applied voltages in this asymmetric ion conditions allowed the Cl^-/Br^- selectivity of 23-fold to be determined. A subsequent derivative **1b** has been reported, with phenolic alcohols in the central macrocycle which displayed enhanced Cl^-/Br^- selectivity of 66-fold.[23] The cooperation of hydrogen bonding and anion–π interactions located within the central macrocycle contributes to the high chloride selectivity of the synthetic channel **1b**.

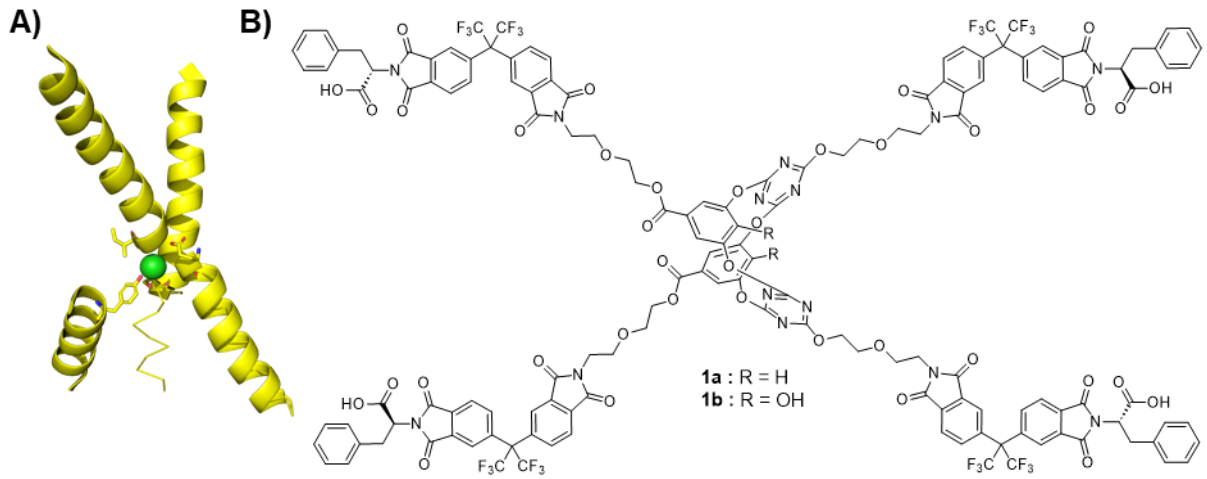

Figure 1.4 Biomimetic unimolecular Cl^- selective ion channel. *A) StClC chloride channel with key helical domains (PDB: 1KPL).[24] B) Structure of unimolecular Cl^- selective ion channel **1**.[22,23]*

Another biomimetic unimolecular channel, comprising of 6 peptide chains appended to a central α-cyclodextrin core (**2**) was reported by Chen and co-workers (**Figure 1.5**).[25] Based on the structure of the K^+ channel from *Streptomyces lividans* (KcsA), the pendant peptide sequence of channel **2** consists of the signature sequence (TVGYG) of the KcsA selectivity filter.[26] The terminal three tryptophan amino acids promoted membrane insertion and served as anchoring groups to stabilise the membrane spanning channel structure. When tested in

LUVs and BLM the channel displayed high activity for K^+ transport, with an 8-fold selectivity preference for K^+/Na^+. Importantly, **2** could be added to pre-formed vesicles to mediate transport, demonstrating efficient incorporation and arrangement into the active pore structure within the membrane (**Figure 1.5B**). The ability of **2** to insert into cell membranes and mediate the transmembrane transport of K^+, was also investigated. Utilising the 3-[4,5-dimethylthiazol-2-yl]-2,5 diphenyl tetrazolium bromide (MTT) assay, **2** (5 µM) was incubated with various cell lines (human breast cancer MCF-7, human cervical cancer HeLa, and human colon cancer HCT-116) to determine the ability of the synthetic transporter to disrupt cellular K^+ homeostasis and eventually trigger apoptosis of cells. Only live cells are capable of reducing MTT to the purple formazan product and as such this colorimetric assay can report on the proportion of cells in a population which are viable (**Figure 1.5C**). Due to the significant reduction of colour detected in the presence of **2** for all cell line compared to the control, this suggests that the cytotoxicity of **2** is likely due to its ability to perturb K^+ homeostasis.

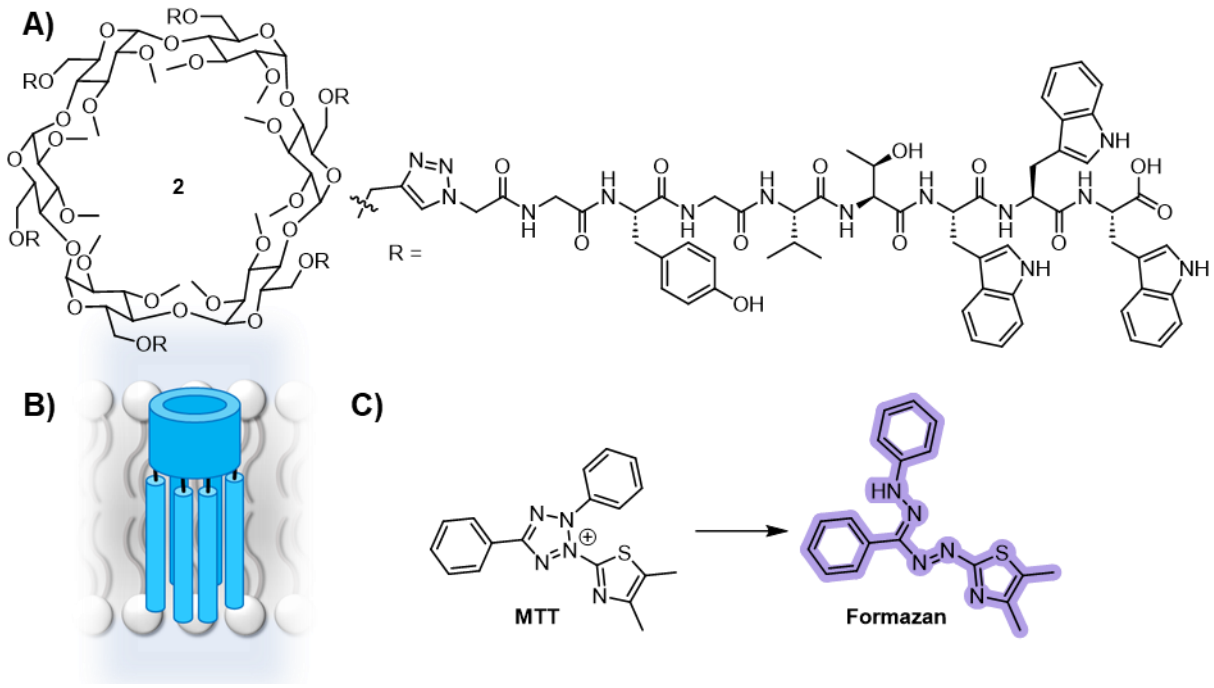

Figure 1.5 Synthetic unimolecular channel with biological activity. *A) Structure of KcsA mimetic peptide appended α-cyclodextrin channel* ***2****. B) Schematic of* ***2*** *embedded in a membrane. C) Structure of MTT and the reduced purple Formazan.*

1.2.2 Synthetic Self-Assembled Ion Channels

Unimolecular channels are in general synthetically more challenging to obtain due to their large molecular size, therefore reports of small molecules which self-assemble into an ion channel in the membrane are more common.[27] Such small molecules typically contain receptor units for ion binding, lipophilic components to promote membrane insertion, and recognition motifs which facilitate self-assembly.[21] A K^+ selective supramolecular ion channel reported by Barboiu and co-workers self-assembled from monomer **3** exemplifies these design criteria. (**Figure 1.6A-B**).[28] The different sized crown ether transporters **3a-b** were added externally to pre-formed LUVs with encapsulated 8-hydroxypyrene-1,3,6-trisulfonate (HPTS, pK_a = 7.2). Addition of NaOH (ΔpH = 0.8) to the extravesicular buffer created a pH gradient across the membrane, which was dissipated by the transporters and observed as a change in the ratiometric fluorescent response of the entrapped HPTS. Analysis of the transport activity data revealed that multiple molecules were implicated in the transport process, likely self-assembling into a membrane spanning stack promoted by intermolecular hydrogen bonding between urea groups. The hexyl chain increased the lipophilicity of the transporter, promoting membrane deliverability of **3a** and **3b**, while the crown ether facilitates cation binding and transport.

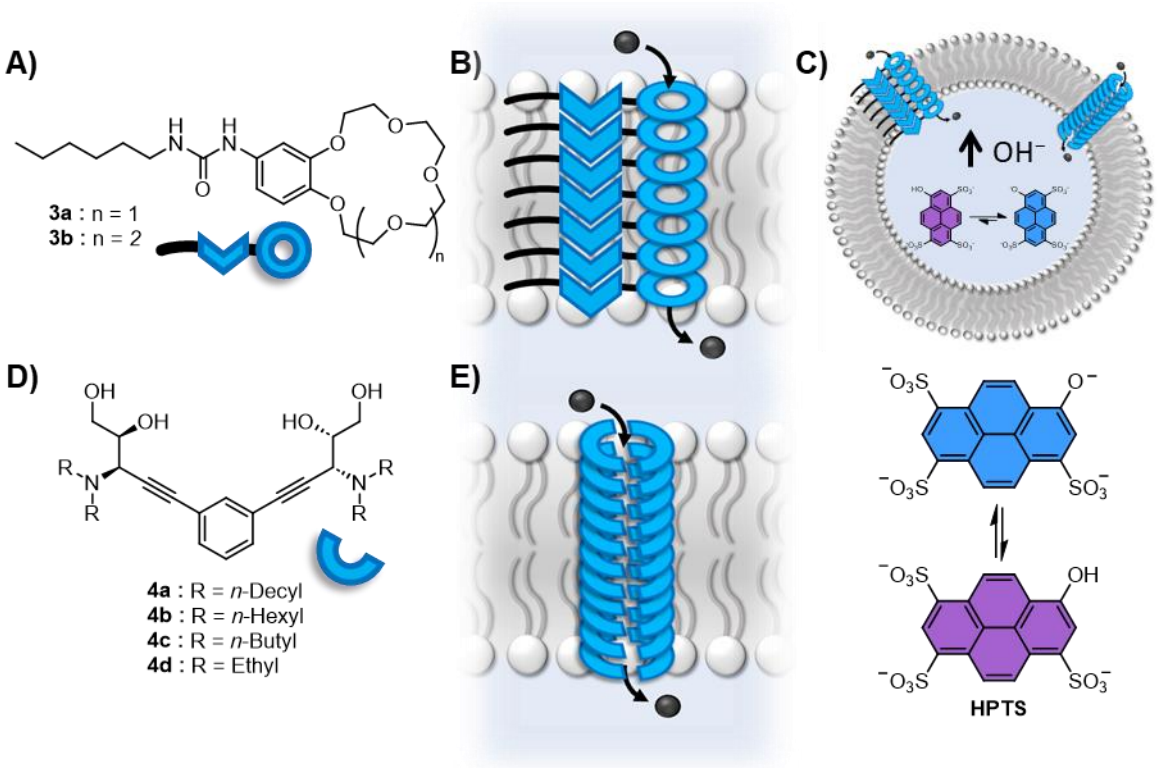

Figure 1.6 Supramolecular self-assembled ion channels mediate intravesicle pH change. *A) Structure of Barboiu's cation transporters* ***3a-b***.[28] *B) Schematic of the self-assembled K^+ ion channel. C) Schematic of transporter mediated intravesicle pH change reported by the fluorescence output of HPTS. D) Structure of Talukdar's bioactive monomer* ***4a-d***.[29] *E) Schematic of the self-assembled Cl^- ion channel.*

Talukdar and co-workers reported a chloride-selective supramolecular ion channel self-assembled from monomer **4**, which was tested in model vesicle and cells.[29] The bis-diol derivatives **4a-d** were tested in HPTS loaded LUVs (**Figure 1.6C-E**). The varying alkyl chain length of the transporters resulted in a significant difference in measured transport activity, with the butyl derivative **4c** showing the highest transport activity. The alkyl chains were suggested to influence the deliverability of the transporter to the membrane and stabilise the supramolecular channel structure through anchoring it at the hydrophobic layer of the membrane. For the longest chain derivative **4a**, the poor transport activity was attributed to the lower aqueous solubility and hence reduced deliverability to the bilayer. The shortest derivative **4d** was more water soluble, but therefore had a lower stabilising effect due to the decreased solubility in the hydrophobic region of the membrane. The terminal diol units were

necessary to promote self-assembly, forming dimers through hydrogen bonding interactions with complementary vicinal diols of the partner molecule. BLM experiments showed periodic opening and closing events for **4c** characteristic of channel formation, which was suggested to involve stacks of dimers in the membrane to form a pore through which ion transport could occur.

The transport activity and subsequent bioactivity of the self-assembling Cl^- ion transporter **4c** was tested in cells (**Figure 1.7**).[29] HeLa cells incubated with the cell-permeable chloride sensitive dye *N*-(ethoxycarbonylmethyl)-6-methoxyquinolinium bromide (MQAE) showed significant quenching of MQAE fluorescence intensity upon addition of **4c**, confirming the ability of this supramolecular channel forming monomer to effect chloride transport across cellular membranes. The cell viability of a range of cell lines was investigated in the presence of **4c**, to access the effect of chloride transport across cell membranes. The impact of **4c** on the viability of a range of cancerous (lung adenocarcinoma epithelial A549, human cervical cancer HeLa, human breast cancer MCF7, and human bone osteosarcoma U2OS) and normal (mouse fibroblast NIH3T3) cell lines was tested using the MTT assay. Incubation of **4c** (10 μM) with the different cell types led to significant cell death, which was shown to be decreased in the absence of chloride in the extracellular media. To investigate the mode of Cl^- ion transport mediated cell death, the effect of **4c** on the mitochondrial membrane potential of HeLa cells was investigated with the dye 5,5',6,6'-tetrachloro-1,1',3,3'-tetraethyl-imidacarbocyanine iodide (JC-1). JC-1 exhibits a red fluorescence emission as a result of *J*-aggregation in healthy mitochondrial membranes, while depolarisation and subsequent dispersion of the dye in the cytosol results in a green fluorescence emission.[30] Incubation of HeLa cells with varying concentrations of **4c** followed by treatment with JC-1 dye resulted in a dose dependent decrease in red fluorescence, with a concurrent increase in green fluorescence, confirming

that **4c** induced a depolarisation of the mitochondrial membrane. As a result of the disruption of the membrane potential, the production of reactive oxygen species (ROS) increased within the cell leading to subsequent release of cytochrome *c* and eventual apoptosis *via* a caspase-dependent pathway. This study on the biological consequences of Cl^- transport mediated by a synthetic supramolecular channel demonstrated that the self-assembly of small molecules in cellular membranes can induce apoptosis in cancer cells and as such may be a potential tool for therapeutic treatment in the future.[31]

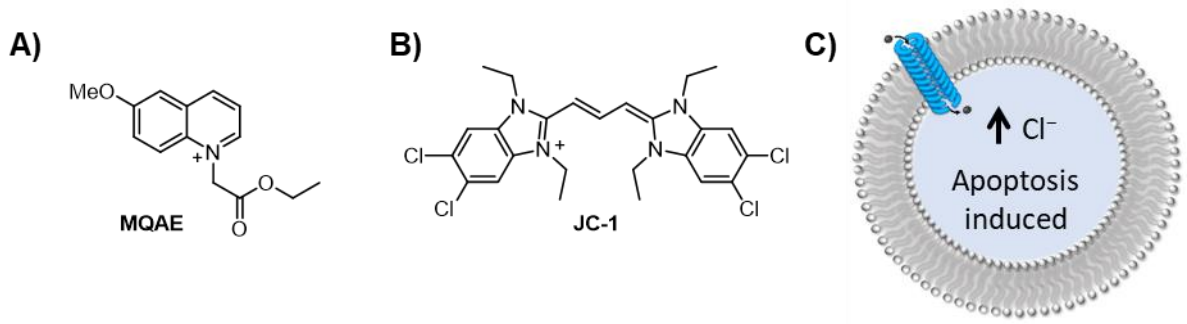

Figure 1.7 Supramolecular self-assembled channel induces apoptosis in cancer cells. *A) Structure of the cell-permeable chloride sensitive dye MQAE. B) Structure of membrane potential sensitive dye JC-1. C) Schematic of Cl^- mediated transport initiating apoptosis.*

1.2.3 Synthetic Mobile Ion Carriers

Small molecules capable of mediating ion transport *via* a mobile carrier mechanism represent the largest group of synthetic transporters reported to date, with anion mobile carriers being the most common.[32] As such a thorough understanding of the design criteria for synthetic mobile carriers has been established.

The mechanism of mobile carrier mediated ion transport involves four key steps (**Figure 1.8A**). First, ion binding to the mobile carrier occurs at the membrane-aqueous interface (**step i**).[33] Second, the ion-transporter complex translocates through the hydrophobic interior of the membrane (**step ii**). Third, the ion dissociates from the mobile carrier and is released at the opposite membrane-aqueous interface from which it was sequestered (**step iii**). Fourth, the

mobile carrier translocates back through the membrane interior to its original position to repeat the cycle (**step iv**). In general, for anion transport the binding of the ion to the mobile carrier at the membrane-aqueous interface (**step i**) is the rate-limiting step of the process.[34,35] Changing mobile carrier design to influence this step therefore controls the activity of the transporter.

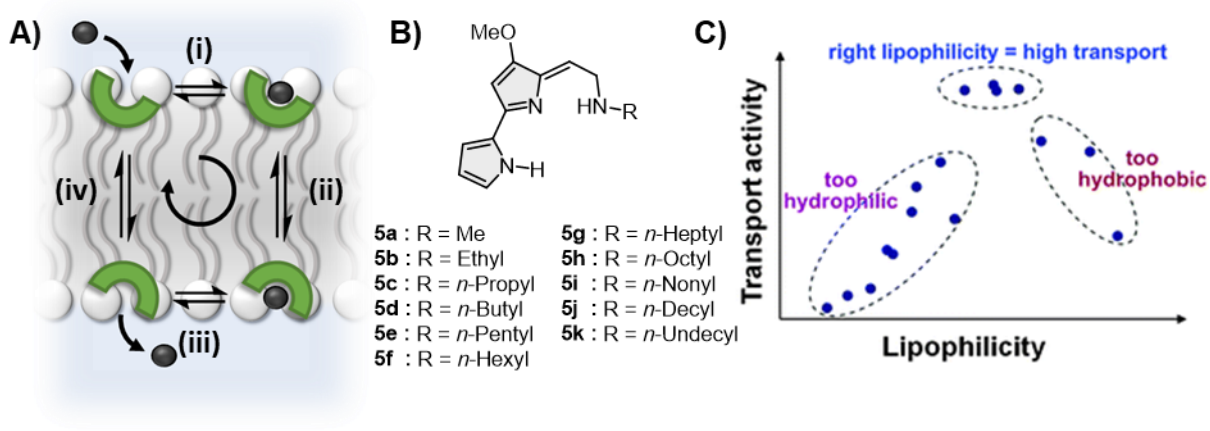

Figure 1.8 The effect of lipophilicity on mobile carrier transport activity. *A) Schematic of the mobile carrier transport mechanism. B) Structure of Quesada's tambjamine derivatives* ***5a-k****.*[36] *C) Relationship of transport activity on the lipophilicity of anion transporters* ***5a-k****, adapted from Quesada et al.*[36]

The role of lipophilicity on the transport activity of mobile carriers has been investigated by Quesada and co-workers.[36,37] A series of tambjamine derivatives **5a-k** were synthesised of varying alkyl chain length and tested for their anion transport capability across POPC LUVs (**Figure 1.8**).[36] The varying length of the R-group gave a series of mobile carriers with the same anion binding strength but varying lipophilicity, which is known to be a parameter of paramount importance in the pharmaceutical industry.[38] Transporter mediated chloride efflux from chloride loaded LUVs in the presence of external bicarbonate was monitored using a chloride ion selective electrode (ISE). The initial rate of chloride efflux was found to follow a gaussian-dependence on the lipophilicity of the transporter, as quantified by the log*P* value with a maximum transport activity observed at log*P* = 4.2.

Gale, Davis and co-workers later expanded on this principle, highlighting the importance of lipophilic balance (**Figure 1.9**).[39] *N*-Arylthioureas **6a-e** were synthesised with the same molecular formula and hence almost identical binding strength and lipophilicity, but different position of the receptor unit relative to the length of the molecule. These derivatives were pre-incorporated into POPC LUVs with lucigenin encapsulated to measure the influx of chloride ions by fluorescence spectroscopy. Pre-incorporation of the transporters during vesicle preparation negated the influence of membrane deliverability which is known to impact transport activity.[40] A gaussian-dependence of the initial rate of chloride influx on the length of R_1 demonstrated the position of the anion binding site in the middle of the mobile carrier design was optimal for transport activity. This was suggested to be a result of a higher energy barrier to the translocation of the anion-mobile carrier through the membrane interior for an amphiphilic, surfactant-like structure compared to a structure with the binding receptor positioned in the centre of the molecule.

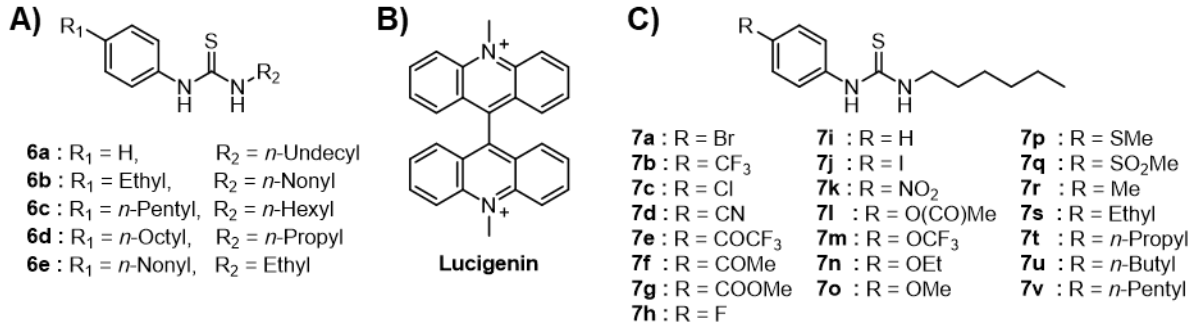

Figure 1.9 Investigating substituent effects on mobile carrier activity. *A) Gale's N-arylthioureas* ***6a-e*** *demonstrated the importance of lipophilic balance.*[39] *B) Chloride sensitive dye lucigenin. C) Gale's para-substituted 1-hexyl-3-phenylthioureas* ***7a-v*** *demonstrated the importance of lipophilicity, molecular shape and hydrogen bond acidity of the binding group.*[41]

Quantitative structure–activity relationship (QSAR) analysis of a family of *para*-substituted 1-hexyl-3-phenylthiourea (**7a-v**) enabled the key structural features which impacted transport activity to be determined (**Figure 1.9C**).[41] After quantification of the transport activity of each derivative using a standard ISE assay with POPC LUVs, QSAR analysis was applied to identify

parameters which correlated with transport activity. Lipophilicity of the transporter was again shown to strongly influence transmembrane anion transport in line with previous studies,[35,36] and to a smaller degree the molecular size and hydrogen bond acidity of the binding group were also shown to impact activity.

A range of intermolecular interactions have been employed for the recognition of ions by mobile carriers, for transmembrane ion transport. Common HB receptor units such as ureas,[42] thioureas,[43] squaramides[44] and thiosquaramides[45] have been reported for anion transport by mobile carriers (**Figure 1.10**). The stronger the electron withdrawing nature of the substituents on the binding receptor the more acidic the proton and therefore the stronger the anion binding interaction.[46] However, increasing the acidity of the hydrogen bond donor can result in deprotonation and generation of an anionic receptor which no longer binds anions and is therefore an ineffective anion mobile carrier.[45]

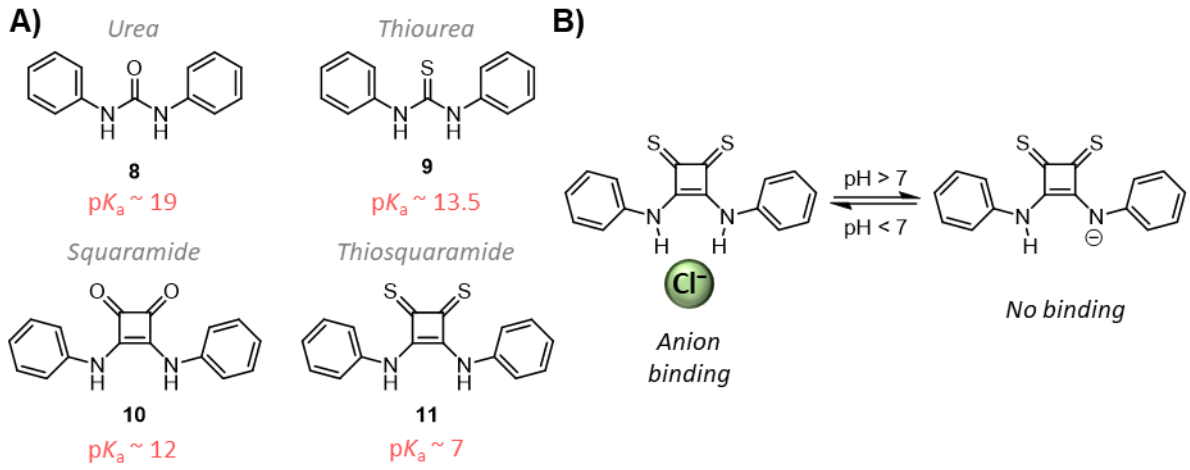

Figure 1.10 Common HB functional groups employed for anion binding. *A) Structure of HB receptor units and corresponding pK_a values of acidic proton. B) pH dependent anion binding by thiosquaramide receptor* ***11****.*[45]

1.2.4 Therapeutic Importance of Selective Anion Transporters

For the application of synthetic ion transporters as therapeutics it is essential to design highly selective transporters. Obtaining high ion specificity will enable the transport of the target ion

for therapeutic activity and minimise off target activity leading to unwanted side effects. The development of chloride selective transporters is an area of current interest for the potential treatment of cystic fibrosis,[47–49] which is caused by mutations in the cystic fibrosis transmembrane conductance regulator (CFTR) gene resulting in defects in the transmembrane protein channel. Malfunctioning CFTR protein channels are generally characterised by a reduced aperture or blocked pore which reduces ion flux and is expressed in patients as a build-up of thick mucus in the lungs. Synthetic transporters have the potential to replace the loss of function from this channelopathy, so long as they are highly chloride selective so as not to perturb the homeostasis of other ion gradients in the body.

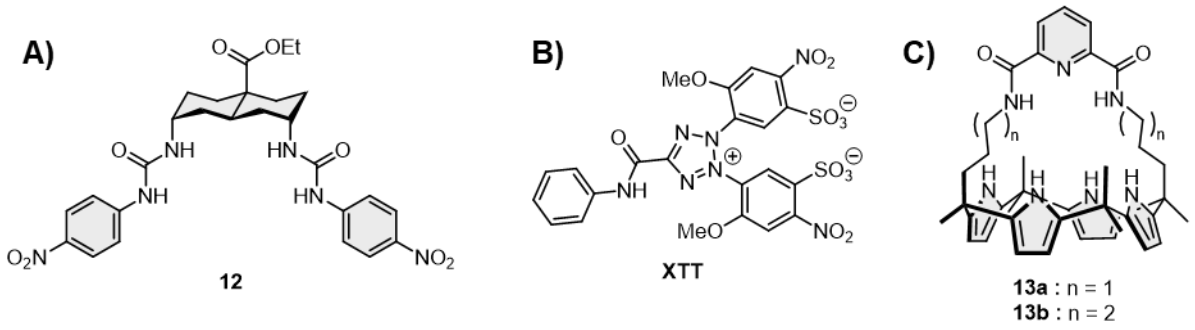

Figure 1.11 Structure of biologically active anionophores. *A) Davis and Sheppard's decalin-based **12** mediates Cl^-/I^- antiport across FRT cell membranes.[50] B) Structure of live cell responsive dye XTT. C) Gale and Sessler's strapped calixpyrroles **13a-b** facilitate Cl^-/Na^+ symport in A549 and HeLa cells.*[51]

Sheppard, Davis and co-workers investigated the activity of synthetic anion carriers in Fischer rat thyroid (FRT) cells with the halide-sensitive yellow fluorescent protein (YFP) expressed within the cells.[50] Through testing a range of cholapod, decalin and cyclohexane-based hydrogen bonding anionophores, the ability of the transporters to effect Cl^-/I^- antiport across the cellular membrane of live cells was assessed. The decalin based transporter **12** was found to be the most active in the live cell assay and was shown to be non-toxic by the sodium 2,3-bis(2-methoxy-4-nitro-5-sulfophenyl)-5-[(phenylamino)-carbonyl]-2H-tetrazolium) (XTT) cell viability assay (**Figure 1.11A-B**). Interestingly, the transport activity in the live cell assay did

not translate well from model LUV studies, demonstrating the importance of studying synthetic anionophores in a range of bilayer environments to fully characterise their mechanism of action. Deliverability of the hydrophobic transporters to LUVs was observed to significantly affect activity, where a loss of transport efficacy from external addition compared to pre-incorporation was determined to be due to poor aqueous solubility and inability to incorporate into the pre-formed vesicle bilayer. To control for differences in deliverability of the anionophores in the live cell assay, all transporters were pre-incorporated into delivery vesicles which were then incubated with the cells prior to perturbing the chloride ion gradient and measuring transport activity. In follow up work by Gale, Sheppard and Davis the FRT cell assay was adapted where wild-type human CFTR or the defective F508del-CFTR mutant was co-expressed in the cells to investigate the effect of synthetic anionophores to recover faulty CFTR activity.[52]

A family of strapped calixpyrroles (**13a-b**) reported by Gale and Sessler demonstrated that transporter mediated chloride transport induced cell apoptosis in a number of cancer cell lines (**Figure 1.11C**).[51] Prior to this work, the direct correlation between a change in cellular chloride anion concentration and cytotoxicity had not been determined for synthetic carriers.[51] However, through time-dependent fluorescent studies the chloride concentration within A549 and HeLa cells could be monitored by YFP and was observed to precede cell apoptosis. These mobile carriers were found to mediate Cl^-/Na^+ symport increasing intracellular concentrations of the two ions, which led to increased cellular ROS levels, causing the release of cytochrome *c* from the mitochondria and initiating caspase-mediated apoptosis. This study, along with results of anticancer activity of Prodigiosin which operates *via* a Cl^-/H^+ symport mechanism,[53] emphasises the importance of characterising the transporter selectivity and ion exchange process. Interestingly, decalin **12** is more active than the calixpyrroles **13a** and **13b** when

tested in LUVs, but did not induce cell apoptosis in HeLa cells even when loaded at a higher concentration, attributed to the Cl^-/I^- antiport mechanism differing from the cytotoxic calixpyrrole Cl^-/Na^+ symport mechanism.

1.2.5 Sigma-Hole Based Mobile Carriers

Synthetic anionophore therapeutics for channelopathies typically rely on Lewis-acidic hydrogen bond donors for anion binding. HB-based motifs, such as the urea and amide functionalities in **12** and **13**, are frequently employed reflecting the strategies developed in the parent field of anion recognition. Recent advances in receptors based on sigma-hole noncovalent interactions such as halogen bonding (XB), chalcogen bonding (ChB), and pnictogen bonding (PnB) to mediate anion recognition[54–56] has inspired their application to anion transport.[57]

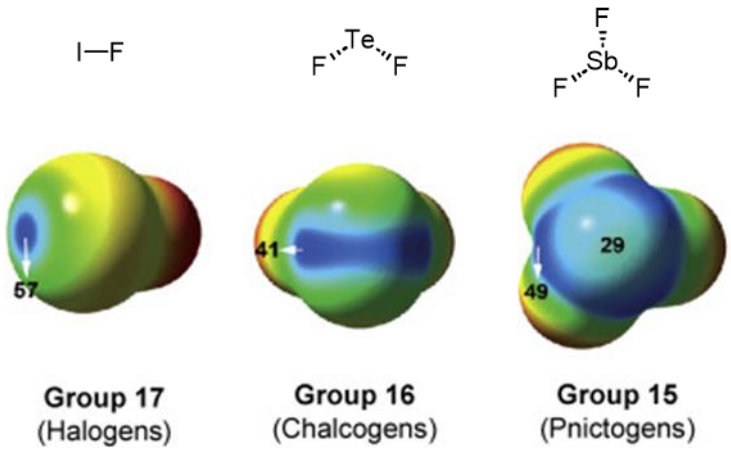

Figure 1.12 Graphical representation of sigma-hole interations. *Computed molecular electrostatic potential surface of Group 15-17 elements of the same period bonded to fluorine with representative sigma-holes shown in blue. Figure adapted from Lim and Beer.*[56]

Sigma-hole interactions are characterised by the Lewis-acidic electron deficient regions, coined 'σ-holes', which arise on main-group 17, 16 or 15 elements (XB, ChB and PnB respectively) bonded to electron-withdrawing functionalities.[56] The main group element exhibits an anisotropic distribution of the electron cloud, with points of partial positive charge

(one for XB, two for ChB and three for PnB, **Figure 1.12**) surrounded by regions of electron density termed the 'electronegative belt.' In sigma-hole interactions, the σ-hole at the pole of the σ* of the R-X bond attractively interacts with Lewis bases (i.e., anions), while the surrounding electronegative belt repels the incoming negative charge resulting in a highly directional interaction. While electrostatics are the dominant component in hydrogen bonding, significant charge-transfer between the main group element and Lewis base in a sigma-hole interaction renders them more resistant to increases in solvent polarity, allowing strong binding even in aqueous media.[58] Therefore, sigma-hole interactions hold great promise for generating highly active and selective anionophores.

Matile and co-workers developed the first sigma-hole based anion mobile carriers employing halogen bonding iodoarene receptors.[59,60] Langton and co-workers later demonstrated that iodotriazole XB receptors also mediate anion transport and that their activity was in general improved relative to the prototriazole HB analogue (**Figure 1.13**).[61] Interestingly, when testing the selectivity of the XB and HB derivative of **14,** the XB transporter **14^{XB}** showed selectivity for halide anions over hydroxide. The transport activity of **14^{XB}** was therefore limited by OH^- transport, while the HB transporter **14^{HB}** displayed Cl^--limited transport activity. The selective transport of $Cl^- > OH^-$ by **14^{XB}** suggests that halogen bonding transporters have great potential as therapeutics in the future to replace the lost function of CFTR for the treatment of cystic fibrosis.

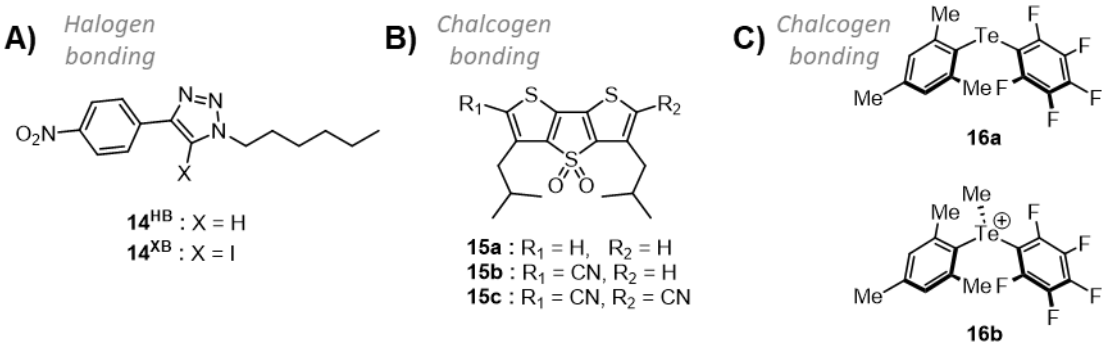

Figure 1.13 Sigma hole-based anion mobile carriers. *A) HB and XB triazoles (**14^{HB}** and **14^{XB}**) reported by Langton and co-workers.[61] B) ChB 2,2'-bithiophene based receptors (**15a-c**) reported by Matile and co-workers.[62] C) Tellurium-based ChB anion mobile carriers (**16a-b**) reported by Gabbaï and co-workers.[63]*

Chalcogen bonding anion mobile carriers were first reported in 2016 by Matile and co-workers (**Figure 1.13**).[62] Two σ-holes on an electron deficient group 16 atom occur, where the σ* orbitals extend in the opposite direction to the C-X bonds. The 2,2'-bithiophene based receptors (**15a-c**) comprising a bidentate chalcogen bonding based receptor unit were synthesised and their transport activity was evaluated in egg yolk L-α-phosphatidylcholine (EYPC) LUVs using the HPTS assay. The addition of electron withdrawing nitrile substituents increased the strength of the binding interaction leading to an increase in the observed transport activity. These transporters utilise sulfide-based receptors with sulfur in the +2 oxidation state, however various oxidation states are available to chalcogens which modulates the strength of the chalcogen bonding interaction. Gabbaï and co-workers demonstrated that the oxidation state of tellurium based mobile carriers impacts the Lewis acidity of the receptor unit and hence chloride anion transport properties.[63] Diaryltelluride **16a** and methyldiaryltelluronium **16b** were synthesised and tested for chloride transport activity in EYPC LUVs using an ISE assay. The improved transport activity of **16b** relative to **16a**, was suggested to be the result of the Te(IV) centre having a deeper σ-hole compared to the Te(II) centre.

The groups of Matile and Gabbaï have pioneered the use of pnictogen bonding anion mobile carriers (**Figure 1.14**).[64] A comparative study reported by Matile and co-workers introduce pnictogen bonding to ion transport and compared this intermolecular interaction to isostructural XB and ChB mobile carriers (**17**).[65] **17^{PnB}** showed diminished transport activity relative to the **17^{ChB}**, but enhanced activity compared to the XB derivative **17^{XB}**. Despite the increase in association constant of Cl^- with **17^{PnB}** compared to **17^{ChB}**, the lower transport activity was attributed to the propensity of the PnB receptors to form supramolecular 3D aggregates with anions which inhibited transport activity. Conducting assays with the self-quenching dye 5(6)-carboxyfluorescein (CF) entrapped within POPC LUVs allowed the ability of compounds to cause membrane disruption to be evaluated. Interestingly, tris-perfluoroarylstibane **18** when tested caused a concentration-dependent increase in CF fluorescence indicative of membrane disruption and leakage of the dye into the extra-vesicular environment. The inactivity of **17^{PnB}** in the CF assay suggested that the observed transport activity was a result of mobile carrier activity, while **18** operates as a self-assembled ion channel confirmed by BLM experiments.

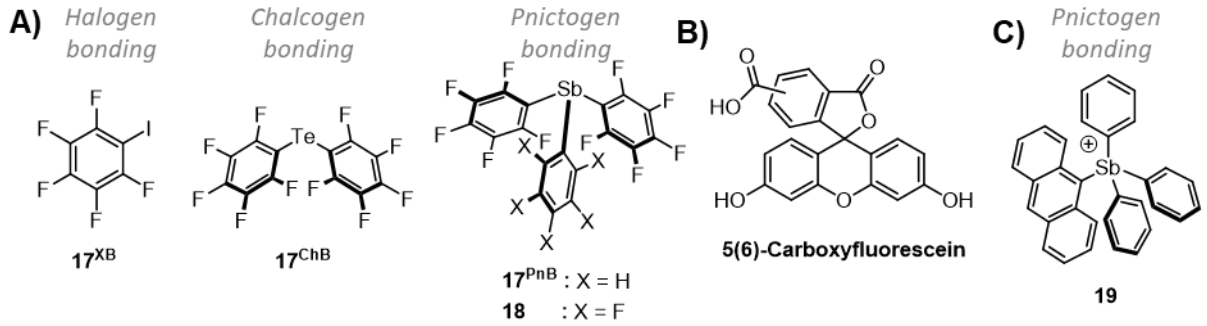

Figure 1.14 Sigma hole-based anion mobile carriers. *A) Matile's XB, ChB and PnB anion transporters (**17-18**).[65] B) Structure of concentration dependence fluorescent dye CF. C) Gabbaï's PnB mobile carrier **19**.[66]*

The fluoride transport activity of tetraarylstibonium and tetraarylbismuthonium cations was evaluated in POPC LUVs by Gabbaï and co-workers.[66,67] The anthracenyltriphenylstibonium **19** was shown to mediate fluoride transport *via* a mobile carrier mechanism across model POPC

membranes and was further tested in a biological setting (**Figure 1.14**). Human red blood cells were exposed to **19** in the presence and absence of fluoride in the extracellular media to investigate the effect of **19** mediated fluoride influx. An intracellular increase in fluoride concentration is known to cause oxidative stress and initiate hemolysis. Transporter **19** alone was found to be nontoxic, while hemolysis was significantly increased in the presence of **19** and fluoride compared to the background activity of fluoride alone. This suggests that the stibonium cation **19** facilitates transport of fluoride anions into RBCs, initiating hemolysis demonstrating the importance of controlling ion transport within biological settings.

1.2.6 Metal Coordination Facilitated Anion Transport

The ability of metal complexes to reversibly bind anions to the metal centre through ligand exchange has been used to mediate anion transport across lipid bilayer membranes (**Figure 1.15**).[68] Tecilla and co-workers demonstrated that the Pd complex **20** mediates anion transport when tested in the HPTS assay.[69] The square planar palladium complex comprises of a bidentate phosphine ligand (inert to ligand exchange) and two exchangeable ligands which can be displaced by a guest anion. The more labile triflate derivative **20b** demonstrated enhanced transport activity relative to the chloro derivative **20a** highlighting the importance of ion exchange at the metal centre for ion transport activity. A further study by the same group found that lipophilicity of the complex played a key role in transport activity.[70]

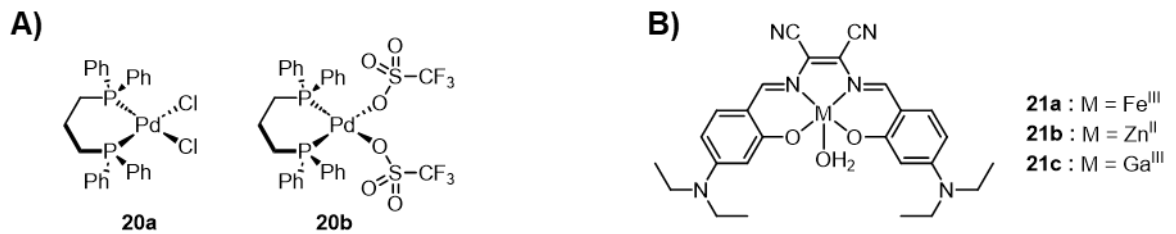

Figure 1.15 Metal complexes which display mobile carrier mediated anion transport activity. *Tecilla's diphosphine-Pd(II) complexes (**20a-b**).[69] Zhang's metal-salen complexes (**21a-c**).[71]*

A range of metal salen-based complexes (**21a-c**) reported by Zhang and co-workers have been tested for ion transport activity in model LUVs and subsequent anticancer activity *in vitro* and *in vivo*.[72] The transport activity of the different metal-salen complexes was tested using the HPTS assay with LUVs comprised of egg yolk L-α-phosphatidylglycerol (EYPG), EYPC, and cholesterol (1:10:2.5 by mass) to mimic organelle membranes. The Zn^{II} and Fe^{III} complexes showed low transport activity, while the Ga^{III} complex showed higher activity likely due to the higher Lewis acidity of this metal centre. The labile axial coordination sites of the Ga^{3+} complex **21c** serves as the binding site for the exchange of anions across the membrane as well as to bind phospholipids to promote membrane localization in the cellular media. The gallium complex had the lowest inhibitory concentration of the three complexes when tested for cytotoxicity. Depolarisation of the mitochondrial membrane by **21c** caused the release of iron-containing coenzymes into the cell which led to the generation of ROS *via* ferroptosis resulting in cell death.

1.2.7 Stimuli-Responsive Behaviour in Synthetic Mobile Carriers

While no stimuli-responsive naturally occurring mobile carriers are known, numerous synthetic systems have now been reported which display gated-mobile carrier activity.[73] Numerous stimuli have been utilised to control transport activity including temperature, membrane potential, pH, chemical stimulation, redox state and light.[74,75] The incorporation of gated-behaviour into synthetic transporters is paramount to their application as therapeutic agents in biological setting, to provide targeted activity reducing unwanted side effects.[76]

Jeong and co-workers reported an enzyme-responsive anion mobile carrier based on a sugar appended pro-carrier strategy (**Figure 1.16**).[77] The glucose group served to block a hydroxyl moiety which had previously been shown to be implicated in the binding of anions by **22a** for

transport across lipid membranes.[78] The transport activity of the pro-carriers **22b** and **22c** were tested in POPC LUVs in the presence and absence of the necessary enzyme using the lucigenin assay. Incubation of the pro-carrier **22b** with glycosylase for 3 hours or **22c** with galactosidase for 30 minutes was necessary to cleave the sugar and initiate transport. The sugar also increased the hydrophilicity of the molecule significantly which was attributed to be the main factor for the observed inactivity of **22b** and **22c** in the lucigenin assay. The galactosylated pro-carrier **22c** was also tested in FRT cells with the halide sensor YFP expressed intracellularly. Only after the addition of the appropriate enzyme (at pH=6) was transport initiated, demonstrating higher activity than free carrier **22a** added directly to the cells highlighting the improved deliverability of **22c** to the cellular membrane.

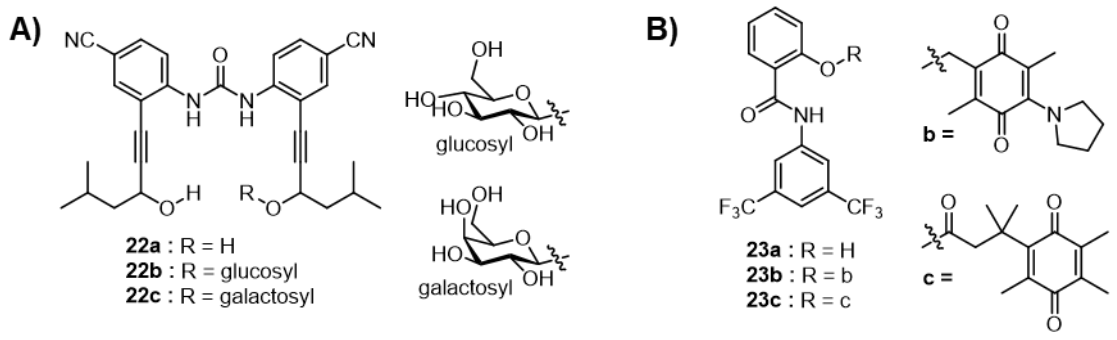

Figure 1.16 Enzyme responsive pro-carrier strategy for anion mobile carriers. *A) Jeong's sugar-appended pro-carrier strategy (**22a-c**).[77] B) Talukdar's NQO1-responsive anion mobile carriers (**23a-c**).[79]*

Talukdar and co-workers employed a similar strategy, demonstrating that enzyme-responsive mobile carriers activated by NAD(P)H dehydrogenase quinone 1 (NQO1, an enzyme abundant in cancer cells) displayed gated H^+/Cl^- symport activity (**Figure 1.16**).[79] The transport efficacy of **23a** was confirmed in HPTS loaded EYPC LUVs, operating as a H^+/Cl^- symport mobile carrier, while **23b** and **23c** showed no activity. The cytotoxicity of the derivatives **23a-c** was then tested in a range of cancer and non-cancer cell lines. Interestingly, the pro-carriers **23b** and **23c** showed significantly higher toxicity in MCF-7 breast cancer cells compared to the non-

cancerous HEK293T cells and MEFs, attributed to the higher concentration of enzyme NQO1, which is overexpressed in cancer cells. This strategy demonstrates the possible application of these pro-carriers as cancer tissue selective therapeutics. The transport process disrupted ion homeostasis in cancer cells and triggered apoptosis *via* mitochondrial membrane depolarisation, lysosomal deacidification, and generation of ROS.

The pro-carrier strategy is irreversible, however systems which show reversible control over activity have the potential to improve targeting for biological applications. Redox-responsive systems may act as reversibly gated-mobile carriers if the oxidation and reduction steps are reversible.[80] A number of irreversibly gated redox-responsive mobile carriers have been reported, however the chemical modulation of oxidation state could not be carried out *in situ*.[81,82] For example, Gale and co-workers reported the cycloaurated 1,3-bis(benzimidazole-2-yl)pyrimidine chloride complex **24b**, capable of reduction-initiation release of the anion transporter **24a** (**Figure 1.17**).[83] The gold complex **24b** displayed minimal transport activity, however in the presence of glutathione (GSH, a reducing agent) activity was restored to that of the parent transporter **24a**. The *in situ* reduction of Au^{III} to Au^{I} deprotects the binding site of this mobile carrier, but reversible complexation of the metal blocking group was not shown. Compounds **24a** and **24b** were also tested in cancerous and non-cancerous cell lines to determine their cytotoxicity. Interestingly, the cytotoxicity of the parent transporter **24a** in non-cancerous cells was higher than the protected carrier **24b**, attributed to the lower GSH concentrations, while comparable toxicity with observed in the cancer cell lines. This indicates that the free chloride transporter is selectively generated in reducing cancer tumour environments.

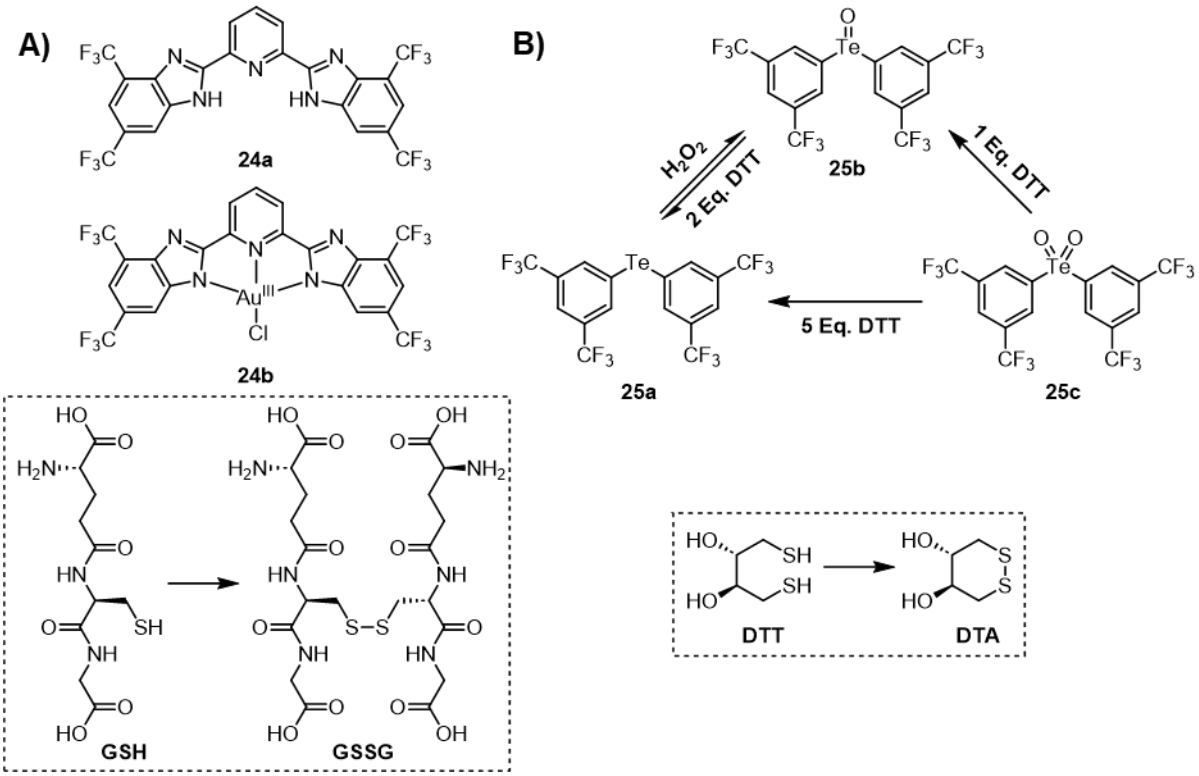

***Figure 1.17 Redox-responsive anion mobile carriers**. A) Gale's Au^{III} protected irreversible strategy (**24a-b**) with insert of GSH to glutathione disulfide (GSSG) redox couple.*[83] *B) Langton's tellurium-based anion mobile carrier reversible system (**25a-c**) with insert of DTT to dithiane (DTA) thiol-disulfide redox couple.*[84]

A tellurium-based ionophore reported by Langton and co-workers was capable of multi-state switching between three oxidation states (**Figure 1.17**).[84] The diaryltellurium receptor **25** does not bind chloride in the Te^{II} (**25a**) and Te^{VI} (**25c**) oxidation states, as revealed by ^{1}H NMR binding titrations, and are inactive transporters. In contrast, the telluroxide (Te^{IV}, **25b**) showed strong chloride binding affinity and as a result excellent transport activity in POPC LUVs with HPTS encapsulated. This three-state system could be efficiently reduced *in situ* with dithiothreitol (DTT), turning transport from OFF (Te^{VI}) to ON (Te^{IV}) and finally back OFF (Te^{II}). However, oxidation was inherently slow with H_2O_2 and could only be achieved switching from OFF (Te^{II}) to ON (Te^{IV}). These effects were justified by the enhanced Lewis acidity of the Te centre with oxidation state, however the additional oxo-group on the tellurone (Te^{VI}, **25c**) reducing steric accessibility of the anion to the Te centre was postulated to be responsible for the inhibited transport activity.

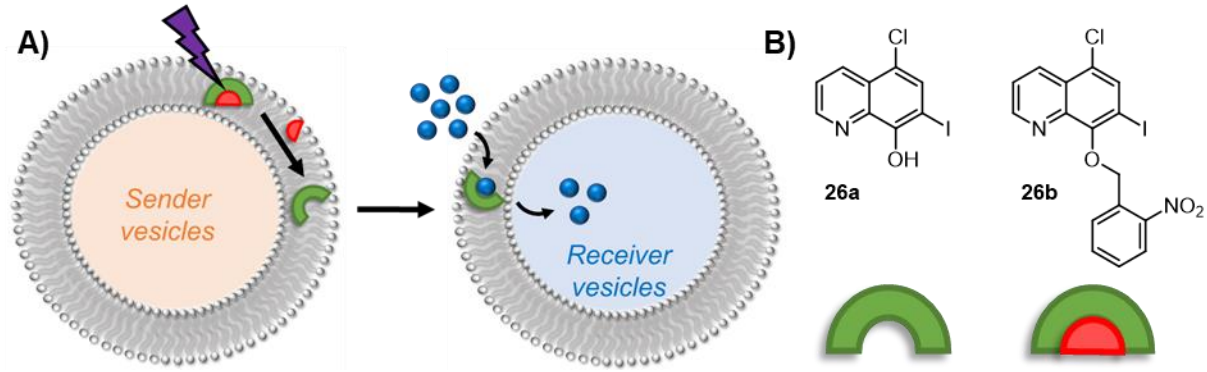

Figure 1.18 Inter-vesicle signalling system with a photo-gated cation mobile carrier. *A) Schematic of the signalling system reported by Langton and co-workers. B) Structure of clioquinol* ***26a*** *and ortho-nitrobenzyl protected* ***26b****.*[85]

Stimulation of synthetic transporters with light is attractive due to the prospect of high spatiotemporal activation using biocompatible wavelengths.[75] Photo-responsive systems may also be addressed without the need for the external addition of a chemical reagent and hence generation of chemical waste during operation. Irreversibly gated mobile carriers have been reported which involve the use of a photo-protecting group (PPG), either to block the binding sight[86,87] or to inhibit the mobility of the carrier.[88] A recently reported system from Langton and co-workers combines both strategies to control communication between artificial vesicles mimetic of the signalling systems adopted by bacteria in quorum sensing (**Figure 1.18**).[85] An *ortho*-nitrobenzyl PPG was used to block the binding site of the Zn^{2+} mobile carrier clioquinol **26a** and simultaneously reduce the aqueous solubility of the pro-carrier **26b**. When embedded within the membrane of sender vesicles the high lipophilicity of **26b** prevents it from migrating into the extravesicular media and into the membrane of receiver vesicles. Upon *in situ* photo-irradiation with 365 nm light the PPG was cleaved, increasing the hydrophilicity of the compound, such that it is able to dissolve in the aqueous buffer and diffuse to receiver vesicles where it can mediate Zn^{2+} influx. This inter-vesicle communication system demonstrated signal amplification as a single diffusible messenger molecule **26a** is capable of transporting many Zn^{2+} ions. Importantly, transport was only facilitated in the

receiver vesicles which had a fluid membrane (POPC, 25 °C) and not in the sender vesicles which had a gel phase bilayer (DPPC, 25 °C).

Numerous molecular switch architectures have been developed,[89] but the majority of reversibly addressable photo-regulated mobile carriers reported to date have incorporated azobenzenes.[90–93] Shinkai *et al.* initially established the application of molecular switches to control ion extraction between two liquid phases.[94] Mobile carriers which transport cations across lipid bilayers have also been reported based on spiropyran,[95] a bis-anthracene couple[96] and azobenzene.[91]

In 2014, Jeong and co-workers were the first to demonstrate anion transport activity in lipid bilayer membranes could be regulated through the use of a molecular switch to modulate the geometry of the mobile carriers **27a-g**.[97] The bis(thio)urea appended azobenzene transporter **27** could be photo-switched between a compact active *Z*-isomer and an open shape inactive *E*-isomer. In the *Z*-isomer the receptor units are brought into close proximity to cooperatively bind a Cl^- anion, with binding constants found to be an order of magnitude greater compared to the corresponding open *E*-isomer (**Figure 1.19A**). These transporters were also investigated within FRT cells, where Cl^- transport was visualised with the halide responsive YFP expressed within the cells. The same activity trend in model membranes was seen across the cellular membrane, where the *Z*-isomer of the mobile carrier was more active than the *E*-isomer. However, reversible, *in situ* switching of transport activity was not achieved in this system. Langton and co-workers subsequently utilised red-shifted tetra-*ortho*-chloroazobenzenes functionalised with squaramide anion binding groups **28a-i** (**Figure 1.19B**) to facilitate reversible visible light (red and blue) responsive control of transport activity in a fully reversible, *in situ* fashion.[92,93]

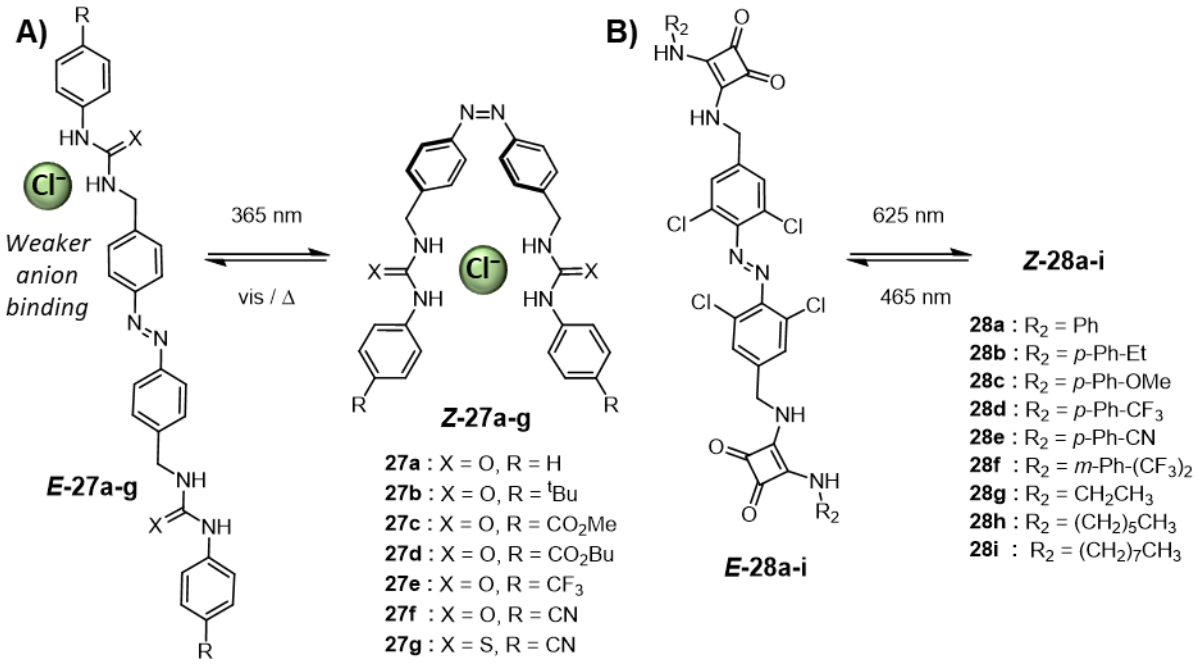

Figure 1.19 Photo-switchable mobile carriers. *A) Jeong's bis-(thio)urea azobenzenes (**27a-g**).*[97] *B) Langton's red-shifted bis-squaramide tetra-chloroazobenzene mobile carriers (**28a-i**).*[93]

Beyond systems demonstrating stimuli-responsive switching between inactive and active states, those which also display high selectivity for a specific ion are highly desirable. Gale, Feringa, Wezenberg and co-workers reported stiff-stilbene based bis(thio)urea molecular switches **29a-g**, which displayed photo-modulated and selective electrogenic Cl^- transport in POPC vesicles (**Figure 1.20**).[98] The *Z*-isomers ***Z*-29a-g** were found to have significantly improved transport activities compared to the respective *E*-isomers, with carrier **29e** displaying a 568-fold difference in activity between the isomers. The *Z*-isomers were highly selective for Cl^-, functioning as electrogenic uniporters, and were able to photo-modulate a membrane potential.

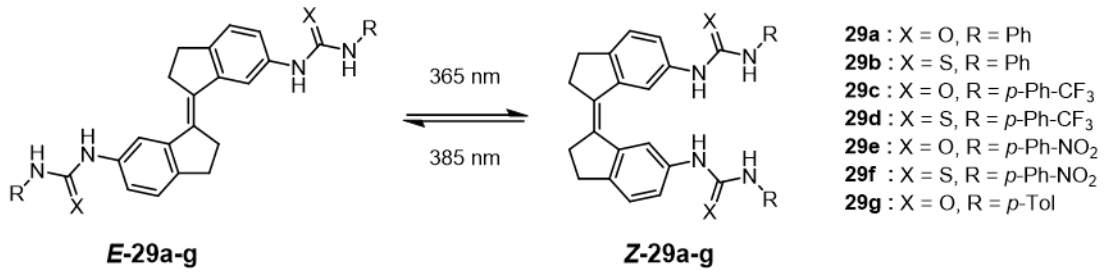

Figure 1.20 Selective mobile carriers based on molecular switches. *Stiff-stilbene photo-responsive Cl^- selective electrogenic transporters* ***29a-g****.*[98]

1.2.8 Stimuli-Responsive Behaviour in Synthetic Channels

Transmembrane protein channels and pumps are the predominant means of regulating ion gradients in biology. Stimuli-responsive opening and closing of gated-channels controls the function of many biological processes within the cell, and engineering of photo-responsive biological machinery in the form of cellular membrane channels is the basis of the field of optogenetics.[99] Many sophisticated examples of regulating protein channels using synthetic molecular photo-switches have been reported, but are beyond the scope of this introduction.[99–101] Wholly synthetic examples have been reported with gated behaviour in response to small molecule binding,[102] membrane tension,[103] pH[104] and light.[105–108]

Very recently molecular motors have been incorporated into the structure of ion channels, to regulate the transport activity with controlled unidirectional rotation of Feringa type light-driven rotary motors (**Figure 1.21**).[109,110] Two such systems have been reported by Barboiu and Giuseppone (**30**), as well as Qu and Bao (**31**), which incorporated benzo-18-crown-6 cation receptor units to elicit potassium cation selective ion channels. Urea motifs were integrated into **30** to promote self-assembly of the channel structure in the membrane. Transport activity experiments in HPTS loaded EYPC LUVs (100 nm) found the channel to be cation selective with the following relative rates of transport: $Rb^+ > K^+ > Na^+$. BLM single channel conductance measurements provided unequivocal evidence of a channel transport mechanism. Under

constant 365 nm irradiation, the transport activity was significantly enhanced both in LUV and BLM studies, where covalently coupling the motor to the channel was shown to be essential to the enhanced transport activity. This enhancement was postulated to be due to the local deformations in microphase and increased fluidity due to local heating through energy dissipation.[111]

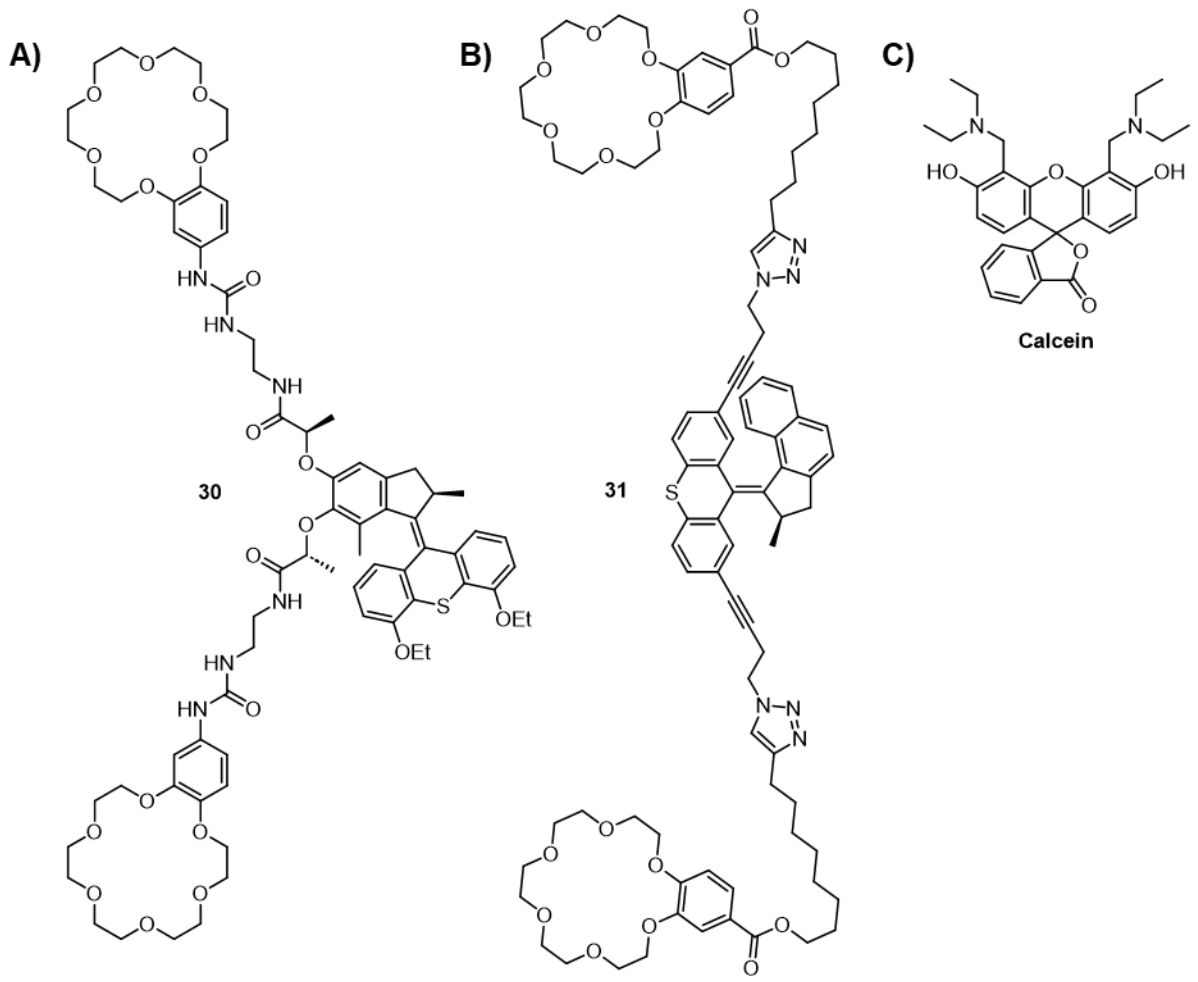

Figure 1.21 Rotation of the molecular motor conjugated to ion channels enhances transport activity. *A) Molecular motor conjugated ion channels reported by Barboiu and Giuseppone (**30**),[109] and B) Qu and Bao (**31**),[110] which display enhanced transport activity under constant irradiation that induces unidirectional rotation. C) Structure of concentration dependent fluorescent dye calcein.*

Interestingly, studies with rotor **31**, reported by Qu, Bao and co-workers, demonstrated the same mechanism of light-driven motor rotation enhanced transport activity.[110] The channel was K^+ selective and displayed enhanced activity with 365 nm irradiation. A calcein leakage

assay demonstrated that even under UV irradiation **31** did not cause appreciable membrane disruption or non-specific leakage. Further studies of **31** in cellular membranes showed the same photo-dependent transport activity for K^+, which induced cell apoptosis in HeLa cells demonstrating the potential of these systems for cancer therapy. This new mechanism of regulating ion transport through the continuous out-of-equilibrium rotation of a molecular motor represents a major step towards the sophisticated operation of biological machinery such as ATP synthase. These systems do not yet demonstrate active transport of ions against a concentration gradient, but the stimuli-responsive regulation of activity with molecular motor motion is a significant step forward in the complexity of membrane bound artificial molecular machines.

1.3 Anchored Ion Carriers

The scope of transporters has, in recent years, been broadened beyond the archetypal classification of either a mobile carrier or membrane spanning channel.[112,113] These new transporters can be categorised as "*anchored ion carriers*": operating *via* molecular machine inspired nanomechanical motion within the bilayer environment, but without the entire construct translocating through the membrane (as for mobile carriers). These are entirely abiotic mechanisms, distinct from biological counterparts. Two clear classes of anchored carriers have emerged, namely unimolecular anchored transporters (where a single binding group facilitates the transport of the analyte through the entirety of the membrane) and relay transporters (where at least two binding groups are required to mediate the passing of the analyte between leaflets of the bilayer *via* an exchange step to enable transport).

1.3.1 Unimolecular Anchored Transporters

A number of systems that act as unimolecular anchored transporters have been reported in recent years, under a plethora of different names, which fall under this description. Zeng and co-workers have been pioneers in this area,[113] developing transport system **32** (**Figure 1.22**), a so-called "molecular ion fisher." The cholesterol unit was used to anchor the system, whilst the flexible linker to the benzo-18-crown-6 K^+ binding motif facilitated transport by this abiotic mechanism.[114] Transporters with different anchoring architectures have been reported, based on a single cholesterol lock,[114] as well as systems with a membrane spanning cross-beam containing two cholesterol units **33**.[115,116] A computational study found that HB between the cholesterol and the phosphate of a lipid restricted lateral translocation, rationalising the efficiency of this anchor group.[117] Interestingly, after prolonged investigations no single-channel current traces were obtained for the mono-cholesterol **32** or a bis-cholesterol anchored system in BLM conductance experiments, indicating that ions were not transported through well-defined channels.[114,115] Ill-defined and transient single-channel current traces were observed for the molecular swing transporter **33** in BLM experiments.[116] This highlights that there are a broad spectrum of possible mechanisms of ion transport, varying from the ill-defined pathway of mobile carriers to the well-defined path of translocation through an ion channel, with the unimolecular immobile carrier mechanism positioned between the two.

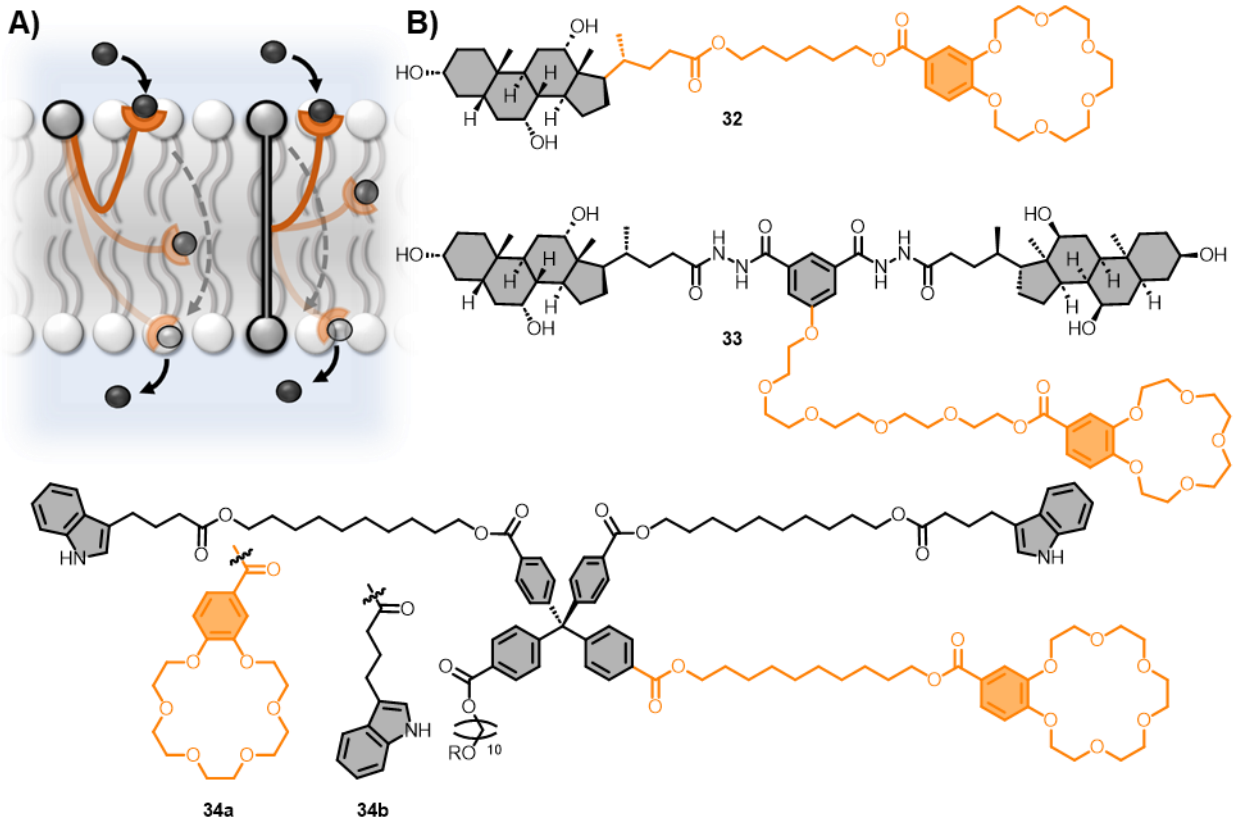

Figure 1.22 Unimolecular anchored carriers. *A) Schematic of the unimolecular anchored carrier transport mechanism. B) Structures of mono-cholesterol anchored* ***32****,*[114] *bis-cholesterol anchored* ***33****,*[116] *tris- and bis-indolyl anchored* ***34a-b****.*[118]

Exchanging the substituent on a tetrasubstituted immobile carrier provided insight into the effect of increasing the number of carrier arms.[118] Derivative **34a** with three indolyl anchoring groups and one benzo-18-crown-6 receptor displayed so-called "molecular fishing" activity, while the immobile carrier **34b** (two anchors, two receptor) displayed >30 times greater activity. The carrier arms therefore operated cooperatively, but whether both receptors bound the ion simultaneously to transport *via* a molecular fishing mechanism, or whether an exchange process occurred within the membrane to transport *via* a relay mechanism, was difficult to confirm. Since no single channel behaviour was observed in BLM experiments, transport activity was determined to be not due to a channel mechanism, and thus can be attributed to an immobile anchored carrier mechanism.

Employing a mechanical bond to link the carrier unit to the anchoring group was demonstrated by Bao, Zhu and co-workers in 2018, who reported a [2]rotaxane shuttle **35** able to transport K^+ *via* a shuttle-type mechanism (**Figure 1.23**).[119] The activity of **35** was found to be linearly dependent on the concentration of transporter in the bilayer, indicative of a single molecule being responsible for transport. Regular square-like signals with long opening times and Ohmic I–V profiles in BLM experiments suggested a stable channel may form within the bilayer. However, a unimolecular dependence of transport activity and the reduced transport activity with decreasing shuttling rate implied that the mobility of the carrier arm along the axle of the rotaxane was responsible for the transport activity.[120]

Bao, Zhu and co-workers have since reported the interlocked transporters **36** and **37** which have unique axle structures and an amide-based crown ether macrocycle carrier arm.[121,122] The transport activity of the interlocked anchored carriers (**36** and **37**) was investigated in EYPC LUVs using the HPTS and lucigenin assays. The transport activity of **36** was shown to be higher than the axle or macrocycle alone, operating *via* a K^+/Cl^- symport mechanism.[121] Interestingly, the rigid *para*-tetraphenylene axle derivative **36** (EC_{50} = 1.75 mol%) displayed enhanced activity relative to the flexible [2]rotaxane **35** (EC_{50} = 3 mol%).[119] Increasing the number of carrier arms in the interlocked transporter was shown to improve the transport activity, with EC_{50} values of 4.3 mol% and 2.0 mol% for the [2]rotaxane (**37a**) and [3]rotaxane (**37b**) respectively.[122] As with the unimolecular anchored carrier system **34**, determination of whether both receptors bind the ion simultaneously to transport *via* a molecular fishing mechanism, or whether an exchange process occurred within the membrane to transport *via* a relay mechanism, was not confirmed.

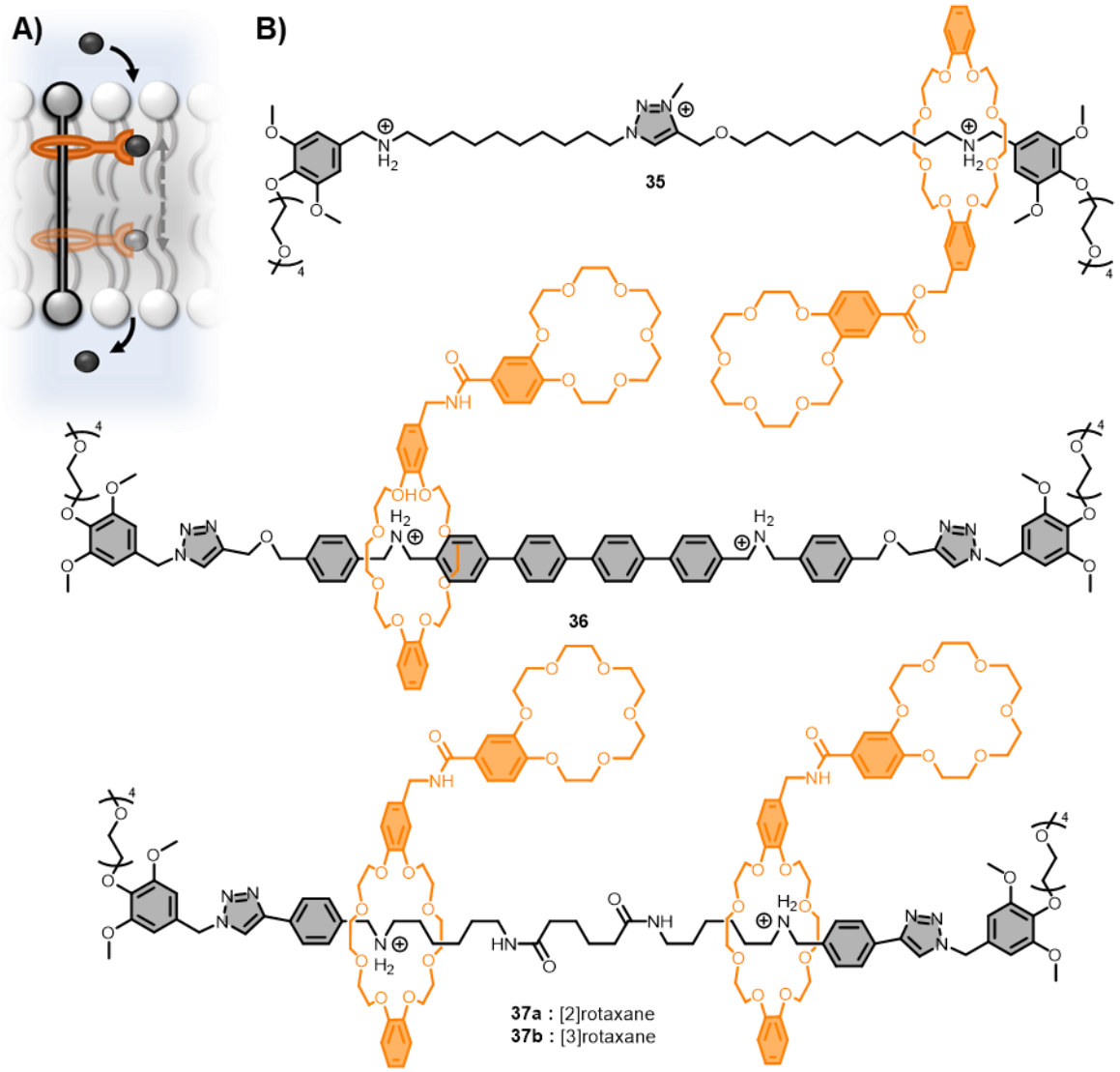

Figure 1.23 Unimolecular anchored carriers based on an interlocked rotaxane architecture. *A) Schematic of a [2]rotaxane ion transporter where shuttling motion facilitates ion transport. B) Structure of [2]rotaxane cation transporter* ***35****, K^+/Cl^- symport [2]rotaxane* ***36*** *and K^+/Cl^- symport [2]rotaxane* ***37a*** *and [3]rotaxane* ***37b****.*

1.3.2 Relay Transporters

Relay transporters operate *via* the exchange of ions between transporters located in opposite leaflets of a lipid bilayer membrane. The relay transport mechanism was first reported by Smith and co-workers in 2008, who demonstrated that a urea appended phospholipid derivative **38** facilitated ion transport by passing anions between transporters immobilised in opposite leaflets of the bilayer (**Figure 1.24**).[123] They established the key principles of this unique transport mechanism, demonstrating that relay transporters must be present in both

leaflets of the bilayer, with no activity observed when loaded into only one leaflet of the membrane. Increasing the electron withdrawing nature of the substituent appended to the urea was shown to significantly improve transport activity, as a result of the improved binding strength for anions. An extensive survey of different phospholipids of varying alkyl chain lengths was also conducted, to explore the effect of bilayer hydrophobic thickness on relay transport rate. Activity was found to incrementally decrease with increasing phospholipid alkyl chain length from 14 to 18 carbons and was completely suppressed for lipid alkyl chain lengths of 20 to 24 carbons. Notably, this trend contrasts with that typically observed for ion channels which display a bell-shaped relationship, where optimal activity was observed for channel structures that matched the thickness of the bilayer,[124] and unlike that of mobile carriers; which is either invariant with membrane thickness when ion binding is rate limiting,[35] or linearly decreased with increasing hydrophobic thickness when translocation of the carrier-ion complex is rate limiting.[7,125]

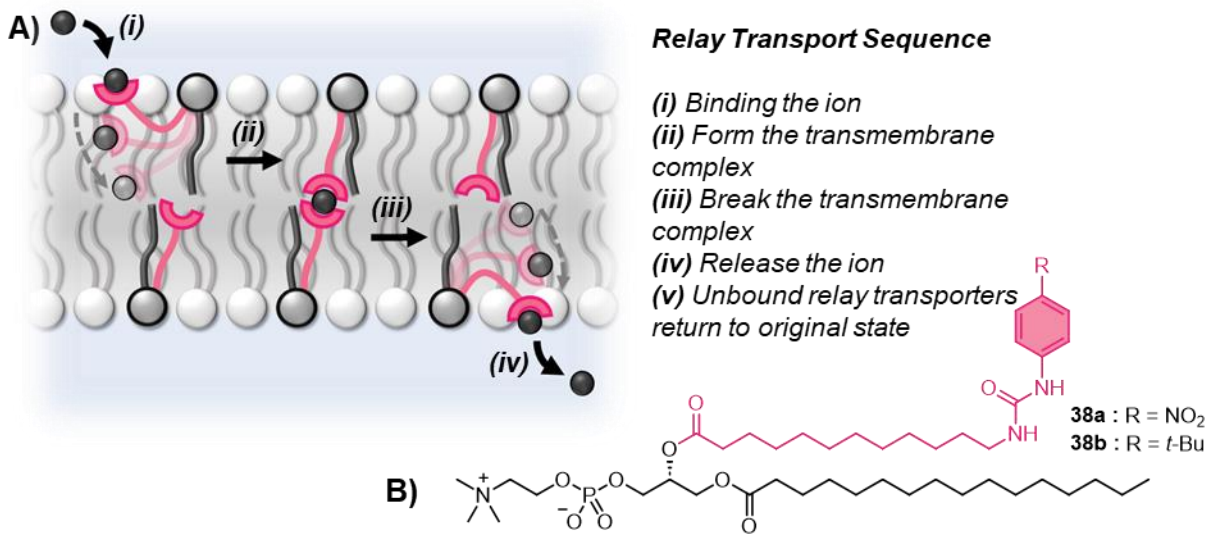

Figure 1.24 Relay transporters. *A) Schematic of the relay transport mechanism. B) Smith's urea relay transporters* ***38a-b****.*

1.4 Project Aims

The following chapters will outline work which builds on the molecular machine inspired abiotic anchored carrier mechanisms of transport, specifically relay transporters. Relay transporters represent an underdeveloped area of ion transport with a unique mechanism which can be exploited for new switchable and selective transport systems. Based on the phosphatidylcholine scaffold reported by Smith and co-workers,[123] relay transporters have the potential for high aqueous solubility and improved pharmacokinetic properties as a result of lipidation for the future application as therapeutics.

Chapter 2 identifies the dependence of membrane thickness on the therapeutically important Cl^- > OH^- anion transport selectivity and describes a novel highly active and selective halogen bonding relay transporter.

Chapter 3 describes a unique photo-switchable relay transport system which regulates transport activity through control of the length of a telescopic carrier arm on the relay transporter, switching with visible light within the membrane in a fully reversible manner.

Chapter 4 expands on the photo-switchable relay transport system, introducing a new anchoring ammonium group facilitates the delivery of relay transporters to both leaflets of pre-formed bilayers.

Chapter 5 outlines the experimental procedures employed in this work.

Chapter 2: Designing Selective Anion Transporters

2.1.1 Therapeutic Importance of Selective Anion Transporters

For the application of synthetic ion transporters as therapeutics it is essential to design highly selective transporters. Obtaining high ion specificity will enable the transport of the target ion for therapeutic activity and minimise off target activity leading to unwanted side effects. As previously described in **Section 1.2.4** synthetic mobile carriers have demonstrated biological activity as anticancer agents and as a potential treatment for channelopathies including cystic fibrosis and Bartter syndrome.[47–49] Synthetic anionophore-based therapeutics tested for biological activity typically rely on Lewis-acidic hydrogen bond donors for anion binding.

Shin and co-workers reported the first synthetic Cl^- transporters that both promote apoptosis and affect autophagy in cells (**Figure 2.1**).[126] The squaramide-based receptors mediate Cl^-/NO_3^- antiport and Cl^-/OH^- antiport transport by a mobile carrier mechanism in POPC LUVs at pH 7.2, but proved ineffective as Na^+ transporters. Interestingly, in cells **39a-c** effectively increased the intracellular Cl^- and Na^+ concentrations, without affecting intracellular K^+ and Ca^{2+} concentrations. These mobile carriers demonstrated high cytotoxicity in the MTT cell viability assay, demonstrating their ability to induce cell death. In the absence of Cl^- or Na^+ in the buffer the cytotoxicity was significantly reduced, highlighting the importance of these ions for **39a-c** induced caspase-dependent apoptosis. In a subsequent study, **39a** was found to promote apoptosis as a result of the osmotic stress caused by the increase in Cl^- and Na^+ concentrations in the cell.[127]

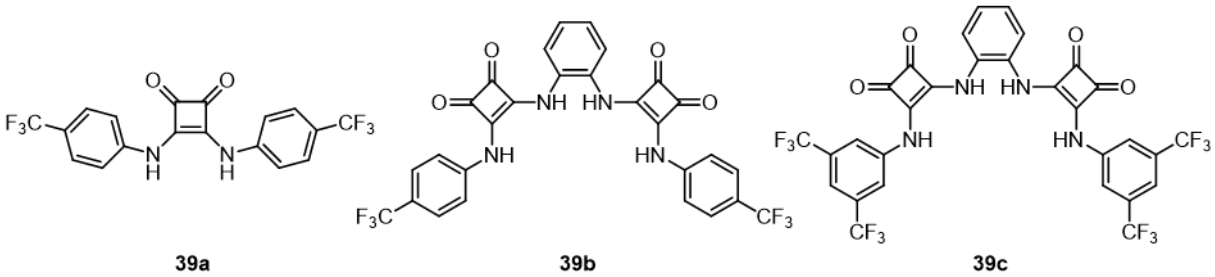

Figure 2.1 Biologically anion transporters induce cell death in cancer cells. *Shin's squaramide-based mobile carriers (**39a-c**).*

2.1.2 Halogen Bonding Anionophores

The significant charge-transfer contribution of a sigma-hole intermolecular interaction, between a main group element and a Lewis base, renders these interactions more resistant to increases in solvent polarity, allowing strong binding even in aqueous media.[58] Therefore, sigma-hole interactions hold great promise for generating highly active and selective anionophores.

A family of calix[6]arenes **40a-d** from the Valkenier group emphasised the key design criteria for the application of synthetic chloride selective XB mobile carriers for the treatment of cystic fibrosis.[128] They employed the calix[6]arene scaffold with different anion binding groups appended including hydrogen bonding urea (**40b**), thiourea (**40c**) and squaramide (**40d**) functional groups and the halogen bonding iodotriazole motif (**40a**) (**Figure 2.2**). Due to the acidic nature of the HB systems, they were found to deprotonate upon release of chloride leading to the net symport of Cl^-/H^+. The XB carrier **40a** however, lacks a labile acidic proton, removing the potential for proton transport which has been linked to cytotoxic activity essential to anticancer activity,[129] but is undesirable for cystic fibrosis treatment. Measuring Cl^-/OH^- selectivity is therefore a key parameter of interest for therapeutic applications. The NMDG assay, recently reported by Gale and co-workers,[130] in which transport activity is measured with and without gramicidin allows the Cl^-/OH^- selectivity of a transporter to be

quantified. *N*-Methyl-D-glucamine chloride (NMDGCl) containing buffer is used for the internal and external LUV solution and a pH gradient is generated by the addition of NMDG to the external solution. Since gramicidin mediates H^+ transport, the test ionophore is only required to facilitate Cl^- transport in its presence, but H^+/Cl^- symport or Cl^-/OH^- antiport in its absence to dissipate the pH gradient. The ratio of activities in the presence and absence of gramicidin in the NMDG assay therefore serves as a selectivity value for the test ionophores $Cl^- > H^+/OH^-$ selectivity. HB calix[6]arenes **40b-d** displayed no selectivity preference for $Cl^- > H^+/OH^-$, while the XB iodotriazole derivative **40a** had a selectivity value >100. Due to the lack of a labile proton on the XB receptor **40a**, this transporter is incapable of H^+ transport and therefore the value represents the $Cl^- > OH^-$ selectivity. Due to the inherent selectivity preference of halogen bonding for the softer halide anions over oxyanions,[131,132] XB based transporters hold great promise for the treatment of cystic fibrosis where Cl^- transport is required but the dissipation of a pH gradient by receptor deprotonation or hydroxide transport could lead to cytotoxic side effects.

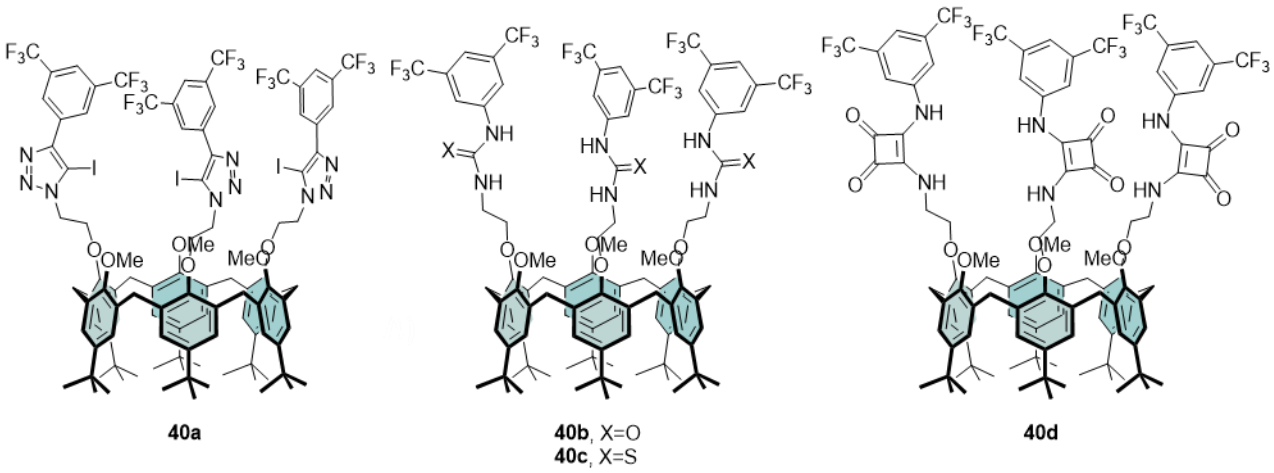

Figure 2.2. Calix[6]arenes developed by the Valkenier group.[128] *The XB iodotriazole derivative **40a** demonstrated Cl^- uniport activity, while the HB urea **40b**, thiourea **40c** and squaramide **40b** displayed Cl^-/H^+ symport transport activity.*

The Langton group has also recently reported a comparative study of bis-1,2,3-triazole based mobile carriers which were functionalised at the 5-position with a proton, iodine or methyltellurium(II) giving **41^{HB}**, **41^{XB}** and **41^{ChB}** respectively.[133] The series of HB, XB and ChB bis-1,2,3-triazoles highlighted sigma-hole interactions for enabling high activity and a strong selectivity preference for Cl^- > OH^- (**Figure 2.3**). The XB and ChB transporters **41^{XB}** and **41^{ChB}** were more active than the hydrogen bonding analogue **41^{HB}**, with **41^{XB}** having the lowest EC_{50} value for any XB mobile carrier reported to date. In terms of anion selectivity, the tellurotriazole chalcogen bonding derivative **41^{ChB}** displayed an impressive 67-fold Cl^- > OH^- selectivity, measured using the NMDG assay. Computational studies were also conducted to determine the free energies of binding and dehydration for Cl^- and OH^- extraction from implicit water to chloroform (as the membrane-mimetic environment). Interestingly, the calculations predicted that binding of OH^- to **41^{XB}** or **41^{ChB}** was stronger compared with Cl^-, opposite to the Cl^- > OH^- transport activity experimentally observed. A pure thermodynamic consideration was therefore insufficient to correctly predict the transport selectivity, however the stronger binding of Cl^- by **41^{XB}** over **41^{ChB}** may account for the improved activity of the former transporter.

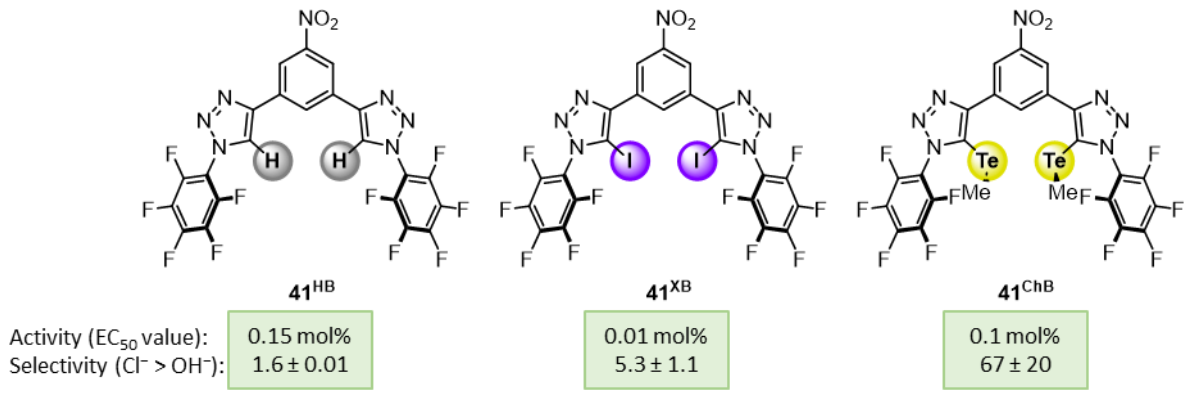

Figure 2.3. Series of bis-1,2,3-triazole based mobile carriers from the Langton group.[133] *The homologous series of anionophores allowed comparison of hydrogen bonding (**41^{HB}**), halogen bonding (**41^{XB}**) and chalcogen bonding (**41^{ChB}**) interactions on transport activity and Cl^- > OH^- selectivity.*

This chapter will investigate the mechanistic basis for the observed Cl^- > OH^- selectivity of mobile carriers and develop halogen bonding relay transporters to understand the impact of transport mechanism on the ion selectivity. Results from this chapter provide additional design criteria for the development of more selective transporters as therapeutics for channelopathies such as cystic fibrosis.

2.2 Synthesis of Mobile Carriers

A number of mobile carriers based on different binding interactions, with various molecular scaffolds were prepared to investigate the pathway of anion transport through lipid bilayer membranes (**Scheme 2.1**). The HB thiourea transporters **T1** and **T2** were prepared *via* condensation of an amine with the corresponding isothiocyanate following literature procedures.[130,134] 3,5-Bis(trifluoromethyl)phenyl isothiocyanate **42** was commercially available, while the tren-based tris-isothiocyanate **44** was prepared by reaction of **43** with carbon disulfide (CS_2) and *N*,*N*'-dicyclohexylcarbodiimide (DCC) in THF at room temperature (rt). The XB iodotriazole based transporter **T3** was prepared by reaction of *n*-hexylamine with the ethylparaben activated ester **45^{XB}**, following a procedure previously reported.[135] This activated ester strategy was employed as iodotriazoles with strongly electron withdrawing substituents have been shown to be susceptible to nucleophilic attack at the iodinated carbon, such that nucleophilic catalysts including 4-dimethylaminopyridine (DMAP) may decompose the iodotriazole motif.[136,137]

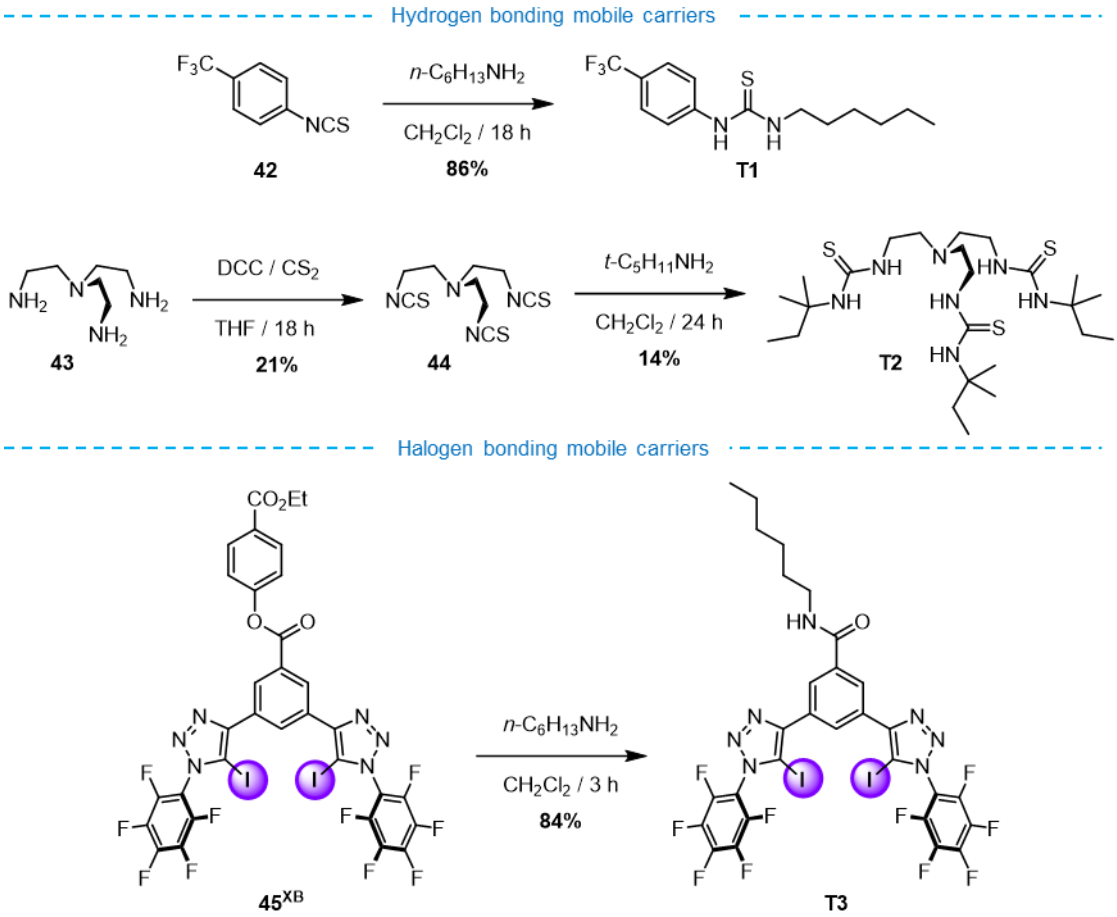

Scheme 2.1. Preparation of HB and XB mobile carriers T1-3. *Compound* ***45^{XB}*** *was prepared by Dr Andrew Docker.*

2.2.1 Quantifying Anion Transport Activity

With the receptors (**T1-3**) in hand, the transport activity of compounds could be readily determined in model vesicle systems.[138,139] The composition of the membrane can be controlled through selection of the composite lipids. The intravesicular and extravesicular aqueous environment can be independently constructed to contain desired electrolytes and the observation of transport activity can be monitored through changes in emission of a fluorescent probe or response from an ion selective electrode.[140,141] The HPTS fluorescence assay is a commonly used vesicle model to determine the activity of different transporters based on their ability to perturb a pH gradient across the membrane through a ratiometric

change in the fluorescence of encapsulated 8-hydroxypyrene-1,3,6-trisulfonic acid dye (HPTS) inside the vesicles.

Large unilamellar vesicles (LUVs, 200 nm) were prepared by extrusion methods (see experimental **Section 5.2.1**) from 1-palmitoyl-2-oleoyl-*sn*-glycero-3-phosphocholine (POPC), to serve as a simple single component membrane model for a cellular bilayer, where the properties of the membrane are homogenous and well characterised for POPC.[142] The POPC LUVs were suspended in 100 mM NaCl solution and buffered to pH 7.0 with 4-(2-hydroxyethyl)piperazine-1-ethanesulfonic acid (HEPES). A high concentration of Na^+ and Cl^- electrolytes in solution was used to prevent the ion concentration from being rate limiting in the transport process. Transporter mediated dissipation of the transmembrane pH gradient was monitored by fluorescence emission of the pH-sensitive fluorophore HPTS (pK_a = 7.2), which was compartmentalized within the vesicle interior only. In a standard HPTS assay, excitation at λ_{ex} = 405 nm (acidic form, HPTS-OH) or λ_{ex} = 460 nm (basic form, HPTS-O^-) leads to fluorescence emission (λ_{em} = 510 nm). Since the fluorophore is membrane impermeable, the time dependent change in the fluorescence ratio R_t, calculated using **Equation 1**, reports on the internal pH of the vesicle.

$$R_t = \frac{\lambda_{ex}460}{\lambda_{ex}405} \quad \textbf{(Equation 1)}$$

In the absence of transporter, the stability of the prepared vesicles can be assessed through measuring a blank. A pulse of NaOH (20 µL of 0.5 M solution, final concentration 5 mM) was added at 40 s to initiate the experiment. A small initial jump in pH was observed immediately due to the small amount of HPTS bound to the exterior surface of the vesicles. For stable vesicles, the pH gradient across the membrane is maintained and minimal dissipation is observed over time. When a test transporter was added at 90 s (various concentrations, in 5

μL DMSO), the ability of the molecule to dissipate the pH gradient is observed as a change in fluorescence. The pH gradient can be dissipated by different ion exchange processes highlighted in **Figure 2.4**, whereby charge neutrality across the membrane is maintained. With an increase in external OH^- concentration, influx of OH^- can equilibrate this concentration gradient with concomitant efflux of an anion to maintain charge neutrality (i.e., Cl^-/OH^- antiport). The effective dissipation of the pH gradient can also be achieved through efflux of H^+, which is functionally equivalent to OH^- influx, with efflux of an anion occurring simultaneously (i.e., Cl^-/H^+ symport). The exchange of cations can also affect the neutralisation of the pH gradient (e.g., Na^+/H^+ antiport). At 290 s Triton X-100 detergent was added to lyse the vesicles and completely dissipate the gradient, allowing calibration of the transport activity. Representative data from a blank run and efficient transport by **T1** in HPTS loaded POPC LUVs is shown in **Figure 2.4B**. After conversion to the time dependent fluorescence intensity ratio R_t, the data was normalised based on **Equation 2** to give the fractional fluorescence intensity (I_{rel}) (**Figure 2.4C**). R_0 is the fluorescence ratio at 65 s after the base pulse but before the addition of the transporter and R_d is the fluorescence ratio at time 350 s, after the addition of detergent.

$$I_{rel} = \frac{R_t - R_0}{R_d - R_0} \quad \textbf{(Equation 2)}$$

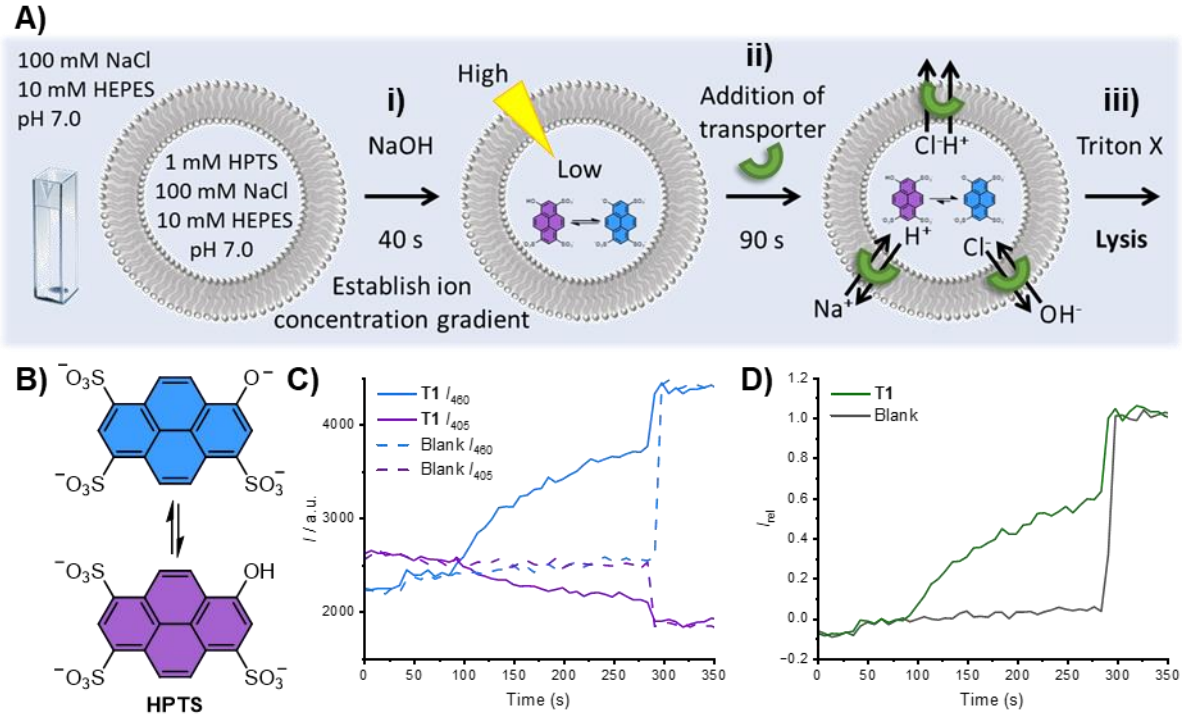

Figure 2.4 Outline of the HPTS assay. *A) Schematic depicting the steps of the HPTS assay i, establishing a pH gradient across the vesicle bilayer, ii, adding the transporter to initiate carrier mediated dissipation of the pH gradient via any ion exchange process and, iii, addition of Triton-X to lyse the vesicles and completely equilibrate the pH. B) Shows the protonation equilibrium of HPTS. C) Shows the absolute emission intensities of HPTS (λ_{em} = 510 nm, λ_{ex} = 405/460 nm) for a blank run and with* ***T1*** *(0.32 mol% to lipid). D) Shows the normalised fluorescence intensity I_{rel} for a blank run and with* ***T1*** *(0.32 mol%).*

Transport studies for each carrier were repeated at numerous concentrations, to determine concentration dependent activity. The transport data for **T1-3** in POPC LUVs is shown in **Figure 2.5**, with activities measured for **T1**[134] and **T2**[130] matching previously reported data.

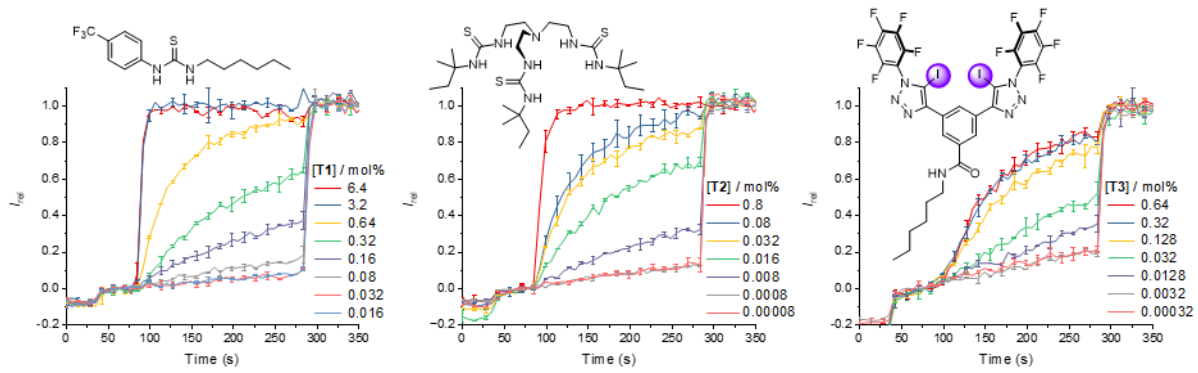

Figure 2.5. HPTS transport assay data for T1-3. *The concentration dependent transport activity of the mobile carriers was measured in 200 nm POPC LUVs (31.25 μM).* ***T1***[134] *and* ***T2***[130] *matched the previously reported activities. Error bars denote the standard deviations from two runs.*

Concentration dependent transport activity can be evaluated using Hill analysis.[134] The fractional fluorescence intensity (I_{rel}) immediately prior to lysis, defined as the fractional activity, y, was plotted as a function of the transporter concentration (x / mol%). Concentration is described in terms of mol%, defined as the percentage of transporter relative to the number of phospholipid molecules. Hill coefficients (n) and EC_{50} values were calculated by fitting to the Hill equation (**Equation 3**). Where y_0 is the fractional activity in the absence of transporter, y_{max} is the fractional activity with excess transporter and x is the transporter concentration in the cuvette.

$$y = y_0 + (y_{max} - y_0)\frac{x^n}{EC_{50}+x^n} \qquad \textbf{(Equation 3)}$$

Hill analysis provides the effective concentration, EC_{50} value, which is defined as the transporter concentration that gives 50% transport activity. This quantification of transport activity allows comparison of transporter efficiency, where a lower EC_{50} value corresponds to improved transport activity. It is important to define the time point to which the EC_{50} value corresponds and the concentration in terms of mole percent with respect to lipid concentration (mol%), to enable comparison of activities between studies. The EC_{50} value can also be viewed as an approximation of the stability of the ion-transporter complex, where the Hill coefficient *n* can provide insight into the stoichiometry of the complex.[143] Provided the assembly of the ion-transporter complex is endergonic (ΔG > 0, thermodynamically unfavourable) the Hill value can provide the stoichiometry of the transient assembly within the bilayer which facilitates transport. However, Hill analysis applied to exergonic assemblies (ΔG < 0, thermodynamically favourable) does not provide information on the stoichiometry of assembly, but can give an EC_{50} value. For example, the bee toxin melittin is known to form self-assembled pores which allow the non-specific leakage of electrolytes across cell

membranes, uncoupling many concentration gradients, leading to pain, swelling and anaphylaxis in some people (**Figure 2.6**).[144] A Hill coefficient n = 4 implies that the transient pore comprises of four monomers, but could also be accounted for by an octamer formed of four stable dimers, a dodecamer formed by four stable trimers, and so on.[143]

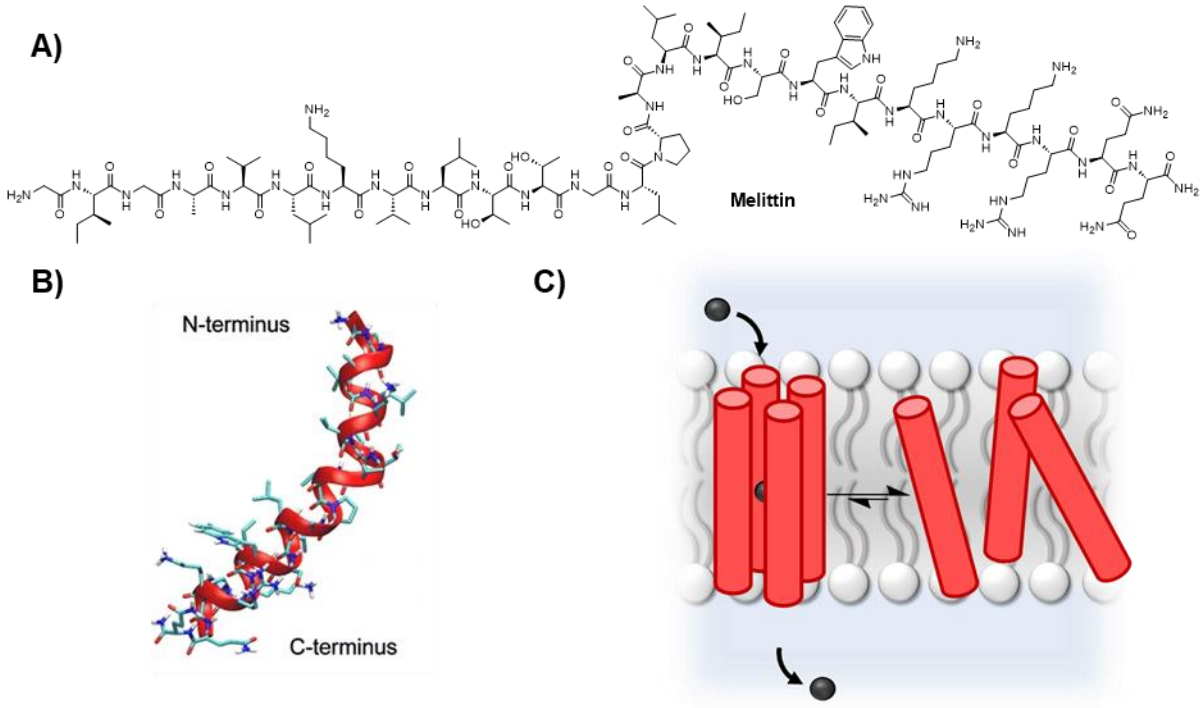

Figure 2.6. The bee toxin melittin forms transient pores in cellular membranes. *A) Structure of the 26-amino acid peptide melittin with a hydrophilic C-terminus to promote membrane insertion. B) The peptide adopts an α-helix structure in the membrane.*[144] *C) Self-assembly of transient pores allows the non-specific leakage of electrolytes across cellular membranes.*

Hill analysis of the fractional activities for **T1-3** in 200 nm POPC LUVs were conducted to elucidate the stoichiometry of the ion-transporter complex responsible for mediating anion transport (**Figure 2.7**). For monothiourea **T1**, $n > 1$ implies that multiple transporter molecules assemble to form an endergonic anion-transporter complex. The value of n = 2.1 ± 0.2 suggests that two molecules are necessary to encapsulate the anion sufficiently to form the hydrophobic supramolecular complex which facilitates transport. This value provides insight into the mechanism of transport and suggests that transporters with an increased number of binding groups would encapsulate the anion more effectively and improve the transport

activity. Indeed, the tren-based tris-thiourea **T2** has a lower EC_{50} value than **T1** (**Table 2.1**), and thus a combination of increased binding strength and improved encapsulation of the anion likely account for the decreased EC_{50} value. The XB transporter **T3** demonstrates efficient transport activity with $n \sim 1$, suggesting that a monomeric complex of bidentate **T3** was responsible for transport activity. This was in line with results from the homologous bidentate iodotriazole **41**^{XB} which was shown to operate as a unimolecular mobile carrier.[133] The ^{1}H NMR binding titration with **T3** and tetrabutylammonium chloride (TBACl) in acetone-d_6 : D_2O (v/v 97.5/2.5) revealed a 1:1 binding stoichiometry for **T3** and Cl^- with a strong association constant (K_a = 4660 M^{-1}) for this competitive organic-aqueous solvent mixture(**Figure 2.7C-D**).

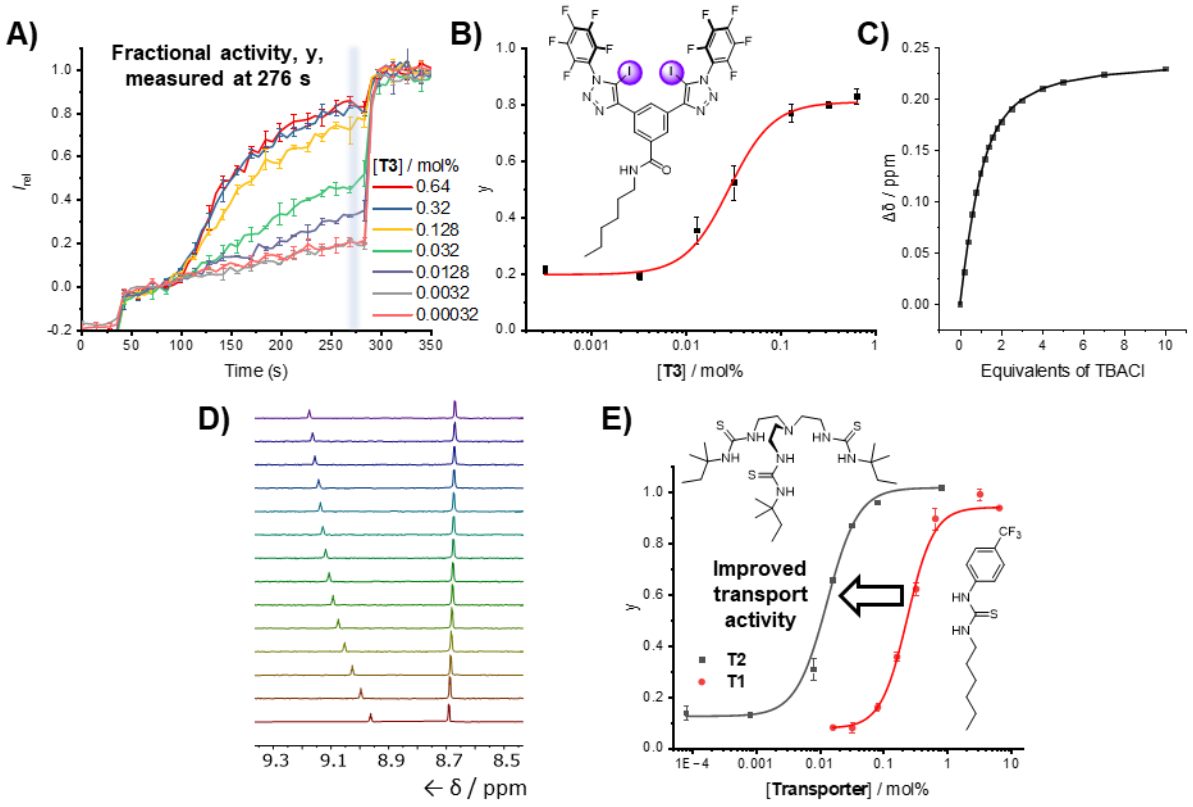

Figure 2.7. Fractional activities of T1-3 from the HPTS assay plotted against concentration and fit to the Hill equation and ^{1}H NMR binding titration for T3*. A) Blue region highlighted indicates the data used to obtain the factional activity values. B) Concentration dependent activity of **T3** fit to the Hill equation. C) Anion binding titration isotherm for **T3** with TBACl, solid points represent the chemical shift perturbation fitted to a 1:1 binding model. D) Stacked partial ^{1}H NMR anion binding titration isotherm for **T3** with TBACl in acetone-d_6 : D_2O (v/v 97.5/2.5) measure by Dr Andrew Docker. C) Transport data for **T1** and **T2** (points) fit to the Hill equation (line) demonstrates the improvement in activity upon increasing the number of binding units in the mobile carrier. Error bars denote the standard deviations from two runs.*

Table 2.1 *Characteristics of the anion transporters* ***T1-3****.*

Transporter	EC_{50}^{a} / mol%	n^{b}
T1	0.23 (0.01)	2.1 (0.2)
T2	0.013 (0.001)	1.8 (0.12)
T3	0.40 (0.09)	0.7 (0.1)

a Effective concentration to reach 50% of maximal activity in the HPTS assay, determined from Hill analysis of the relative fluorescence intensity at t = 276 s, immediately prior to vesicle lysis. Experiments conducted in LUVs of POPC (mean diameter 200 nm) loaded with HPTS (1 mM), with NaCl (100 mM) solution buffered to pH 7.0 with 10 mM HEPES in the intravesicle and extravesicle environment. b Hill coefficient. Errors at the 95% confidence limit.

2.2.2 Determining Chloride Over Hydroxide Selectivity

Previous reports describing **T1-2** transport activity have shown that they operate as mobile carriers, facilitating Cl^-/OH^- antiport or Cl^-/H^+ symport.[145,146] The novel XB transport **T3** was expected to follow the same mobile carrier mediated Cl^-/OH^- antiport mechanism previously shown for the isostructural transporter **41**$^{\mathbf{XB}}$.[133] To quantify Cl^- > H^+/OH^- anion transport selectivity, the HPTS assay can be conducted in the presence and absence of the protonophore carbonyl cyanide-*p*-trifluoromethoxyphenylhydrazone (FCCP).[147] The protonophore mediates fast electrogenic H^+ transport, thereby uncoupling the H^+/OH^- transport from that of Cl^- such that the assay reports on the now rate limiting Cl^- transport (**Figure 2.8A**). The observed transport activity of thiourea **T1** was independent of the presence of FCCP, indicating that Cl^- transport is rate limiting for this transporter in line with previous unselective monothiourea mobile carriers (**Figure 2.8B**).[134] In contrast, the tren-based **T2** is known to display Cl^- > H^+/OH^- anion transport selectivity,[130] and indeed an increase in activity was observed in the presence of FCCP (**Figure 2.8C**). This observation of improved selectivity with **T2** has previously been attributed to the thermodynamic parameters of binding strength and anion encapsulation accounting for the improved anti-Hofmeister selectivity.[130,146] The novel XB anionophore **T3** also displayed enhanced transport activity in the presence of FCCP

demonstrating that **T3** is limited by OH^- transport (or functionally equivalent H^+ transport) analogous to the isostructural mobile carrier **41**^{XB} (**Figure 2.3**).[133] However, given the low basicity of the triazole anionophore ($pK_aH \sim 0$–1), **T3** is likely incapable of H^+ transport and therefore the assay reports on the $Cl^- > OH^-$ transport selectivity (**Figure 2.8D**). The selectivity for $Cl^- > H^+/OH^-$, $F'(Cl^-/OH^-)$, can be quantified by the ratio of EC_{50} values using **Equation 4**, to provide a means of comparing the selectivity of transporters.

$$F'(Cl^-/OH^-) = \frac{EC_{50}(OH^-)^{no\ FCCP}}{EC_{50}(Cl^-)^{FCCP}} \qquad \textbf{(Equation 4)}$$

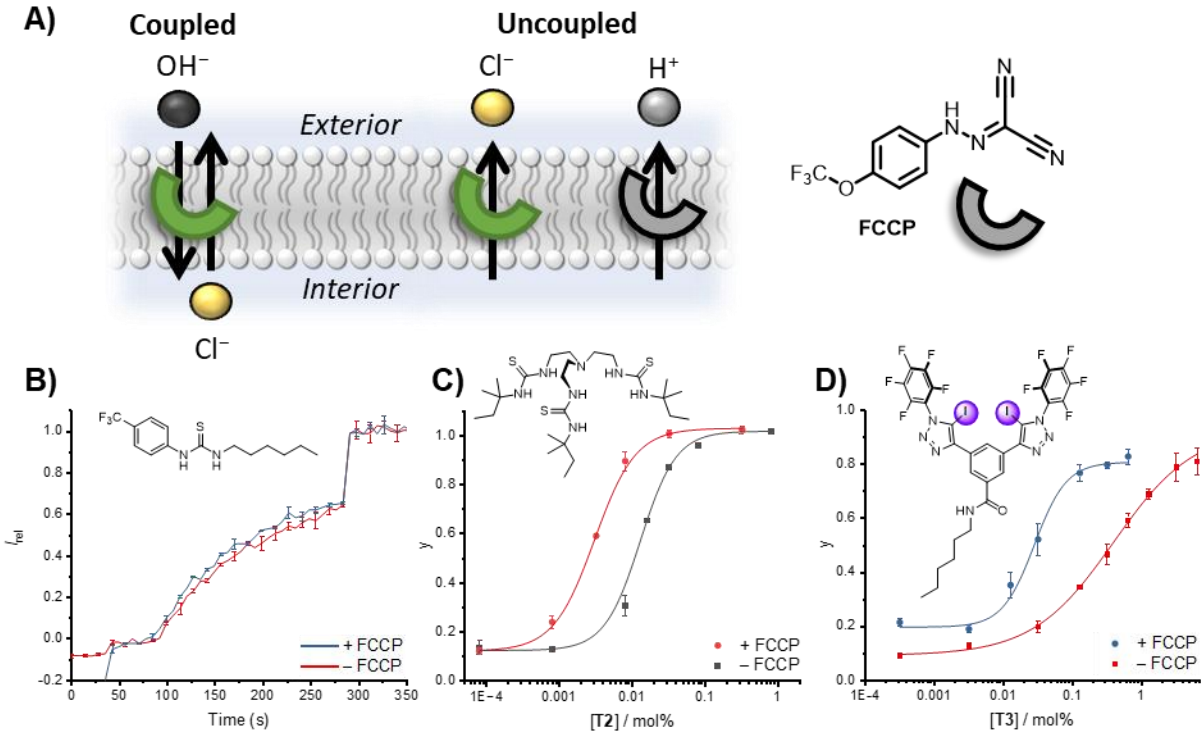

Figure 2.8. Investigating $Cl^- > H^+/OH^-$ anion transport selectivity of mobile carriers with FCCP. *A) Schematic of the coupled Cl^-/OH^- antiport mechanism (without FCCP) and uncoupled Cl^- transport (with FCCP). B)* ***T1*** *(0.32 mol%) transport activity invariant with FCCP (0.8 mol% to lipid). C)* ***T2*** *and D)* ***T3*** *transport data (points) with and without FCCP (0.8 mol%) fit to the Hill equation (line) demonstrating $Cl^- > H^+/OH^-$ transport activity. Error bars denote the standard deviations from two runs.*

Table 2.2 *Characteristics of the anion transporters **T1-3** anion selectivity.*

Transporter	EC_{50}[a] / mol%	EC_{50}^{FCCP} [a] / mol%	$F'(Cl^-/OH^-)$ [b]
T1	0.23 (0.01)	-[c]	<1
T2	0.013 (0.001)	0.0031 (0.0001)	4
T3	0.40 (0.09)	0.028 (0.006)	14

*a Effective concentration to reach 50% of maximal activity in the HPTS assay, in the presence or absence of FCCP (0.8 mol%), determined from Hill analysis of the relative fluorescence intensity at t = 276 s, immediately prior to vesicle lysis. Experiments conducted in LUVs of POPC (mean diameter 200 nm) loaded with 1 mM HPTS, NaCl (100 mM) and buffered at pH 7.0 with 10 mM HEPES. b Factor of enhancement in the transport rate between Cl^- and OH^- ($F'(Cl^-/OH^-) = EC_{50}/EC_{50}^{FCCP}$) using the FCCP assay. c Hill analysis was not conducted as transport activity of **T1** (0.32 mol%) was equivalent in the presence and absence of FCCP. Errors at the 95% confidence limit.*

Halogen bonding mobile carrier **T3** was found to have a greater selectivity for Cl^- > OH^- (**Table 2.2**, F'=14), compared to the previously reported **41^{XB}** (F'=5). While the binding motif of these two mobile carriers is equivalent, they differ in the *para*-position substituent of the central benzene ring. The nitro group of **41^{XB}** is more electron withdrawing than the amide of **T3**, illustrated by the respective Hammett parameters σ 0.78 and 0.36.[148] The stronger electron withdrawing nature of the nitro group, polarises the C-I bond more and accounts for the increased binding strength of **41^{XB}** (K_1^{Cl} = 6073 M^{-1}) compared to **T3** (K_1^{Cl} = 4660 M^{-1}) as determined by ^{1}H NMR titrations with TBACl in acetone-d_6 : D_2O (v/v 97.5/2.5). The increase in binding strength accounts for the improved transport activity of **41^{XB}** (EC_{50} = 0.01 mol%) relative to **T3** (EC_{50} = 0.4 mol%). However, the hexyl chain of **T3** will affect the parameters which influence carrier mobility within the bilayer including log*P* and molecular shape,[149,150] which is postulated to account for the difference in selectivity value.

In order to establish the origins of the anion transport selectivity, the rate determining step of the transport process was determined. To this end the transport activity of a family of transporters with and without FCCP were determined to resolve the Cl^- > H^+/OH^- selectivity,

in a range of lipids to ascertain how the selectivity factor changes with hydrophobic thickness of the membrane.

2.2.3 Impact of Membrane Hydrophobic Thickness on Mobile Carrier Anion Selectivity

The rate of ion transport mediated by mobile carriers which facilitate anion transport is typically dominated by the interfacial binding rate (*i.e.* the product of the ion association rate and transporter concentration, k_a·[transporter], for a given ion concentration) when not under saturation conditions (where all the carriers would be complexed).[35] Anion transport activity has therefore been shown to be strongly dependent on receptor binding strength,[151,152] as well as the nature of the membrane-aqueous interface[35] which both impact the ion association rate. Gale and co-workers showed that for a series of different lipids with the same alkyl chains but different headgroups the transport activity for a range of anionophores was significantly affected.[35]

In contrast, a study of valinomycin mediated rubidium cation transport found that translocation of the cation-transporter complex through the hydrophobic membrane interior was rate-limiting.[153] Increasing the membrane thickness and cholesterol content reduced the transport rate of the charge dense cation, demonstrating that the energy barrier to translocation of the hydrophilic cation-transporter complex determined activity. Interestingly, a family of cholapod-based mobile carriers reported by Smith and Davis displayed translocation-limited mobile carrier mediated anion transport activity.[151] Transport activity was observed to decrease incrementally with increasing hydrophobic thickness of the membrane, for the bulky bidentate cholapod mobile carrier. This represents a rare example of a mobile anion carrier which is dependent on both the interfacial binding rate of an anion, as well as the translocation rate of the anion-transporter complex.

The transporters **T1-3** all operate *via* a mobile carrier mechanism where typically anion binding is rate-limiting (**Figure 2.9**). Measuring the transport activity of unselective **T1** using the HPTS assay with LUVs composed of lipids with different alkyl chain lengths allowed the effect of membrane hydrophobic thickness on transport rate to be assessed. As expected, the transport activity of **T1** was invariant with membrane thickness (**Figure 2.9B**), in line with the general understanding that for the mobile carrier mechanism anion binding at the water-membrane interface is rate-limiting, rather than translocation of the complex across the membrane. Since the transport activity of **T1** was invariant in the presence of FCCP, the binding of Cl^- ions rather than H^+/OH^- was the rate-limiting step of the transport mechanism. In the presence of FCCP, Cl^- transport was rate limiting for **T3** and Hill analysis of multiple concentrations of transporter in a thinner membrane (1,2-dipalmitoleoyl-*sn*-glycero-3-phosphocholine, 16 : 1 PC) and a thicker membrane (1,2-dioleoyl-*sn*-glycero-3-phosphocholine, 18 : 1 PC) revealed no change in activity (**Figure 2.9C**).

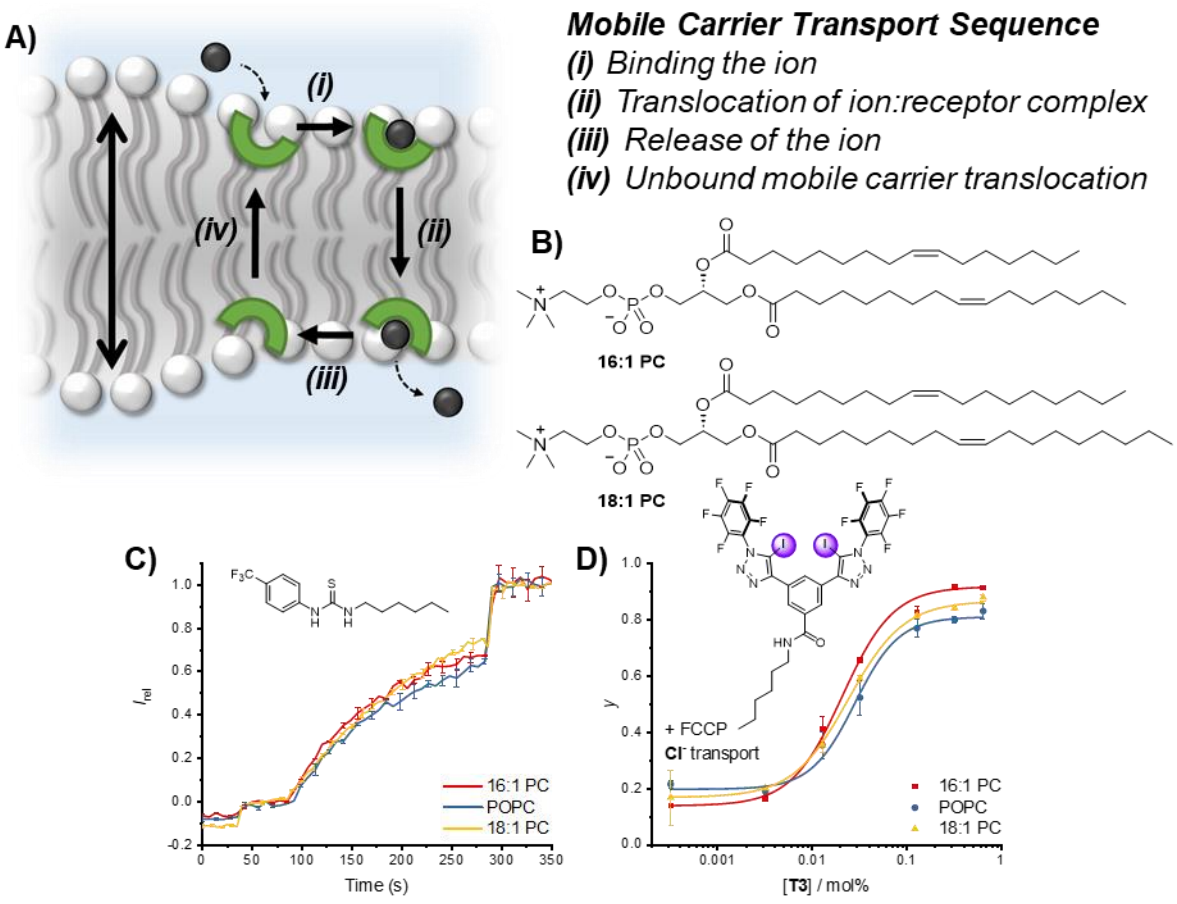

Figure 2.9. Effect of membrane thickness on mobile carrier anion transport. *A) Schematic of the mobile carrier transport sequence. B) Structure of phospholipids used in study with different alkyl chain lengths. C) HPTS transport assay data* for ***T1*** *(0.32 mol% to lipid) and D) HPTS transport assay data* for ***T3*** *(0.00032-6.4 mol% to lipid, points) in the presence of FCCP (0.8 mol%) in 200 nm LUVs prepared from lipids with different alkyl chain lengths (16:1 PC, POPC, 18:1 PC, 31.25 μM) fit to the Hill equation (lines). Error bars denote the standard deviations from two runs.*

Surprisingly however, **T3** mediated hydroxide transport (in the absence of FCCP) exhibited a strong dependence on bilayer thickness, in which activity decreased with increasing lipid chain length (**Figure 2.10**). A change in hydrophobic thickness of the membrane would not affect anion binding at the membrane interface, but would change the energy barrier to translocation of the ion-transporter complex through the membrane. For the charge dense hydroxide anion, the increasing energy barrier to translocation of the hydroxide-transporter complex through the hydrophobic membrane interior leads to a decrease in activity. The implication is therefore that the diffusion of the hydroxide-transporter complex through the membrane is rate-limiting. In contrast, for the less charge dense chloride anion the barrier to

translocation of the chloride-transporter complex is diminished and no longer rate-limiting. Chloride transport is characterised by the expected anion binding rate-limited transport activity which is invariant in LUVs with different hydrophobic thicknesses. The observation of translocation-limited hydroxide transport provides a new understanding to the factors which impact anionophore activity. Interestingly, the Cl^- > OH^- selectivity factor is therefore determined by kinetic control of the membrane translocation step rather than the thermodynamic parameters of anion binding at the interface as previously assumed.[154]

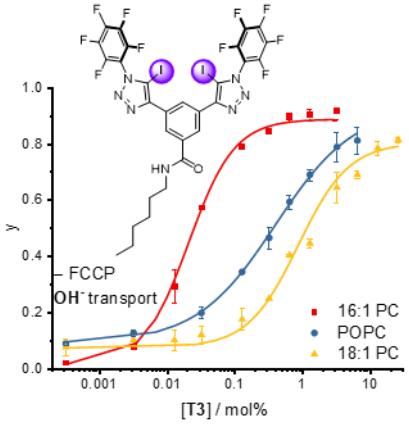

***Figure 2.10. Translocation-limited hydroxide transport activity of T3**. HPTS transport assay data for **T3** (0.00032-25.6 mol% to lipid, points) in 200 nm LUVs prepared from lipids with different alkyl chain lengths (16:1 PC, POPC, 18:1 PC, 31.25 μM) fit to the Hill equation (lines).Hill analysis of transport activity shows the EC_{50} of **T3** decreases as the alkyl chain length of the lipid decreases. Error bars denote the standard deviations from two runs.*

The overall rate equation for **T3** mediated hydroxide transport is therefore a function of both the interfacial binding rate and membrane translocation rate of the hydroxide-transporter complex. The chloride transport rate equation for **T3** is dependent solely on the rate of binding. Since the membranes used differ only in length of the phospholipid tails and have identical headgroups, the interfacial anion binding rates are expected to be near identical between lipids. With the rate of Cl^- transport not changing upon varying membrane thickness, but that of OH^- changing, the Cl^- > OH^- selectivity factor *F'* was enhanced with increasing membrane thickness. The implication is therefore that the different rates of membrane

translocation of the chloride and hydroxide complexes of **T3** are responsible for the observed selectivity for chloride in the thicker membranes (step ii, **Figure 2.9**), and not binding selectivity at the interface as was previously assumed (step i, **Figure 2.9**).[154,155]

These results suggest that in the case of hydroxide transport mediated by the XB carrier **T3**, it is the comparatively slow rate of translocation of the 1:1 hydroxide-carrier complex through the hydrophobic region of the bilayer which dominates the overall transport rate in the thicker 18:1 PC and POPC membranes. In contrast, for the thinnest membrane (16:1 PC) the $Cl^- > OH^-$ selectivity is lost, suggesting that the translocation of the hydroxide-carrier complex in this case is now faster than the interfacial binding rate. This result emphasises the importance of measuring transporter anion selectivity in vesicles comprised of lipids with different alkyl chain lengths, as the selectivity factor can change with membrane thickness. This observation is also of importance for the translation of synthetic mobile carriers to therapeutics for the treatment of cystic fibrosis, where cellular membranes are comprised of many different lipids with different membrane thicknesses. It is postulated that this observation may provide new opportunities to develop membrane targeted mobile carriers which facilitate selective transport only in membranes of a specific hydrophobic thickness.

Several previously reported $Cl^- > OH^-$ selective mobile carriers (**T2**, **41^{XB}** and **41^{ChB}**)[133,146] were explored, to determine whether the chloride selectivity was in general dependent on membrane thickness (**Figure 2.11**). The transport rates were measured for Cl^- and OH^- with **T2**, **41^{XB}** and **41^{ChB}** in the three membranes of varying thickness previously described, to determine the anion selectivity and hence whether the selectivity arises from differing rates of membrane translocation of the chloride and hydroxide/proton complexes. In each case, as with **T3**, the rate of chloride transport (in the presence of FCCP) was invariant of membrane

thickness. The hydroxide transport activity (for **41^{XB}** and **41^{ChB}** or functionally equivalent H^+ transport for **T2**) decreased with increasing lipid length, resulting in increasing Cl^- > OH^- selectivity as the membrane thickness increased. This suggests that across all four chloride-selective carriers studied which span a range of structures, anion binding groups and intermolecular interactions, the observed Cl^- > OH^- selectivity arises from differing rates of membrane translocation of the chloride and hydroxide complexes.

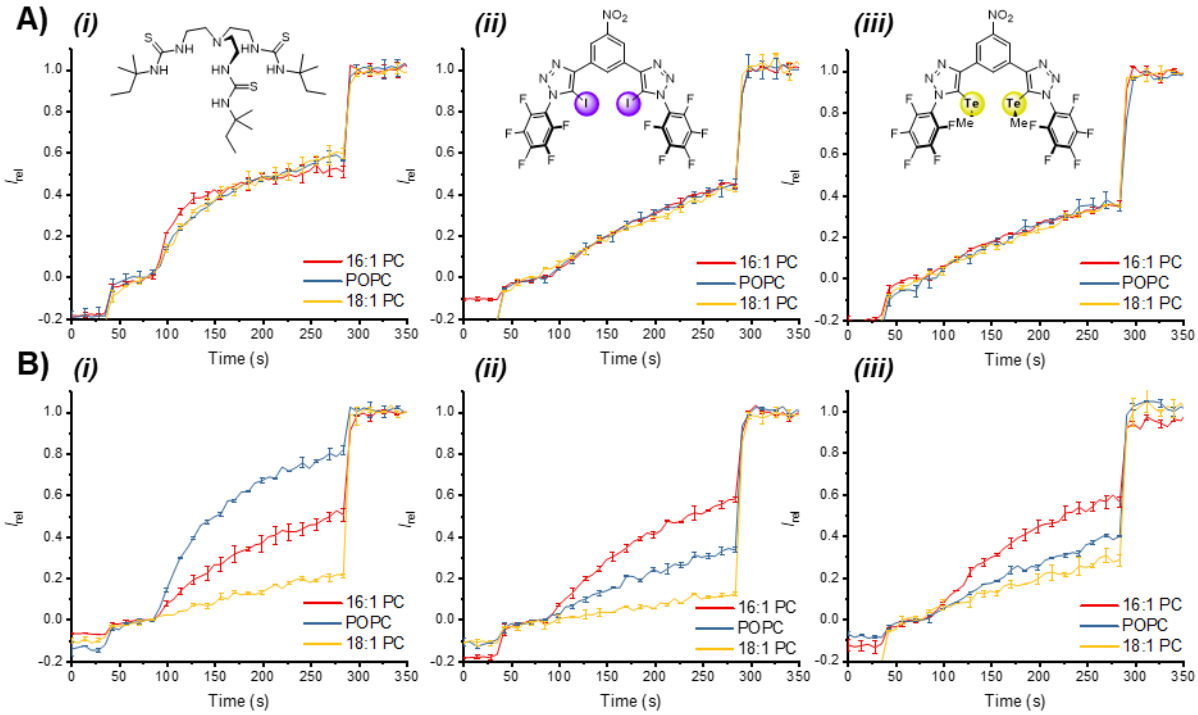

Figure 2.11 Effect of changing hydrophobic thickness on OH^- and Cl^- transport activity of mobile carriers T2, 41^{XB} and 41^{ChB}. *A) HPTS transport data in the presence of FCCP (0.8 mol%) reports Cl^- transport activity in 200 nm LUVs prepared from lipids with different alkyl chain lengths (16:1 PC, POPC, 18:1 PC, 31.25 μM) for i) **T2** (0.0032 mol%) ii) **41^{XB}** (0.0032 mol%) and iii) **41^{ChB}** (0.01 mol%). B) HPTS transport data in the absence of FCCP reports OH^- transport activity in 200 nm LUVs prepared from lipids with different alkyl chain lengths (16:1 PC, POPC, 18:1 PC, 31.25 μM) for i) **T2** (0.016 mol%) ii) **41^{XB}** (0.016 mol%) and iii) **41^{ChB}** (0.1 mol%). Error bars denote the standard deviations from two runs.*

2.3.1 Anti-Hofmeister Selectivity in Halogen Bonding Relay Transporters

Current efforts to develop more selective anionophores have relied on developing carriers with improved encapsulation of the anion which inevitably increases the hydrophobicity of the transporter. Whilst mobile carriers with high Cl^- > OH^- selectivities have been reported,[128,154] the problem of deliverability of these hydrophobic organic compounds to

cellular membranes in aqueous environments is a significant challenge.[156] Relay transporters based on a phospholipid scaffold which are aqueous soluble may provide a strategy to overcome this issue. The XB receptor unit on the phospholipid-based **T4^{XB}** was chosen to provide Cl^- > OH^- selectivity to the transporter, whilst the amphiphilic lipid architecture would provide aqueous solubility and improved pharmacological properties for future therapeutic applications.[123]

2.3.2 Synthesis of Relay Transporters

The phosphocholine lipid scaffold was chosen to provide compatibility with the model POPC membranes used to measure transport activity, enabling efficient incorporation in the lipid membrane and ensuring a homogenous distribution in the bilayer. The synthesis of the lipid-based transporters **T4^{XB}** and **T4^{HB}** is shown in **Scheme 2.2**. Fmoc protected 12-aminododecanoic acid **47** was prepared by reaction of 9-fluorenylmethyl chloroformate (Fmoc-Cl) with amine **17** under basic conditions. Synthesis of the lysolipid **49** was achieved *via* a tin-mediated regioselective acylation of glycerophosphorylcholine **48**. The organo-tin reagent dibutyltin(IV) oxide (DBTO) forms a diol-tin ketal with **48** which promotes the acylation by palmitoyl chloride at the primary alcohol over the secondary alcohol.[156] While complete conversion was reported in the literature, this was not observed and column chromatography on silica was necessary to isolate the desired product. Lysolipid **49** is susceptible to intramolecular transesterification to the 2-*O*-Palm-PC regioisomer, promoted by exposure to silica or elevated temperatures in solution. To prevent this undesired decomposition pathway, a short silica plug was conducted to remove **48** and the solvent was removed *in vacuo*, with the water bath not heated above 30 °C. The hydroscopic product was then recrystallised from EtOH/acetone and stored as a white solid in the freezer.

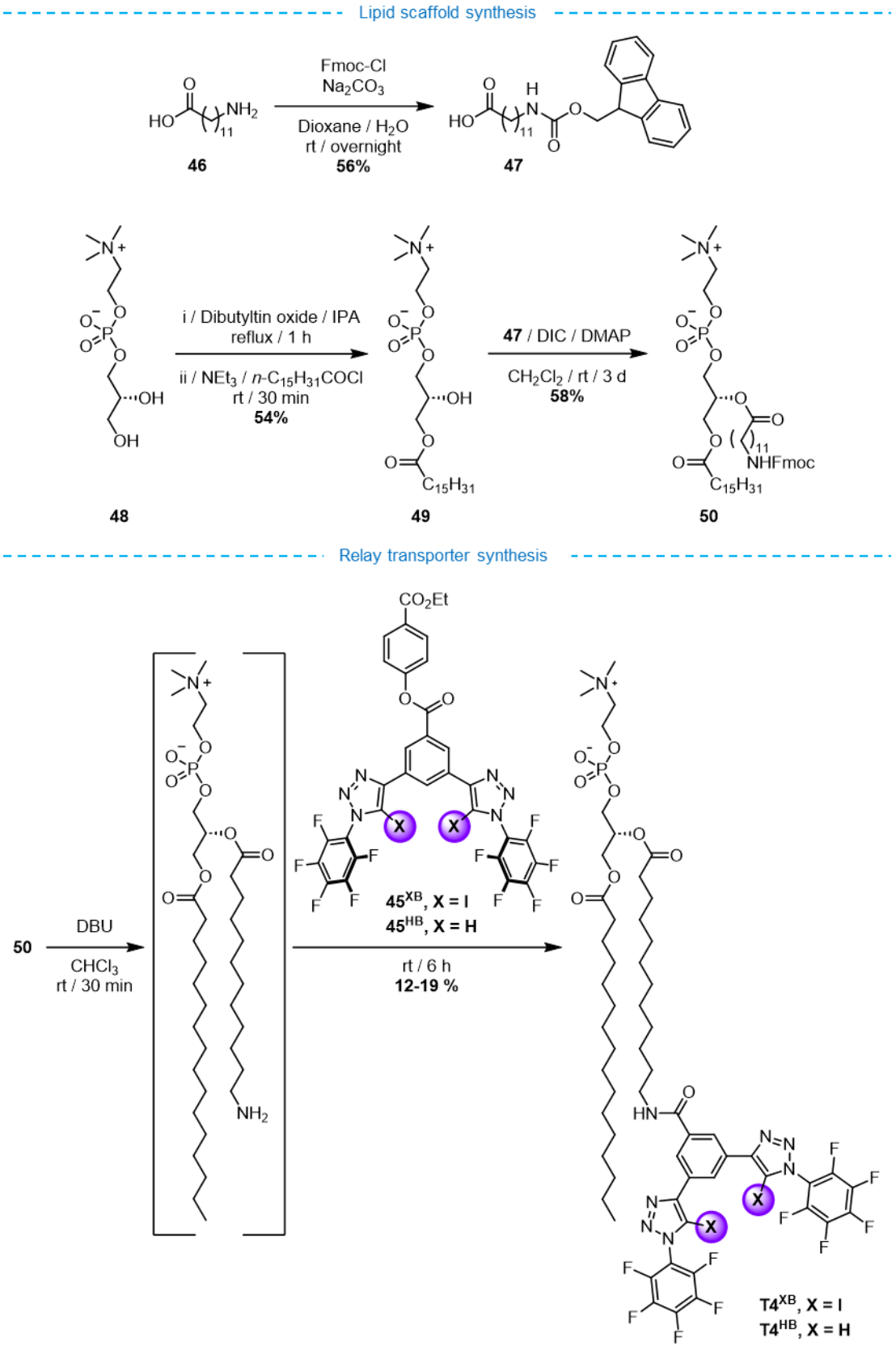

Scheme 2.2 Synthesis of HB and XB relay transporters $T4^{HB}$ and $T4^{XB}$. *Compounds **45^{HB}** and **45^{XB}** were prepared by Dr Andrew Docker.*

Reaction of the lysolipid **49** with the aliphatic carboxylic acid **47** in anhydrous CH_2Cl_2 with *N*,*N*'-diisopropylcarbodiimide (DIC) coupling reagent and stochiometric DMAP nucleophilic catalyst gave the desired bisacylated lipid **50**. Reaction at this secondary alcohol is known to proceed slowly, but elevated reaction temperatures cannot be utilised as this promotes the undesired intramolecular transesterification reaction. A procedure developed by Hadju and co-workers which employs sonication and glass beads in the reaction mixture to provide a higher surface area for reaction, was also attempted in order to obtain improved yields with shorted reaction times.[157] This procedure was also successful (yield = 38%), but care to maintain the temperature of the sonicator bath below 30 °C was necessary to minimise intramolecular transesterification. Bisacylated lipids lack a free alcohol and are therefore stable to transesterification. To isolate the bisacylated lipid **50**, DMAP must first be removed as it co-elutes with phosphocholine lipids in normal phase chromatography on silica. The sulfonic acid functionalised ion exchange resin Dowex 50W X8 was employed to sequester the basic nucleophilic catalyst, by stirring the resin with the reaction mixture for 45 minutes and removing the solid by filtration.[123] To improve the process, the concentrated reaction mixture was purified through a plug of Dowex 50W X8. Eluting with chloroform/MeOH (75/25 v/v) removed non-phosphocholine compounds and then chloroform/MeOH/H_2O (65/25/4 v/v) eluted the phosphocholine products, leaving DMAP on the stationary phase. The desired **50** could be further purified from other phosphocholine-based compounds by flash chromatography on silica eluting with 0 – 4% H_2O / 25% MeOH / $CHCl_3$.

Deprotecting Fmoc-protected **50** with the non-nucleophilic base 1,8-diazabicyclo(5.4.0)undec-7-ene (DBU) in anhydrous chloroform for 30 minutes gave the primary amine in preparation for amide coupling. The XB or HB ethylparaben activated ester **45** was then added to the reaction mixture and left to react for 6 h. As previously stated, an

activated ester strategy was employed as the nucleophilic catalyst DMAP may abstract iodine from the iodotriazole XB binding motif.[137] Eluting the reaction mixture through a plug of Dowex 50W X8, as previously described, served to remove the DBU which coelutes during flash chromatography on silica with phosphocholine lipids. With the HB and XB relay transporters in hand their transport capabilities could be assessed in model vesicles.

2.3.3 Relay Transport Activity in POPC LUVs

The transporters **T4^{HB}** and **T4^{XB}** were inspired by the design of Smith's urea relay transporter **38** (**Figure 1.24**).[123] The polar zwitterionic headgroup inhibits membrane translocation and thus confines the transporter to one membrane leaflet – an essential feature for relay transport. To further polarise and hence improve the binding interaction of the C-H, or C-I bond on the bis-triazole motif, strongly electron withdrawing perfluorobenzene groups were used.[56] Not only does the integration of perfluorinated moieties enhance the HB or XB donor potency, but also serves to increase receptor lipophilicity which has been demonstrated for mobile carriers to improve transport activity.[156] The HB bis-prototriazole **T4^{HB}** was also prepared to serve as an unselective control compound, while the XB bis-iodotriazole **T4^{XB}** was expected to display strong Cl^- > OH^- transport selectivity.

The transport activity of the XB and HB transporters **T4^{XB}** and **T4^{HB}**, respectively, were established using ion transport assays with HPTS encapsulated POPC LUVs. As expected, when added in a solution in DMSO (5 µL DMSO, 1 mol% with respect to lipid, **Figure 2.12A-B**) to pre-formed LUVs, no ion transport was observed. This is a result of the zwitterionic headgroup preventing membrane translocation of the transporter – with the transporter in the outer leaflet of the membrane transport only, a relay mechanism is not possible. To confirm the inactivity was due to the immobilisation of the transporter in the outer leaflet and not due to

poor membrane deliverability of **T4**, the incorporation efficiency was determined by UV-vis analysis. In this experiment, POPC LUVs were prepared as for the transport studies, but without HPTS. Addition of **T4^{XB}** (1.25 mM in DMSO, 50 µL, 5 mol% to lipid) to 2.5 mL of POPC LUVs (200 nm, 0.50 mM lipid; internal and external buffer comprising 100 mM NaCl, 10 mM HEPES, pH 7.0) and recording the UV-vis spectrum before and after size-exclusion chromatography (Sephadex G-25 column) allowed quantification of the membrane incorporation efficiency. A high incorporation efficiency of >95% for **T4^{XB}** in POPC LUVs (**Figure 2.12C**) revealed that the lipid architecture promoted efficient delivery of the transporter to the membrane. The lack of detectable transport activity (1 mol% loading) when present in the outer leaflet only, demonstrated that transporters **T4^{XB}** and **T4^{HB}** were both incapable of a mobile carrier anion transport mechanism.

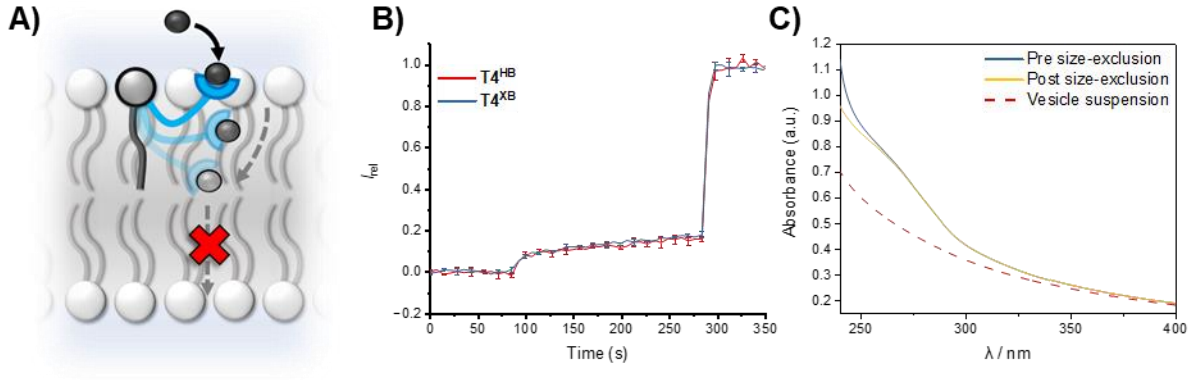

Figure 2.12 Relay transport is not facilitated when the transporter is present in only the outer leaflet of the membrane. *A) Schematic of inactive relay transporter. B) HPTS transport data for **T4^{XB}** and **T4^{HB}** added externally (5 µL DMSO, 1 mol% to lipid) to POPC LUVs (31.25 µM) prior to the start of the measurement with the base pulse (20 µL, 0.5 M $NaOH_{(aq)}$) added at 90 s. Error bars denote the standard deviations from two runs. C) UV-vis spectra of **T4^{XB}** (5 mol% to lipid) embedded in POPC LUVs pre- and post-size exclusion and blank POPC LUVs (200 nm, 0.25 mM lipid, 100 mM NaCl, 10 mM HEPES, pH 7.0). Incorporation efficiency was determined to be >95%.*

The transport activity of the XB and HB relay transporters (**T4^{XB}** and **T4^{HB}**) was tested when incorporated into both leaflets of the membrane (**Figure 2.13**). To obtain an equal distribution in both leaflets, the lipid-based transporters were pre-incorporated into the membrane during LUV preparation. Stock solutions of **T4^{XB}** and **T4^{HB}**, respectively, were prepared in

chloroform and stored in the freezer. Combining the transporter and lipid stocks in various ratios for lipid film preparation allowed vesicles with various mole percentages of transporter to be obtained, and the concentration dependent transport activity to be determined (**Figure 2.13B,E**). Hill analysis was performed based on the fractional activity at 276 s, immediately prior to lysis (**Figure 2.13C,D**). **T4^{XB}** and **T4^{HB}** exhibited EC_{50} values of 0.18 mol% and 0.58 mol% in POPC LUVs when pre-incorporated, respectively, in line with a previous study which showed HB prototriazole mobile carriers to be less active than their XB iodotriazole analogues.[61] This is a result of the stronger binding strength of the XB iodotriazole motif compared to the HB analogue, exemplified by the strong binding of Cl^- by the analogous XB receptor **T3** in a competitive solvent previously described (**Section 2.2.2**).

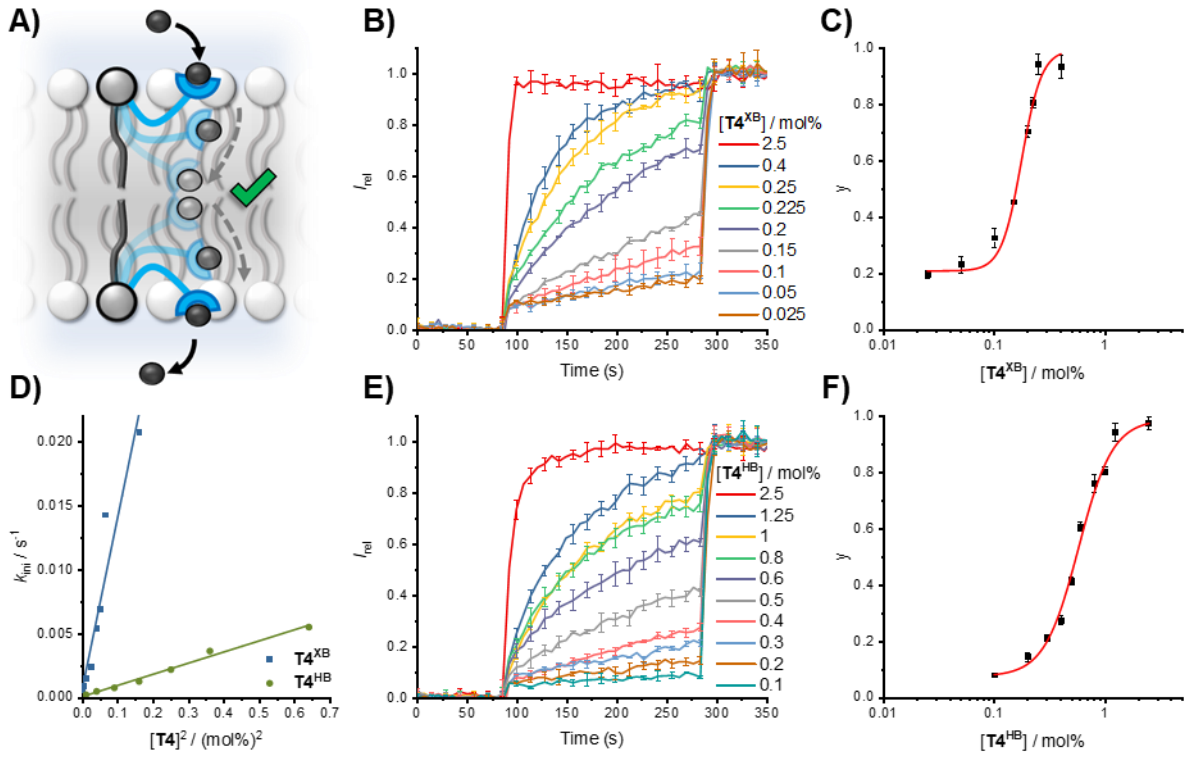

Figure 2.13. Relay transport activity of T4^{XB} and T4^{HB} in POPC LUVs. *A) Schematic of effective relay transport, where exchange of an ion between transporters in opposite leaflets of the membrane facilitates transport. B) HPTS transport data for **T4^{XB}** (0.025 – 2.5 mol% to lipid) pre-incorporated in POPC LUVs (200 nm, 0.25 mM lipid, 100 mM NaCl, 10 mM HEPES, pH 7.0) and C) Hill analysis of the fractional activity at 276 s, just prior to lysis. D) Concentration dependence of relay activity with pre-incorporated **T4^{XB}** and **T4^{HB}**, and linear relationship for the initial rate, k_{ini} with respect to [**T4**]^2. E) HPTS transport data for **T4^{HB}** (0.1 – 2.5 mol%) pre-incorporated in POPC LUVs. F) Hill analysis of the fractional activity at 276 s, just prior to lysis. Error bars denote the standard deviations from two runs.*

Table 2.3 *Characteristics of the anion relay transporters* ***T4^{XB}*** *and* ***T4^{HB}***.

Transporter	$EC_{50}{}^{a}$ / mol%	n^{b}	*Order of dependence of k_{ini} on [**T4**]*
T4^{XB}	0.18 (0.01)	4.8 (0.8)	Bimolecular
T4^{HB}	0.58 (0.03)	2.8 (0.3)	Bimolecular

a Effective concentration to reach 50% of maximal activity in the HPTS assay, determined from Hill analysis of the relative fluorescence intensity at t = 276 s, immediately prior to vesicle lysis. Experiments conducted in POPC LUVs (mean diameter 200 nm) loaded with 1 mM HPTS, NaCl (100 mM) and buffered at pH 7.0 with 10 mM HEPES. b Hill coefficient. Errors at the 95% confidence limit.

For both **T4^{XB}** and **T4^{HB}** the Hill coefficient *n* is greater than one (**Table 2.3**), demonstrating that the assembly of the anion-transporter complex within the membrane is endergonic.[143] The corresponding Hill coefficients of 4.8 ± 0.8 and 2.8 ± 0.3 for **T4^{XB}** and **T4^{HB}**, respectively, are consistent with multiple relay transporters in the rate-limiting step of the transport process. However, as previously noted the absolute values are very sensitive to conditions and minor structural changes, therefore provide minimal information about stoichiometry compared to kinetic analysis. Fitting the transport kinetics curves (I_{rel} vs *t*) to the first order exponential function (**Equation 5**) allowed the initial rate of transport, k_{ini}, to be determined using **Equation 6**.

$$I_{rel} = a - e^{-\frac{kt}{b}} \qquad \textbf{(Equation 5)}$$

$$k_{ini} = \frac{1}{b} \qquad \textbf{(Equation 6)}$$

The observed initial rate of anion transport, k_{ini}, plotted against concentration of pre-incorporated relay transporter was found to have a non-linear relationship for both **T4^{XB}** and **T4^{HB}**. The non-linear dependence of transport rate on the concentration of relay transporter suggests multiple molecules are implicated in the rate-determining step of ion transport, consistent with a Hill coefficient $n > 1$. Plotting k_{ini} versus [**T4**]^2 for both **T4^{XB}** and **T4^{HB}** gave a linear relationship revealing transport activity was limited by a bimolecular rate-determining

step (**Figure 2.13D**). For the relay mechanism, at least two transporter molecules are required, with one in each leaflet of the membrane. The observed linear relationship of k_{ini} versus [**T4**]^2 is consistent with this mechanism, and implies the exchange step between transporters in opposite leaflets is rate-limiting.

2.3.4 Activity of Relay Transporters with Asymmetric Bilayer Distributions

To probe which step of the relay transport mechanism was rate-limiting, an asymmetric distribution of relay transporters across the bilayer was prepared (**Figure 2.14**). This was achieved by externally adding **T4^{XB}** (1.05 mol% to total lipid in 5µL DMSO) to a suspension of POPC LUVs with **T4^{XB}** pre-incorporated (0.15 mol% to total lipid). This generated a membrane with an excess of relay transporters immobilised in the outer leaflet compared to the inner leaflet (1:15 in:out, 1.2 mol% with respect to lipid in total). The transport activity was observed to be the same for the symmetric distribution as the asymmetric distributions, with 15 times the number of transporters immobilised in the outer leaflet (**Figure 2.14B**). This result is consistent with our hypothesis that the inter-relay exchange step within the membrane is rate-limiting, and not anion binding at the interface, as the latter would be expected to increase in rate with transporter concentration in the outer membrane leaflet. Interestingly, it also implies that dissociation of the 2:1 transmembrane relay-anion complex is rate-limiting (**Figure 2.14**, step iii), as the rate of transmembrane complex formation would be expected to increase with the number of relay transporters in the outer leaflet. Identifying the dissociation of the 2:1 transmembrane complex as rate-limiting can be rationalised by considering that the low polarity environment of the membrane interior will enhance ion association to the receptors.[158,159]

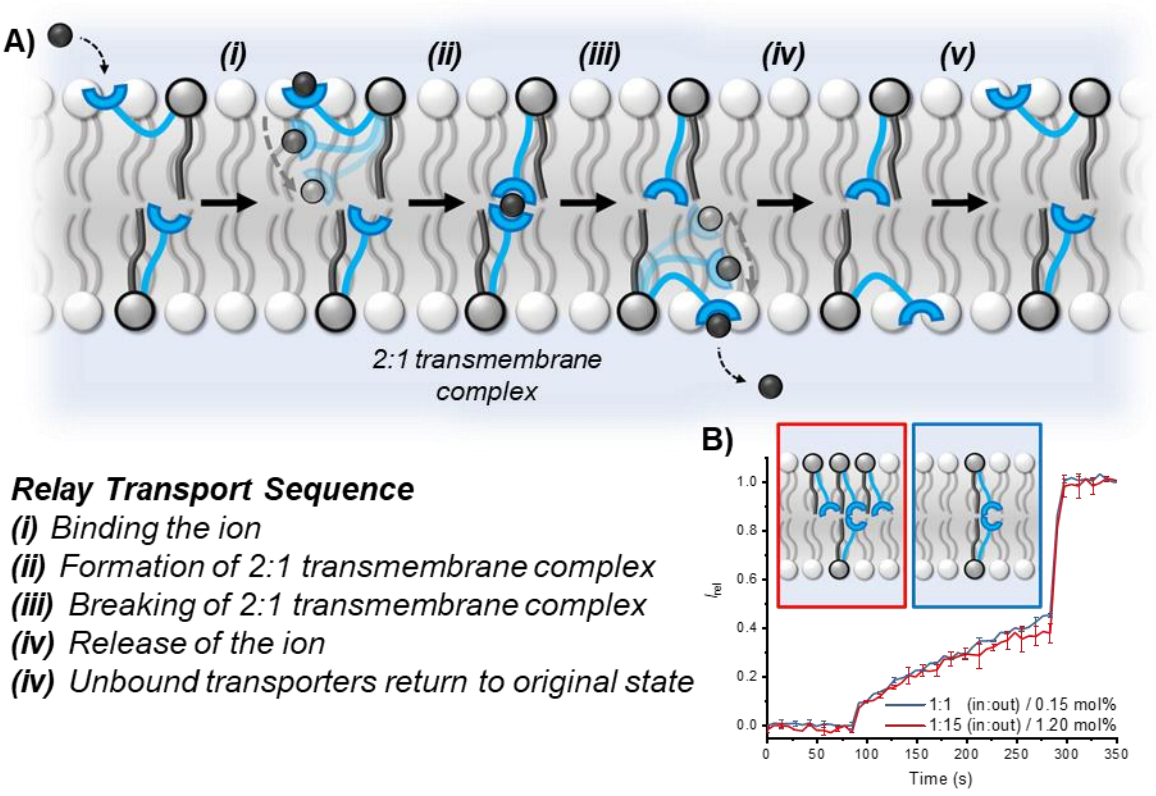

Figure 2.14. Effect of an asymmetric distribution of transporters on relay transport. *A) Schematic of the relay transport sequence. B) HPTS transport data for* ***T4^{XB}*** *with a symmetric loading (0.15 mol% to lipid, pre-incorporated, blue data) and an asymmetric loading (0.15 mol% to lipid, pre-incorporated with a further 1.05 mol% added externally in DMSO, red data). Error bars denote the standard deviations from two runs.*

2.3.5 Investigating The Effect Of Membrane Fluidity On Relay Mediated Anion Transport

Performing the HPTS assay with 1,2-dipalmitoyl-*sn*-glycero-3-phosphocholine (DPPC) lipids allowed the effect of membrane fluidity on transport activity to be explored (**Figure 2.15**). At room temperature, DPPC membranes are in the gel phase which prevents the mobility of transporters within the bilayer, therefore arresting mobile carrier activity which is dependent on carrier translocation. Channel activity is generally unaffected by membrane fluidity and hence the DPPC assay is commonly used to interrogate if a channel mechanism is operating.[160] The effect of membrane fluidity on the relay transport mechanism had not previously been investigated.[123] At room temperature DPPC LUVs with **T4^{XB}** pre-incorporated (0.2 mol% to lipid) showed no transport activity, demonstrating that the mobility of the carrier arm of relay transporters is essential for their activity. This also confirmed that **T4^{XB}** does not operate *via*

a channel mechanism. Transport activity was recovered when the DPPC LUVs where heated to 45 °C, above the gel–liquid phase transition temperature (T_m = 41 °C), where mobility of the relay transporter carrier arm was restored.

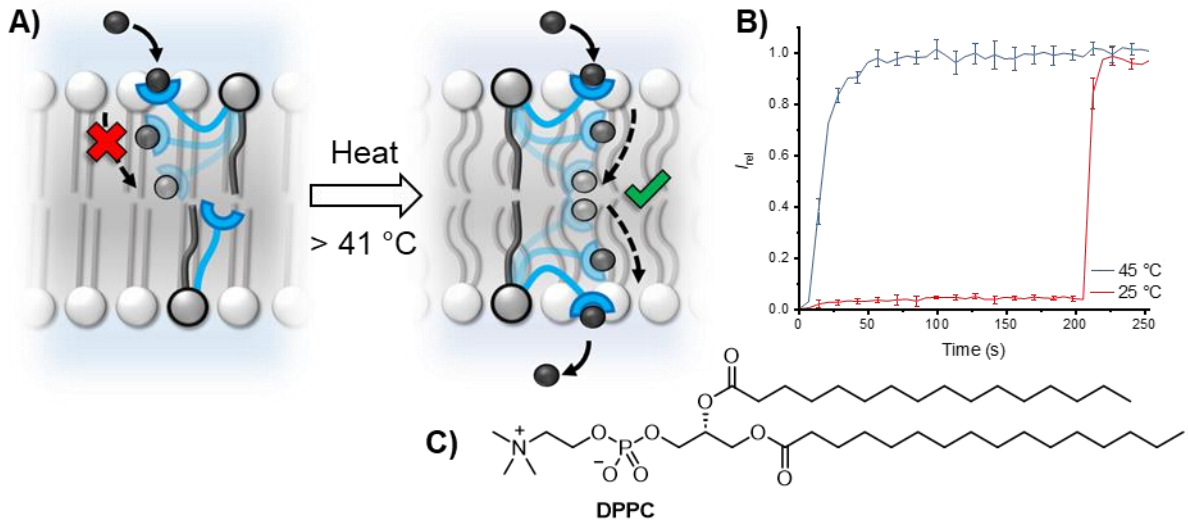

***Figure 2.15. Effect of membrane fluidity on relay transport**. A) Schematic of relay transport arrested in a gel phase membrane and restored in a liquid phase membrane. B) HPTS transport activity of **T4^{XB}** (0.2 mol% to lipid, pre-incorporated) in DPPC LUVs at 25 °C (gel phase) and 45 °C (liquid phase). Error bars denote the standard deviations from two runs. C) Structure of DPPC.*

2.3.6 Determining the Ion Selectivity of Relay Transporters

To interrogate which ions are exchanged across the membrane by **T4^{XB}** relay mediated dissipation of a pH gradient, a number of control experiments were performed (**Figure 2.16**). Utilising a phospholipid with the same fatty acid tails, but a different headgroup, will maintain the properties of the membrane interior but change the surface characteristics of the vesicles. To this end 1-palmitoyl-2-oleoyl-*sn*-glycero-3-phospho-(1'-*rac*-glycerol) (POPG), which has an anionic headgroup, was utilised to prepare POPG LUVs with **T4^{XB}** (0.2 mol%) pre-incorporated. The observed transport inhibition is characteristic of an anion dependent process,[35] where electrostatic repulsion at the surface of the vesicle with the incoming anion reduces the anion association rate with the relay transporter and hence overall transport activity (**Figure 2.16A-C**). The cation dependent Na^+/H^+ antiport process can therefore be ruled out and indicates

T4^{XB} may be operating *via* either a Cl^-/OH^- antiport or functionally equivalent Cl^-/H^+ symport process. Given the low basicity of triazole receptors ($pK_aH \sim 0–1$),[161] the relay transporter **T4^{XB}** likely dissipates the pH gradient by Cl^-/OH^- antiport, which is in agreement with observations from previous studies on XB-mediated anion transport.[61,133,162]

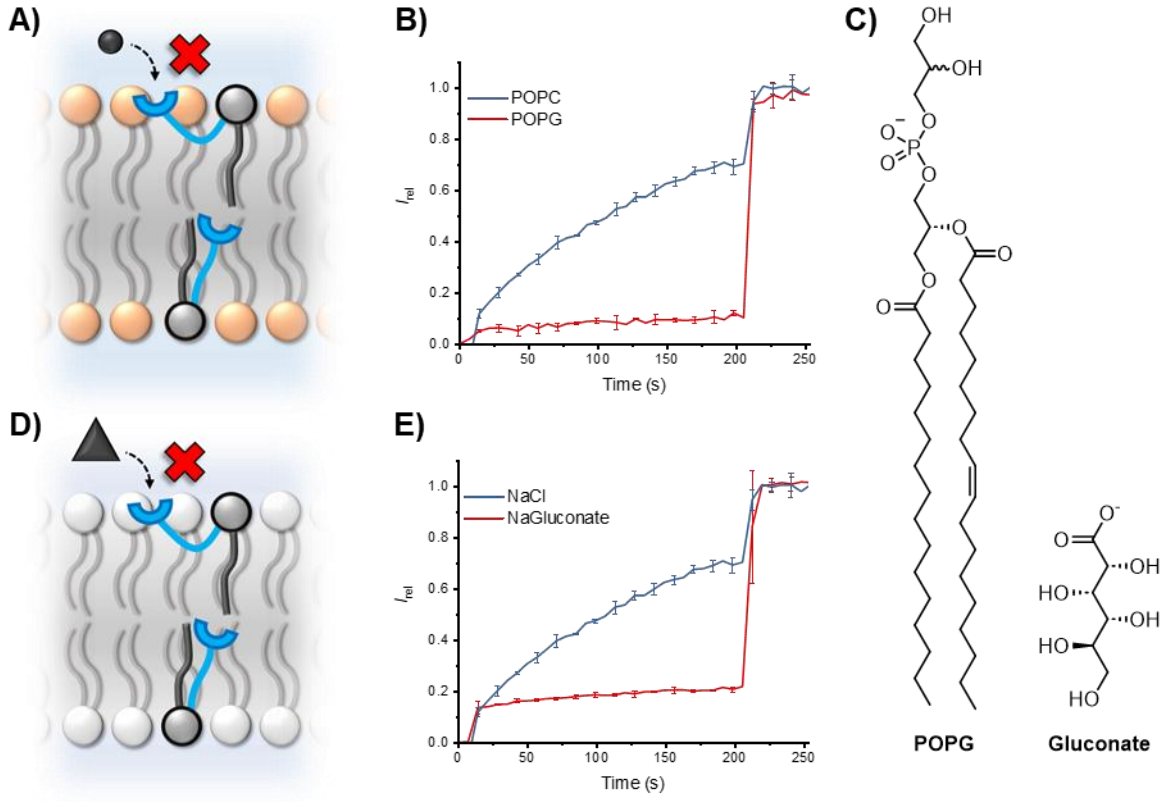

Figure 2.16. Inhibiting the binding of anions arrests relay transport activity. *A) Schematic of changing the lipid headgroup inhibiting anion binding. B) Comparison of HPTS transport data for **T4^{XB}** (0.2 mol% to lipid, pre-incorporated) in POPC and POPG LUVs. C) Structure of POPG and the gluconate anion. D) Schematic of changing the anion inhibiting binding. E) Comparison of HPTS transport data for **T4^{XB}** (0.2 mol% to lipid, pre-incorporated) in POPC LUVs with NaCl or NaGluconate in the internal and external buffer solution (100 mM NaX, 10 mM HEPES, pH 7.0). Error bars denote the standard deviations from two runs.*

Further evidence for the Cl^-/OH^- antiport mechanism was provided by experiments in which the chloride in the intra and extravesicular buffer was replaced with gluconate, a larger hydrophilic anion. Transport was not detected with the gluconate anion (**Figure 2.16C-E**) which is consistent with **T4^{XB}** being incapable of either cation transport (*via* H^+/Na^+ antiport) or overcoming the significant dehydration penalty required for a OH^-/gluconate antiport

process. The experiment also serves as a control to demonstrate that the transporter does not lead to non-specific leakage through disruption of the bilayer at this loading (0.2 mol%), since no change in the ratiometric emission of HPTS was observed.

The transport activity of **T4^{XB}** and **T4^{HB}** was measured in the presence of FCCP to uncouple the Cl^- transport from OH^-, for a discussion of how the FCCP assay operates see **Section 2.2.2**. For both triazole-derived relay transporters **T4^{XB}** and **T4^{HB}**, given the probable Cl^-/OH^- antiport mechanism, the assay reports Cl^- > OH^- selectivity. Hill analysis of **T4^{XB}** and **T4^{HB}** transport activity in the presence and absence of FCCP was conducted for a range of concentrations pre-incorporated in POPC LUVs (**Table 2.4**), following the analysis previously described for the mobile carriers (see **Section 2.2.2**). The measured transport activity of **T4^{HB}** was found to be independent of the presence of FCCP (**Figure 2.17A**), indicating little selectivity for Cl^- > OH^- (*F'*=1.2) in line with previous results for unselective prototriazole mobile carriers.[133] In contrast, the observed activity of the halogen bonding derivative **T4^{XB}** in the presence of FCCP was significantly enhanced (**Figure 2.17B**) demonstrating appreciable Cl^- > OH^- selectivity (*F'*=5). In the presence of FCCP, **T4^{XB}** was five times more active with an EC_{50} value of 0.036 mol% constituting a significant enhancement on Smith's relay transporter (~3 mol%) by 2-orders of magnitude.[123] Fitting the Cl^- transport activity of **T4^{XB}** to the Hill equation (**Equation 3**) gave an *n* value of 2.4±0.2 indicating that an endergonic assembly of multiple molecules within the bilayer remained the rate-limiting step to facilitate transport.

Plotting $k_{ini}(Cl^-)$ against the concentration of transporter squared again gave a linear relationship, indicating that the rate-limiting step for Cl^- transport was also bimolecular (**Figure 2.17C**). Given that the rate-limiting process is dissociation of the transporter–anion complex in the centre of the membrane, the observed overall rate of transport is therefore

related to the product of the dissociation rate constant, k_d, and the concentration of the 2:1 relay-anion (A^-) complex in the membrane, k_d[2**T4**^{XB}·**A**$^-$]. The selectivity observed is therefore based on kinetic parameters, specifically the difference in the product of the dissociation rate constant and the concentration of the membrane spanning 2:1 relay-anion complex for each anion. The observed preference of **T4**^{XB} for Cl^- > OH^- in the relay transport mechanism therefore results from the more facile exchange of chloride between the halogen bonding donors anchored in opposite leaflets. This is consistent with previous theoretical calculations which revealed stronger hydroxide binding to iodotriazole derivatives than chloride in apolar solvent,[133] demonstrating that the 2**T4**^{XB}–OH^- complex is likely more stable in the bilayer than the 2**T4**^{XB}–Cl^- complex.

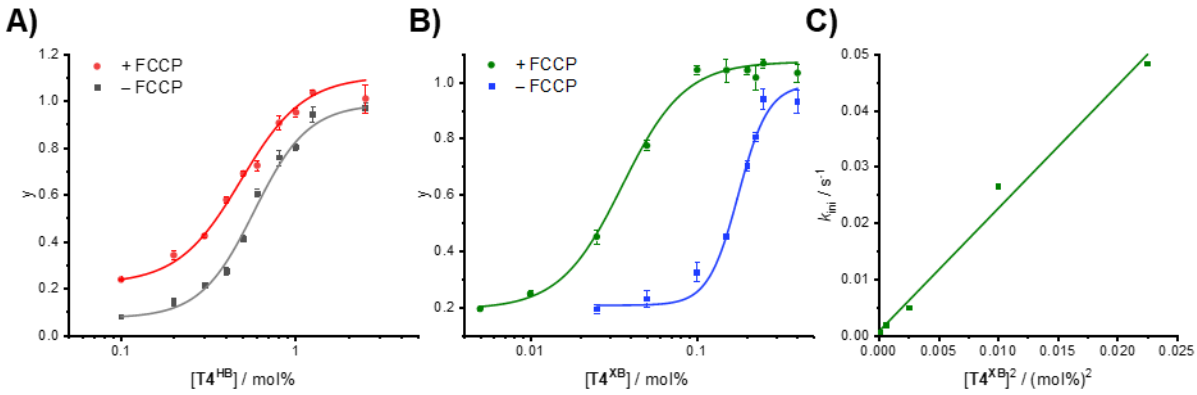

Figure 2.17. Cl^- > OH^- anion transport selectivity of relay transporters. *A)* ***T4***^{HB} *and B)* ***T4***^{XB} *concentration dependent activity (points) in POPC LUVs (31.25 μM) with and without FCCP (0.8 mol%) fit to the Hill equation (lines). C) Concentration dependence of pre-incorporated* ***T4***^{XB} *relay activity with FCCP (0.8 mol%), and linear relationship for the initial rate, k_{ini} with respect to [**T4**^{XB}]^2. Error bars denote the standard deviations from two runs.*

Table 2.4 *Characteristics of the anion relay transporters* ***T4***^{XB} *and* ***T4***^{HB} *anion selectivity*

Transporter	EC_{50}[a] / mol%	EC_{50}^{FCCP}[a] / mol%	$F'(Cl^-/OH^-)$[b]
T4^{XB}	0.18 (0.01)	0.036 (0.002)	5.0
T4^{HB}	0.58 (0.03)	0.49 (0.02)	1.2

a Effective concentration to reach 50% of maximal activity in the HPTS assay, in the absence or presence of FCCP (0.8 mol%), determined from Hill analysis of the relative fluorescence intensity at t = 276 s, immediately prior to vesicle lysis. Experiments conducted in LUVs of POPC (mean diameter 200 nm) loaded with 1 mM HPTS, NaCl (100 mM) and buffered at pH 7.0 with 10 mM HEPES. b Factor of enhancement in the transport rate between Cl^- and OH^- ($F'(Cl^-/OH^-) = EC_{50}/EC_{50}^{FCCP}$) using the FCCP assay. Errors at the 95% confidence limit.

2.3.7 Impact of Membrane Thickness on Relay Transporter Anion Selectivity

A strong dependence of transport rates on lipid bilayer thickness was demonstrated by Smith to be characteristic of relay transport.[123] In contrast, mobile carriers are typically characterised by anion binding limited activity, which is independent of membrane thickness (see **Section 2.2.3** for discussion). Transporter **T4^{XB}** displays the characteristic decrease in activity with increasing bilayer thickness of relay transport, whilst maintaining a constant phosphocholine headgroup across the series of 16:1 PC, POPC and 18:1 PC (**Figure 2.18**). This strong rate dependence on membrane thickness served as further evidence that the exchange step of relay transport is rate-limiting, as this step would be expected to be markedly affected by a change in the thickness of the hydrophobic region of the bilayer. As the thickness of the hydrophobic region of the membrane decreases, the dielectric constant at the centre of the bilayer increases and therefore can be considered less nonpolar. This increase in effective dielectric constant would result in weaker binding of the anion[161] in the transmembrane 2:1 relay-anion complex in thinner membranes increasing the dissociation rate constant, to promote faster transport.

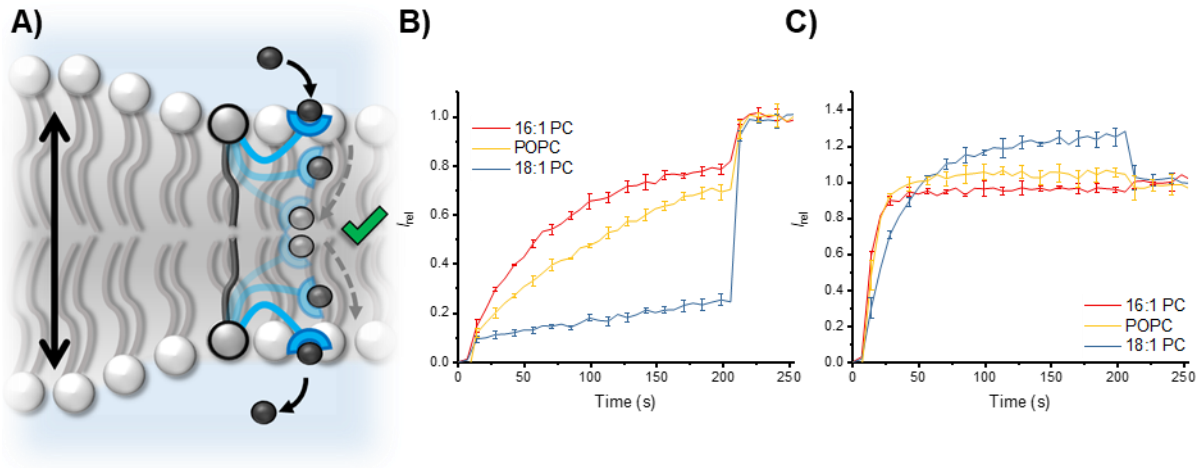

Figure 2.18. Effect of membrane thickness on relay transport activity and selectivity. *A) Schematic of relay transport upon changing the thickness of the hydrophobic region of the bilayer. B) HPTS transport activity of **T4^{XB}** (0.2 mol% to lipid, pre-incorporated) in 200 nm LUVs (31.25 μM) prepared from lipids with different alkyl chain lengths (16:1 PC, POPC, 18:1 PC) in the absence of FCCP (C) and in the presence of FCCP (0.8 mol%). Error bars denote the standard deviations from two runs.*

The dependence of **T4^{XB}** mediated chloride transport activity (with FCCP) was determined in LUVs comprised of lipids of different alkyl chain lengths. In the presence of FCCP, **T4^{XB}** mediated transport was also dependent on membrane thickness, decreasing with increasing alkyl chain length of the phospholipid which comprised the bilayer (**Figure 2.18C**). The relay transporter **T4^{XB}** maintained the anti-Hofmeister Cl^- > OH^- selectivity preference across the range of membrane thicknesses, in contrast to the analogous XB mobile carrier **T3**, which lost Cl^- > OH^- anion selectivity in the thinnest membrane (16:1 PC). The selectivity factor, *F*(Cl^-/OH^-), was used to quantify the Cl^- > OH^- selectivity in terms of initial rate of transport at a specific transporter loading (**Equation 7**).

$$F(\mathrm{Cl^-/OH^-}) = \frac{k_{ini}(\mathrm{Cl^-})^{FCCP}}{k_{ini}(\mathrm{OH^-})^{no\ FCCP}} \qquad \textbf{(Equation 7)}$$

The selectivity of the relay transporter **T4^{XB}** for Cl^- > OH^- was found to improve with increasing hydrophobic thickness (**Table 2.5**). Based on the selectivity factor, *F*(Cl^-/OH^-), increasing the alkyl chain length of the phospholipid by 2-carbons was found to improve the selectivity by a factor of 6 from 16:1 PC (*F*=4) to 18:1 PC (*F*=24). While this same trend was observed for the mobile carrier analogue **T3**, the basis of the selectivity is different for the relay transporter. The selectivity of **T4^{XB}** arises from the difference in dissociation rate constant between the Cl^- and OH^- transmembrane 2:1 relay-anion complex, assuming the concentration of the two structures are equal. Since the binding of the more hydrophilic anion (OH^-) would be expected to be more significantly affected by a change in dielectric constant, the increase in hydrophobic thickness likely slows the rate of hydroxide dissociation more than that of chloride, accounting for the increase in selectivity.

Table 2.5 *Characteristics of the anion relay transporters* ***T4^{XB}*** *and* ***T4^{HB}*** *anion selectivity in different membrane thicknesses*

Transporter in various lipids		$k_{ini}{}^{a}(Cl^-)^{FCCP}/10^{-3}$ s^{-1}	$k_{ini}{}^{a}(OH^-)/10^{-3}$ s^{-1}	$F(Cl^-/OH^-)$ ^{b}
T4^{XB}	16:1 PC	82 (2)	20.8 (0.1)	4.0
	POPC	64 (2)	5.2 (0.1)	12
	18:1 PC	22 (1)	0.9 (0.1)	24
T4^{HB}	POPC	3.7 (0.1)	3.6 (0.2)	1.0

a Initial rates of chloride transport (k_{ini}) obtained using the HPTS assay for each transporter in the presence of FCCP (0.8 mol%). b Initial rates of hydroxide transport (k_{ini}) obtained using the HPTS assay for each transporter. c Factor of enhancement in the transport rate between Cl^- and OH^- ($F(Cl^-/OH^-) = k_{ini}(Cl^-)/k_{ini}(OH^-)$) determined using the FCCP assay. Errors at the 95% confidence limit.

2.4 Conclusions of Chapter 2 and Future Work

For the application of synthetic ion transporters as therapeutics it is essential to design highly selective transporters. The phospholipid-anchored transporter **T4^{XB}** displays the highest transport activity for a relay transporter reported to date. It also shows therapeutically important anti-Hofmeister Cl^- > OH^- selectivity, as a result of the sigma-hole XB binding interaction. The selectivity of **T4^{XB}** was shown to arise from the difference in dissociation rate constant between the Cl^- and OH^- transmembrane 2:1 relay-anion complex, which was experimentally confirmed to be the rate determining step of the relay transport mechanism. Interestingly, when studying both relay transporters and mobile carriers in a range of lipid bilayer thicknesses the unique trends of the two transport mechanisms were elucidated. Mobile carriers, which characteristically display anion binding limited transport activity, demonstrated invariant activity in different bilayer thicknesses when Cl^- transport was rate-limiting. However, for OH^--limited transport activity the mobile carriers demonstrated membrane thickness dependent transport activity – indicative of rate-limiting translocation of the anion-mobile carrier complex. These mechanistic insights into the kinetically controlled anion selectivity of both mobile carriers and relay transporters provide a basis for the design

of selective anionophores for future therapeutic applications, and also highlight the unique properties of relay transporters over their mobile carrier counterparts.

To further improve the transport activity of relay transporters, future work to develop a membrane spanning unimolecular relay transporter is proposed. Tethering two phospholipid-based relay transporters together *via* the *sn*-1 position (**Figure 2.19**) is hoped to improve the transport activity. For the relay transporters described in this chapter, the self-assembly of the membrane spanning 2:1 relay-anion complex is essential for activity. Covalently linking together relay transporters, such that the exchange step of relay transport now occurs intramolecularly is expected to significantly improve the transport activity. The effect of changing the linker length (R) of this new anchored transporter is expected to control both transport rate and selectivity to generate highly Cl^- > OH^- selective transporters.

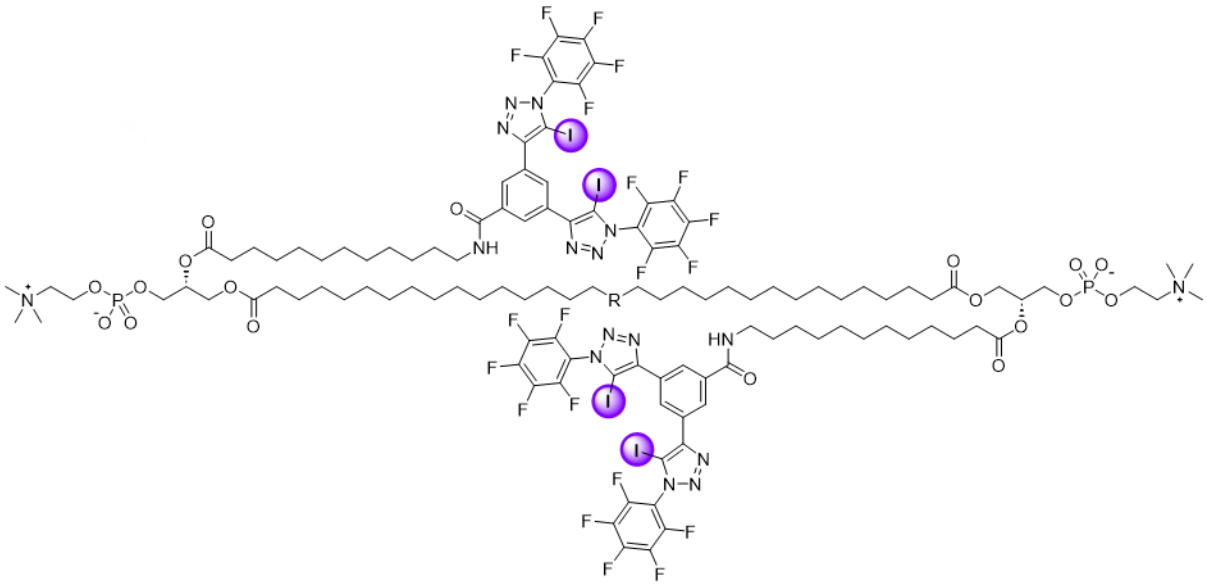

Figure 2.19 Proposed unimolecular relay transporter, where R denotes various linking groups.

Chapter 3: Photo-Responsive Relay Transporters

3.1 Therapeutic Importance of Stimuli-Responsive Anion Transporters

The development of highly selective synthetic transporters is of vital importance for their application as therapeutics, where they may compensate for the inactivity of highly selective transmembrane proteins to treat channelopathies.[163] As well as exquisite specificity over the ions transported, protein channels also commonly display gated behaviour. The ability to control the flux of ions through protein channels in response to stimuli such as membrane potential, ligand binding, membrane tension and light is integral to their function of maintaining ion gradients at homeostasis.[6,73] Synthetic transporters which display stimuli responsive activity have therefore become highly desirable, to mimic the function of biological gated channels and hence provide more targeted control over activity for their application in biological settings. Stimuli responsive behaviour allows for high spatiotemporal control, reducing off target transport activity and preventing unwanted side effects as well as the build-up of resistance in pharmacological treatment.[75] For the future development of bottom-up synthetic biology, stimuli-responsiveness will be a prerequisite of synthetic transporters to function in biological environments in cooperation with biotic counterparts.

Changes in pH have commonly been adopted as a stimulus to control the anion transport activity of mobile carriers.[74] Numerous examples of anionophores which operate only below a specific pH have been described, as a result of receptor deprotonation, including thiosquaramide **11** described in **Section 1.2.3**.[45] Hydrogen bonding receptors are by far the most commonly employed recognition unit for anionophores. Such receptors are however prone to deprotonation, as the acidic protons responsible for binding are highly polarised to promote stronger interactions and therefore are more liable to dissociate entirely

deprotonating the receptor. Deprotonated anionic receptors no longer bind anions, as a result of electrostatic repulsion and therefore are ineffective anion mobile carriers.

Gale and co-workers reported the first example of a pH responsive anion mobile carrier, based on the thiosquaramide anion binding unit (**Figure 3.1A**).[45] Thiosquaramide receptors bind anions more strongly than their oxosquaramide counterparts owing to the more acidic NH protons, demonstrated by the significant change in pK_a values (pK_a(thiosquaramide) ~ 7, pK_a(oxosquaramide) ~ 10). Through measuring the transport of the anionophores **51a-b** at various pH values (4-9) using an ISE assay, the change in activity was quantified by an initial rate of chloride efflux. The oxosquaramide **51a** displayed no change in transport activity, as receptor deprotonation was not significant below the pK_a of the receptor. Interestingly, the thiosquaramide **51b** displayed sigmoidal activity with changing pH where activity was lost above an apparent pK_a value of 6.0±0.2 in the membrane environment. In this way the subsequent transport activity could be used as a reporter of the deprotonation equilibrium of the anionophore in the bilayer to determine the apparent pK_a.

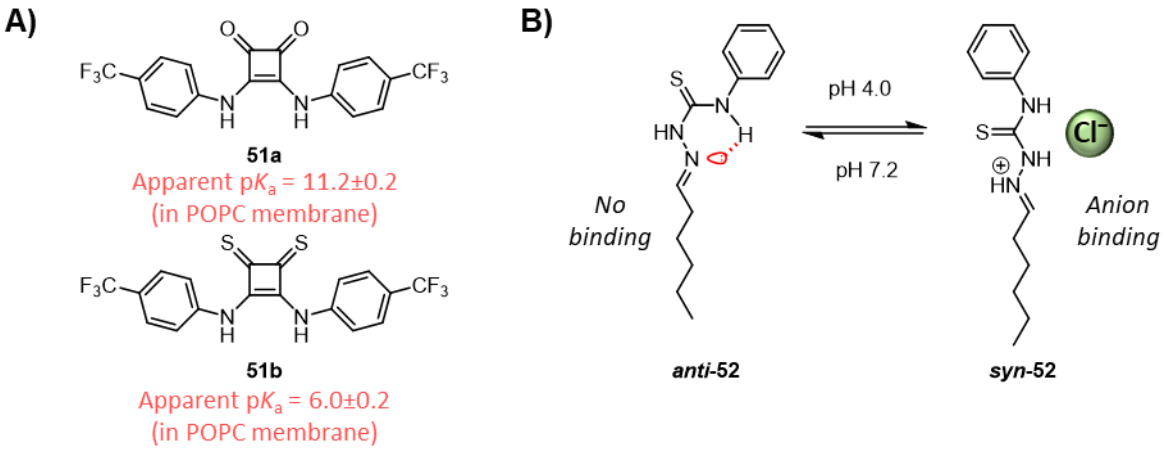

Figure 3.1 pH-Responsive anion mobile carriers. *A) Oxosquaramide (**51a**) displayes no change in activity with pH (4-9), while thiosquaramide (**51b**) was active below pH 7 and inactive above. B) pH-Triggered conformational change of **52** regulates anion binding and hence transport activity.*

pH-Responsive anionophores have also been reported which display switchable activity due to pH induced structural changes of the binding unit. Gale and co-workers investigated the transport activity of phenylthiosemicarbazone molecular switch **52**, which changes conformation in response to the protonation state of the receptor (**Figure 3.1B)**.[164] A 640-fold increase in activity was observed, switching from the inactive ***anti*-52** (pH 7.2) to the active ***syn*-52** (pH 4.0) where both NH thiourea hydrogen bond donors were available to bind Cl^-. The anionophore facilitated highly selective H^+/Cl^- symport under acidic conditions as only the ***syn*-52·**HCl complex was neutral and therefore membrane permeable. This pH-responsive molecular switch demonstrated the importance of both regulating transport activity and ensuring high selectivity in ion transport.

Employing photo-switches within mobile carrier designs has enabled regulation of ion transport with high spatiotemporal control as described in **Section 1.2.7**.[80] Photo-switchable mobile carriers most commonly rely on azobenzene as the photo-responsive unit.[92,93,165] However, stiff-stilbene[166,167] and acylhydrazone systems[168] have been reported. Talukdar and co-workers reported a 2-pyridyl acylhydrazone receptor (**53**) and investigated the photo-switchable transport activity in vesicles (**Figure 3.2**).[168] Compound **53** could be photo-switched from the thermodynamically stable open *E*-conformation with 312 nm light to the closed Z-conformation. In the *Z*-conformation the binding pocket is blocked by the pyridyl group, which forms an intramolecular hydrogen bond preventing anion binding. Carrier ***E*-53** showed efficient ion binding and transport activitiy, whilst anion binding and transport activity was significantly attenuated by around 80 % upon photo-isomerization to ***Z*-53** using 312 nm light *ex situ*. The active species (***E*-53**) could be regenerated using trifluoroacetic acid as a stimulus. Such reversibly gated ion transport activity triggered by both light and acid/base stimuli could be repeated over numerous cycles.

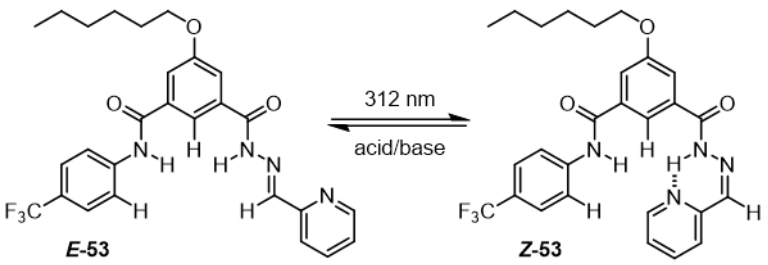

Figure 3.2 Photo-switchable anion mobile carrier. *Talukdar's acylhydrazone photo-switchable anion transporter **53**.*[168]

Beyond the classical mobile carrier and channel mechanisms of ion transport, *anchored carriers* have recently been reported which function through an entirely abiotic mechanism of transport. In 2018, Bao, Zhu and co-workers first reported the application of a mechanical bond to couple the carrier unit to a membrane spanning anchor in a [2]rotaxane shuttle **35**, capable of K^+ transport (**Figure 1.23**).[119] The activity of **35** was found to be dependent on the shuttling motion of the interlocked carrier unit, which facilitated the transport of cations across model lipid membranes. In a related system the shuttling motion could be controlled through incorporation of a photoswitch into the interlocked architecture, thereby enabling photo-gated transport activity of the unimolecular anchored carrier **54** (**Figure 3.3**).[169] An azobenzene was incorporated within the membrane spanning axle, such that shuttling of the macrocycle, and hence mobility of the anchored carrier arm, could be restricted through photo-switching the azobenzene moiety to ***Z*-54** to switch off cation transport. The system was shown to be fully reversible, with *in situ* light-gated transmembrane activity measured in LUVs and BLM experiments. Single-channel conductance experiments showed regular square-like signals after irradiation with 450 nm visible light forming ***E*-54**, while the ***Z*-54** displayed no current signal after long detection times. This unique molecular machine-inspired anchored carrier transporter combined the properties of molecular switches with the dynamic motion of interlocked components to control transport across lipid membranes. The structure of the axle was key to its function as an anchor, orienting the molecule as a bolaamphiphile to span

the membrane, and enabling the shuttling motion of the [2]rotaxane to transport ions across the membrane.

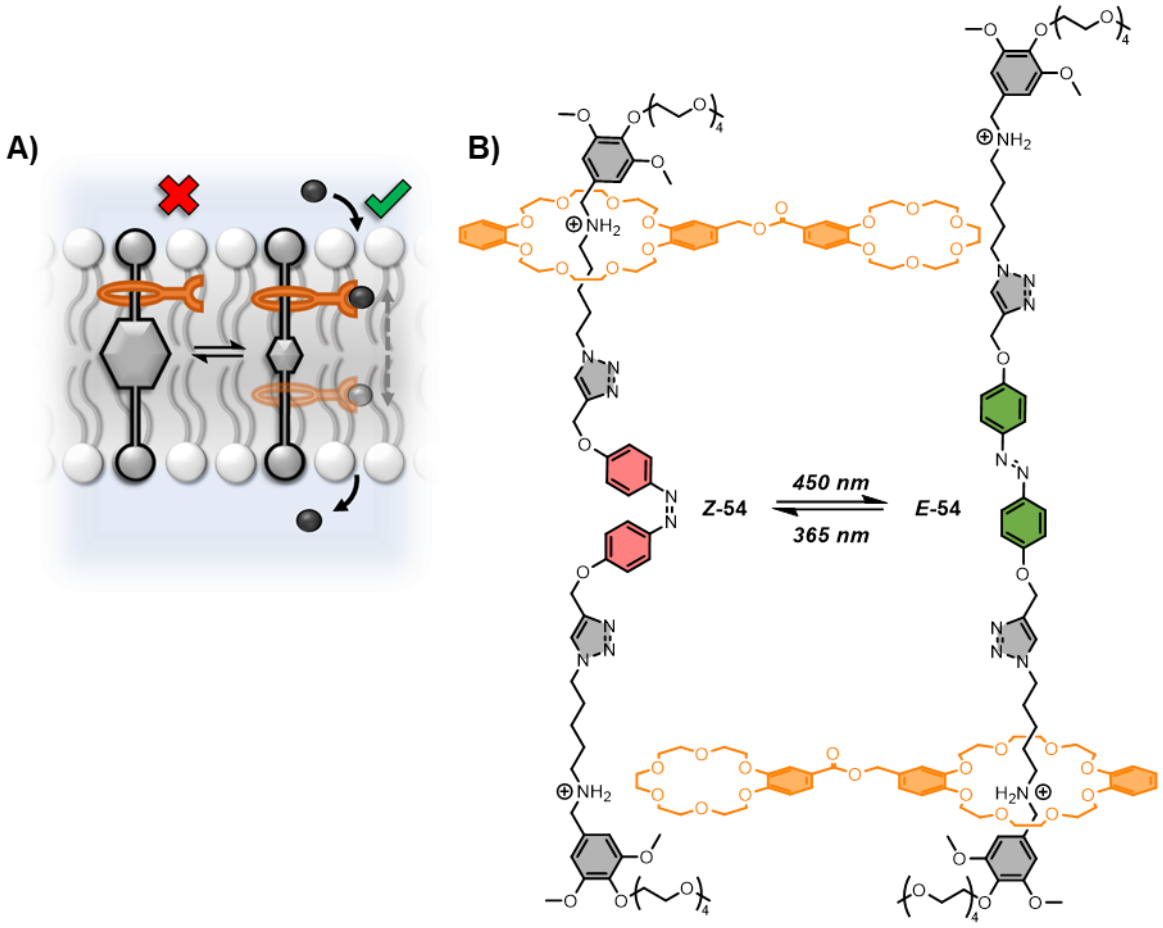

Figure 3.3 [2]Rotaxane shuttles which operate via a unimolecular anchored carrier mechanism*. A) Schematic of photo-regulated shuttling controlling ion transport. B) Structures of photo-switchable [2]rotaxane ion transporter* ***54****.*[169]

In this chapter, photo-switchable relay transporters will be described which expand the field of stimuli-responsive anchored carriers beyond the only other example reported by Bao and Qu of a membrane immobilised [2]rotaxane shuttle.[169] Relay transporters based on a phospholipid architecture were targeted for their desirable aqueous solubility and potential for pharmacological application. The relay mechanism is reliant on the exchange of an ion between receptors immobilised in opposite leaflets of the membrane, so it was envisioned that controlling the length of these carrier arms through incorporation of a molecular switch may serve to regulate relay transport activity.

3.2.1 Synthesis of Photo-switchable Relay Transporters

To access a photo-switchable relay transporter, the *tetra*-fluoroazobenzene switch developed by Hecht[170] was incorporated into the carrier arm of a phospholipid based immobile carrier. Two photo-switchable cores were prepared, including the asymmetric carboxylate methylene functionalised core **61** and the symmetric *para*-dicarboxylate structure **64**. The asymmetric core was prepared to provide the most compact azobenzene derivative possible, as it was envisioned the length of the carrier arm would impact the switching of the transport activity and the shorter telescopic arm would have a better off state. The carboxylic acids would be coupled to the lipid anchor group *via* amides as Hecht and co-workers demonstrated that amide derivatives had improved switching properties compared to esters. The diamide structure displayed near quantitative switching (PPS_Z^{530} = 92%, PPS_E^{405} = 96%)[171] between conformers in the PSS distribution with visible light, albeit with a longer total structure length.

The asymmetric *tetra*-fluoroazobenzene core was synthesised *via* a Mills reaction, with condensation of nitroso benzene derivative **60** with aniline **58**, in acidic conditions (**Scheme 3.1**). Aniline **58** was accessed by cyanation of bromobenzene **55** with subsequent reduction of nitrile **56** to the primary amine **57** which was trapped with Fmoc-Cl. The Rosenmund–von Braun nucleophilic aromatic substitution of **55** with copper (I) cyanide was found to proceed with improved yields and shorter reaction times using microwave assisted reactions compared to standard solution phase heating. Interestingly, the compound prepared *via* microwave assisted reaction[172] was white and more crystalline compared to the purple solid obtained from solution phase heating overnight. The primary amine **57** was found to be unstable and therefore was trapped with Fmoc-Cl immediately, giving the stable carbamate protected aniline **58**. Base catalysed hydrolysis of nitrile **56** gave carboxylic acid **59** after acid work-up.

Oxidation of **59** under biphasic conditions with oxone,[173] yielded the reactive nitroso compound **60** which was green in organic solution. The nitroso **60** was more soluble in the organic media than the *N*-arylhydroxylamine intermediate and aniline precursor **59**, enabling efficient isolation by separation of the two phases. Nitroso **60** was used immediately once prepared, stirred with aniline **58** under acidic conditions at room temperature to give the asymmetric azobenzene **61**. For a Mills reaction, it is favourable for electron-rich aniline derivatives to couple with electron-poor nitroso compounds in acetic acid.[173] Due to the poor nucleophilicity of the fluorinated aniline **58**, the more acidic trifluoroacetic acid (TFA) was employed to promote reaction which proceeded in 37% yield.

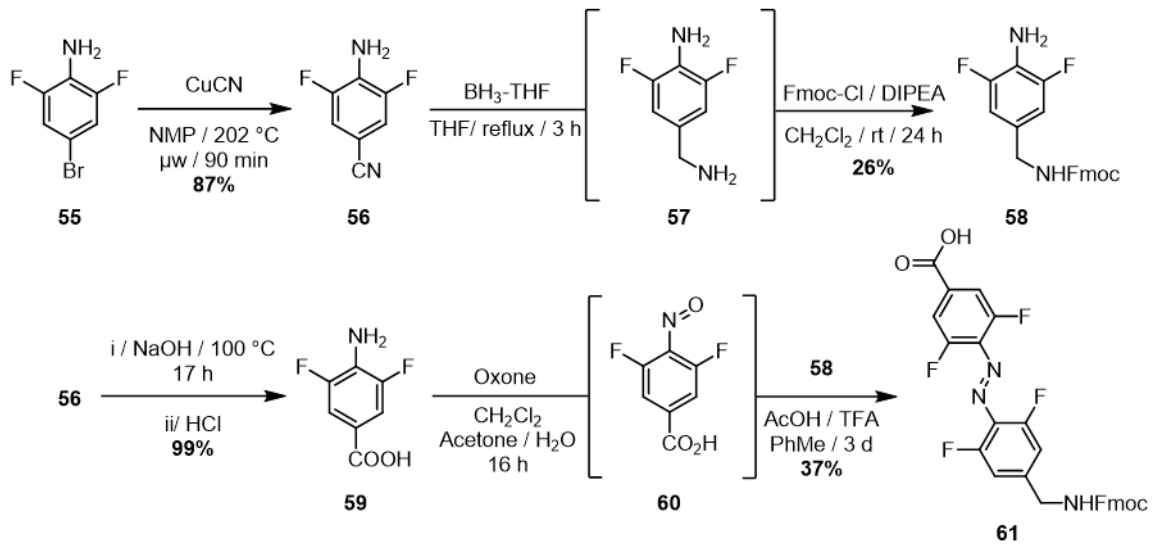

Scheme 3.1 Synthesis of compact azobenzene core 61.

The symmetric biscarboxylic acid *tetra*-fluoroazobenzene **64** was prepared according to a new oxidative coupling procedure[174] and the desymmetrisation to compound **67a** was achieved *via* a method developed by Vázquez (**Scheme 3.2**).[175] Carboxylic acid **59** was protected as the ethyl ester **62** for the azo-coupling. Using a recently developed procedure by Lin,[174] oxidative coupling of aniline **62** with *N*-chlorosuccinimide (NCS) and DBU in CH_2Cl_2 at -78 °C gave **63** in 64% yield after just 10 minutes compared to standard Fe(III)/Mn(VII) oxidative conditions

which generally are slow and low yielding (<25%).[170] Reaction of 9 equivalents of 1,2-diaminoethane **65a** with 4-methyltrityl chloride (Mtt-Cl) under basic conditions gave the mono-Mtt protected diamine **66a** in 93% yield. Base catalysed hydrolysis of **63** gave bis-carboxylic acid **64** in quantitative yield, which could be desymmetrised to mono-amide **67a** through limiting the stoichiometry of the coupling reagent hexafluorophosphate azabenzotriazoletetramethyluronium (HATU, 1.2 equivalents) used in the reaction with amine **66a**. Carboxylic acid **67a** was isolated by flash column chromatography (CH_2Cl_2/MeOH 45:1 + 3% NEt_3) as the triethylammonium salt.

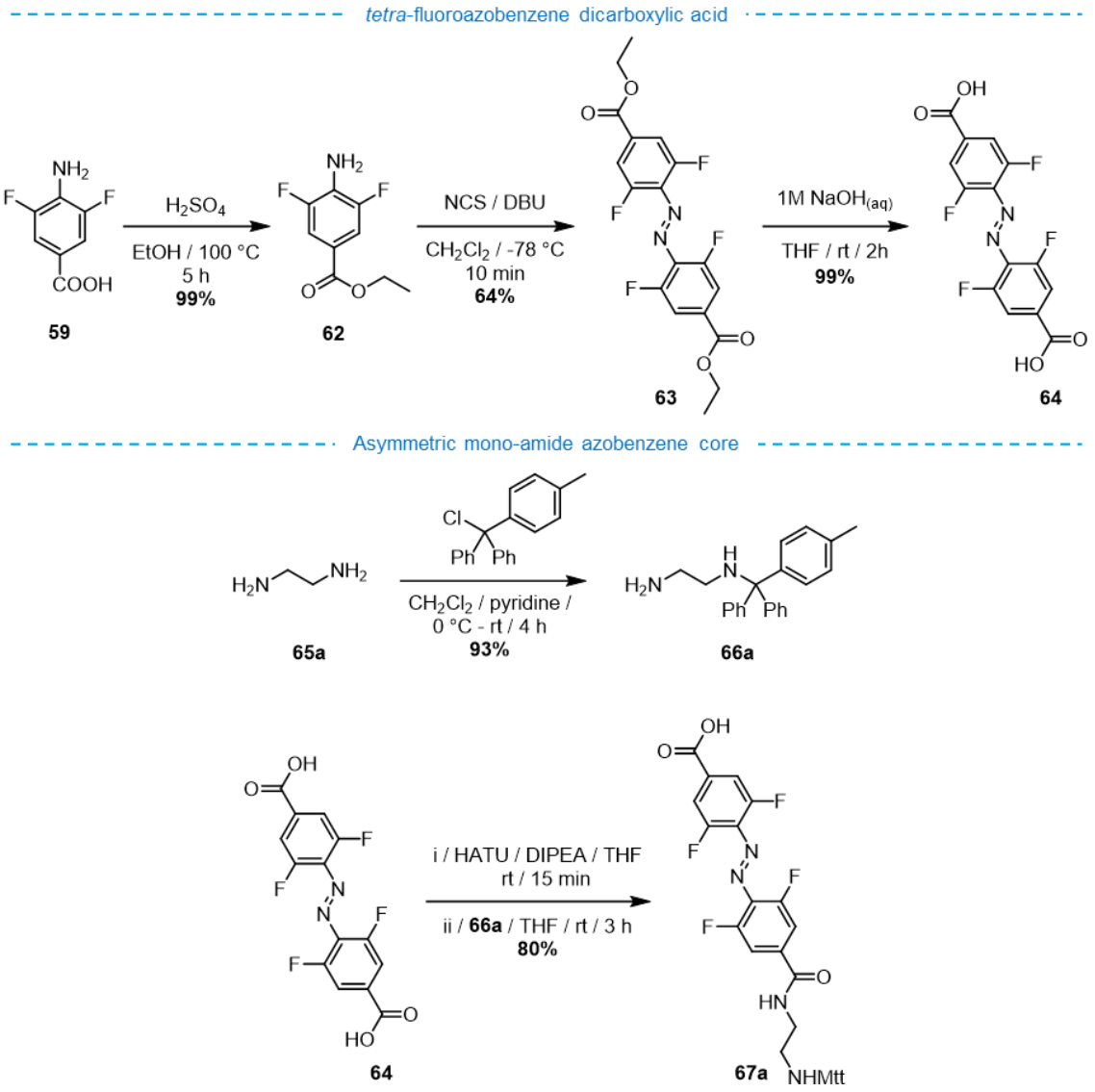

Scheme 3.2 Synthesis of mono-amide tetra-fluoroazobenzene core 67a.

The azobenzene core was then linked to the lipid through amide coupling and subsequent deprotection of the primary amine, where reaction with isothiocyanate gave the desired photo-switchable relay transporter (**Scheme 3.3**). Due to the orthogonal protecting groups on the two azobenzene cores (**61** or **67a**), two separate orthogonally protected glycine capped lipids (**68^{Boc}** or **68^{Fmoc}**) were required. Lysolipid **49** was prepared according to the aforementioned method (**Section 2.3.2**) and reacted with Boc-protected glycine, with DIC and DMAP in CH_2Cl_2 for 3 days to give phospholipid **68^{Boc}**. Lipid **68^{Boc}** was deprotected with TFA in $CHCl_3$ and the primary ammonium TFA salt was used without further purification for amide coupling after excess TFA was removed *in vacuo*. Two equivalents of *N*,*N*-diisopropylethylamine (DIPEA) were used to neutralise the equivalent of TFA and basify the reaction mixture to promote reaction with the HATU coupling reagent. The azobenzene carboxylic acid **61** was added and left to react overnight giving the azobenzene functionalised lipid **69** in 52% yield. Following base catalysed Fmoc-deprotection of **69** with DBU in $CHCl_3$, *para*-trifluoromethylphenyl isothiocyanate was added to yield the photo-switchable relay transporter **T5**, which was isolated by silica gel flash chromatography (0 - 2% H_2O / 25% MeOH / $CHCl_3$) in 46% yield. The combined fractions containing product from normal phase chromatography were concentrated and redissolved in $CHCl_3$ before filtration through a syringe filter to remove silica particles. The longer photo-switchable relay transporter **T6**, was prepared from an Fmoc-protected glycine functionalised lipid **68^{Fmoc}**. DBU catalysed deprotection of **68^{Fmoc}** gave the primary amine which was subjected to HATU and carboxylic acid **67a** to give azobenzene functionalised lipid **70**. TFA catalysed deprotection, prior to addition of NEt_3 to basify the reaction mixture for thiourea formation with *para*-trifluoromethylphenyl isothiocyanate yielded transporter **T6** in 37% yield.

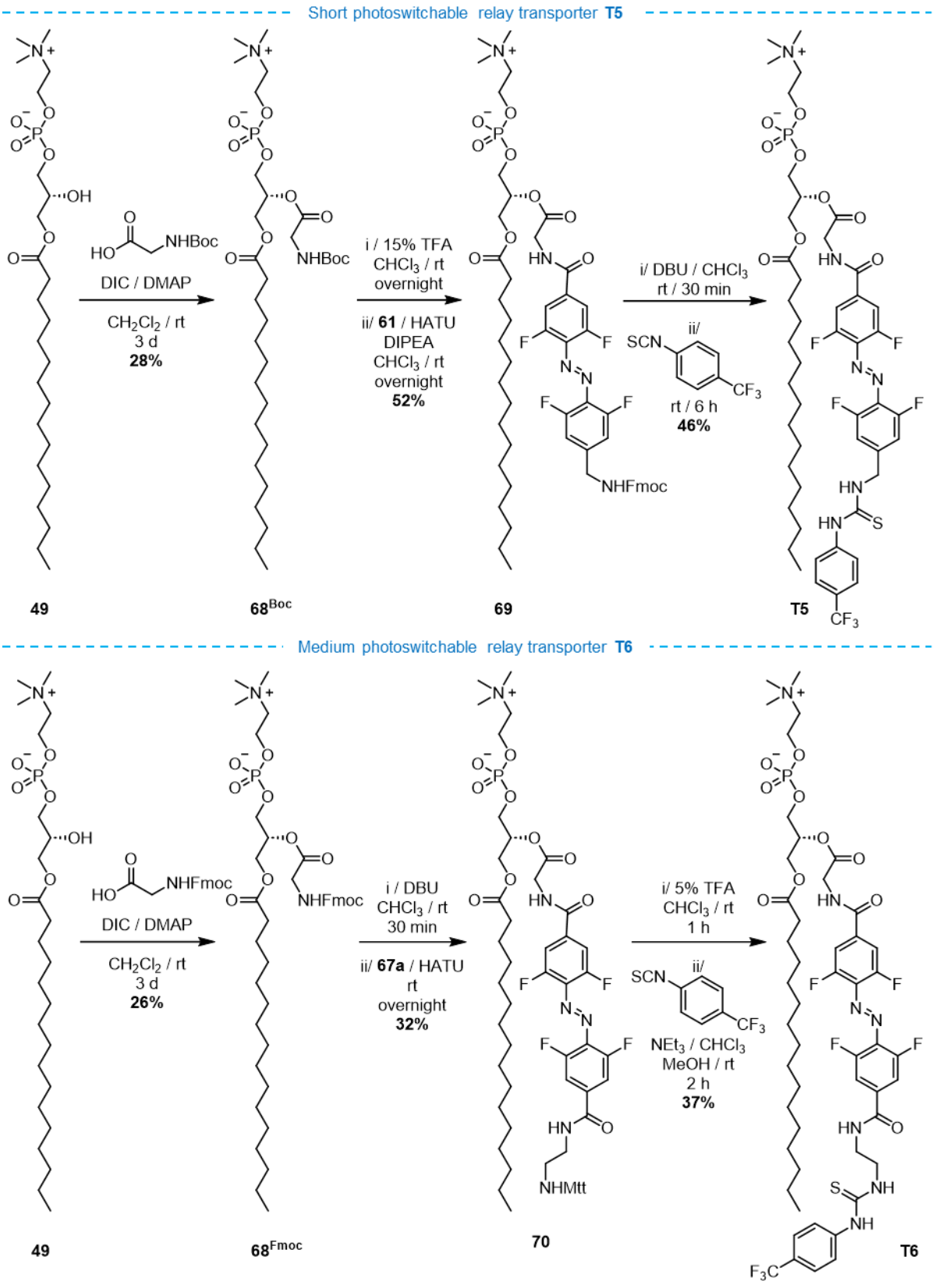

Scheme 3.3 Synthesis of photo-switchable relay transporters T5 and T6.

3.2.2 Photophysical Analysis of The Azobenzene Derivatives in Solution

Photo-irradiation of liquid samples was carried out using Thorlabs high-power LEDs (models M530L4 (530 nm, 370 mW) and M405L4 (405 nm, 1000 mW)) mounted on a custom-built setup with optical components from Thorlabs, see **Section 5.3** for more detail. Samples were irradiated for sufficient time to reach the photo-stationary state (PSS), as confirmed by ^{1}H NMR or UV-vis experiments.

The PSS composition for all azobenzene compounds was determined by ^{1}H NMR analysis following irradiation of the sample in solution in an NMR tube with LEDs (405 nm or 530 nm) until there was no further change in isomer distribution. The analysis for photo-switchable relay transporter **T5** is shown (**Figure 3.4**) as an example, with the PSS data found in **Table 3.1** for each photo-switchable relay transporter.

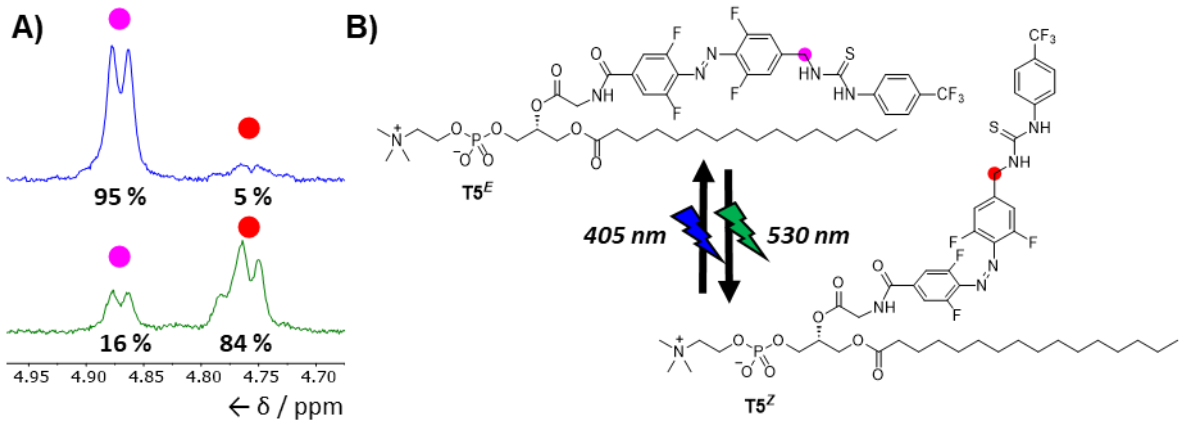

Figure 3.4 PSS distribution determination in DMSO-d_6 at 298K by ^{1}H NMR. *A) Partial ^{1}H NMR spectra of **T5^{E}/T5^{Z}** (DMSO-d_6, 400 MHz, 298 K) showing the PSS achieved by irradiation with blue 405 nm (top blue line, 95% E) and green 530 nm (bottom green line, 84% Z) light. B) Structure of the two configurations of the photo-switchable lipid **T5**.*

Table 3.1 *Photo-stationary state distribution of **T5** and **T6** in DMSO-d_6, 298K determined by ^{1}H NMR analysis*

Transporter	$PSS_{405}{}^{E}$ [%]	$PSS_{530}{}^{Z}$ [%]
T5	95	84
T6	96	90

The *tetra*-fluoroazobenzene is known to have well separated n - π* bands in the visible range of the absorption spectrum, which enables high *E*/*Z* photoconversions.[170,171] The *ortho*-fluorine atoms on the azobenzene reduce the energy of the LUMO (π*) of the *Z*-isomer more than that of the *E*-isomer LUMO (π*), generating the well separated n-π* bands. Since fluorine has a relatively small radius, the planar geometry of the *E*-isomer is not disrupted and as such orbital energies are not significantly altered compared to the non-fluorinated azobenzene. The n-orbital (HOMO) in the *Z*-isomer is lower in energy compared to the *E*-isomer, further increasing the n - π* energy transition difference. The introduction of electron withdrawing substituents at the *para*-position of the *tetra*-fluoroazobenzene core increase this effect and therefore improve the *E*/*Z* photoconversions.[171,176] As expected, **T6** showed improved photoconversion to the major isomer in both PSS distributions compared to **T5**. This is a result of the *para*-bis-diamide structure rather than the *para*-amide/methylene combination, which is less electron withdrawing than the former.

Analysis by UV-vis spectroscopy provided information about the absorption maxima and n - π* band separation for the azobenzene derivatives. The compounds were dissolved in DMSO-d_6 and irradiated with 405 nm light until at their PSS, as confirmed by ^{1}H NMR spectroscopy. Aliquots of this stock solution were then added to a cuvette of DMSO to obtain UV-vis spectra of four different concentrations for the *E*-isomers. The absorbance at the maximum of the n - π* transition was plotted against concentration (Beer-Lambert plot) to determine the molar extinction coefficient ε. For each compound, the most concentrated final *E*-isomer sample was irradiated with 530 nm light to generate the *Z*-isomer PSS, and the UV-vis spectrum was measured. Both the PSS_{405} and PSS_{530} were normalised to units of ε and overlaid. The PSS could be confirmed by further irradiation of the sample in the cuvette to obtain a consistent UV-vis spectrum. The Beer-Lambert plot of **T5*E*** and UV-vis spectra of PSS distributions of **T5** in

DMSO at 298 K are shown (**Figure 3.5**) with all other absorption spectra included in the experimental **Section 5.5.2**.

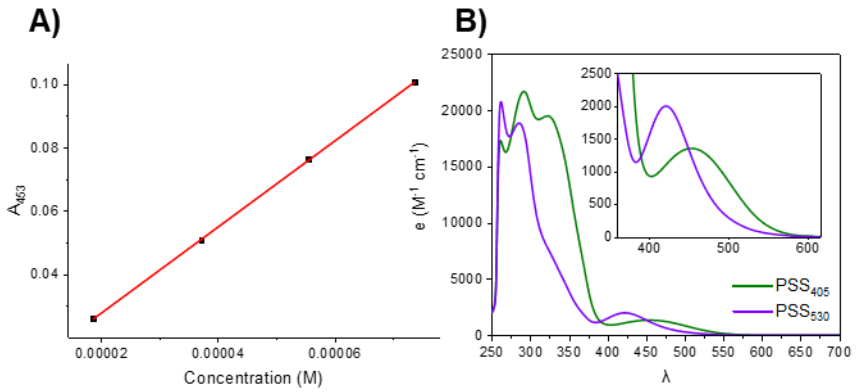

Figure 3.5 UV-vis spectroscopic analysis of T5 in solution. *A) Beer-Lambert plot for* ***T5^{E}****, absorption maxima at 453 nm plotted against compound concentration in DMSO. B) UV-vis spectra of PSS distributions of* ***T5*** *in DMSO at 298 K, measured after irradiation with 405 nm (95% E) or 530 nm (84% Z) light.*

3.2.3 Photophysical Analysis of The Azobenzene Functionalised Lipids in The Membrane Environment

To measure the photo-switching of **T5** within the bilayer environment, the incorporation efficiency of the functionalised lipid into the membrane of pre-formed POPC LUVs was first analysed by UV-vis spectroscopy (**Figure 3.6**). POPC LUVs (200 nm, 0.50 mM lipid; internal and external buffer comprising 100 mM NaCl, 10 mM HEPES, pH 7.0) were prepared following the procedure described in **Section 5.2.1** containing no dye within the vesicle lumen. The UV-vis spectrum of these blank vesicles displayed the expected non-zero background absorption due to the scattering of light passing through the sample by the 200 nm vesicles in suspension (seen in **Figure 2.12**). This background absorption was removed from all UV-vis spectra containing vesicles to give a normalised value. **T5^{E}** in DMSO (10 mM, 6.25 µL, 5 mol% to lipid) was added to a stirred solution of POPC LUVs (2.5 mL) and left for 10 minutes. An aliquot (1.75 mL) of this solution was eluted through a size exclusion Sephadex G-25 column with buffer solution (100 mM NaCl, 10 mM HEPES, pH 7.0) to remove **T5** molecules which did not

effectively incorporate into the vesicle membrane. Assuming complete recovery of all the POPC LUVs, the collected vesicles (post-size exclusion sample, 3.5 mL) were now diluted by a factor of two. A comparative pre-size exclusion sample was prepared by diluting an aliquot (0.5 mL) of the initial solution to a final volume of 1.0 mL with buffer solution (0.5 mL, 100 mM NaCl, 10 mM HEPES, pH 7.0). The UV-vis spectra of the post-size exclusion and pre-size exclusion samples were then measured and compared to determine the incorporation efficiency of **T5**, which was found to be greater than 90%.

The same analysis was conducted with POPC LUVs prepared with **T5** (5 mol% to lipid) pre-incorporated, to confirm that a transporter loaded bilayer did not reduce the incorporation efficiency of additional transporter added externally (**Figure 3.6C**). Indeed, by UV-vis analysis the incorporation of further **T5** in DMSO (5 mol% to lipid) to POPC LUVs with **T5** (5 mol% to lipid) pre-incorporated also showed an incorporation efficiency greater than 90%.

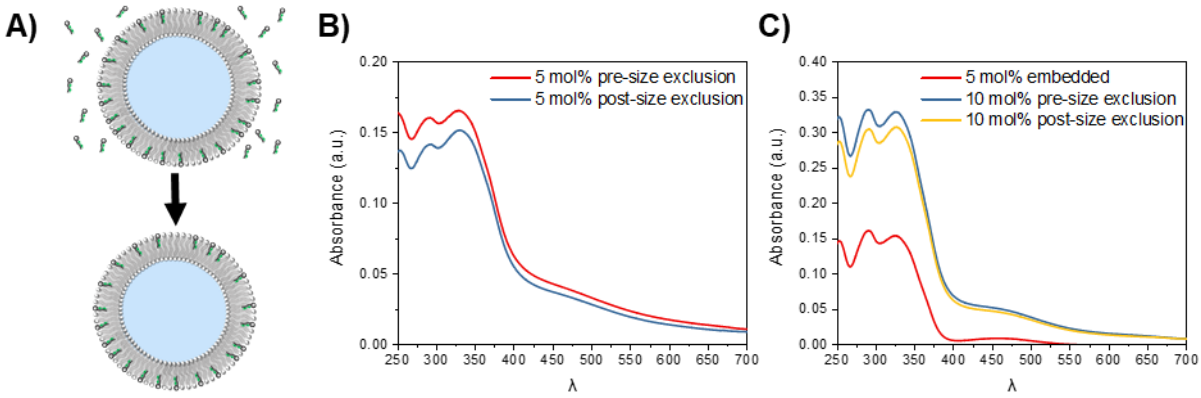

Figure 3.6 Determining incorporation efficiency of T5 into preformed POPC LUVs. *A) Schematic of photolipid externally added to preformed LUVs pre- and post-size exclusion. B) UV-vis spectra of* ***T5^{E}*** *(5 mol% to lipid) externally added to POPC LUVs pre- and post-size exclusion. Incorporation efficiency was determined to be ~90%. C) UV-vis spectra of* ***T5^{E}*** *(5 mol% to lipid) pre-incorporated into POPC LUVs is shown in red compared to the UV-vis spectra of* ***T5^{E}*** *(10 mol% to lipid: 5 mol% pre-incorporated plus 5 mol% externally added as a DMSO solution) pre- and post-size exclusion. Incorporation efficiency was determined to be ~90%.*

The *in situ* photo-switching of **T5** in the bilayer of POPC LUVs was investigated to determine if the membrane environment affected the photophysical properties of the azobenzene core

(**Figure 3.7**). POPC LUVs with **T5** (31 mol% to lipid) externally added were passed through a Sephadex G-25 size exclusion column to remove unincorporated **T5**. Irradiation of the vesicle suspension for 3 minutes with either blue light (405 nm) or green light (530 nm) was sufficient to obtain the PSS distribution of $\mathbf{T5}^{E}$ or $\mathbf{T5}^{Z}$ in bilayer, respectively, confirmed by UV-vis analysis. **T5** demonstrated high photostability, recovering the PSS distribution after multiple photo-isomerisation cycles within the bilayer (**Figure 3.7A**). The repeated *E*/*Z* isomerisation without noticeable degradation after 5 cycles highlighted the robustness of the *tetra*-fluoroazobenzene lipid scaffold.

The PSS distribution of **T5** in the membrane could be determined through comparison of the UV-vis spectrum of **T5** irradiated in the membrane or pure DMSO, respectively, dissolved into equivalent solutions (**Figure 3.7B**). **T5** loaded POPC LUVs were pre-irradiated with 405 nm or 530 nm and dissolved in DMSO (25% aqueous LUV suspension, 75% DMSO) prior to measurement of the UV-vis spectrum. Separately, **T5** was pre-irradiated in DMSO-d_6 solution and the PSS was confirmed by ^{1}H NMR analysis. This sample was diluted in an equivalent solution of 25% aqueous buffer (100 mM NaCl, 10 mM HEPES, pH 7.0) / 75% DMSO. The in-membrane photo-isomerised spectra and in-DMSO photo-isomerised spectra were identical (**Figure 3.7B**), demonstrating that the PSS obtained in the bilayer environment was equivalent to that observed in DMSO solution (PSS_{405} = 95% $\mathbf{T5}^{E}$; PSS_{530} = 84% $\mathbf{T5}^{Z}$)

The thermal half-life of $\mathbf{T5}^{Z}$ in a POPC membrane was measured at several temperatures, following the change in absorption intensity at 330 nm over time (**Figure 3.7C**). **T5** loaded POPC LUVs were pre-irradiated with 530 nm light for 3 minutes immediately prior to starting the experiment. Data for 25 °C and 45 °C showed only minor conversion to the thermodynamically favoured $\mathbf{T5}^{E}$ isomer over 15 hours. Only at 60 °C was appreciable thermal

relaxation of the *ortho*-tetrafluorozobenzene core observed, in agreement with previously reported long-lived, thermally stable *Z*-isomers of these photoswitches.[171,177] The thermally promoted conversion of **T5^{Z}** to **T5^{E}** at 60 °C was fit to an exponential decay curve to enable the thermal half-life to be calculated. Unfortunately, a full Arrhenius analysis could not be conducted as the thermal-switching at lower temperatures (< 60 °C) was too slow to allow quantification and higher temperatures (> 60 °C) would compromise the integrity of the membrane. This data confirms that, due to the long half-life of the photoswitch in the bilayer environment, thermal relaxation was negligible under the conditions and timescales of all assays in this work.

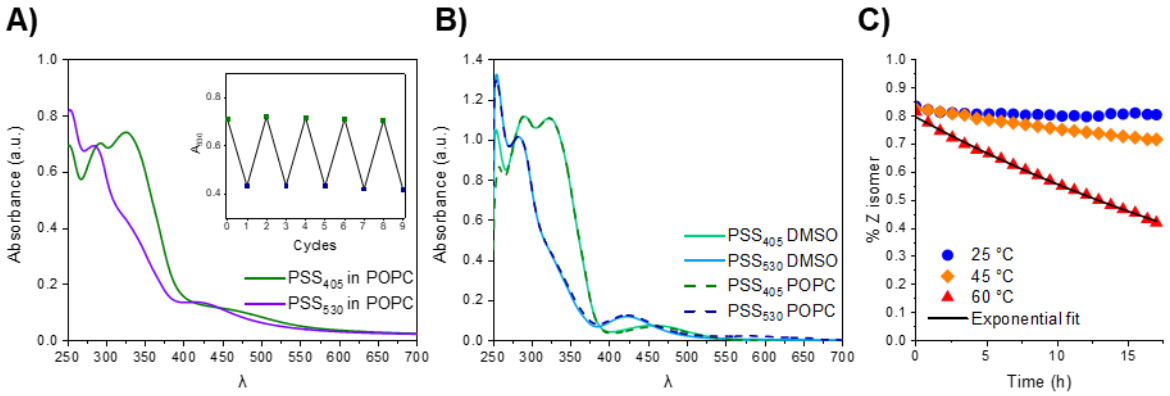

Figure 3.7 Photo-switching of T5 in the POPC membrane. *A) UV-vis spectrum of **T5** (31 mol% to lipid) in POPC LUVs measured after irradiation with 405 nm or 530 nm light for 3 min. Insert shows the reversibility of photo-switching within the bilayer, monitoring the absorbance at 330 nm. B) UV-vis spectrum of **T5** in 25% aqueous buffer (100 mM NaCl, 10 mM HEPES, pH 7.0) 75% DMSO. **T5** was pre-irradiated in the bilayer of POPC LUVs or DMSO solution with 405 nm or 530 nm light for 3 min prior to being diluted with DMSO or aqueous buffer and DMSO respectively. Data is normalised to 1 at the isosbestic point at 278 nm. C) Thermal relaxation of **T5^{Z}** to **T5^{E}** in the lipid bilayer of POPC LUVs was monitored over time at three different temperatures. Monitoring the absorbance wavelength at 330 nm allowed for the determination of %Z isomer in the bilayer. The black line represents the first order exponential decay fitted to the 60 °C data (half-life = 24 hours).*

3.2.4 Confirming The Relay Transport Mechanism

Having confirmed that the photophysical properties of the azobenzene switch were maintained within the bilayer environment, the effect of this extension and contraction on the transport activity could be investigated. To confirm **T5** operated *via* a relay transport mechanism, the equivalent control experiments as in Chapter 2 were conducted. POPC LUVs

(200 nm, 31.25 µM, 100 mM NaCl, 10 mM HEPES, pH 7.0) with HPTS encapsulated (1 mM) were prepared to assess the transport ability of both *E*- and *Z*-isomers of the lipid-based transporter **T5** added externally in DMSO (5 mol% to lipid). As is characteristic for this class of ion transporters, when incorporated into only one leaflet of the bilayer transport activity was not observed (**Figure 3.8 (i)**). The high incorporation efficiency of **T5** into the POPC membrane (>90%, by UV-vis) had previously been confirmed and therefore could be ruled out as the explanation for the lack of transport activity. In contrast, pre-incorporation of **T5^E** (5 mol%) into POPC LUVs generated an equal distribution of the relay transporter in both leaflets of the membrane, such that ion transport activity was now observed (**Figure 3.8 (ii)**). Since the activity for the same concentration of transporter externally added was significantly less than when the transporter was pre-incorporated, this confirmed that flip-flop of the lipid-based **T5** did not occur to equilibrate the distribution of relay transporters between the two leaflets. The difference in transport activity between external addition and pre-incorporation also confirmed the necessity of the transporters being present in both leaflets of the membrane in order to facilitate anion transport *via* the relay mechanism.

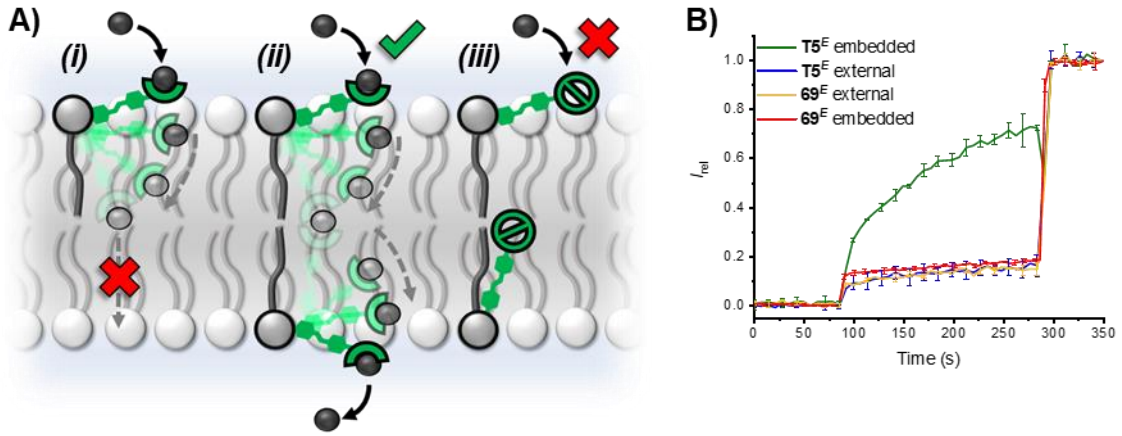

***Figure 3.8 Effect of external and pre-incorporation on relay transport**. A) Schematic of (i) external addition, (ii) pre-incorporation of the relay transporter **T5** and (iii) pre-incorporation of a photolipid with no binding group **69**. B) HPTS transport activity data for **T5^E** (5 mol% to lipid) added externally in DMSO or pre-incorporated into POPC LUVs compared to **69^E** (5 mol%, pre-incorporated and externally added in DMSO). Error bars denote the standard deviations from three runs.*

The Fmoc-protected analogue **69** was also tested in POPC LUVs loaded with HPTS by external addition and pre-incorporation. The *E*-isomers of **69** (5 mol% to lipid) showed complete inactivity whether incorporated in only the outer leaflet (external addition) or both leaflets (pre-incorporation). This control compound demonstrated that an analogous structure loaded into an equivalent bilayer showed no transport activity, suggesting that transporter **T5** was not leading to non-specific leakage of ions from the vesicles.[178]. A ^{1}H NMR titration of an Fmoc-protected control compound **71** with TBACl in acetone-d_6 showed no perturbation of proton signals (**Figure 3.9A**), confirming no binding of Cl^-, indicating that the carbamate proton of Fmoc is unable to facilitate chloride transport in **69**. In comparison, *n*-hexyl-4-trifluoromethylphenylthiourea **T1** displayed a binding constant for Cl^- in acetone-d_6 too high to be determined (>10^4 M^{-1}) by ^{1}H NMR titration with TBACl (**Figure 3.9B**), demonstrating that the stronger binding of anions by the equivalent thiourea receptor unit of **T5** was therefore required for efficient relay transport activity.

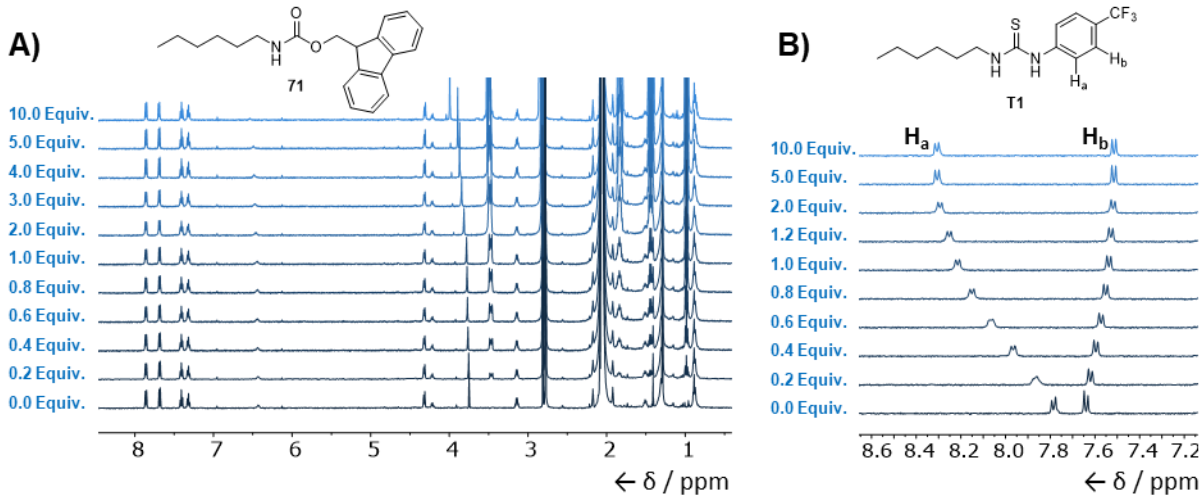

Figure 3.9 Comparison of anion binding strength of different receptor units by ^{1}H NMR spectroscopy. *A) Stacked partial ^{1}H NMR of hexyl Fmoc carbamate **71** (1 mM, acetone-d_6, 500 MHz, 298 K) titrated with TBACl (no binding observed in this solvent). B) Stacked partial ^{1}H NMR of hexyl thiourea **T1** (1 mM, acetone-d_6, 500 MHz, 298 K) titrated with TBACl, showing the perturbation of protons H_a and H_b.*

The concentration dependence of relay transport activity with pre-incorporated **T5^E** (1 – 10 mol% to lipid) was investigated in POPC LUVs (**Figure 3.10A**). Hill analysis of the dose response curve from **T5^E** fractional transport activity immediately prior to lysis (276 s) gave an EC_{50} value of 4.5±0.5 mol% (**Figure 3.10B**). The Hill coefficient was also determined to be n = 2.3±0.4, which suggests that multiple relay transporters assembled into an endergonic structure during the rate-determining step of transport. The observed initial anion transport rate, k_{ini}, was determined using the methodology as was described in **Section 2.3.3**. The dependence of the initial rate, k_{ini}, on the concentration of pre-incorporated **T5^E** was non-linear, indicative of multiple molecules of **T5^E** in the rate-limiting step of the transport process. A linear relationship was obtained for k_{ini} versus [**T5^E**]^2 (**Figure 3.10C**), suggesting that two molecules of **T5^E** are required to mediate transport, consistent with the proposed relay mechanism.

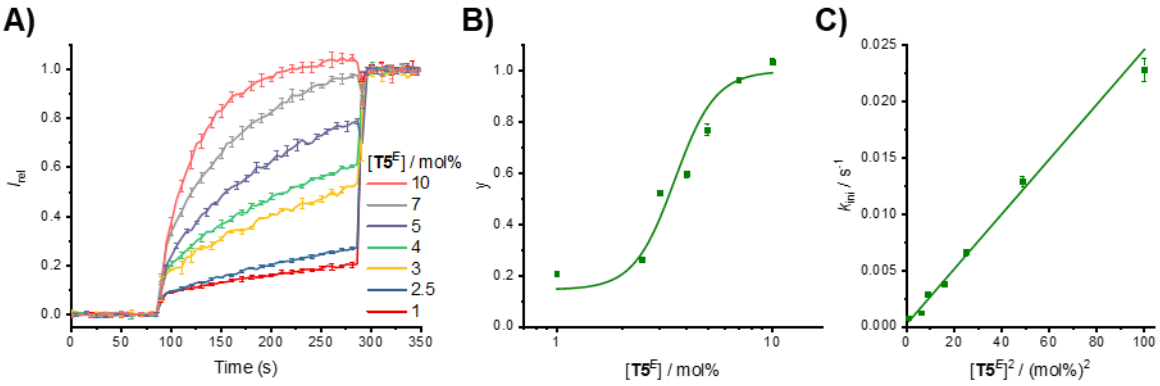

Figure 3.10 Characterisation of pre-incorporated T5^E transport activity. *A) HPTS transport data for **T5^E** (1- 10 mol%, in POPC LUVs). B) Dependence of the fractional transport activity (y, 276 s from the HPTS assay) on the concentration of transporter fitted to the Hill equation. C) Dependence of the initial rate of transport on [**T5^E**]^2 fitted to a linear plot. Error bars denote the standard deviations from three runs.*

To establish which ions **T5^E** was exchanging to effect the change of internal pH in the LUVs, the salts in the buffer were exchanged (**Figure 3.11**). Replacing chloride ions for the hydrophilic gluconate anion in the internal and external buffer of POPC LUVs with **T5^E** (5 mol% to lipid) pre-incorporated resulted in loss of transport activity (**Figure 3.11B**). This attenuation of transport activity demonstrated **T5^E** is incapable of transporting the large hydrophilic

gluconate anion or facilitating a cation-dependant H^+/Na^+ antiport process. Instead, the observed transport in the presence of chloride must result from a Cl^-/OH^- antiport or functionally equivalent Cl^-/H^+ symport process which are cation independent. Inactivity with gluconate buffer also demonstrated that **T5^E** (≤5 mol% to lipid) did not disrupt the membrane leading to non-specific leakage of ions.

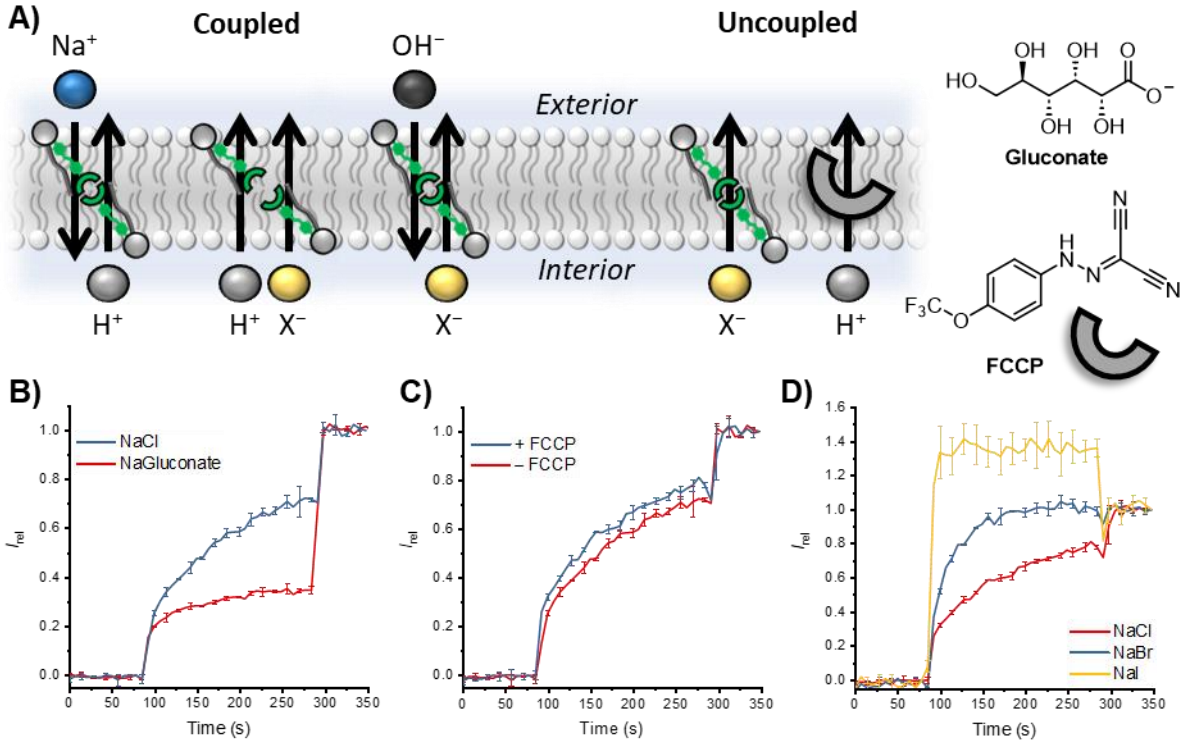

Figure 3.11 Probing the anion selectivity of the relay transporter T5^E. *A) Schematic of the possible ion exchange processes that deacidify the vesicle interior and the effect of adding a protonophore to uncouple transport processes. Structure of gluconate anion and protonophore FCCP. B) HPTS transport data **T5^E** (5 mol%, in POPC LUVs) with NaCl or NaGluconate in both the internal and external buffer. C) HPTS transport data **T5^E** (5 mol%, in POPC LUVs in NaCl buffer) with and without the addition of FCCP (0.8 mol%, in DMSO, -10 s). D) HPTS transport data **T5^E** (5 mol%, in POPC LUVs) with NaCl, NaBr or NaI in both the internal and external buffer in the presence of FCCP (0.8 mol%, in DMSO, -10 s). Error bars denote the standard deviations from three runs.*

To determine whether the Cl^- or H^+/OH^- exchange process by **T5^E** was rate limiting, transport activity was measured in the presence of FCCP. Fast electrogenic H^+ transport mediated by FCCP, decoupled proton transport from the relay-mediated Cl^-/OH^- antiport (or Cl^-/H^+ symport process). In the presence of excess protonophore (0.8 mol% to lipid, externally added in DMSO) the assay reported on the rate-limiting relay-mediated chloride transport. An

increase in transport rate with **T5*E*** in the presence of FCCP, indicated that H^+/OH^- transport was rate-limiting for the relay mechanism (**Figure 3.11C**). To determine the ion selectivity profile of the relay transporter, the assay was repeated with various monovalent anions in the internal and external buffer to compare the relative relay-mediated transport rates for the halide anions. As seen in **Figure 3.11D**, the rate of transport was dependent on the Hofmeister series where the greater the dehydration enthalpy of the anion the slower the rate of transport (rate of transport: $I^- > Br^- > Cl^- > OH^-$).

Measuring the transport activity of **T5*E*** pre-incorporated into anionic POPG LUVs, allowed the effect of the lipid headgroup on transport kinetics to be investigated (**Figure 3.12**). Compared to POPC with a zwitterionic phosphocholine headgroup, the analogous anionic phosphatidylglycerol lipid (POPG) showed no change in transport activity (**Figure 3.12B**). Zwitterionic POPC and anionic POPG have identical lipid chains, thus the hydrophobic region of the bilayer is constant in these experiments, demonstrating that anion binding or release at the interface was not rate-limiting for the relay transport process. Interestingly, when egg-yolk phosphatidylglycerol (EYPG) was used, the rate of transport was significantly enhanced. EYPG is a mixture of lipids, all with the same phosphoglycerol headgroup but with a range of different alkyl chains, suggesting that a change in the hydrophobic region of the bilayer was responsible for the enhanced transport activity (**Figure 3.12B**). This result emphasises the importance of measuring transport activity in bilayers composed of pure single lipids to distinguish the different effects on transport activity.

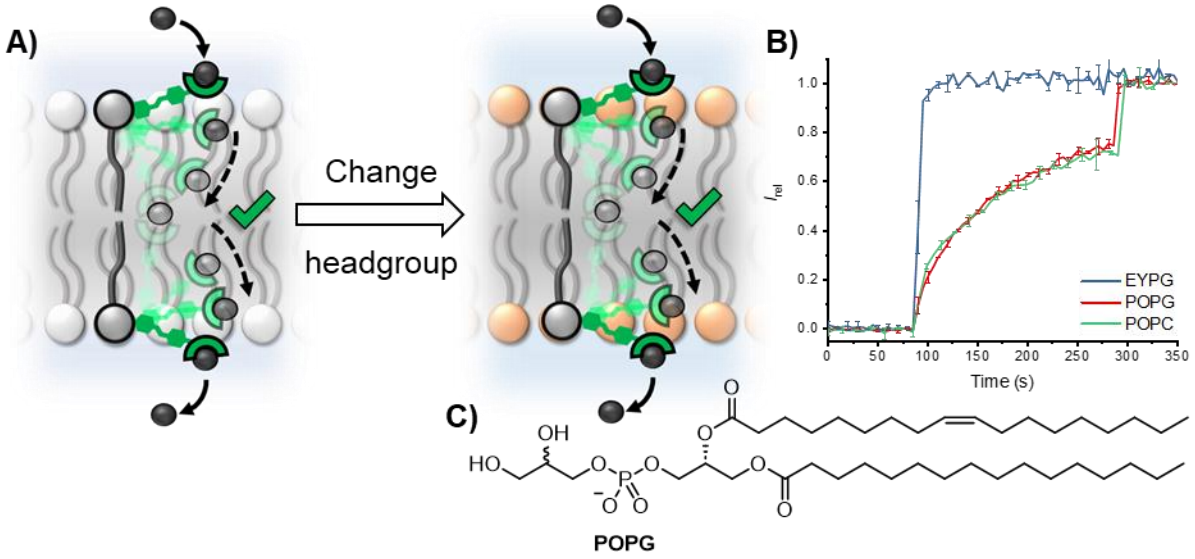

Figure 3.12 Effect of changing the lipid headgroup on T5^E relay transport activity. *A) Schematic of different lipid headgroups effecting the relay transport mechanism. B) HPTS transport data for* ***T5^E*** *(5 mol%, pre-incorporated) in LUVs comprised of EYPG, POPG or POPC respectively. Error bars denote the standard deviations from three runs. C) Structure of POPG.*

The observed change in activity upon measuring transport with a mixture of alkyl chain lengths in EYPG spurred further investigation into changing the thickness and fluidity of the hydrophobic portion of the membrane on relay transport. Through varying the concentration of cholesterol loaded in the bilayer of POPC LUVs, the thickness and fluidity of the membrane could be modulated (**Figure 3.13**). Increasing cholesterol content in a POPC bilayer decreases the membrane fluidity and increases the thickness of the hydrophobic region.[179] The concentration of cholesterol dissolved in the POPC membrane was kept below 30% to ensure no phase separation occurred to form immiscible cholesterol plaques.[180] With increased cholesterol loaded in the POPC membrane the measured anion transport activity of **T5^E** (5 mol%, pre-incorporated) decreased (**Figure 3.13C**). Given that the mobility of the carrier arm through the bilayer, as well as formation and dissociation of the transmembrane complex would be affected by these physical changes to the membrane, one of these steps was implicated to be rate-limiting.

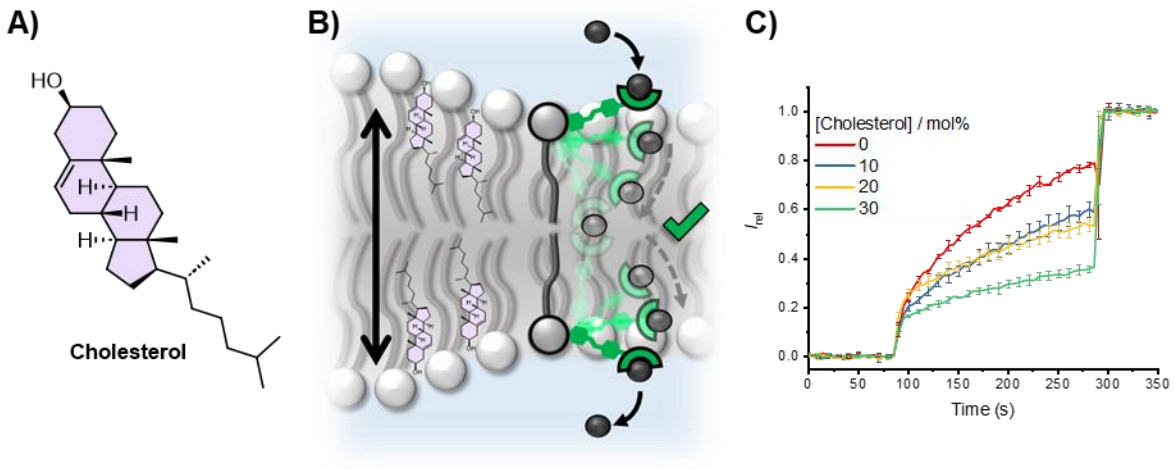

Figure 3.13 Effect of Cholesterol on the rate of relay mediated anion transport. *A) Structure of cholesterol. B) Schematic of membrane thickening due to cholesterol impacting relay transport. C) HPTS transport data for* ***T5^E*** *(5 mol% to POPC) in POPC LUVs with cholesterol pre-incorporated (0-30 mol% to POPC). Error bars denote the standard deviations from three runs.*

Measuring relay-mediated transport of **T5^E** in different membrane phases provided information about the requirement for mobility of the transporter within the bilayer (**Figure 3.14**). DPPC LUVs at 25 °C (lipid gel phase) with **T5^E** (5 mol%) pre-incorporated showed complete inhibition of activity, which was restored at 45 °C, above the gel–liquid phase transition temperature (T_m = 41 °C) (**Figure 3.14B**). This result was comparable to characteristic data from mobile carriers, where translocation in the gel phase was entirely arrested inhibiting transport activity.[13] The mobility of the carrier arm of the relay transporter must similarly be capable of unrestricted motion within the membrane to allow ion transport to occur (**Figure 3.14A**). In the gel phase motion of the carrier arm was suppressed preventing relay transport, while in the fluid phase at 25 °C relay transport was achieved. These experiments also rule out ion channel formation, for which the activity would be expected to be independent of membrane fluidity.

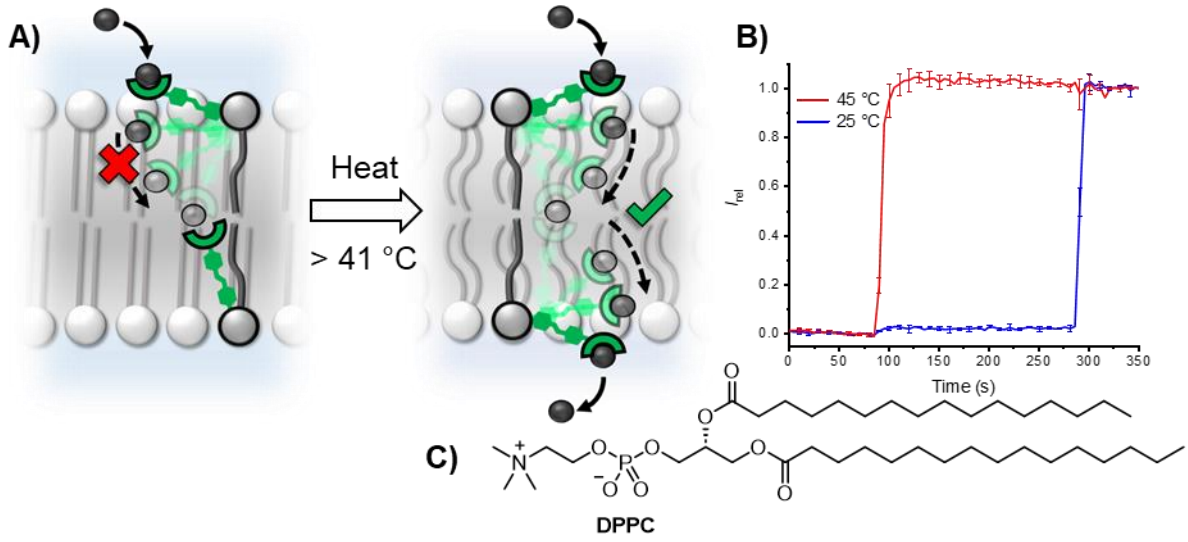

Figure 3.14 Effect of membrane phase on relay transport activity. *A) Schematic of changing membrane phase on relay transport. B) HPTS transport data for* ***T5^E*** *(5 mol% to lipid, pre-incorporated) in DPPC LUVs at 25 °C (gel phase) and 45 °C (liquid phase) Error bars denote the standard deviations from three runs. C) Structure of DPPC.*

An asymmetric distribution of **T5^E** in the two leaflets of the membrane was utilised to probe the mechanism of relay transport (**Figure 3.15**). To POPC LUVs with pre-incorporated **T5^E** (5 mol% to total lipid), addition of further **T5^E** (5 mol% to total lipid, >90% incorporation efficiency by UV-vis) in DMSO yielded vesicles with a 3:1 excess of relay transporters in the outer leaflet of the membrane compared to the inner leaflet (arrangement ii). The observed transport activity was unaffected by the addition of an increased number of relay transporters in the outer leaflet (**Figure 3.15B**). This demonstrated that the extraction of anions from the aqueous phase into the membrane by the relay was not rate-limiting. For the same total loading of **T5^E** (10 mol% to total lipid) but with transporters symmetrically distributed across both leaflets (arrangement iii), an increase in transport activity was observed. Increasing the concentration of relay transporter pre-incorporated within the membrane increases the concentration of transmembrane relay pairs, suggesting that this supramolecular structure may be implicated in the rate-limiting step of the transport process. The observed dependence of the transport rate on [**T5^E**]^2 (**Figure 3.10A**) indicated the exchange occurred *via* a transient transmembrane 2:1 receptor-anion complex. Additional relay transporter in

the outer membrane would be expected to promote the rate of formation of a transmembrane 2:1 relay-anion complex. However, given that the rate of transport was unaffected by the addition of more relay transporters in the outer leaflet the experimental evidence suggested a transient membrane spanning 2:1 relay transporter-anion complex formed as an intermediate and that breaking of this complex was rate-limiting. This is plausible given that the low dielectric constant in the hydrophobic centre of the bilayer[158,159] will increase the hydrogen bonding strength of transporter–anion complexation,[181] compared to the binding interaction at the more polar interface region.

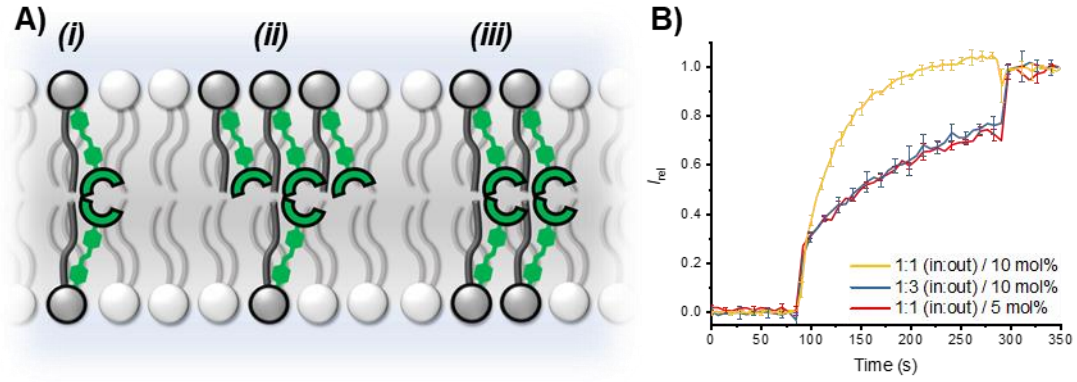

Figure 3.15 An asymmetric distribution of relay transporters confirmed anion binding is not rate-limiting. *A) Schematic of different distributions of relay transporters in each leaflet of the membrane. B) HPTS transport data for asymmetric loading of* ***T5^E*** *to the inner and outer leaflet of POPC LUVs. Symmetric loading was achieved by pre-incorporation of 5 or 10 mol%* ***T5^E*** *during LUV preparation (red and yellow data, respectively). A 3:1 excess of* ***T5^E*** *in the outer leaflet was achieved by external addition of* ***T5^E*** *(5 mol%, in DMSO) to LUVs loaded with* ***T5^E*** *(5 mol%, pre-incorporated, blue data). Error bars denote the standard deviations from three runs.*

Measuring transport activity in a range of membrane thicknesses can be used to determine the transport mechanism which is operating.[182] Transporter **T5^E** was pre-incorporated into LUVs independently prepared from a lipid from the homologous series of varying acyl chain lengths (16:1 PC, 18:1 PC, and 20:1 PC) (**Figure 3.16A**). As the hydrophobic thickness of the membrane increased the observed transport activity of **T5^E** (5 mol% to lipid) decreased, consistent with a relay mechanism (**Figure 3.16B**). This behaviour contrasts with the Gaussian-shaped dependence observed for ion channels, where maximum activity is observed when

membrane thickness matches the length of the channel.[124] It also contrasts with a mobile anion carrier transport profile, which as previously described in **Chapter 2** is generally independent of membrane thickness as diffusion across the tail region of the bilayer is not rate-limiting.[34,183] Relay transport is characterised by a decrease in activity with increasing membrane thickness, with an abrupt loss of activity entirely after a certain hydrophobic thickness.[123] This activity profile results from the requirement of binding groups immobilised in opposite leaflets, to be sufficiently close to exchange an ion. As membrane thickness increases the dielectric constant at the centre of the membrane increases,[184] making the transmembrane transporter-ion complex dissociation step more prohibitive.

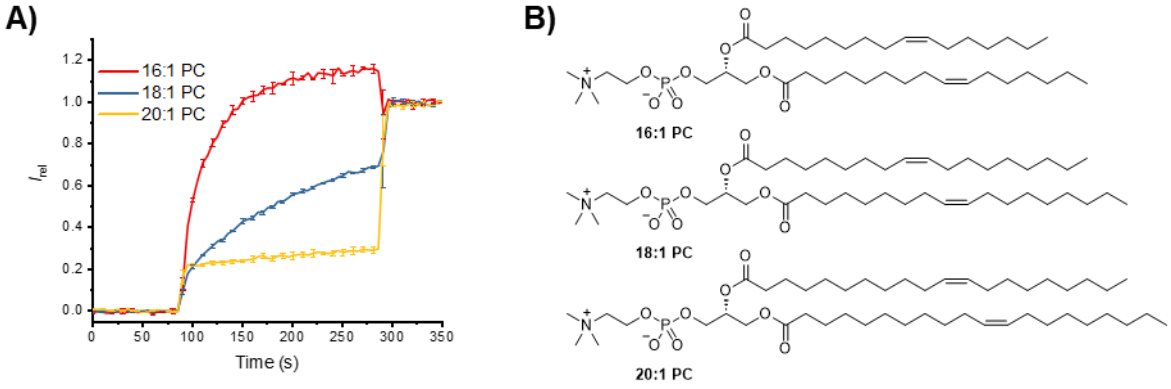

Figure 3.16 Effect of membrane thickness on relay transport activity. *A) HPTS transport data for* ***T5^E*** *(5 mol% to lipid, pre-incorporated) in LUVs prepared from different lipids. Error bars denote the standard deviations from three runs. B) Structure of 16:1 PC, 18:1 PC and 20:1 PC.*

3.2.5 Photo-switchable Relay Transport Activity

All previous studies carried out with **T5^E** pre-incorporated were conducted with irradiation of the vesicle suspension with 405 nm (2 minutes, 1 W) which generated the PSS distribution (**T5^E** PSS_{405} = 95:5 *E*:*Z*) prior to the measurement of transport. UV-vis analysis had previously confirmed the irradiation time necessary to achieve the PSS distribution in the membrane and demonstrated that the isomer distribution was equivalent to that measured in DMSO (**Figure 3.7B**). Irradiation of POPC LUVs containing pre-incorporated **T5** with 530 nm light (2 minutes,

370 mW) generated **T5^{Z}** (PSS_{530} = 16:84 *E*:*Z*) within the membrane. Measurement of the transport activity of **T5^{Z}** pre-incorporated in POPC LUVs at a range of concentrations was conducted (**Figure 3.17A**). The **T5^{Z}**-rich PSS initial rate of relay transport was found to be consistently less than the **T5^{E}**-rich PSS distribution for all concentrations and followed the same linear dependence on the [**T5**]^2 (**Figure 3.17B-C**). This was attributed to the contracted state of the relay carrier arm in the *Z*-isomer, which inhibited the exchange of the anion between thiourea-binding groups of transporters in opposite leaflets of the membrane.

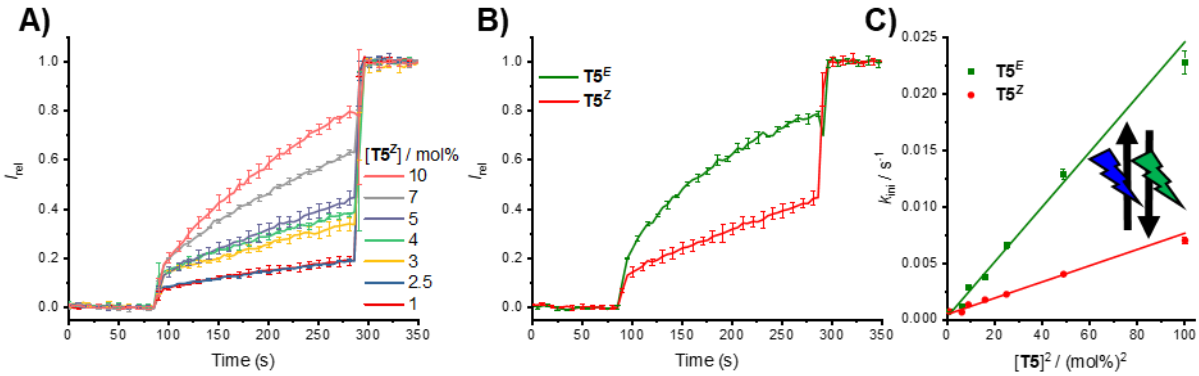

Figure 3.17 Transport activity of contracted relay transporter T5^{Z}. *A) HPTS transport data for **T5^{E}** (1-10 mol% to lipid, pre-incorporated) in POPC LUVs. B) Comparison of **T5^{Z}** (PSS_{405} = 95:5 E:Z) to **T5^{E}** (PSS_{530} = 16:84 E:Z) transport activity in POPC LUVs. C) Dependence of the initial rate of transport on [**T5**]^2 showing both data for **T5^{E}** and **T5^{Z}** fitted to a linear plot. Error bars denote the standard deviations from three runs.*

Relay transporter **T5^{Z}** was observed to display the same general trends in activity as **T5^{E}** for the cholesterol and DPPC fluidity experiments, POPG headgroup investigation, gluconate and halide anion exchange studies and membrane thickness tests with other lipid acyl chain lengths (**Section 5.5.5**). The only difference in the observed trend was for the iodide transport measurements, where **T5^{E}** transport activity was unexpectedly greater than that of **T5^{Z}**. These results supported the proposed mechanism that upon contracting the length of the telescopic relay carrier arm, the binding groups of transporters immobilised in opposite leaflets of the membrane are held further from one another and transport activity was reduced. Photo-isomerisation from **T5^{E}** to **T5^{Z}** decreased the effective length of the telescopic carrier arm by

approximately 0.8 nm, where the gap between thiourea-binding sites for two **T5^{Z}** relays (~1.6 nm) was reasoned to cause the inhibition of transport. A gap of 1.1 nm was previously reported as the upper limit for cation hopping between crown ether derivatives in a membrane spanning channel.[185] The observed transport rates for each state were independent of the order of photo-isomerisation demonstrating that the photo-switchable relay transport system was fully reversible.

Transporter **T5^{Z}** demonstrated some transport activity in the contracted off state, attributed to the non-quantitative photo-switching of the relay transporter and hence presence of 16% **T5^{E}** in the membrane. To further assess the contribution of the residual extended conformer **T5^{E}** in the PSS_{530} off state, another wavelength of light was used to generate a new PSS distribution to assess transport activity. Irradiation with 455 nm light generated an equal distribution (PSS_{455} 50:50 *E*:*Z*) of relay transporter conformations in the bilayer. The transport activity of **T5** (6 mol%, pre-incorporated in POPC LUVs) after irradiation with 455 nm light was only slightly diminished compared to **T5^{E}** (**Figure 3.18**) demonstrating the significant contribution of the **T5^{Z}**-**T5^{E}** exchange to the transport activity. Three simultaneous equations could be derived relating the observed initial rates of transport to the composition of isomers in each PSS (**Equations 8-10**). Solving these equations allowed the absolute activities of each combination of relay transporters (**Figure 3.19Ai-iii**) to be accessed, where **(i)** is the **T5^{E}**-**T5^{E}** on state, **(ii)** is the mixed **T5^{Z}**-**T5^{E}** state exchange activity and **(iii)** is the **T5^{Z}**-**T5^{Z}** off state. Conducting this analysis at a number of time intervals based on the observed transport activity of **T5** (6 mol%, pre-incorporated in POPC LUVs) after irradiation with the three wavelengths of light (405 nm, 455 nm, 530 nm) allowed the contribution of each relay pair to be quantified and plotted (**Figure 3.19C**). The low background absolute activity of the **T5^{Z}**-**T5^{Z}** state confirms that in the fully contracted state the relay transport system is incapable of anion transport.

The absolute activities of **T5^{E}-T5^{E}** state and the mixed **T5^{Z}-T5^{E}** state are comparable in activity, demonstrating the requirement for both relay transporters immobilised in opposite leaflets of the bilayer to be in the contracted state to turn off transport activity. The presence of the residual 16% **T5^{Z}** in the PSS_{530} off state therefore contributes significantly to the effective activity meaning that the observed transport activity is not fully off.

$$0.9025a + 0.095b + 0.0025c = y_{405} \qquad \textbf{(Equation 8)}$$

$$0.25a + 0.5b + 0.25c = y_{455} \qquad \textbf{(Equation 9)}$$

$$0.0256a + 0.2688b + 0.7056c = y_{530} \qquad \textbf{(Equation 10)}$$

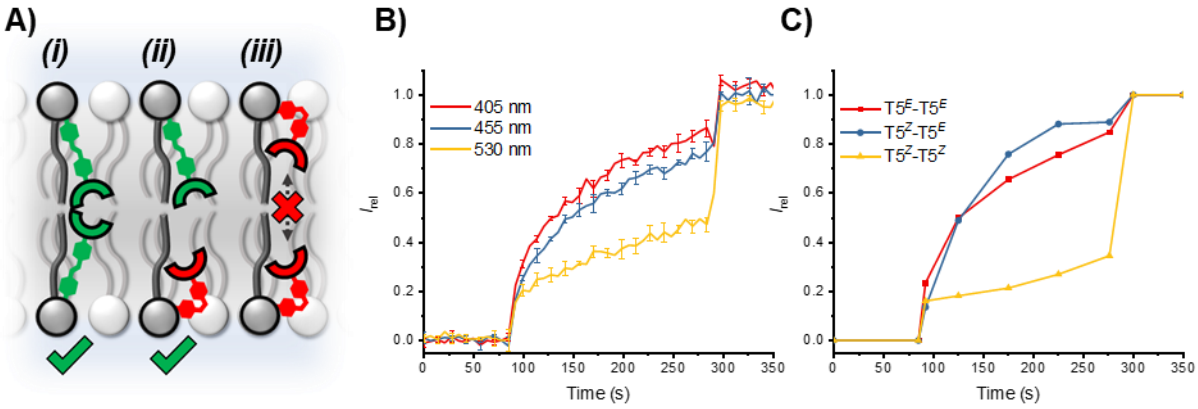

Figure 3.18 Assessing the exchange of the anion between different relay transporter conformations. *A) Schematic of (i) the fully extended relay pair **T5^{E}-T5^{E}** (ii) the mixed relay pair **T5^{Z}-T5^{E}** and (iii) the fully contracted relay pair **T5^{Z}-T5^{Z}**. B) HPTS transport data for **T5** (6 mol% to lipid, POPC LUVs) after irradiation with different wavelengths of light (2 mins). Error bars denote the standard deviations from three runs. C) Calculated transport activity of the three unique relay pairs for **T5** (6 mol% to lipid, POPC LUVs).*

The transport activity of relay transporter **T6** with the diamide tetra-fluoroazobenzene core was also assessed. The photo-switchable transporter **T6** displayed a slightly improved PSS distributions (PSS_{405} 96:4 *E*:*Z*, PSS_{530} 10:90 *E*:*Z)* in comparison to **T5**, due to the increased electron withdrawing nature of the *para*-substitution pattern. External addition of each isomer of **T6** (5 mol% to lipid, in DMSO) to pre-formed POPC LUVs lead to no observed transport activity (**Figure 3.19A-B**), supporting the requirement for transporters to be present

in both leaflets of the bilayer for the relay transport mechanism. Comparison of the transport activity of **T6** (5 mol% to lipid, pre-incorporated) in POPC LUVs with either NaCl or sodium gluconate in both the internal and external buffer confirmed **T6** operated as an anion transport relay (**Figure 3.19C**). The activity of **T6** (5 mol%, pre-incorporated) with NaCl buffer demonstrated appreciable dissipation of the transmembrane pH gradient, while no transport activity was observed with the sodium gluconate buffer. As has previously been described, gluconate is a large hydrophilic anion with a high dehydration enthalpy, and the lack of transport activity confirms the anion selective nature of **T6** relay transport activity. The inactivity of **T6** in POPC LUVs with sodium gluconate buffer also demonstrates that the photo-switchable lipid does not cause appreciable leakage from the vesicles in either conformation.

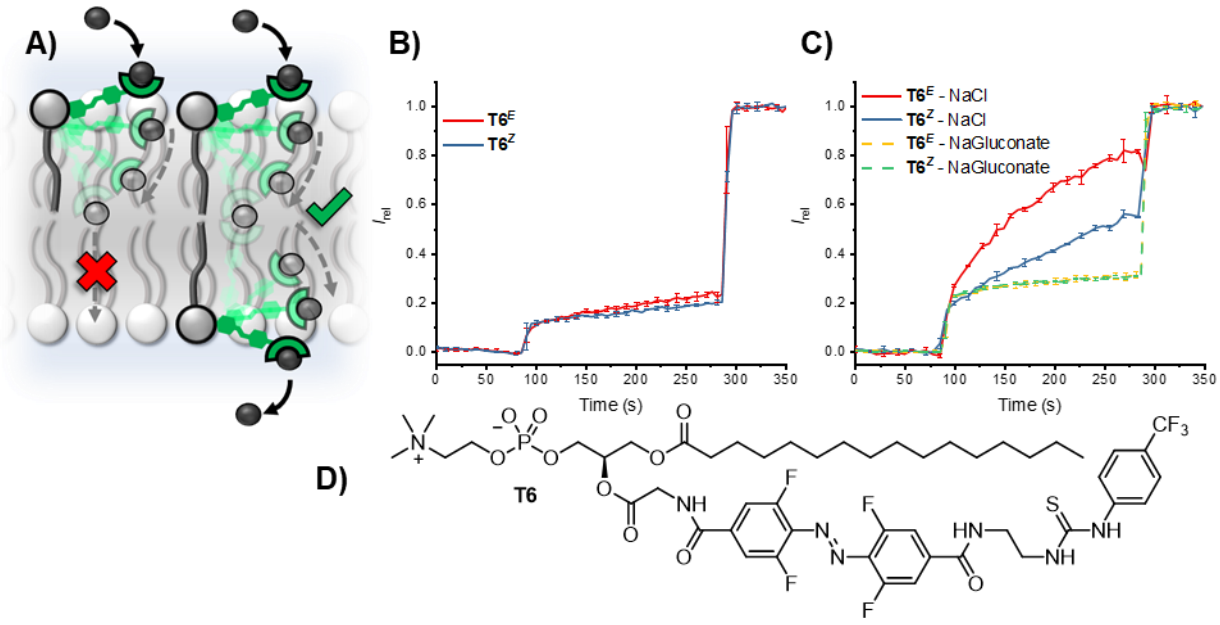

Figure 3.19. Comparing external addition and pre-incorporation of T6 on transport activity. *A) Schematic of the relay transport mechanism with transporter in one or both leaflets of the bilayer. B) HPTS transport data for* ***T6^Z*** *and* ***T6^E*** *added externally (5 mol% to lipid, in DMSO) to POPC LUVs. C) HPTS transport data for* ***T6^Z*** *and* ***T6^E*** *(5 mol% to lipid, pre-incorporated) in POPC LUVs with NaCl or NaGluconate buffer in the external and internal environment. Error bars denote the standard deviations from three runs. D) Structure of photo-switchable relay transporter* ***T6^E****.*

To confirm that the PSS distribution was achieved within the membrane various irradiation times of **T6** (5 mol%, pre-incorporated) loaded POPC LUVs were used (**Figure 3.20**). The observed transport activity was within error for the various different irradiation times (30 s,

120 s, 10 mins) with each wavelength (405 nm or 530 nm) demonstrating that the PSS was achieved within 30 seconds of irradiation (**Figure 3.20A-B**). Pre-irradiating **T6** (in $CHCl_3$) with 530 nm prior to lipid film formation allowed the PSS_{530} (10:90 *E*:*Z*) to be achieved without irradiation of the vesicle suspension to remove the requirement of exposing the vesicle suspension to light. The **T6^Z** conformation is the thermodynamically less stable state, so the lipid film was prepared the same day as the vesicles were extruded and transport activity was measured. Exposure to light during vesicle preparation was minimised by conducting the extrusion and freeze-thaw cycles in the dark and storing the stock solutions in the dark. Vesicles prepared with **T6^Z** (5 mol% to lipid) irradiated *ex situ* displayed similar transport activity to **T6^Z** generated *in situ* (**Figure 3.20C**), demonstrating that irradiation of the vesicle suspension generated the same PSS distribution as in solution. The slightly higher transport activity of **T6^Z** generated *ex situ* indicated that some of transporters had relaxed to the more stable **T6^E** isomer and irradiation of the vesicles could restore **T6^Z** *in situ* generated activity. This experiment also confirms that the switching of the relay transporter in the membrane was not detrimental to activity.

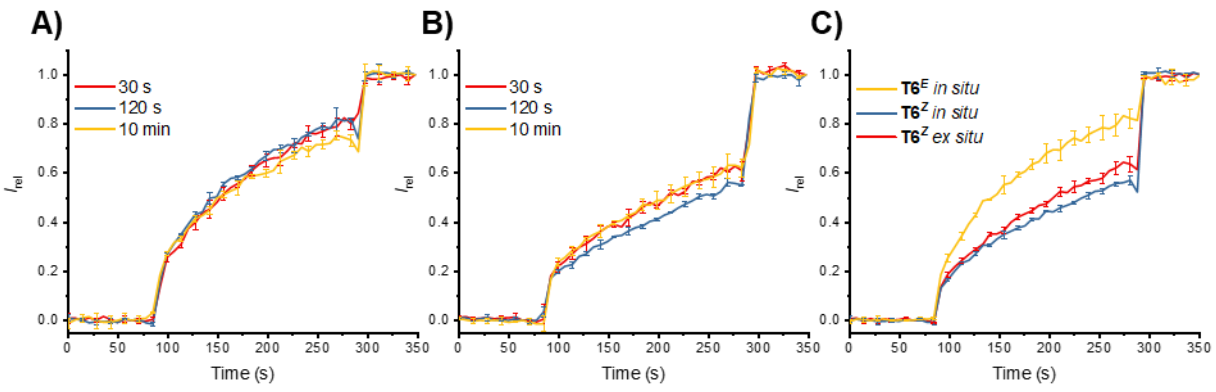

Figure 3.20 Varying irradiation times of pre-incorporated T6 and ex situ prepared T6^Z pre-incorporated into POPC LUVs. *A) HPTS transport data for **T6^E** (5 mol% to lipid, POPC LUVs) with varying irradiation times with 405 nm light. B) HPTS transport data for **T6^Z** (5 mol% to lipid, POPC LUVs) with varying irradiation times with 530 nm light. C) HPTS transport data for **T6^Z** (5 mol% to lipid, irradiated with 530 nm prior to vesicle preparation – ex situ) and in situ irradiated **T6** (5 mol% to lipid, POPC LUVs) with 405 nm and 530 nm light. Error bars denote the standard deviations from three runs.*

POPC LUVs containing the thiourea mobile carrier **T1** (0.32 mol% to lipid) showed no variation in the measured transport activity with or without photo-irradiation (405 nm or 530 nm light, < 5 minutes) (**Figure 3.21A**). This control experiment confirmed that pre-irradiation of the vesicle suspension did not detrimentally affect the integrity of the lipid membrane or bleach the dye in a way to alter the measured transport activity. Furthermore, control experiments with *in situ* photo-switching of **69^{E}** (lacking the anion-binding site) did not lead to transport (**Figure 3.21B**), ruling out photo-thermal effects. Together, these control experiments demonstrate that photo-isomerisation does not lead to membrane disruption or non-specific ion leakage.

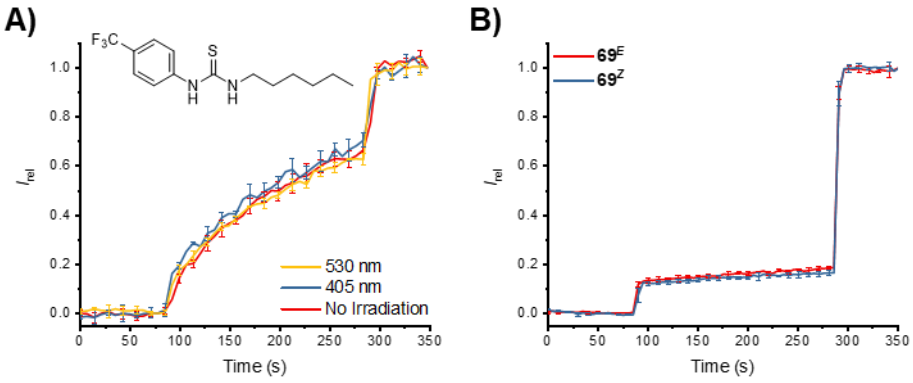

Figure 3.21 Photo-irradiation of control compounds does not affect transport activity. *A) Thiourea mobile carrier **T1** (0.32 mol% to lipid, POPC LUVs) showed no change in transport activity with or without photo-irradiation (405/530 nm light, 5-minute irradiation of **T1** in POPC LUVs). B) Irradiation (405/530 nm light, 2 minutes) of POPC LUVs with **69** (5 mol% to lipid, pre-incorporated) resulted in no transport activity. Error bars denote the standard deviations from three runs.*

Relay transporters **T6^{E}** and **T6^{Z}** were accessed in different membrane thicknesses, to determine the dependence of transport activity of each isomer on the hydrophobic thickness of the membrane. As for POPC, the transport activity of **T6^{E}** was consistently enhanced relative to **T6^{Z}** in all the membrane thicknesses tested (**Figure 3.22**), with transport activity arrested entirely in the thickest 20:1 PC lipid bilayer. This dependence of transport activity on membrane thickness provided further support of the proposed relay mechanism by which **T6** transports anions.

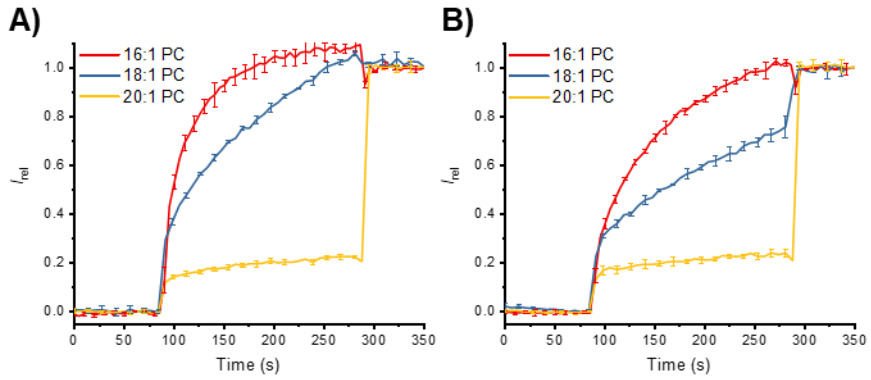

Figure 3.22 Measuring transport activity of T6^Z and T6^E in different membrane thicknesses. *A) HPTS transport data for **T6^E** (5 mol% to lipid, pre-incorporated) in LUVs comprised of a lipid with different alkyl chain lengths. B) HPTS transport data for **T6^Z** (5 mol% to lipid, pre-incorporated) in LUVs comprised of a lipid with different alkyl chain lengths. Error bars denote the standard deviations from three runs.*

The transport activity of **T6** was assessed in the same way as previously described, through pre-incorporating different concentrations of the relay transporter in LUVs and irradiating the vesicle suspension just prior to measuring transport activity. Increasing the concentration of **T6** pre-incorporated in POPC LUVs increased the observed transport activity, with **T6^E** consistently displaying enhanced activity relative to **T6^Z** (**Figure 3.23**). The initial rate of transport for each concentration was determined as previously described and found to follow a linear dependence on [**T6**]^2 (**Figure 3.23C**), implying that **T6** followed the same bimolecular relay transport mechanism.

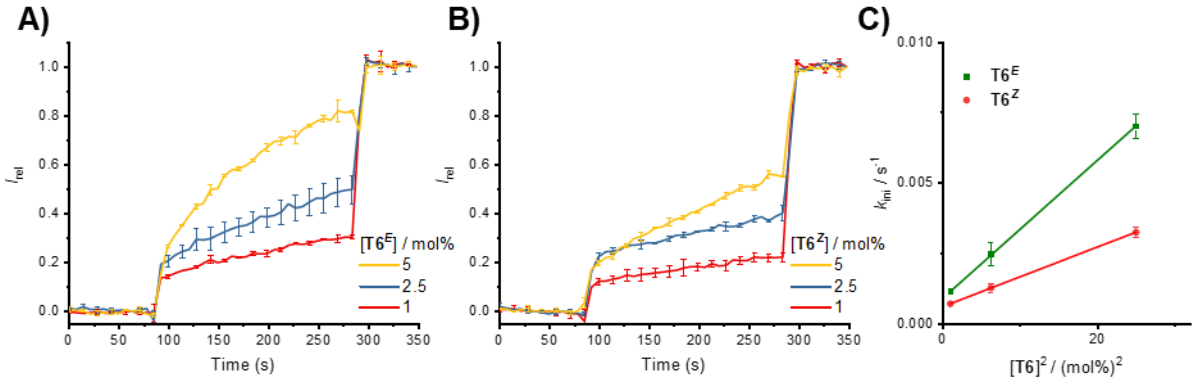

Figure 3.23 Transport activity of T6 at various concentrations in POPC LUVs*. A) HPTS transport data for **T6^E** (1-5 mol% to lipid, pre-incorporated) in POPC LUVs. B) HPTS transport data for **T6^Z** (1-5 mol% to lipid, pre-incorporated) in POPC LUVs. C) Dependence of the initial rate of transport on [**T6**]^2 showing both data for **T6^E** and **T6^Z** fitted to a linear plot. Error bars denote the standard deviations from three runs.*

The ability of the two relay transporters (**T5** and **T6**) to switch activity between an on and off state was compared, to evaluate the efficiency of photo-switchable transport activity. The initial rates of transport of **T5** and **T6** when pre-incorporated at 5 mol% in POPC LUVs, and in LUVs composed of other lipids is shown in **Table 3.2**. The ratio of transport rates for switching **T6** ($k_{ini,\mathbf{T6E}}/k_{ini,\mathbf{T6Z}}$ = 2.2 ± 0.1) was decreased relative to **T5** ($k_{ini,\mathbf{T5E}}/k_{ini,\mathbf{T5Z}}$ = 3.0 ± 0.1). The carrier arm of **T6** was however longer than **T5** by three atoms, which may account for the reduced difference between the two states, despite the fact that the PSS distribution was improved. This demonstrates that an improved PSS state distribution would help to increase the difference in activity of the on and off states, but increasing the length of the carrier arm further is detrimental to this difference. The ratio of transport rates between isomers of a transporter embedded in membranes of a different thickness were consistent, showing minor variation. Switching was however completely lost in the bilayer composed of 20:1 PC which was has the largest hydrophobic portion of the membrane, where relay transport is entirely arrested.

Table 3.2 *Characteristics of the anion relay transporters **T5** and **T6** in LUVs composed of different lipids*

Transporter in various lipids		POPC	16:1 PC	18:1 PC	20:1 PC
T5	$k_{ini(E)}$ / 10^{-3} s^{-1}	6.6 (0.3)	25.5 (0.2)	5.0 (0.1)	0.57 (0.08)
	$k_{ini(Z)}$ / 10^{-3} s^{-1}	2.2 (0.1)	13.4 (0.2)	2.3 (0.2)	0.8 (0.1)
	$S_{(E/Z)}$	3.0 (0.1)	1.9 (0.05)	2.1 (0.2)	0.7 (0.2)
T6	$k_{ini(E)}$ / 10^{-3} s^{-1}	7.0 (0.4)	25.5 (0.9)	12.3 (0.2)	0.52 (0.02)
	$k_{ini(Z)}$ / 10^{-3} s^{-1}	3.3 (0.2)	14.4 (0.7)	5.0 (1)	0.47 (0.01)
	$S_{(E/Z)}$	2.2 (0.1)	1.8 (0.1)	2.3 (0.4)	1.1 (0.05)

Initial rates of chloride transport (k_{ini}) obtained using the HPTS assay for each transporter. $S_{(E/Z)}$ Switching factor of enhancement in the transport rate between E and Z ($S_{(E/Z)} = k_{ini}(E)/k_{ini}(Z)$, ratio of rate constants for the E-rich PSS over the Z-rich PSS). Errors at the 95% confidence limit.

3.3 Chapter 3 Conclusions and Future Work

The ability of protein channels to control the flux of ions in response to environmental changes is essential to their function within cells, operating away from equilibrium. These photo-addressable relay transporters have demonstrated that through controlling the length of the carrier arm, the activity of relay transport can be regulated. This stimuli-responsive system operates *via* an entirely abiotic mechanism, inspired by the controlled nano-mechanical motions of molecular machines. This approach is likely to be a powerful method to translate the controlled molecular motion of molecular machines into useful functions in a biological context.

The two photo-switchable relay transporters **T5** and **T6** could be efficiently switched within the bilayer environment with visible light, achieving the same PSS distribution as in solution. Incorporation of the transporters in both leaflets of the bilayer was necessary for transport activity, which is a prerequisite for the relay mechanism. A linear dependence of the initial rate of transport on [**relay transporter**]^2 implicated two relay transporters in the rate-limiting step of the transport mechanism. As was seen for the halogen bonding relay transporter **T4^{XB}** in **Chapter 2**, the addition of more relay transporters to the outer leaflet of the membrane did not alter transport activity implying that the breaking of the 2:1 transmembrane relay-anion complex was rate-limiting. The photo-switchable relay transporters **T5** and **T6** therefore operated *via* the same mechanism of relay transport as was previously confirmed for the non-responsive relay transporter **T4**. The extended *E*-conformation of the carrier arm was consistently found to have an enhanced transport activity for both **T5** and **T6**, compared to the contracted *Z*-conformation. This is in contrast to observations for photo-switchable mobile carriers where the more compact *Z*-isomer is generally the more active form,[93] further

supporting the alterative *anchored carrier* mechanism of transport for these relay transporters.

Relay transporter **T5** with the shorter carrier arm length demonstrated the greatest difference in activity between the two states. However, due to the significant proportion of the extended *E*-conformer in the PSS_{530} off state the background transport activity was increased. The transport of anions between $\mathbf{T5}^{Z}$-$\mathbf{T5}^{E}$ relay pairs had appreciable activity and therefore even a small proportion of $\mathbf{T5}^{E}$ in the PSS distribution enhanced the background transport activity. Whilst the PSS distribution of **T6** had less $\mathbf{T6}^{E}$ in the PSS_{530} distribution, the high background transport activity was attributed to the increased length of the carrier arm of **T6**. Therefore, for the future development of photo-addressable relay transporters a more compact relay carrier arm which incorporates a photoswitch with a near quantitative PSS distribution in the off state is necessary. From this first proof of principle study on photo-switchable relay transporters, design criteria for a second-generation derivative have been identified and work is currently underway to develop an arylazopyrazole[186] based system (**Figure 3.24**).

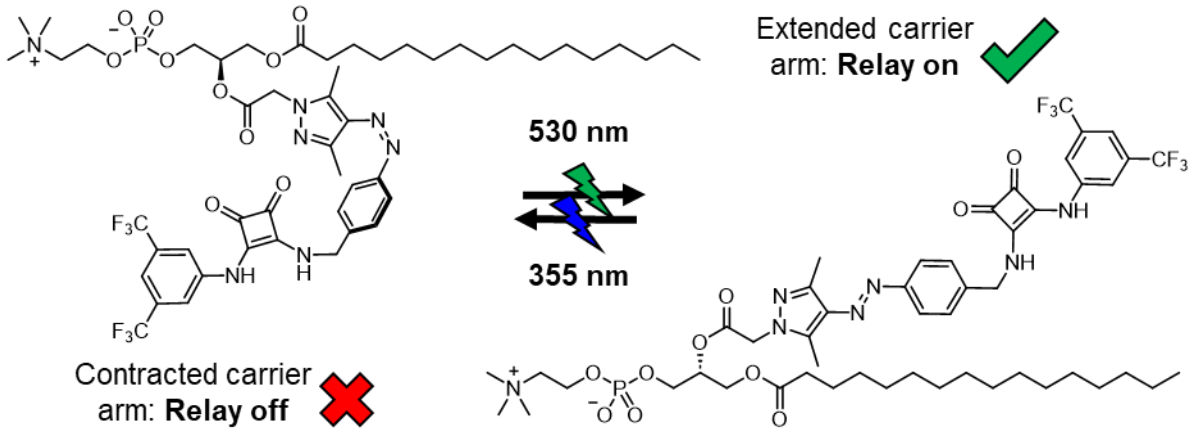

Figure 3.24 Structure of second-generation photo-switchable relay transporter. *Arylazopyrazole[186] based photoswitch core for improved PSS distribution and compact length. Squaramide receptor group for enhanced binding.*

Chapter 4: Photo-Switching Between Unique Ion Transport Mechanisms

4.1 The Influence of Phospholipid Binding on Mobile Carrier Activity

The importance of developing stimuli-responsive synthetic transporters for their application as therapeutics, replacing the loss of normal function in diseased cells (channelopathies) or for the disruption of ion gradients in cancerous cells (cancer therapy), was previously described in **Chapter 3**. In nature the mechanism of ion transport dictates whether ion flux may be gated or not, since only protein ion channels display stimuli-responsive behaviour enabling or restricting the flow of ions through the cellular membrane, dictated by environmental factors such as light, ligand binding or membrane tension.[187,188] Natural product mobile carriers, however, do not display stimuli-responsive activity. The inherent differences between the control of ion transport mediated by biological channels and mobile carriers inspired the design of the transporters described in this chapter, which are capable of switching between unique mechanisms of operation for the control of ion transport.

A recent study of mobile carrier anionophores with separated anion binding groups by Valkenier and co-workers demonstrated the detrimental effect of a secondary binding site on mobile carrier transport activity (**Figure 4.1**).[189] The *ortho*-phenylene bisurea **72a** contains two urea groups preorganized to bind the same anion and as such displayed efficient transport activity even when loaded at 1:10000 (transporter:lipid) in LUVs composed of POPC and cholesterol (7:3). However, the *meta*-phenylene bisurea **72b** was incapable of dissipating the chloride gradient, even when loaded at the higher concentration of 1:100 (transporter:lipid). The separation of the two urea binding groups was suggested to be detrimental to activity as a result of the second receptor unit binding to the phospholipid headgroup. This design

feature impeded mobile carrier transport activity, but suggested to us that a secondary binding unit sufficiently well separated from the primary anion receptor may act as an anchoring group such that the transporter could instead operate as a relay transporter.

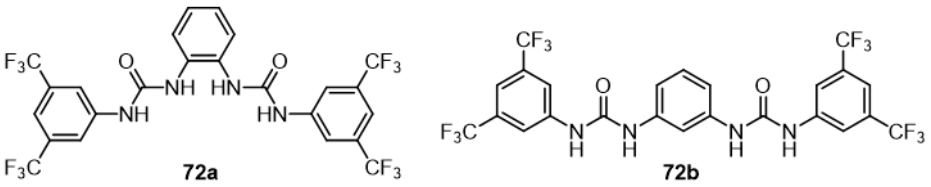

Figure 4.1 The detrimental effect of a secondary binding site. *Bis-urea anionophores **72a** and **72b** reported by Valkenier.*[189]

Numerous photo-switchable mobile carriers have now been reported, where the control over the proximity of two binding groups regulates transport activity.[190] In general, the more compact *Z*-isomer where the two receptors can cooperatively bind an anion is more active than the open *E*-isomer with the binding units well separated.[191] Analysis of the basis for switchable activity has focused on the difference in binding strength between the two isomers, however Valkenier's results suggest that binding of the phospholipid headgroup in the open *E*-isomer may also play a role in inhibiting activity in this state.[189]

Bis(amidopyrrole) stiff-stilbene photo-switchable receptors (**73a-b**) recently reported by Wezenberg and co-workers have also been investigated for photo-modulated anion transport (**Figure 4.2**).[192] Interestingly, both the open *E*-isomer and compact *Z*-isomer displayed comparable binding affinities for chloride and other anions. This was attributed to the inability of the ***Z*-73** to cooperatively bind a single anion, instead the same 2:1 (anion:receptor) binding stoichiometry was observed for both geometric isomers of the photo-switchable receptor **73a** and **73b**, respectively. This observation was in contrast to the previously described stiff-stilbene based photo-switchable mobile carriers (**29a-g**, **Figure 1.20**) which were able to cooperatively bind chloride in the *Z*-isomer, with an average 5-fold enhancement in binding

constant.[98] The transport activity of **73a** and **73b** was however demonstrated to be dependent on the geometry of the transporter, despite the equivalent binding strength of the two states in solution. For both derivatives, the *Z*-isomer displayed enhanced transport activity relative to the *E*-isomer, attributed to the better mobility and partitioning of the more compact *Z*-isomer in the membrane,[150] in addition to the improved anion encapsulation ability.[193]

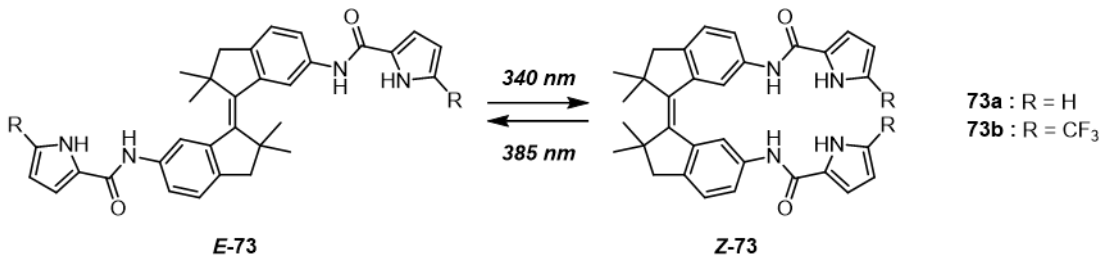

Figure 4.2 Controlling anion transport activity independently of binding affinity. *Wezenberg's stiff-stilbene bis(amidopyrrole) photo-switchable anion mobile carriers **73a** and **73b**.*[192]

Inspired by the observation that a secondary binding group can serve as an anchoring unit,[189] this chapter describes a series of transporters (**T7$^{C2\text{-}C6}$, Figure 4.3**) with an ammonium anchoring group and thiourea receptor unit separated by alkyl spacers of varying length to determine the required length for relay mediated transport activity. Wezenberg's demonstration that photo-switchable mobile carrier activity could be modulated independently of receptor binding interaction[192] motivated the incorporation of an *ortho*-tetrafluoroazobenzene photoswitch[170] within the core of **T7$^{C2\text{-}C6}$** to investigate the regulation of the transport mechanism and activity. A thiourea binding group was employed as the receptor unit in the transporters (**T7$^{C2\text{-}C6}$**) as it has been shown to be effective in both mobile carrier and relay transporter design.[194,195]

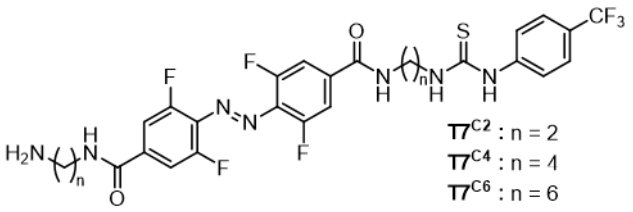

Figure 4.3 Design of ammonium anchored transporter capable of photo-switching between different ion transport mechanisms.

4.2.1 Design and Synthesis of Photo-switchable Transporters Operating Via Relay and Carrier Mechanisms

The dual mechanism anion transporters follow a simple design in which the *ortho*-tetrafluoroazobenzene at the centre acts to instil photo-switchable transport behaviour through modulation of the transport mechanism between carrier and relay pathways. A primary amine acts as the anchor at one end of the molecule and a thiourea as the receptor unit at the other of **T7**. In between, alkyl chains of varying length are incorporated to enable investigation of the dependence of relay transport activity on the spanning length of the relay transport system. A primary ammonium anchoring group was identified as it would improve aqueous solubility of the transporters for external addition to pre-formed vesicles, and whilst in the protonated state was anticipated to prohibit the translocation of the transporter through the membrane. However, the low population of the deprotonated, neutral amine form[196] would allow the distribution of transporters between the two leaflets of the bilayer even after external addition (which is not possible with the lipid-anchored relays in **Chapter 2 and 3**). Urea,[123] thiourea[195] and iodotriazole[34] anion binding groups have previously been shown to facilitate chloride transport *via* a relay mechanism based on a phospholipid anchoring architecture. The thiourea binding group was adopted for **T7** due to the stronger chloride binding strength compared to urea and hence more efficient transport activity,[197] and

for its compact structure compared to the bis-iodotriazole receptor unit which may impede transport activity.

The *ortho*-tetrafluoroazobenzene photoswitch was previously shown to affect the regulation of **T5** and **T6** transport activity,[195] operating with visible light and displaying exceptionally high photoconversion between the two isomers even within the membrane environment (**Chapter 3**). The biocompatibility of the visible light-addressability and long thermal half-lives of both isomers of this photoswitch are desirable for the potential translation of these transporters to a biological setting for therapeutic applications.[198]

The synthesis of *ortho*-fluoroazobenzene dicarboxylic acid **64** was previously described in **Section 3.2.1**. In order to access **T7$^{C2\text{-}C6}$**, a synthetic scheme was initially employed that aimed to desymmetrise the structure in the final step, forming the mono-thiourea **T7** from the bis-amine **77** (**Scheme 4.1**). Initially, mono-Boc protected diamines **74a-c** of varying lengths were prepared using a 10-fold excess of the diamine **65a-c** to favour mono-functionalisation, following a literature procedure.[199] These alkyl amines (**74a-c**) were then linked *via* amide coupling with the acid chloride of the azobenzene core **75**, generated *in-situ* using oxalyl chloride to give compounds **76a-c**. Pleasingly the product precipitated from the reaction mixture and could be readily isolated through filtration and washing with excess CH_2Cl_2, with the longer alkyl chain lengths being less soluble than shorter derivatives. Following Boc-deprotection with TFA and isolation of bis-amine **77a-c**, 4-(trifluoromethyl)phenyl isothiocyanate was added to an excess of **77a-c** under basic conditions in an attempt to generate the mono-thiourea derivative **T7**. The corresponding bis-thiourea was obtained in each case by trituration with acetone as the major product, but unfortunately no mono-thiourea **T7** was isolated.

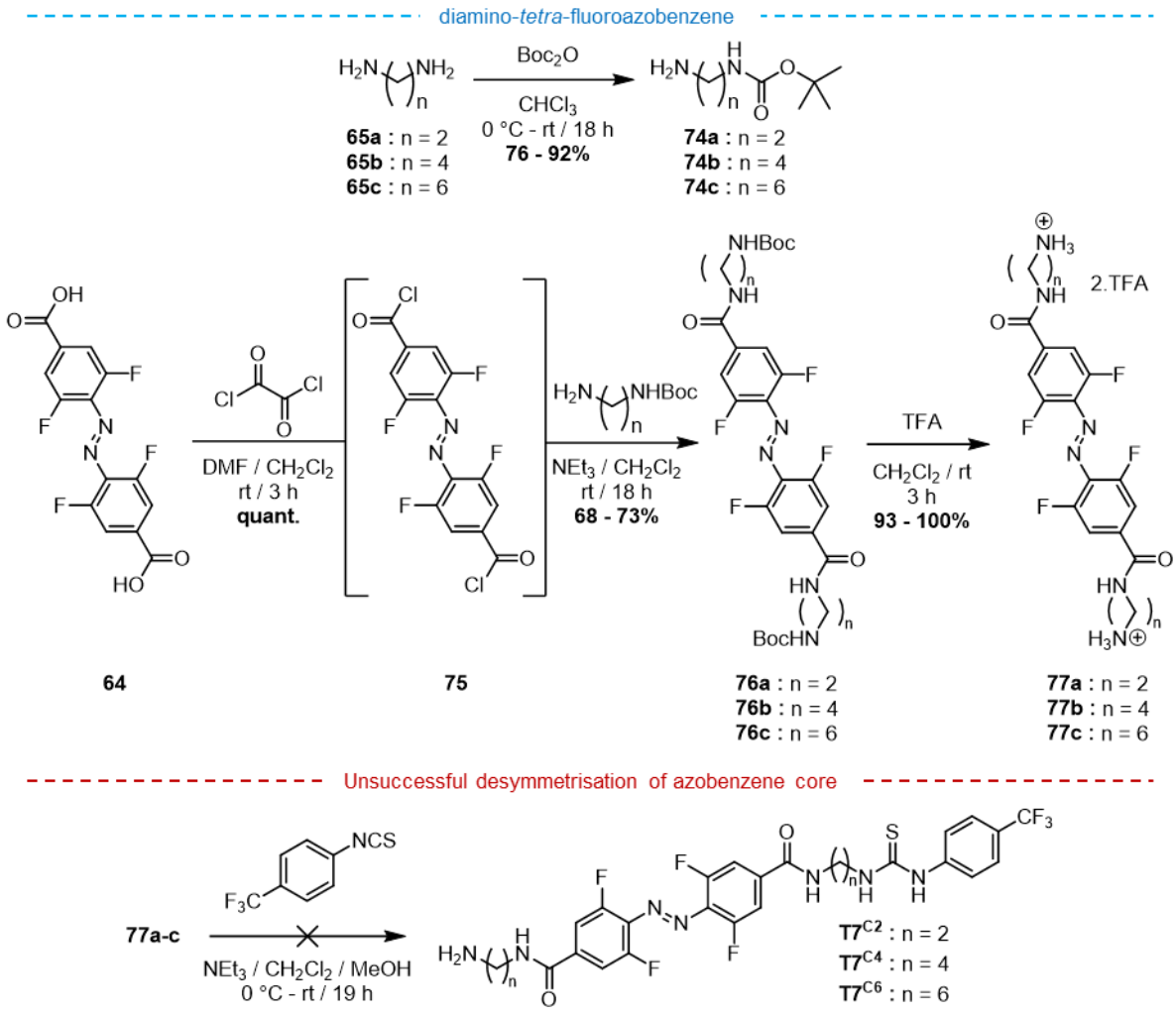

Scheme 4.1 Initial synthetic scheme to obtain the light-responsive anion transporter T7.

An alternative approach to access asymmetric **T7** is to desymmetrise the dicarboxylic acid **64** to a mono-amide **67** as was described in **Chapter 3 Section 3.2.1**. Using a procedure reported by the Vázquez group,[200] the asymmetric mono-amide azobenzenes **67a-c** were obtained limiting the equivalents of HATU relative to the dicarboxylic acid **64** (0.75:1 HATU:**64**) favoured the generation of the mono-activated ester, to form the desired mono-amide derivatives **67a-c**. The methyltrityl protected product **67a** was also found to have greater solubility compared to the Boc-protected equivalent, which aided purification. The bis-amide product **80** was isolated as a minor product from the reaction of **64** with **66a**, limiting the equivalents of HATU (0.75:1 HATU:**64**), but was favoured when in excess (2.2:1 HATU:**64**) giving **80** in 64% yield.

Condensation of 4-(trifluoromethyl)phenyl isothiocyanate with a 7-fold excess of diamines **65a-c** gave the mono-thioureas **78a-c** of varying alkyl chain lengths. HATU coupling of **67a-c** with mono-thiourea diamines **78a-c** of corresponding chain length gave the protected transporters **79a-c**, which after deprotection with dilute TFA in CH_2Cl_2 and purification by trituration with CH_2Cl_2 yielded transporters **T7** of varying alkyl chain length (**Scheme 4.2**).

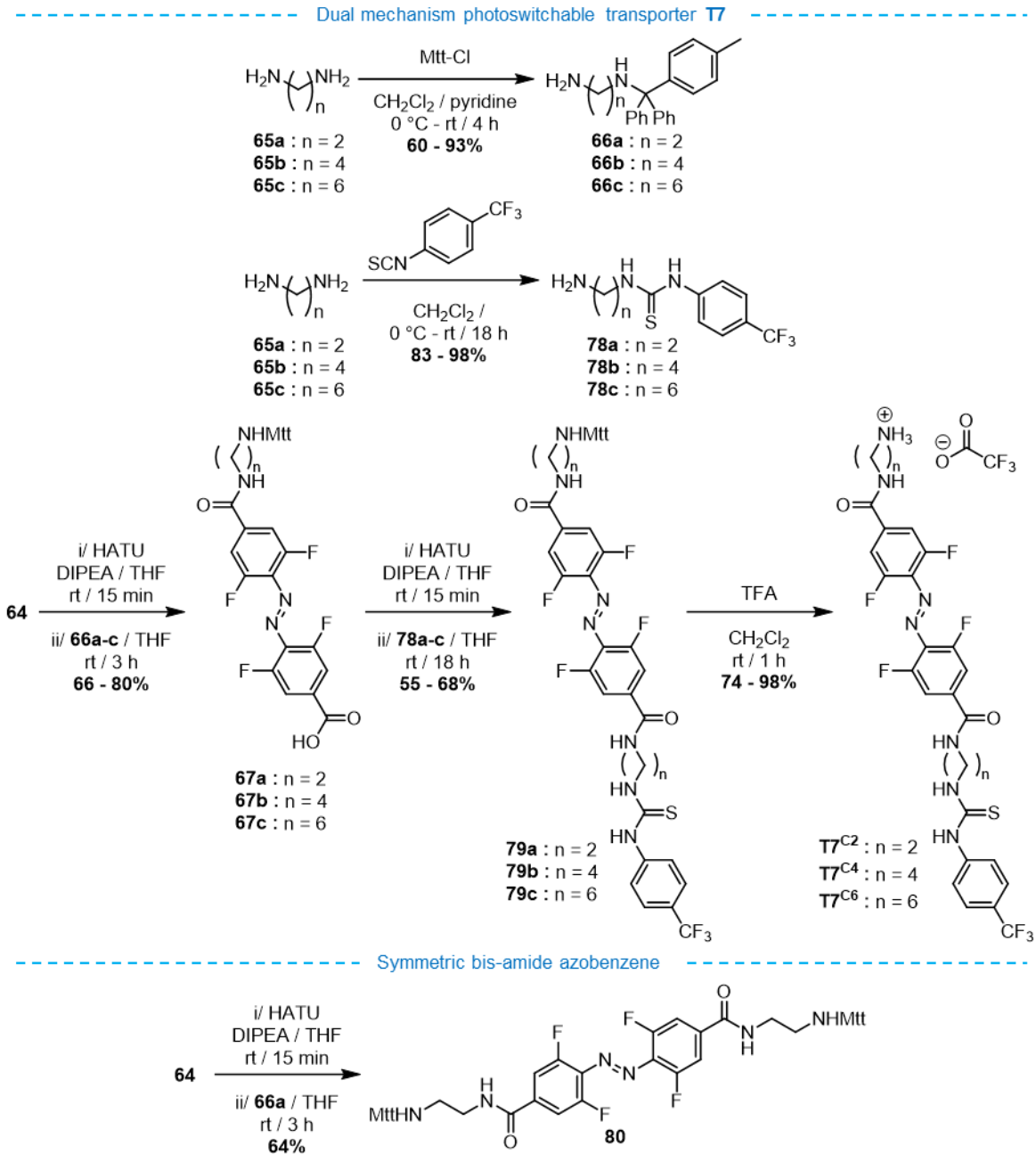

Scheme 4.2 Final synthetic scheme used to access the transporter T7.

To establish the effect of the primary amine on transport activity described in **Section 4.2.3**, a pair of simple non-photo-responsive thiourea mobile carriers were synthesised (**Scheme 4.3**). Reaction of the isothiocyanate with *n*-pentylamine or 1,4-diaminobutane gave **T8** and **T9** respectively. A 7-fold excess of 1,4-diaminobutane was necessary to favour the formation of the mono-thiourea **T9** product, which was isolated by flash chromatography on silica eluted with $CHCl_3$/MeOH/H_2O (65:25:4) in 98% yield. The neutral thiourea transporter **T8** was similar in structure to *n*-hexylarylthiourea **T1**, which has previously been shown to mediate very efficient anion transport and was described earlier in **Chapter 2**.[34,134]

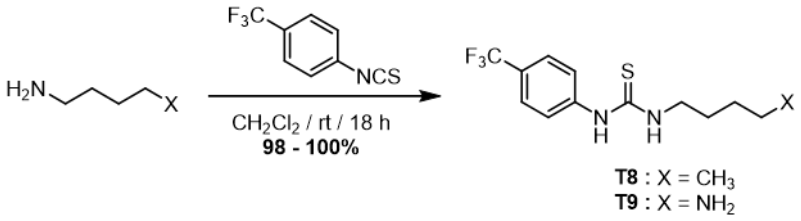

Scheme 4.3 Synthesis of n-pentyl thiourea mobile carrier (T8) and amine anchored thiourea (T9).

4.2.2 Photophysical Studies

The *ortho*-tetrafluoroazobenzene photoswitch has been used in a wide variety of applications including in photo-responsive polymers,[201] MOFs[202] and in biological environments.[200,203] Substitution directly onto the core of the azobenzene is known to affect the photophysical properties most strongly, altering the thermal half-life of the *Z*-isomer as well as the PSS distribution.[204] Substituents capable of conjugation into the aromatic system have a mesomeric effect on the electronic structure of the photoswitch strongly impacting the wavelength of light used to switch between isomers, thus altering the PSS distribution.[205] However, substituents not conjugated to the core appended remotely to the photoswitch do not alter the photophysical properties significantly.[206]

The photophysical properties of different *para*-substituted *ortho*-tetrafluoroazobenzenes were measured to confirm their switching capability. Measuring the ^{1}H NMR spectrum of a compound in solution after irradiation with 405 nm or 530 nm light until no further change in isomer ratio was observed allowed quantification of the PSS distribution (**Figure 4.4**). The effect of changing from bis-ester **63** (PSS_{405} 97:3 *E*:*Z*, PSS_{530} 10:90 *E*:*Z*, MeCN, 25 °C) to bis-amide **76a** (Boc-protected) (PSS_{405} 94:6 *E*:*Z*, PSS_{530} 8:92 *E*:*Z*, DMSO, 25 °C) only subtly changed the PSS distribution, consistent with similar derivatives previously reported.[204] Changing the substituent at the end of the pendant alkyl chains of the bis-amide between Boc-protected **76a** and Mtt-protected **80**, had no effect on the PSS distributions, demonstrating that altering this remote group did not impact the photophysical properties of the azobenzene core.

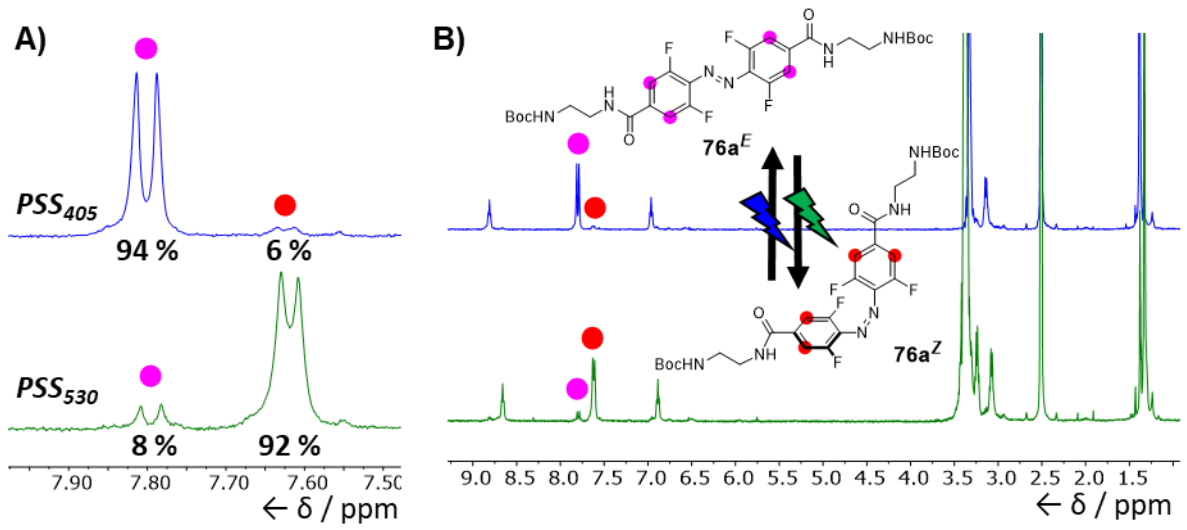

Figure 4.4 Determining the PSS distribution of a substituted para-diamide-ortho-tetrafluoroazobenzene photoswitch in DMSO-d_6 at 25 °C by ^{1}H NMR spectroscopy. *A) Partial and (B) complete ^{1}H NMR spectra of **76a** after irradiation with 405 nm (top, PSS_{405} = 94% E) and 530 nm (bottom PSS_{530} = 92% Z) light.*

The UV-vis spectrum of each isomer of **80** was measured in DMSO to determine the separation of the n-π* bands for the two isomers (**Figure 4.5**). The UV-vis of **80** was measured at four different concentrations to allow the spectrum to be reported in terms of molar extinction coefficient (ε) after construction of a Beer-lambert plot (**Figure 4.5B**). As can be seen in **Figure**

4.5C, the *E*-isomer is generally redshifted relative to the *Z*-isomer characteristic of the increased conjugation of this isomer. The large n-π* band separation is a result of the electron withdrawing nature of the fluorine atoms and *para*-amide functional groups lowering the energy level of the LUMO (π *) of **80^{Z}** more than that of the LUMO of **80^{E}**, hence blueshifting the **80^{Z}** n-π * band. The large separation of the n-π* bands enables the high photoconversion of the switch in both directions with visible light.

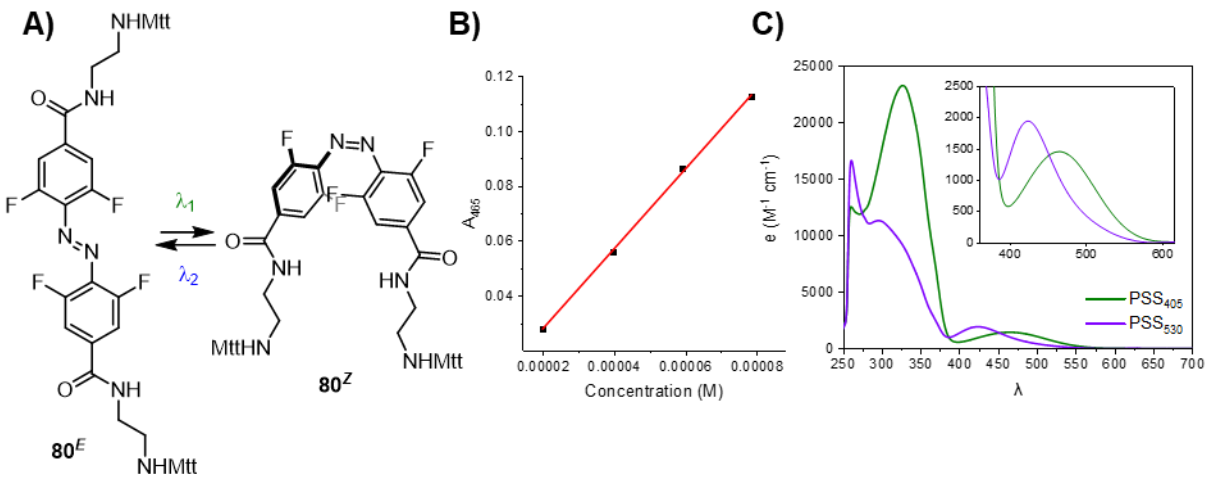

Figure 4.5 UV-vis analysis of substituted ortho-tetrafluoroazobenzene. *A) Structure of the two isomers of **80**. B) Beer-Lambert plot for **80^{E}**, absorption maxima at 465 nm plotted against compound concentration in DMSO, at 298 K. C) UV-vis spectra of PSS distributions of **80** in DMSO at 298 K, measured after irradiation with 405 nm (94% E) or 530 nm (92% Z) light.*

4.2.3 The Effect Of An Ammonium Group On Mobile Carrier Mediated Anion Transport

Having confirmed the photo-addressability of the azobenzene core, attention was directed to assessing the transport activity of the derivatives. POPC LUVs were prepared with the pH-sensitive dye HPTS encapsulated to quantify transport activity, as previously described. The activity of the thiourea control compound **T8** was first investigated, by addition of the carrier in DMSO to pre-formed LUVs, which enabled the dose dependent transport activity of this mobile carrier to be measured (**Figure 4.6**). Plotting the fractional activity, *y* (measured at 276 s, just prior to lysis) against concentration of the transporter gave a dose dependent activity plot which could be fitted to the Hill equation (**Figure 4.6B-C**). The EC_{50} of this novel

transporter was 0.33±0.06 mol% with respect to lipid, in line with transporters of a similar structure.[134] Transporter **T8** was found to be less active than the longer *n*-hexyl derivative **T1** (EC_{50} = 0.23±0.01 mol%), which likely results from the decreased lipophilicity based on the clog*P* values 4.4 and 4.9, of **T8** and **T1** respectively. As with **T1**, the Hill coefficient of **T8** (*n* = 2.2±0.6) was greater than 1 indicative of multiple transporters forming an endergonic supramolecular structure in the bilayer responsible for ion transport. Based on the studies of the isostructural **T1**, **T8** likely follows the same mobile carrier mediated ion transport mechanism.

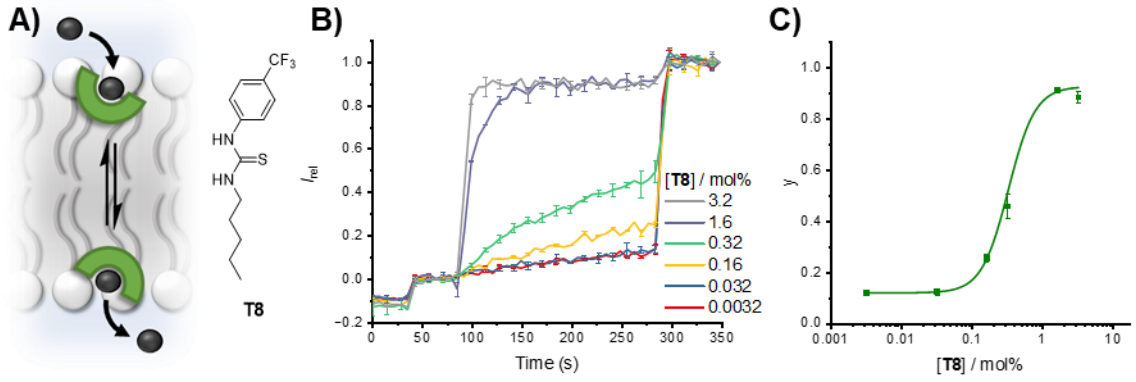

Figure 4.6 Transport activity of a simple thiourea T8. *A) Schematic of the mobile carrier mechanism and structure of* ***T8****. B) HPTS transport data of* ***T8*** *(0.0032-3.2 mol% to lipid) externally added in DMSO to POPC LUVs. C) Concentration dependent activity of* ***T8*** *(points) fit to the Hill equation (line). Error bars denote the standard deviations from two runs.*

The transport activity of **T9** was measured to establish the anchoring ability of the primary amine to restrict membrane translocation of the mobile carrier (**Figure 4.7**). The transport activity of **T9** was investigated in HPTS loaded LUVs in a solution buffered to pH 7.0 with HEPES and observed to be completely arrested (0.32 mol%) at the same concentration at which **T8** displayed 50% transport activity (**Figure 4.7B**). This demonstrated that substituting the terminal carbon of the aliphatic chain for the primary amine (pK_a ~ 10.5)[207] significantly inhibits transport activity, likely as a result of the positive charge of the ammonium. In the conditions of the transport assay the primary amine will exist primarily as the protonated form

resulting in a significantly higher energy barrier to membrane translocation. A range of concentrations of **T9** were tested, to evaluate the capacity of the primary amine to anchor the transporter to the aqueous-membrane interface restricting membrane translocation (**Figure 4.7C**). Minimal transport activity was observed at 3.2 mol% as a result of the small percentage (< 0.01%) of neutral amine capable of membrane translocation and ion transport.[208]

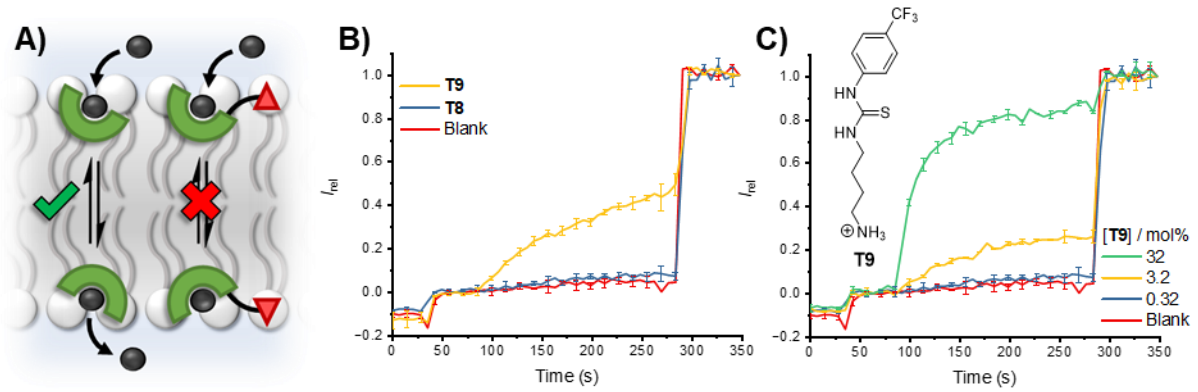

Figure 4.7 Primary amine anchored mobile carrier transport activity. *A) Schematic of the anchor group (red triangle) arresting the transport activity of the anchored carrier preventing membrane translocation. B) HPTS transport data of **T8** (0.32 mol% to lipid) added in DMSO to POPC LUVs compared to **T9** (0.32 mol% to lipid, in DMSO) and a blank (5 µL DMSO, 90 s). C) HPTS transport data for **T9** (0.32 – 32 mol% to lipid, in DMSO) in POPC LUVs. Error bars denote the standard deviations from two runs.*

4.2.4 Transport Activity of Contracted Azobenzene Ammonium-Anchored Transporters

The transport activity of the contracted *Z*-isomers of **T7** were studied in POPC LUVs to establish the effect of changing the spacer alkyl chain length. Pre-irradiation of **T7** transporters in DMSO with 530 nm light (370 mW LED) for 10 minutes was sufficient to establish the PSS_{530} (8:92 *E*:*Z*, DMSO, 25 °C), as confirmed by ^{1}H NMR spectrometry. Addition of varying concentrations of each ***Z*-T7** transporter to POPC LUVs allowed the dose dependent transport activity of each derivative to be assessed and fit to the Hill equation to quantify the transport activity. Here the transport activity of the representative butylene derivative ***Z*-T7^{C4}** is discussed in detail (**Figure 4.8**) to convey the characteristic transport activity of all the derivatives, with full transport data for each derivative available in the experimental **Section 5.6.2**. The EC_{50} of ***Z*-**

T7^{C4} was 2.8±0.1 mol% with respect to lipid, demonstrating that the incorporation of the *Z*-isomer of *ortho*-tetrafluoroazobenzene into the transporter improved transport activity relative to the simple ammonium anchored **T9**. Since the azobenzene likely did not alter the pK_a of the anchoring amine, the increase in lipophilicity of the transporter is presumably the principal factor which contributed to the improvement in transport activity. Transporter ***Z*-T7^{C4}** had a Hill coefficient of n ~ 1, which suggested that self-assembly of the transporter did not occur within the membrane to facilitate ion transport. In fact, the observed initial anion transport rate was found to be linearly dependent on the concentration of transporter (**Figure 4.8C**), indicative of a single molecule of the *Z*-isomer in the rate-limiting step of the transport process. This unimolecular transport mechanism was further evidence in support of a mobile carrier mediated ion transport process (rather than via a bimolecular relay mechanism). The unimolecular dependence of transport activity on **T7** was likely a result of the prohibitive effect of higher order transporter-anion complexes having a net positive charge as a result of the ammonium anchor.

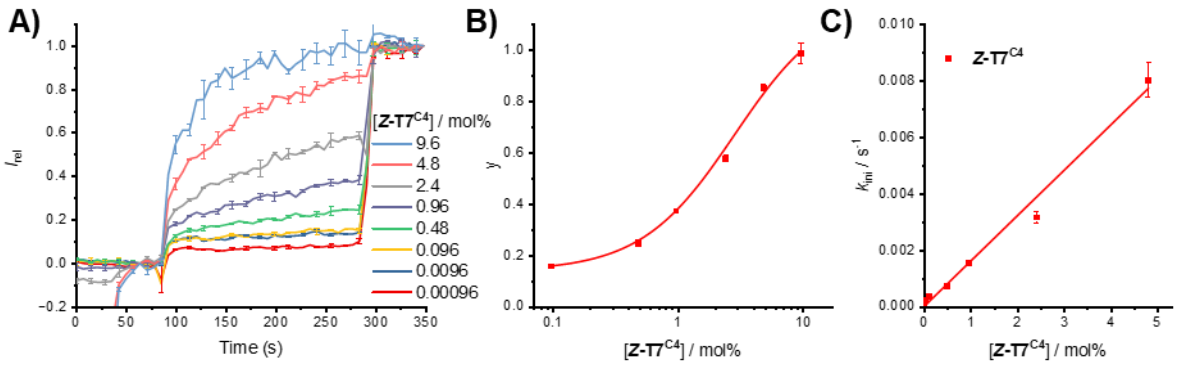

Figure 4.8 Ammonium anchored mobile carrier transport activity of Z-T7^{C4}. *A) HPTS transport data for **Z-T7^{C4}** (0.00096 – 9.6 mol% to lipid, PSS$_{530}$ = 8:92 E:Z) added externally in DMSO to POPC LUVs. B) Concentration dependent activity of **Z-T7^{C4}** fit to the Hill equation. C) Dependence of k_{ini} on [**T7^{C4}**] for the E-rich PSS generated by ex situ photo-isomerisation with 530 nm light fit to a straight line. Error bars denote the standard deviations from two runs.*

The shorter and longer derivates of **T7** were similarly tested, with 530 nm pre-irradiation of the DMSO stock solution to generate the *Z*-rich PSS for ion transport studies. All three different

alkyl chain length derivates of ***Z*-T7** had an n ~ 1 (**Table 4.1**), implicating the same unimolecular mobile carrier mechanism operated for each derivative. The observed EC_{50} value decreased across the *Z*-isomer series of increasing alkyl chain length, depicting an improvement in transport activity (**Figure 4.9, Table 4.1**). Lipophilicity has previously been highlighted as a key parameter determining the efficiency of a mobile carrier mechanism.[150] The improved transport activity of ***Z*-T7** with increasing alkyl chain length, is therefore likely a result of the increasing lipophilicity of the mobile carrier across the series.

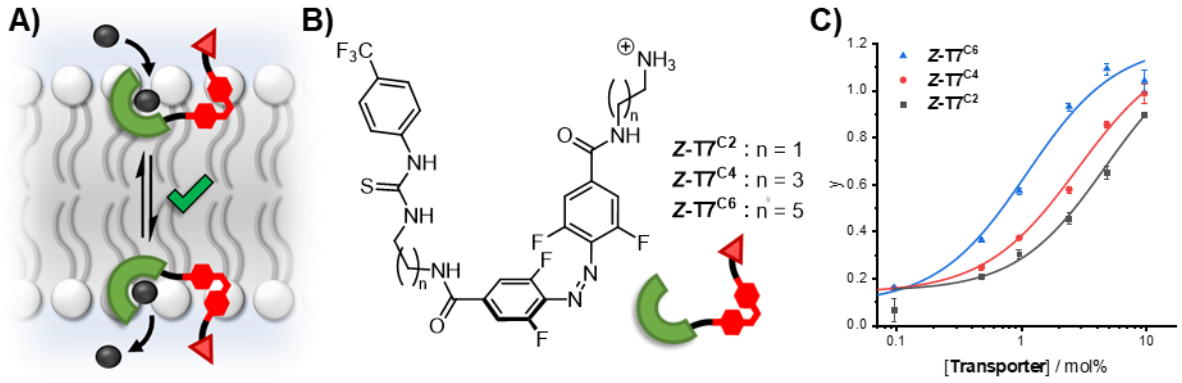

Figure 4.9 Increasing lipophilicity of ammonium anchored Z-T7 improved mobile carrier mediated transport activity. *A) Schematic of the mobile carrier mechanism. B) Structure of the Z-isomer of the ammonium anchored transporter* ***T7****. C) Comparison of concentration dependent activity for* ***Z-T7^{C2}*** *(grey data),* ***Z-T7^{C4}*** *(red data) and* ***Z-T7^{C6}*** *(blue data) fit to the Hill equation. Error bars denote the standard deviations from two runs.*

Table 4.4 *Characteristics of the Z-isomer* ***T7*** *anion transporters.*

Transporter	EC_{50}[a] / mol%	n[b]	clog*P*[c]	Order of dependence of k_{ini} on [**T7**]
***Z*-T7^{C2}**	4.7 (0.5)	1.2 (0.1)	2.8	Unimolecular
***Z*-T7^{C4}**	2.8 (0.1)	1.17 (0.06)	4.7	Unimolecular
***Z*-T7^{C6}**	1.1 (0.1)	1.2 (0.1)	6.5	Unimolecular

a Effective concentration to reach 50% of maximal activity in the HPTS assay, determined from Hill analysis of the relative fluorescence intensity at t = 276 s, immediately prior to vesicle lysis. Experiments conducted in LUVs of POPC (mean diameter 200 nm) loaded with 1 mM HPTS, NaCl (100 mM) and buffered at pH 7.0 with 10 mM HEPES. b Hill coefficient. c Calculated logP of ammonium species.

To determine the ion exchange process responsible for ***Z*-T7^{C4}** transport activity, the anion in the internal and external buffer of POPC LUVs was replaced with gluconate. With the large

hydrophilic gluconate anion as the sole anionic electrolyte in the buffer, transport activity of ***Z*-T7^{C4}** was entirely arrested (**Figure 4.10B**). This confirmed that a gluconate/OH^- antiport (or functionally equivalent gluconate/H^+ symport) process was not facilitated by the transporter, or a cation dependent Na^+/H^+ antiport process. Azobenzene based amphiphiles have previously been reported for their ability to cause membrane disruption to release cargo from lipid bound compartments, when in the *Z*-state.[209,210] Measuring transport activity with gluconate in the buffer also served as a control to confirm ***Z*-T7^{C4}** did not disrupt the membrane leading to non-specific leakage from the vesicle lumen, since no change in fluorescence emission was observed. No change in transport activity was observed in the presence of FCCP compared to in its absence (**Figure 4.10C**), therefore highlighting the rate-limited chloride transport activity of ***Z*-T7^{C4}**.

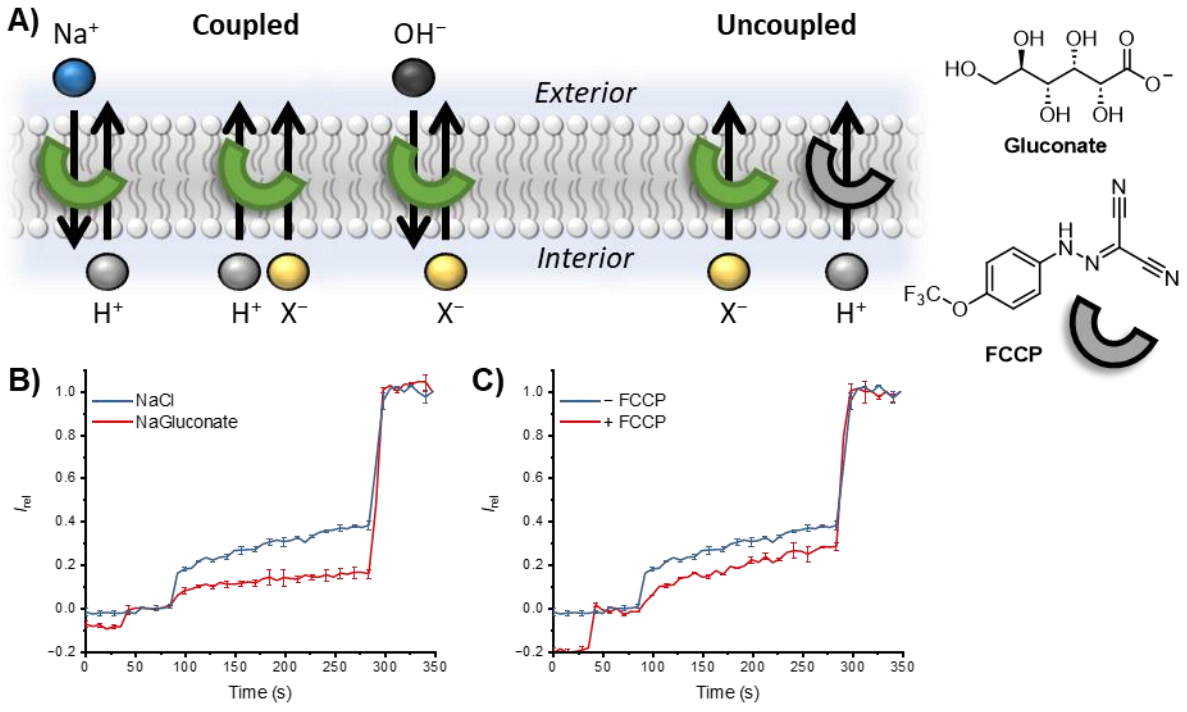

Figure 4.10 Evaluating the ion exchange process of Z-T7^{C4} transport activity. *A) Schematic of ion exchange processes and structures of FCCP and gluconate. B) HPTS transport data of **Z-T7^{C4}** (0.96 mol% to lipid, PSS_{530} = 8:92 E:Z) added externally in DMSO to POPC LUVs with NaCl (100 mM) or NaGluconate (100 mM) in the internal and external buffer. C) HPTS transport data of **Z-T7^{C4}** (0.96 mol% to lipid, PSS_{530} = 8:92 E:Z) added externally in DMSO to POPC LUVs in the absence or presence of FCCP (0.8 mol% to lipid, added at – 10 s in DMSO). Error bars denote the standard deviations from two runs.*

The transport activity of the *Z*-rich **T7^{C4}** PSS distribution was subsequently determined in different lipid membrane phases, to further interrogate the mechanism of ion transport (**Figure 4.11**). Pre-irradiation of the **T7^{C4}** DMSO stock solution with 530 nm light established the PSS distribution (PSS_{530} = 8:92 *E*:*Z*, DMSO, 25 °C), which was added to DPPC LUVs at different temperatures for transport studies. At 25 °C, below the gel–liquid phase transition temperature (T_m = 41 °C) of DPPC lipids the membrane was in a gel phase which prevented the transport activity of **T7^{C4}**. This confirmed that ion transport was not mediated by a channel mechanism, which would be expected to display transport activity independent of the membrane phase.[160] At 45 °C, the transport activity of **T7^{C4}** was restored conveying the requirement for mobility of this transporter within the membrane to facilitate ion transport, in line with the proposed mobile carrier mechanism.

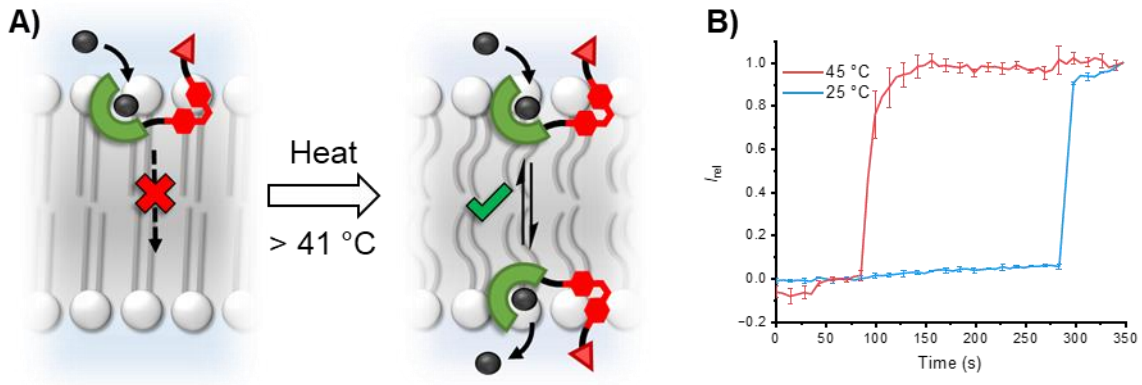

Figure 4.11 Effect of membrane phase on ammonium anchored mobile carrier transport activity of Z-T7^{C4}. *A) Schematic of a gel phase membrane restricting transporter translocation and liquid phase membrane allowing mobile carrier mediated transport. B) HPTS transport data for **Z-T7^{C4}** (2.4 mol% to lipid, PSS_{530} = 8:92 E:Z, in DMSO) added externally in a pre-irradiated solution of DMSO to DPPC LUVs at 25 °C (gel phase) and 45 °C (liquid phase). Error bars denote the standard deviations from two runs.*

To determine which step of the transport process for the *Z*-isomer of the ammonium anchored mobile carrier **T7^{C4}** was rate-limiting, the transport activity was evaluated in a series of membranes of different hydrophobic thickness (**Figure 4.12**). The transport activity of ***Z*-T7^{C4}** was tested in LUVs (200 nm) composed of 16:1 PC, POPC and 18:1 PC respectively at

equivalent transporter loadings (0.96 mol% to lipid). Unlike most unanchored mobile carriers which characteristically are limiting by anion binding at the membrane-aqueous interface,[34,211] ammonium-anchored ***Z*-T7^{C4}** displayed membrane thickness dependent transport activity - indicative of translocation-limited transport. The observation of translocation-limited mobile carrier transport activity demonstrated that the ammonium-anchor effectively inhibits the mobility of the ion-carrier complex such that crossing the hydrophobic membrane interior is the rate-limiting step of the transport process. Anion transport mediated by large cholapod-based mobile carriers with high anion affinities,[151] and the transport of anionic transporter-OH^- complexes described in **Chapter 2**,[34] have previously been observed to have translocation-limited transport activity. However, these are rare cases and the majority of synthetic anionophores display binding-limited transport activity.[211]

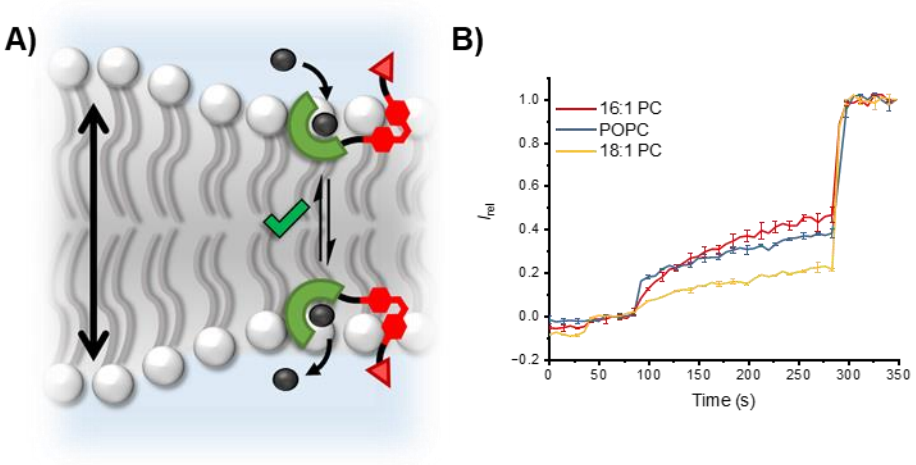

Figure 4.12 Effect of changing the hydrophobic thickness of the membrane on the transport activity of the ammonium-anchored mobile carrier Z-T7^{C4}. *A) Schematic of changing membrane hydrophobic thickness on ammonium-anchored mobile carrier mediated transport. B) HPTS transport data for **Z-T7^{C4}** (0.96 mol% to lipid, PSS_{530} = 8:92 E:Z, in DMSO) added externally in a pre-irradiated solution of DMSO to LUVs composed of 16:1 PC, POPC or 18:1 PC. Error bars denote the standard deviations from two runs.*

4.2.5 Transport Activity of Extended Azobenzene Ammonium-Anchored Transporters

Pre-irradiation of the transporter stock solutions in DMSO with 405 nm light allowed the transport activity of the *E*-rich **T7** PSS (PSS_{405} = 94:6 *E*:*Z*, in DMSO, 25 °C) to be evaluated. The external addition of various concentrations of ***E*-T7^{C2}** in DMSO to POPC LUVs allowed the dose dependent transport activity to be measured (**Figure 4.13A**). Plotting the fractional transport activity *y* from the HPTS assay against the concentration of the transporter and fitting the data to the Hill equation allowed the quantification of ***E*-T7^{C2}** transport activity (**Figure 4.13B**). Interestingly the transport activity of ***E*-T7^{C2}** (EC_{50} = 2.3±0.1 mol%) was enhanced relative to the more compact ***Z*-T7^{C2}** (EC_{50} = 4.7±0.5 mol%), which was in contrast to other azobenzene based mobile carriers where the more compact *Z*-isomer was the more active transporter relative to the *E*-isomer.[98,191] For the previously reported azobenzene based transporters, the presence of two binding groups brought into closer proximity in the *Z*-isomer promoted stronger binding and improved transport activity as a result of the increased binding rate. Since the **T7** derivatives only have a single thiourea binding receptor the rate of interfacial binding is expected to be equivalent for the two isomers. Instead, the change in azobenzene geometry presumably impacts the rate of transporter translocation through the membrane by altering the dipole of the molecule and hence lipophilicity. The effect of photo-switching lipophilicity of a mobile carrier has previously been reported for an azobenzene-based charged sulfonate peptide transporter, which was also likely rate-limited by membrane translocation and hence displayed a faster transport rate for the less polar *E*-isomer compared to the more polar *Z*-isomer.[212]

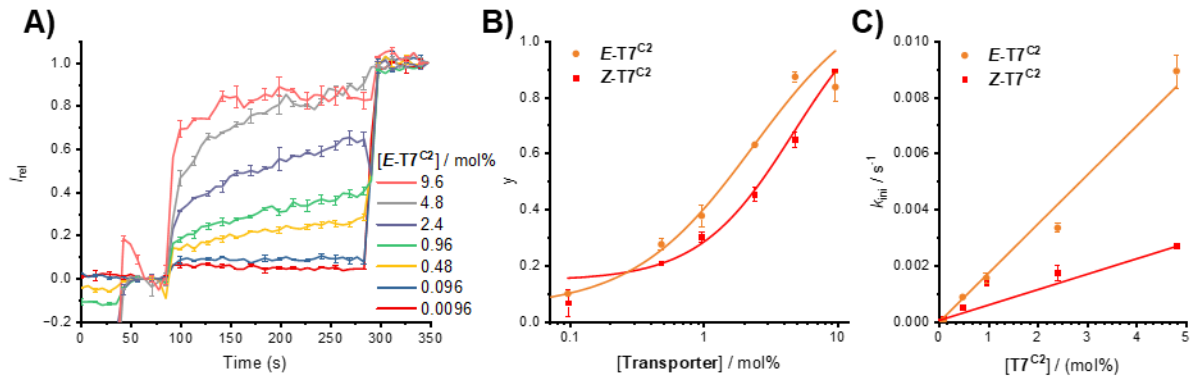

Figure 4.13 Analysis of mobile carrier mediated transport activity of T7^{C2}. *A) HPTS transport data for **E-T7^{C2}** (0.0096 – 9.6 mol% to lipid, PSS$_{405}$ = 94:6 E:Z) added externally in a pre-irradiated solution of DMSO to POPC LUVs. B) Comparison of the concentration dependent activity of **E-T7^{C2}** (orange data) and **Z-T7^{C2}** (red data) fit to the Hill equation. C) Dependence of k_{ini} on [**T7^{C2}**] for the E-rich PSS generated by ex situ photo-isomerization with 530 nm light fit to a straight line. Error bars denote the standard deviations from two runs.*

Hill analysis of the dose dependent transport activity of ***E*-T7^{C2}** provided information about the self-assemble of transporters within the bilayer environment. A Hill coefficient n~1 demonstrated that transporters did not self-assemble into an endergonic supramolecular structure in order to facilitate transport. Indeed, a linear dependence of the observed initial rate of transport on ***E*-T7^{C2}** concentration demonstrates that a single transporter is implicated in the rate-determining step of transport, responsible for activity. This suggests that the mechanism of transport does not vary between isomers of **T7^{C2}**, with both the *Z*- and *E*-isomers operating as unimolecular mobile carriers (**Figure 4.14**). The change in activity between ***Z*-T7^{C2}** and ***E*-T7^{C2}** is a result of the difference in translocation rate between the two anion-transporter complexes through the membrane.

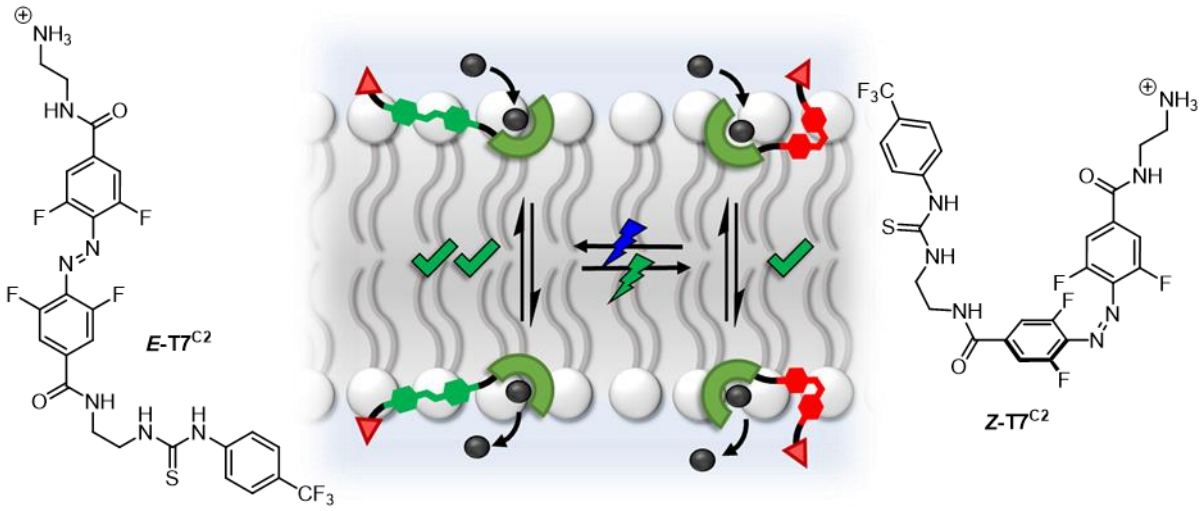

Figure 4.14 Schematic of the two isomers of photo-switchable T7^{C2} which mediate mobile carrier mediated anion transport. *E-T7^{C2} (Left) mediates faster transport than Z-T7^{C2} (Right) as a result of the change in geometry of the azobenzene core changing lipophilicity of the unimolecular mobile carrier.*

The derivative ***E*-T7^{C4}** with the medium length C4 alkyl spacer was also investigated in HPTS loaded POPC LUVs (**Figure 4.14**). Similarly to **T7^{C2}**, the *E*-rich PSS of **T7^{C4}** (EC_{50} = 0.8±0.1 mol%) displayed more efficient transport activity than the *Z*-rich PSS of **T7^{C4}** (EC_{50} = 2.8±0.1 mol%) (**Figure 4.15B**). However, in contrast to the shorter derivative, a Hill coefficient $n > 1$ was observed for ***E*-T7^{C2}** (n = 1.7±0.1) which demonstrated that multiple molecules self-assembled within the bilayer in the rate-limiting step to mediate ion transport. The non-linear dependence of the observed initial rate of transport on concentration of the transporter in the membrane also implicated multiple molecules in the rate-determining step of transport. The initial rate was found to be linearly dependent on [***E*-T7^{C4}**]^2 (**Figure 4.15C**), indicative of a second order dependence of the transport rate on ***E*-T7^{C4}**. This indicates that the rate-limiting step of ***E*-T7^{C4}** mediated transport is bimolecular, rather than unimolecular for ***Z*-T7^{C4}**. The difference in Hill value and order with respect to transporter in the rate equation between the two isomers of **T7^{C4}** suggests a change in transport mechanism by which each isomer operates.

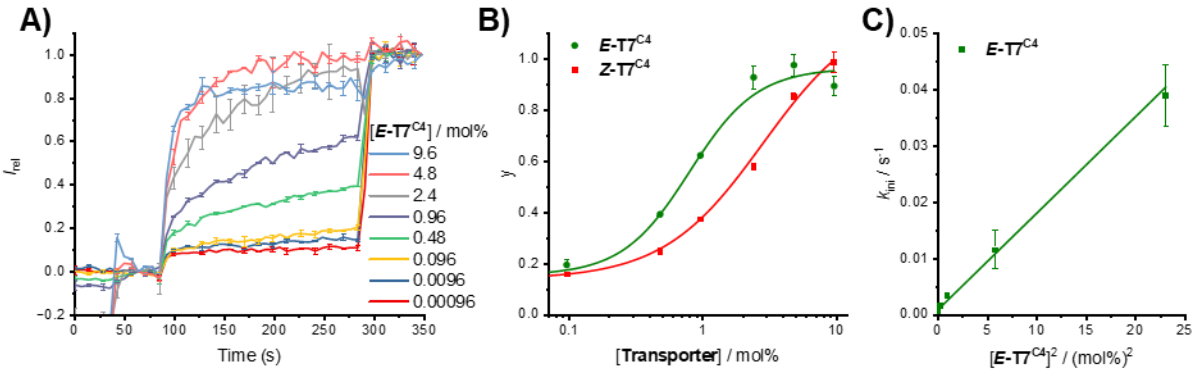

Figure 4.15 Analysis of E-T7^{C4} transport activity. *A) HPTS transport data for* ***E-T7^{C4}*** *(0.00096 – 9.6 mol% to lipid, PSS$_{405}$ = 94:6 E:Z) added externally in a pre-irradiated solution of DMSO to POPC LUVs. B) Comparison of the concentration dependent activity of* ***E-T7^{C4}*** *(green data) and* ***Z-T7^{C4}*** *(red data) fit to the Hill equation. C) Dependence of k_{ini} on [**T7^{C4}**]^2 for the E-rich PSS generated by ex situ photo-isomerization with 530 nm light fit to a straight line. Error bars denote the standard deviations from two runs.*

An increase in the number of transporters implicated in the transport mechanism of ***E*-T7^{C4}**, together with an improved transport activity compared to the *Z*-isomer, suggested that ***E*-T7^{C4}** does not operate *via* a mobile carrier mechanism. The strict adherence of the unimolecular dependence of transport activity by the compact ***Z*-T7** series of transporters was ascribed to the positive charge of **T7** arresting the transport activity of higher order mobile carrier-anion complexes. The positive charge of **T7** was anticipated to similarly restrict the mobile carrier activity of all geometric isomers such that the extended ***E*-T7** derivatives would be expected to follow a first order dependence on transport activity. The shorter derivative ***E*-T7^{C2}** follows a unimolecular dependence of k_{ini} on the concentration of transporter expected of a mobile carrier mechanism, however the longer ***E*-T7^{C4}** demonstrates a bimolecular dependence of k_{ini} on transporter concentration. This change in order of transporter-anion complex implicated in the transport process suggests that ***E*-T7^{C4}** does not operate *via* a mobile carrier mechanism.

The possibility of a 2:1 transporter:anion complex involved in the rate limiting step of a carrier mediated process, which would also result in a bimolecular dependence of k_{ini}, can be ruled out. Increasing the number of transporters in the ion-transporter complex would be predicted

to reduce the rate of membrane translocation, on both molecular weight arguments and the fact that the overall complex would be charged (whereas a 1:1 carrier-anion complex is neutral). The rate of the biomolecular ***E*-T7^{C4}** transport mechanism would therefore be expected to be slower compared to the unimolecular ***Z*-T7^{C4}** if they both operated *via* a mobile carrier mechanism. Instead, the bimolecular dependence of ***E*-T7^{C4}** transport activity is indicative of a relay transport mechanism, due to the requirement of at least one relay transporter in each leaflet of the bilayer (**Figure 4.16**).[34,123,195] The length dependence of transporter order implicated in the rate equation, second order for the longer ***E*-T7^{C4}** and first order for the shorter ***E*-T7^{C2}**, provided further mechanistic evidence to support the relay-mediated anion transport by the longer derivative. For the shorter ***E*-T7^{C2}** the formation of a membrane spanning 2:1 transporter-anion complex for a relay-mediated transport mechanism is likely too prohibitive as a result of the short total length of the complex, requiring the charged ammonium anchor groups to be positioned deeper into the membrane interior. The medium length ***E*-T7^{C4}** is presumably therefore of sufficient length such that the membrane spanning 2:1 transporter-anion complex matched well with the length of the POPC bilayer, to have the charged amine anchors positioned in the aqueous phase without a large desolvation penalty to being positioned in the hydrophobic interior of the bilayer.

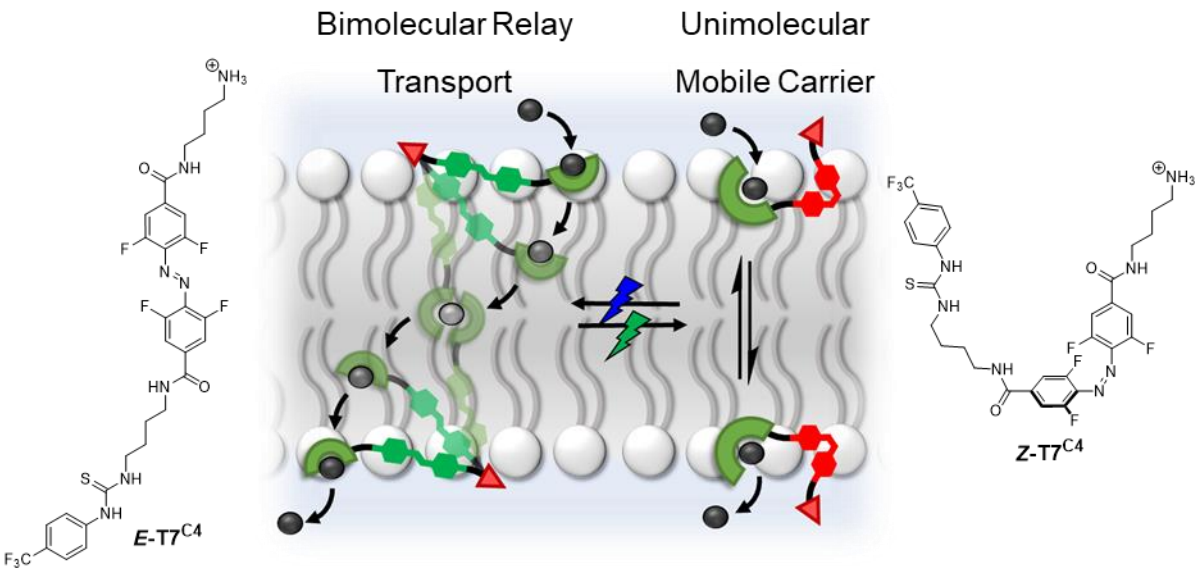

Figure 4.16 Schematic of the two unique mechanism of transport proposed to operate for the two isomers of T7^{C4} which can be accessed through photo-switching with visible light. *Left, the bimolecular relay transport mechanism which requires an anchored transporter in each leaflet of the bilayer to facilitate the exchange of the anion and Right, the unimolecular mobile carrier mechanism.*

Complete inhibition of ***E*-T7^{C4}** transport activity was observed with gluconate replacing chloride in the buffer of POPC LUVs (**Figure 4.17A**). This demonstrated that ***E*-T7^{C4}** was incapable of mediating cation (Na^+/H^+ antiport) transport and that the *E*-isomer did not disrupt the membrane at the tested loading (0.96 mol%) leading to non-specific leakage. The lack of background leakage in the gluconate buffer transport studies confirms that ***E*-T7^{C4}** mediates transport of anions through selective binding interactions *via* a controlled process.

Evaluating the transport activity of ***E*-T7^{C4}** in the presence and absence of FCCP allowed the rate-limiting anion of the transport process to be determined (**Figure 4.17B**). FCCP was added in a solution of DMSO just prior to the start of the transport experiment, at a concentration that had no background transport activity. The transport activity of ***E*-T7^{C4}** was invariant with the addition of FCCP, demonstrating that proton or hydroxide transport was not rate-limiting, since FCCP would enhance the rate of the functionally equivalent H^+ transport. Therefore, chloride transport mediated by a bimolecular step was rate-limiting for ***E*-T7^{C4}** mediated anion

transport. This chloride-limited relay transport activity is comparable to the thiourea based relay transporters described in **Chapter 3**, where the hydrogen bonding relay transport system displayed no rate enhancement in the presence of FCCP.[195]

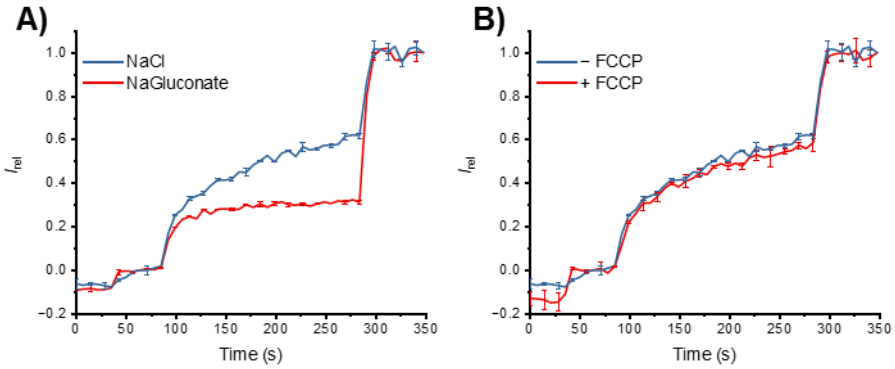

Figure 4.17 Measuring the selectivity of the anion transporter E-T7^{C4}. *A) HPTS transport data for **E-T7^{C4}** (0.96 mol% to lipid, PSS_{405} = 94:6 E:Z) added externally in DMSO to POPC LUVs with NaCl (100 mM) or NaGluconate (100 mM) in the internal and external buffer. C) HPTS transport data of **E-T7^{C4}** (0.96 mol% to lipid, PSS_{405} = 94:6 E:Z) added externally in DMSO to POPC LUVs in the absence or presence of FCCP (0.8 mol% to lipid, added at – 10 s in DMSO). Error bars denote the standard deviations from two runs.*

The effect of membrane fluidity on the relay-mediated transport activity of ***E*-T7^{C4}** was investigated in DPPC LUVs (**Figure 4.18**). A stock solution of **T7^{C4}** in DMSO was pre-irradiated with 405 nm to reach the *E*-rich PSS (PSS_{405} = 94:6 *E*:*Z*, in DMSO, 25 °C) before addition to pre-formed DPPC LUVs at 25 °C or 45 °C. The transport activity of ***E*-T7^{C4}** at 25 °C (lipid gel phase) was entirely arrested confirming that a channel mechanism was not responsible for the observed transport activity in fluid POPC LUVs. Recovery of ***E*-T7^{C4}** transport activity at 45 °C (lipid fluid phase) demonstrated the requirement for transporter mobility within the membrane in line with a relay-mediated anion transport mechanism.

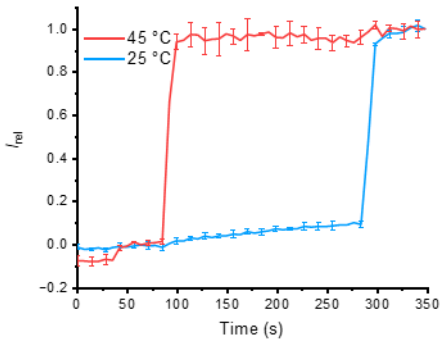

Figure 4.18 Effect of membrane fluidity on E-T7^{C4} relay transport activity. *HPTS transport data for **E-T7^{C4}** (2.4 mol% to lipid, PSS_{405} = 94:6 E:Z) added externally to DPPC LUVs at 25 °C or 45 °C in a DMSO solution pre-irradiated with a 405 nm, 980 mW LED. Error bars denote the standard deviations from two runs.*

Changing the alkyl chain length of the lipid which comprised the LUVs enabled the membrane thickness dependence of ***E*-T7^{C4}** transport activity to be determined (**Figure 4.19**). Relay transporter ***E*-T7^{C4}** was added externally to LUVs composed of 16:1 PC, POPC, and 18:1 PC respectively, to evaluate the transport activity in a range of membranes of different hydrophobic thickness. Since the headgroup of the lipids in the series of investigation were constant, the rate of anion binding and dissociation at the membrane-aqueous interface was expected to be unaffected. However, the rate of translocation of the transporter-ion complex (mobile carrier mechanism) or the rate of exchange of the ion between transporters immobilised in opposite leaflets of the bilayer (relay mechanism) would be altered by changing hydrophobic thickness. A strong dependence of chloride transport activity of ***E*-T7^{C4}** on hydrophobic thickness of the lipid bilayer (**Figure 4.19**) provided further evidence in support of the relay mediated transport mechanism operating when the transporter was in the extended *E*-geometry. Due to the prohibitive positive charge of the 2:1 transporter:anion complex a mobile carrier mechanism is unlikely, whilst a relay mechanism facilitates the transport of the ion without the positive charge of the ammonium anchors having to pass through the hydrophobic interior of the membrane.

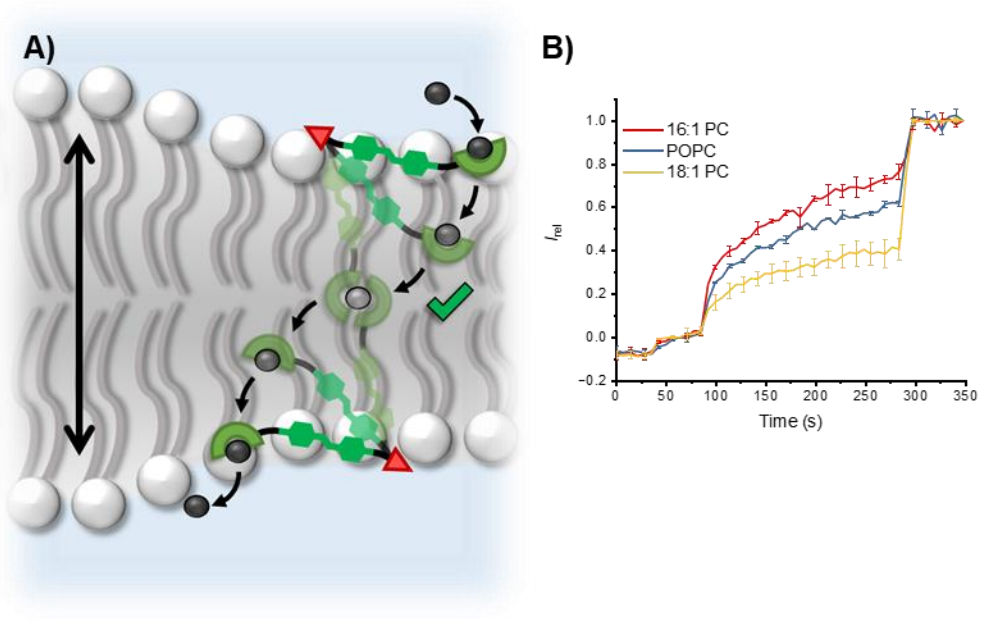

Figure 4.19 Effect of membrane thickness of the transport activity of E-T7^{C4}. *A) Schematic of the effect of changing membrane thickness on **E-T7^{C4}** relay mediated transport. B) HPTS transport data for **E-T7^{C4}** (0.96 mol% to lipid, PSS_{405} = 94:6 E:Z) added externally to LUVs composed of each of the lipids 16:1 PC, POPC and 18:1 PC respectively. Error bars denote the standard deviations from two runs.*

Testing the longer derivative ***E*-T7^{C6}** with the C6 alkyl spacer in HPTS loaded POPC LUVs allowed the effect of increasing alkyl chain length on transport activity to be investigated (**Figure 4.20**). The dose dependence of ***E*-T7^{C6}** transport activity on concentration of transporter was analysed by fitting to the Hill equation (**Figure 4.20B**). In line with the observations for **T7^{C2}** and **T7^{C4}**, the *E*-rich PSS_{405} of **T7^{C6}** was a more efficient transporter than the *Z*-rich PSS_{530}, with EC_{50} values of 0.7±0.1 mol% and 1.10±0.09 mol% respectively. A Hill coefficient $n > 1$ was observed, indicative of multiple transporter molecules assembled into an endergonic supramolecular structure in the rate-determining step of anion transport. The linear dependence of observed transport rate on [***E*-T7^{C6}**]^2 (**Figure 4.20C**). is indicative of a bimolecular transporter species in the rate-determining step of anion transport. Consistent with the experimental evidence for **T7^{C4}**, the biomolecular dependence of the rate equation on ***E*-T7^{C6}** suggests this derivative also operates *via* a relay mechanism.

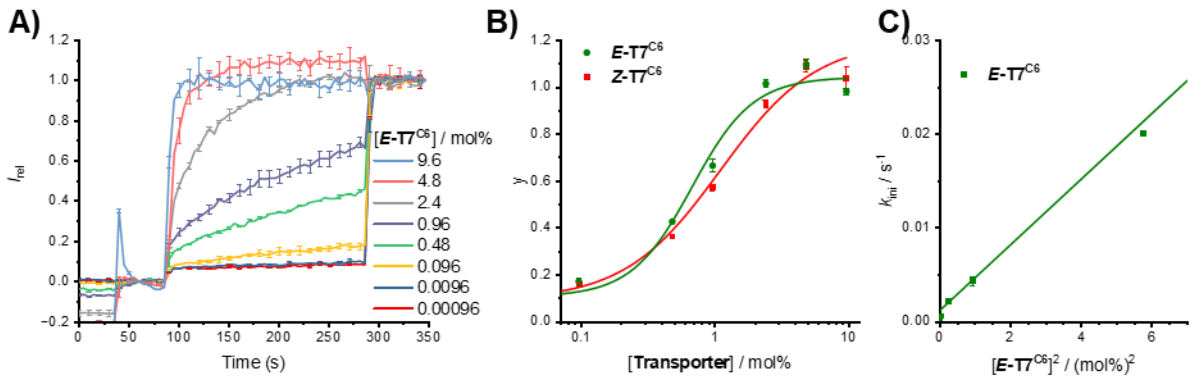

Figure 4.20 Analysis of E-T7^{C6} transport activity. *A) HPTS transport data for **E-T7^{C6}** (0.00096 – 9.6 mol% to lipid, PSS$_{405}$ = 94:6 E:Z) added externally in a pre-irradiated solution of DMSO to POPC LUVs. B) Comparison of the concentration dependent activity of **E-T7^{C6}** (green data) and **Z-T7^{C6}** (red data) fit to the Hill equation. C) Dependence of k_{ini} on [**T7^{C6}**]^2 for the E-rich PSS generated by ex situ photo-isomerization with 530 nm light fit to a straight line. Error bars denote the standard deviations from two runs.*

The work in the previous **Chapters 2 and 3** have demonstrated that the breaking of the transmembrane transport-anion complex is the rate determining step of relay mediated transport.[34,195] The longer hexyl derivative **T7^{C6}** displayed the same change in transport mechanism as **T7^{C4}** evidenced by the change in Hill coefficient and modulation of the order of dependence in the rate equation on transporter molecules (1st order for the Z isomer, 2nd order for the *E*-isomer). The small difference in transport activity between ***E*-T7^{C4}** and ***E*-T7^{C6}** (**Figure 4.21**) therefore demonstrates that the change in alkyl chain length did not significantly impact the stability of this membrane spanning supramolecule characteristic of the relay transport mechanism.

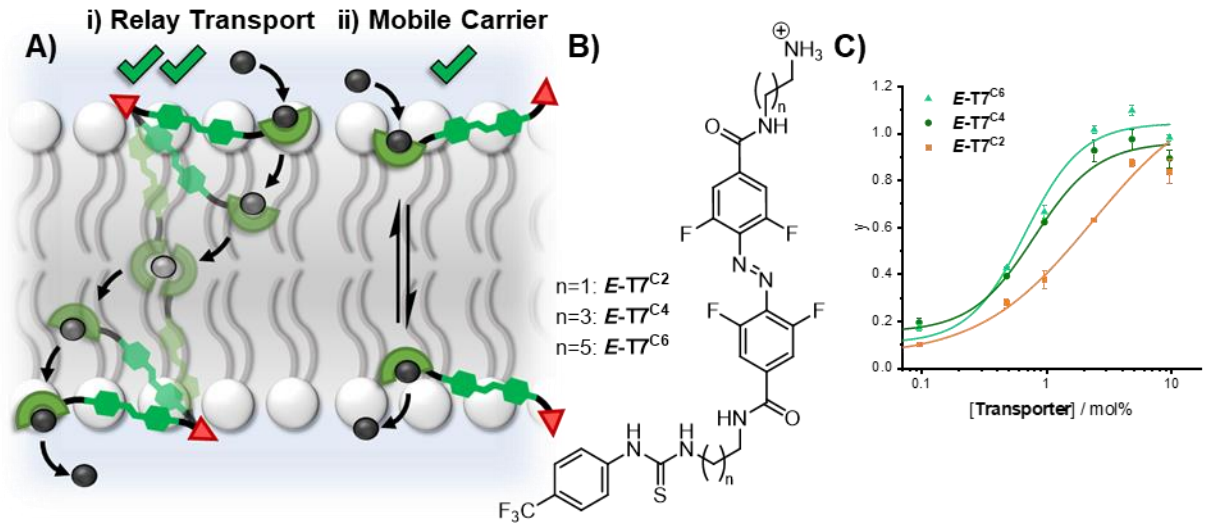

Figure 4.21 Relay and mobile carrier mediated transport by extended ammonium anchored transporters E-T7 or varying length. *A) Schematic showing the relay transport mechanism facilitated by the longer transporters (i, for **E-T7^{C4}** and **E-T7^{C6}**) and the mobile carrier mechanism followed by the shortest transporter (ii, for **E-T7^{C2}**). B) Structure of the E-isomer of the ammonium anchored transporter **T7**. C) Comparison of concentration dependent activity for **E-T7^{C2}** (orange data), **E-T7^{C4}** (dark green data) and **E-T7^{C6}** (light green data) fit to the Hill equation. Error bars denote the standard deviations from two runs.*

Table 4.5 *Characteristics of the E-isomer **T7** anion transporters.*

Transporter	EC_{50}[a] / mol%	n[b]	clog$P$[c]	Order of dependence of k_{ini} on [**T7**]
***E*-T7^{C2}**	2.3 (0.1)	1.0 (0.1)	2.8	Unimolecular
***E*-T7^{C4}**	0.8 (0.1)	1.7 (0.2)	4.7	Bimolecular
***E*-T7^{C6}**	0.7 (0.1)	1.9 (0.6)	6.5	Bimolecular

a Effective concentration to reach 50% of maximal activity in the HPTS assay, determined from Hill analysis of the relative fluorescence intensity at t = 276 s, immediately prior to vesicle lysis. Experiments conducted in LUVs of POPC (mean diameter 200 nm) loaded with 1 mM HPTS, NaCl (100 mM) and buffered at pH 7.0 with 10 mM HEPES. b Hill coefficient. c Calculated log P of ammonium species.

In summary, for the extended ***E*-T7** series of transporters with varying spacer length, there is the same increase in activity as the alkyl chain length increases, as was observed for the contracted ***Z*-T7** series. However, there is a clear change in transport mechanism across the extended ***E*-T7** series highlighted by the order of dependence of initial rate of transport on the concentration of transporter (**Table 4.2**). For the shortest derivative ***E*-T7^{C2}** with the ethylene spacer, a unimolecular dependence of the rate on transporter is observed demonstrating that a mobile carrier mechanism must operate. However, increasing the spacer length to butyl and

hexyl for ***E*-T7^{C4}** and ***E*-T7^{C6}** respectively, resulted in a change in the mechanism by which the transporters operate from a carrier to a relay transport system, indicated by the change to a bimolecular dependence of the rate on transporter. Since a 2:1 transporter:anion complex would be positively charged it would be prohibitive for it to cross the hydrophobic interior of the membrane. However, when the spacers are of sufficient length to mediate the exchange of the anion between transporters immobilised in opposite leaflets of the bilayer, the anion is transported *via* a relay mechanism (**Figure 4.21**).

The results reported in the chapter so far demonstrate that the modulation of transporter lipophilicity and molecular length through photo-switching of the *ortho*-tetrafluoroazobenzene core enabled control of transport activity. The factor of enhancement upon switching from the contract *Z*-state to the extended *E*-state can be represented by the ratio of EC_{50} values (S = EC_{50}^{405} / EC_{50}^{530}) shown in **Table 4.3**. The shortest ethylene spacer derivative **T7^{C2}** displayed a modest 2-fold enhancement upon switching to the *E*-isomer (both isomers acting as carriers), presumably due to the increased lipophilicity improving the rate of the carrier-anion complex translocation through the membrane. The medium length butylene spacer derivative **T7^{C4}** showed improved switching as a result of the change in transport mechanism, where the relay mediated transport activity of ***E*-T7^{C4}** was 3.5-fold greater than the mobile carrier mediated activity of ***Z*-T7^{C4}**. The longest hexyl derivative **T7^{C6}** showed diminished switching in transport activity between isomers compared to the butyl spacer derivate **T7^{C4}**, with a factor of enhancement of 1.6-fold, despite still showing the same modulation of transport mechanism. This loss of switching in activity results from an increase in the relative activity of the mobile carrier mediated transport by ***Z*-T7^{C6}** compared to ***Z*-T7^{C4}** because of the increase in lipophilicity, while the relay mediated transport activity of ***E*-T7^{C6}** was only slightly improved relative to ***E*-T7^{C4}** (**Figure 4.22**).

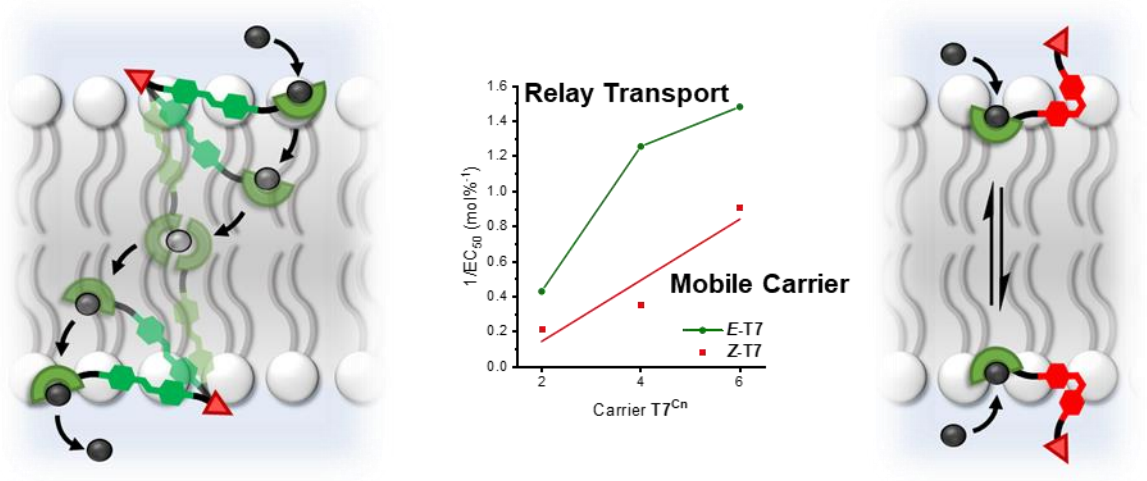

Figure 4.22 Summary of transport activity data (reported as $1/EC_{50}$) for both isomers of the three different length derivatives of T7. *The relay mechanism results in a significant improvement in transport activity relative to the mobile carrier mechanism.*

Table 4.6 *Switchable characteristics of ammonium anchored photo-switchable anion transporters* ***T7****.*

Transporter	$EC_{50}^{405\,a}$ / mol%	$EC_{50}^{530\,a}$ / mol%	$S^b(E/Z)$
$T7^{C2}$	2.3 (0.1)	4.7 (0.5)	2.0
$T7^{C4}$	0.8 (0.1)	2.8 (0.1)	3.5
$T7^{C6}$	0.7 (0.1)	1.1 (0.1)	1.6

a Effective concentration to reach 50% of maximal activity in the HPTS assay, determined from Hill analysis of the relative fluorescence intensity at t = 276 s, immediately prior to vesicle lysis. Experiments conducted in LUVs of POPC (mean diameter 200 nm) loaded with 1 mM HPTS, NaCl (100 mM) and buffered at pH 7.0 with 10 mM HEPES. b Switching factor of enhancement in the transport activity between the extended E-state and the contracted Z-state ($S(E/Z) = EC_{50}^{530}/EC_{50}^{405}$).

4.2.6 Photo-switching Transport Activity of Ammonium Anchored Transporters *in situ*

In the previous section the transport activity of the two PSS distributions of the **T7** derivatives were evaluated by *ex situ* irradiation of the transporter in DMSO, prior to external addition to pre-formed LUVs. However, the *in situ* PSS of each isomer could be generated by irradiation of LUVs loaded with transporter (**Figure 4.23**). To confirm the PSS state distribution obtained within the bilayer environment was that same as that established in DMSO, varying irradiation times were used to measure the impact on the observed transport activity. The *Z*-rich PSS (PSS_{530} = 8:92 *E*:*Z*, in DMSO, 25 °C) of **$T7^{C4}$** was established in solution by 530 nm irradiation of

a DMSO stock solution. Addition of ***Z*-T7^{C4}** to POPC LUVs and irradiating the vesicle suspension for different lengths of time with 405 nm light prior to starting the experiment enabled comparison of the *in situ* generated PSS_{405} transport activity with the *ex situ* prepared ***E*-T7^{C4}** (PSS_{405} = 94:6 *E*:*Z*, in DMSO, 25 °C) transport activity (**Figure 4.23A**). Repeating the equivalent experiment with the opposite isomer allowed the *in situ* ***Z*-T7^{C4}** generated with 530 nm irradiation of the molecule in the lipid environment to be evaluated (**Figure 4.23B**). Irradiation of the vesicle suspension for up to 2 mins with either wavelength (980 mW 405 nm LED or 480 mW 530 nm LED) of light was found not to alter the transport activity beyond the activity established after just 30 seconds. The PSS distribution in the vesicle environment was therefore established within just 30 seconds of irradiation. This efficient generation of a PSS distribution in a lipid environment was equivalent to studies of previously reported *ortho*-tetrafluoroazobenzene switches anchored within POPC LUVs described within **Chapter 3**.[195] The *in situ* generated isomers of **T7^{C4}** were observed to have equal transport activity to the *ex situ* prepared samples, confirming that the *in situ* generated PSS distribution was equivalent to the distribution measured in DMSO solution (PSS_{405} 94:6 *E*:*Z*, PSS_{530} 8:92 *E*:*Z*, DMSO, 25 °C).

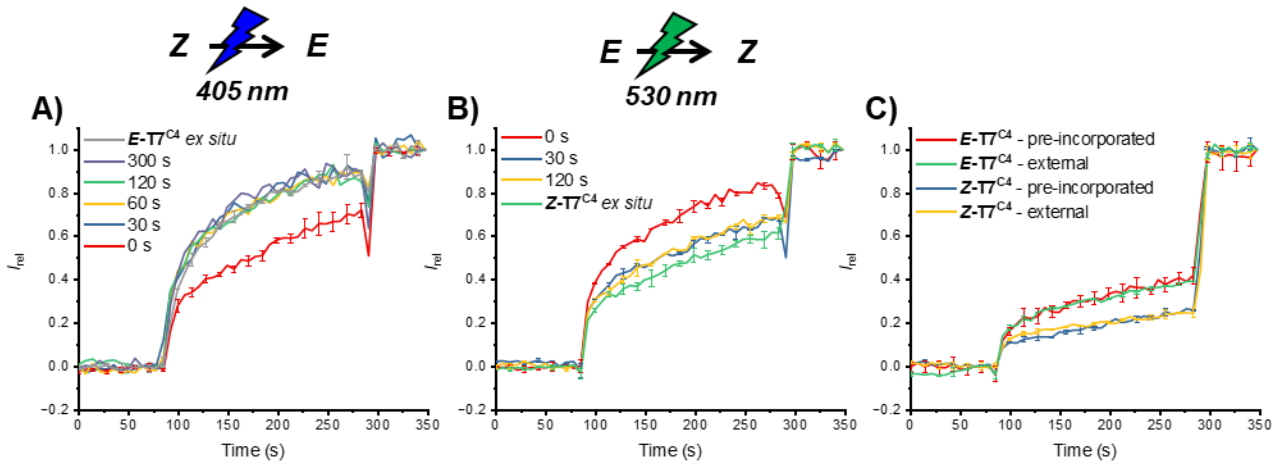

Figure 4.23 In situ irradiation of photo-switchable transporter T7^{C4} for the modulation of anion transport in POPC LUVs. *A) HPTS transport data for **Z-T7^{C4}** (2.4 mol% to lipid, PSS$_{530}$ = 8:92 E:Z) added externally in a pre-irradiated solution of DMSO to POPC LUVs and irradiated in situ with 405 nm (980 mW) for varying lengths of time prior to the start of the transport experiment compared to **E-T7^{C4}** (2.4 mol% to lipid, PSS$_{405}$ = 94:6 E:Z, pre-irradiated in a DMSO solution). B) HPTS transport data for **E-T7^{C4}** (1.92 mol% to lipid, PSS$_{405}$ = 94:6 E:Z) added externally in a pre-irradiated solution of DMSO to POPC LUVs and irradiated in situ with 530 nm (480 mW) for varying lengths of time prior to the start of the transport experiment compared to **Z-T7^{C4}** (1.92 mol% to lipid, PSS$_{530}$ = 8:92 E:Z, pre-irradiated in a DMSO solution). C) HPTS transport data for **T7^{C4}** (0.5 mol% to lipid) added externally in DMSO to POPC LUVs compared to pre-incorporated during vesicle preparation, with in situ irradiation of 530 nm (480 mW, PSS$_{530}$ = 8:92 E:Z) or 405 nm (980 mW, PSS$_{405}$ = 94:6 E:Z) for 2 mins prior to the start of the experiment. Error bars denote the standard deviations from two runs.*

To confirm that the transporters were efficiently delivered to the lipid membrane when externally added, the transport activity was compared to that of transporter pre-incorporated in POPC LUVs (**Figure 4.23C**). The irradiation of vesicles with **T7^{C4}** pre-incorporated was known to generate the same PSS distribution as in DMSO, having previously confirmed the efficient *in situ* generation of each isomer within the bilayer (**Figure 4.23A-B**). Irradiation with 405 nm or 530 nm light of the vesicles with **T7^{C4}** pre-incorporated (0.5 mol% to lipid) allowed the transport activity of each isomer to be evaluated. The pre-incorporated and externally added transport activity was found to be equivalent for each geometric isomer respectively, confirming highly efficient membrane uptake of the transporters when externally added to pre-formed vesicles. The equivalent transport activity of this relay transporter **T7^{C4}** when added externally or pre-incorporated, also implies that the ammonium anchor allows the transporters to cross the membrane, unlike the lipid anchored systems in **Chapters 2 and 3**. Presumably, the low population of the deprotonated, neutral amine form[196] allows a

distribution of transporters across both leaflets of the bilayer to be established to facilitate transport *via* a relay mechanism. The delivery of transporters to pre-formed vesicles has previously been identified as a significant challenge for the future development of synthetic ionophores,[50] with a number of different strategies having been reported to overcome this issue.[213,214] The efficient delivery of an ammonium-anchored relay transporter even when externally added to pre-formed vesicles represents a significant advancement.

4.3 Conclusions of Chapter 4

In this chapter a series of different length azobenzene-based transporters were synthesised and tested for photo-switchable transport activity. The influence of a primary amine to inhibit transporters from translocating across the hydrophobic membrane interior through protonation as a charged ammonium anchor was reported. The more compact ***Z*-T7** series of transporters were found to act as unimolecular mobile carriers for anions, increasing in activity with increasing spacer chain length. Through testing the activity of **Z-T7^{C4}** in membranes of different hydrophobic thickness, the translocation step of transport was shown to be rate-limiting. The resultant increase in lipophilicity of the mobile carriers, with increasing alkyl chain length, therefore must improve the rate of translocation of the transporter-anion complex through the membrane which is the rate-limiting step of the transport mechanism. Unusually, the extended *E*-isomers of **T7** were found to have improved transport activity relative to the compact Z-isomers, which is uncommon for mobile carriers. Interestingly, the butyl and hexyl spacers were of sufficient length to enable these extended transporters to facilitate relay transport of anions – accounting for the improved transport activity in the *E*-state in line with previously reported photo-switchable relay transporters.

The ***E*-T7** series of transporters serve as guide to measure the distance required of the transmembrane transporter-anion complex, which must span the membrane in order to facilitate relay transport. The shortest derivative with the ethylene linker ***E*-T7^{C2}** was not of sufficient length to mediate relay transport, instead following a unimolecular mobile carrier mechanism. However, for the butyl (***E*-T7^{C4}**) and hexyl (***E*-T7^{C6}**) derivatives a bimolecular dependence of the rate equation for transport activity on transporter concentration is indicative of relay transport. This series of transporters is a unique example of ionophores which are capable of switching between two separate mechanisms of transport. Through modulation of transport mechanism, the activity of these anchored transporters can be regulated with visible light. The ammonium anchor enables the external addition of water-soluble transporters to preformed vesicles to support relay transport bringing this abiotic mechanism of transport within reach of cellular systems.

Chapter 5: Experimental Procedures

5.1 Materials and Methods

All reagents and solvents were purchased from commercial sources and used without further purification. Lipids were purchased from Avanti polar lipids and used without further purification. Where necessary, solvents were dried by passing through an MBraun MPSP-800 column and degassed with nitrogen. Triethylamine was distilled from and stored over potassium hydroxide. Normal phase silica gel flash column chromatography was performed manually using Merck® silica gel 60 under a positive pressure of nitrogen or on a Buchi Pure C-815 Flash automated column chromatography system using FlashPure EcoFlex silica cartridges. Where mixtures of solvents were used, ratios are reported by volume. NMR spectra were recorded on a Bruker AVIII 400, Bruker AVII 500 (with cryoprobe) and Bruker AVIII 500 spectrometers. Chemical shifts are reported as δ values in ppm. Mass spectra were carried out on a Waters Micromass LCT and Bruker microTOF spectrometers. Fluorescence spectroscopic data were recorded using a Horiba Duetta fluorescence spectrophotometer, equipped with a Peltier temperature controller and stirrer. UV-Vis spectra were recorded on a V-770 UV-Visible/NIR Spectrophotometer equipped with a Peltier temperature controller and stirrer, using quartz cuvettes of 1 cm path length. Experiments were conducted at 25 °C unless otherwise stated.

Vesicles were prepared as described below using Avestin “LiposoFast” extruder apparatus, equipped with polycarbonate membranes with 200 nm pores. GPC purification of vesicles was carried out using GE Healthcare PD-10 desalting columns prepacked with Sephadex G 25 medium.

5.2 Anion Transport Experiments

5.2.1 Vesicle Preparation

For vesicles with pre-incorporated transporter, a thin film of lipid (2.1875 µmol, 66.5 µL of 25 mg mL^{-1}) and transporter in various ratios was formed by evaporating a chloroform solution under reduced pressure on a rotary evaporator (20 °C) and then under high vacuum for 6 h. For vesicles containing no transporter, a thin film of lipid (8.75 µmol, 266 µL of 25 mg mL^{-1}) was prepared as above.

The lipid film was hydrated by vortexing with the prepared buffer (1 mL, 100 mM NaCl, 10 mM HEPES, 1 mM 8-hydroxypyrene-1,3,6-trisulfonic acid trisodium salt (HPTS), pH 7.0). The lipid suspension was then subjected to 5 freeze-thaw cycles using liquid nitrogen and a water bath (40°C) followed by extrusion 19 times through a polycarbonate membrane (pore size 200 nm). Extrusion was performed at 50°C in the case of DPPC lipids. Extra-vesicular components were removed by size exclusion chromatography on a Sephadex G-25 column eluted with 100 mM NaCl, 10 mM HEPES, pH 7.0.

Final conditions transporter-loaded vesicles: LUVs (0.625 mM lipid, 3.5 mL vesicle suspension); inside 1 mM HPTS, 100 mM NaCl, 10 mM HEPES, pH 7.0; outside: 100 mM NaCl, 10 mM HEPES, pH 7.0.

Final conditions for free vesicles: LUVs (2.5 mM lipid, 3.5 mL vesicle suspension); inside 1 mM HPTS, 100 mM NaCl, 10 mM HEPES, pH 7.0; outside: 100 mM NaCl, 10 mM HEPES, pH 7.0.

Vesicles with other salts in the buffer were prepared following the same procedure, substituting NaCl for NaGluconate, NaBr, $NaNO_3$, NMDG-Cl or NaI in the buffer solution (NaX = 100 mM).

Vesicles prepared with various lipids were prepared following the same procedure, substituting POPC for 16:1 PC, 18:1 PC, 20:1 PC, POPG, EYPG or DPPC.

Vesicles prepared with varying concentrations of cholesterol in POPC were prepared following the same procedure, with the addition of cholesterol as a stock solution in chloroform prior to lipid film preparation.

5.2.2 Transport assays with HPTS

In a typical experiment, the LUVs containing HPTS with transporter pre-incorporated (100 µL, final lipid concentration 31.25 µM) were added to buffer (1880 µL of 100 mM NaCl, 10 mM HEPES, pH 7.0) at 25°C under gentle stirring. For LUVs loaded with HPTS but not containing pre-incorporated transporter (25 µL, final lipid concentration 31.25 µM) was added to buffer (1950 µL of 100 mM NaCl, 10 mM HEPES, pH 7.0)

For LUVs containing pre-incorporated transporter, a pulse of NaOH (20 µL of 0.5 M solution, final concentration 5 mM) was added at 90 s to initiate the experiment. For LUVs not loaded with transporter, a pulse of NaOH (20 µL of 0.5 M solution, final concentration 5 mM) was added at 40 s to initiate the experiment. The test transporter (various concentrations, in 5 µL DMSO) was then added at 90 s.

After 290 s, detergent (25 µL of 11% Triton X-100 in 7:1 (v/v) H_2O-DMSO) was added to lyse the vesicles and calibrate the assay. The fluorescence emission was monitored at λ_{em} = 510 nm (λ_{ex} = 405/460 nm). After conversion to the time dependent fluorescence intensity ratio R_t using **Equation 1**, the data was normalised based on **Equation 2** to give the fractional fluorescence intensity (I_{rel}). R_0 is the fluorescence ratio at 65 s after the base pulse but before the addition of the transporter and R_d is the fluorescence ratio at time 350 s, after the addition

of detergent. For each compound, each individual concentration was repeated at least twice and averaged; error bars represent standard deviations.

$$R_t = \frac{\lambda_{ex}460}{\lambda_{ex}405} \quad \textbf{(Equation 1)}$$

$$I_{rel} = \frac{R_t - R_0}{R_d - R_0} \quad \textbf{(Equation 2)}$$

The fractional fluorescence intensity (I_{rel}) at 276 s just prior to lysis, defined as the fractional activity, y, was plotted as a function of the transporter concentration (x / μM). Hill coefficients (n) and EC_{50} values were calculated by fitting to the Hill equation (Equation 3). Where y_0 is the fractional activity in the absence of transporter, y_{max} is the fractional activity with excess transporter and x is the transporter concentration in the cuvette.

$$y = y_0 + (y_{max} - y_0)\frac{x^n}{EC_{50} + x^n} \qquad \textbf{(Equation 3)}$$

Fitting the transport kinetics curves (I_{rel} vs t) to the first order exponential function (**Equation 5**) allowed the initial rate of transport, k_{ini}, to be determined using **Equation 6**.

$$I_{rel} = a - e^{-\frac{kt}{b}} \qquad \textbf{(Equation 5)}$$

$$k_{ini} = \frac{1}{b} \qquad \textbf{(Equation 6)}$$

The observed initial rate of anion transport, k_{ini}, plotted against concentration of transporter allowed the order of dependence of k_{ini} on transporter concentration to be determined.

Experiments with DPPC lipids were conducted in the same way. For elevated temperature studies, the buffer was equilibrated at 45°C for 5 minutes prior to initiating the experiment.

Experiments in the presence of protonophore trifluoromethoxy carbonylcyanide phenylhydrazone (FCCP) were carried out using the above procedure, except that a DMSO

solution of FCCP (5 µL of 100 µM solution, final concentration 0.25 µM/0.8 mol%) was added to the vesicle suspension prior to the addition of the NaOH pulse. At this concentration, FCCP does not cause appreciable dissipation of the transmembrane pH gradient alone.

For experiments involving *in situ* irradiation, the cuvettes were prepared and then irradiated with the corresponding wavelength of light for a designated length of time just prior to starting the transport experiment.

5.3 Photo-switching Experiments

Photo-irradiation of liquid samples was carried out using Thorlabs high-power LEDs (models M530L4 (green, 530 nm, 480 mW), M455L3 (royal blue, 455 nm, 1020 mW), M405L3 (violet, 405 nm, 980 mW), M365L2 (UV, 530 nm, 360 mW)) mounted on a Thorlabs cuvette holder (CVH100/M). A 1A current was supplied to the LED, controlled by a Thorlabs T-Cube LED Driver (LEDD1B). Samples were irradiated for sufficient time to reach the photo-stationary state, as confirmed by ^{1}H NMR or UV-vis experiments.

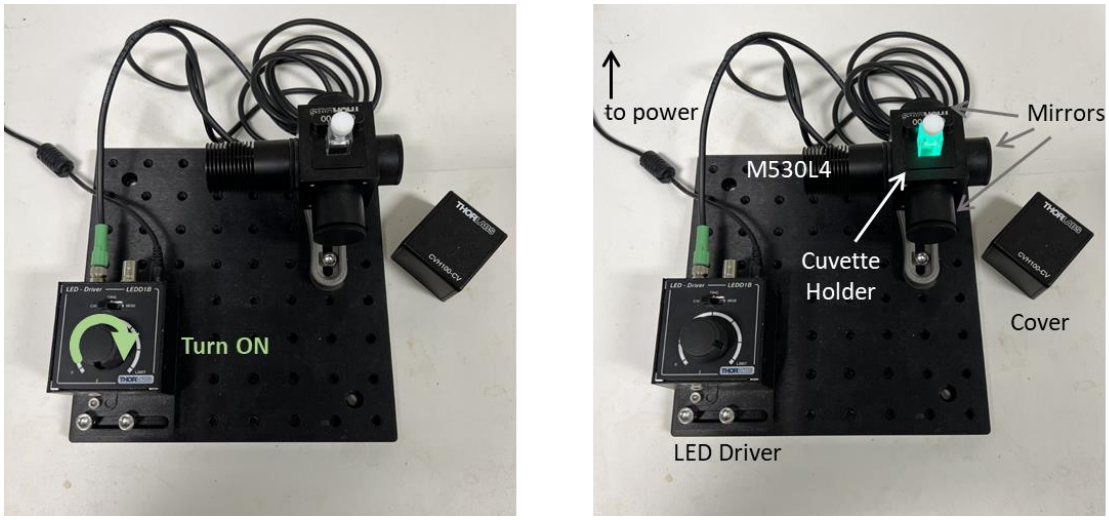

Figure 5.1 Photo-irradiation apparatus. *Used for photo-irradiating cuvettes and liquid samples in small vials.*

For UV-vis experiments, extinction coefficients were determined by recording a spectrum at four different concentrations of the *E*-isomer. The absorbance at the maximum of the π - π* transition of the *E*-isomer was plotted against concentration (Beer-Lambert plot) to determine the molar extinction coefficient ε. The most concentrated *E*-isomer sample was then irradiated with the appropriate wavelength of light to generate the *Z*-rich photo-stationary state, and another spectrum was run. This spectrum was normalised to units of ε and overlaid with the *E*-rich PSS spectrum.

5.4.1 Chapter 2 Synthetic Procedures

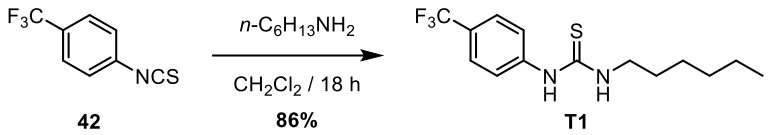

42 T1

T1. Prepared according to the literature procedure.[134] Data consistent with that given in the literature.

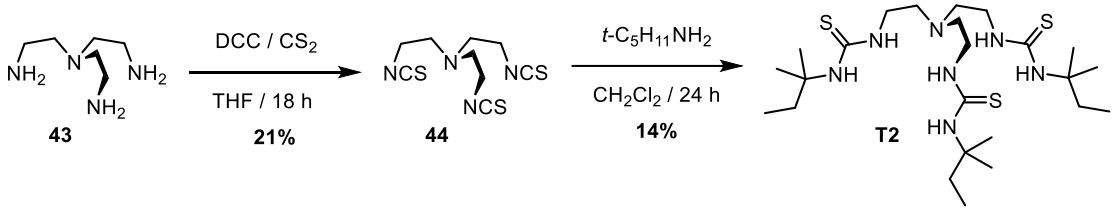

43 44 T2

T2. Prepared according to the literature procedure.[130] Data consistent with that given in the literature.

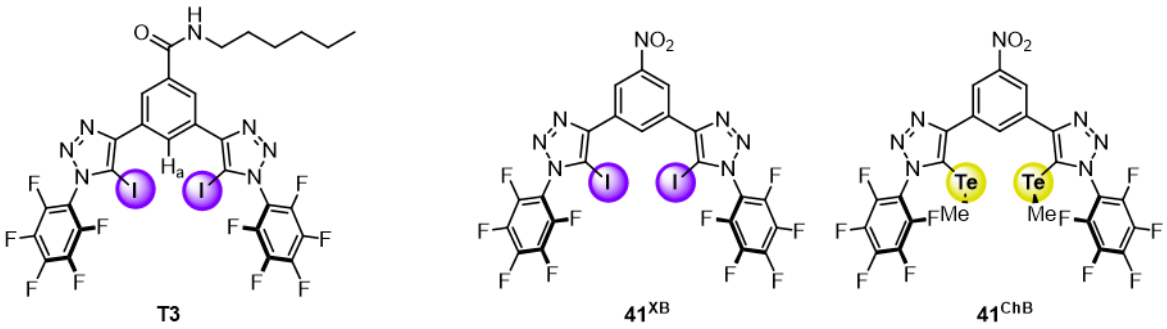

T3 41^{XB} 41^{ChB}

T3, 41^{XB} and **41^{ChB}**. Prepared by Dr Andrew Docker according to the published procedures.[34,215]

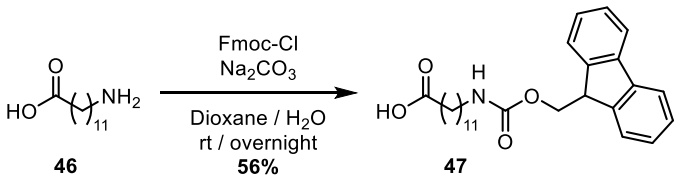

46 47

47. Prepared according to the literature procedure.[216] Data consistent with that given in the literature.

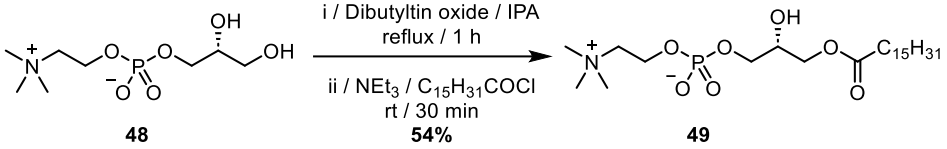

49. Prepared according to the literature procedure.[217] Data consistent with that given in the literature.

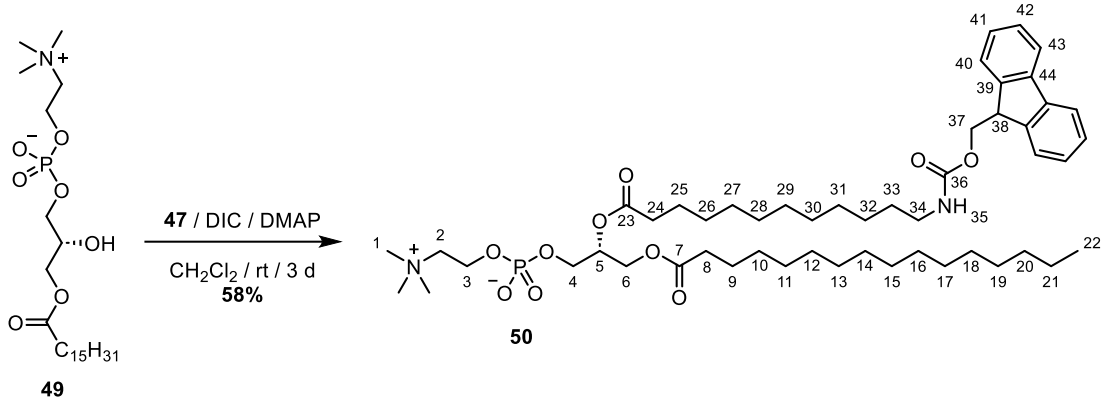

50. This known compound[218] was prepared *via* a novel procedure: 12-(Fmoc-amino)dodecanoic acid **47** (2.2 g, 4.9 mmol, 5 Equiv.), DIC (1.2 mL, 7.9 mmol, 8 Equiv.) and DMAP (180 mg, 1.5 mmol, 1.5 Equiv.) were added to a solution of 16:0 lyso PC **49** (490 mg, 1.0 mmol, 1 Equiv.) in anhydrous CH_2Cl_2 (72 mL) under N_2. After stirring the reaction mixture for 3 days, DOWEX 50 WX2-400 was added to remove DMAP. The solution was allowed to stir for 45 minutes. The reaction mixture was filtered, washed with $CHCl_3$:MeOH (1:1, 100 mL) and concentrated. The crude material was purified by silica gel flash chromatography (0 - 2% H_2O / 25% MeOH / $CHCl_3$) to afford the title compound as a white solid (524 mg, 0.57 mmol, 58%). The characterisation matches that reported in the literature.[218]

^{1}H NMR (400 MHz, $CDCl_3$:CD_3OD (2:1)) δ 7.74 (d, *J* = 7.5 Hz, 2H, H_{43}), 7.59 (d, *J* = 7.4 Hz, 2H, H_{40}), 7.37 (t, *J* = 7.4 Hz, 2H, H_{42}), 7.29 (td, *J* = 7.4, 1.0 Hz, 2H, H_{41}), 5.84 (t, *J* = 5.4 Hz, 1H, H_{35}), 5.23 – 5.18 (m, 1H, H_5), 4.42 – 4.33 (m, 3H, $H_{6\ \&\ 37}$), 4.28 – 4.15 (m, 3H, $H_{3\ \&\ 38}$), 4.14 (dd, *J* =

12.1, 7.2 Hz, 1H, H_6), 3.96 (t, *J* = 6.0 Hz, 2H, H_4), 3.64 – 3.54 (m, 2H, H_2), 3.18 (s, 9H, H_1), 3.10 (t, *J* = 6.5 Hz, 2H, H_{34}), 2.33 – 2.26 (m, 4H, $H_{8\ \&\ 24}$), 1.65 – 1.51 (m, 4H, $H_{9\ \&\ 25}$), 1.50 – 1.42 (m, 2H, H_{33}), 1.34 – 1.18 (m, 38H, $H_{10\text{-}21\ \&\ 26\text{-}32}$), 0.85 (t, *J* = 6.8 Hz, 3H, H_{22}).

LRMS-ESI (m/z) Calculated for $C_{51}H_{84}O_{10}N_2P$ $[M+H]^+$, 915.59; found 915.483.

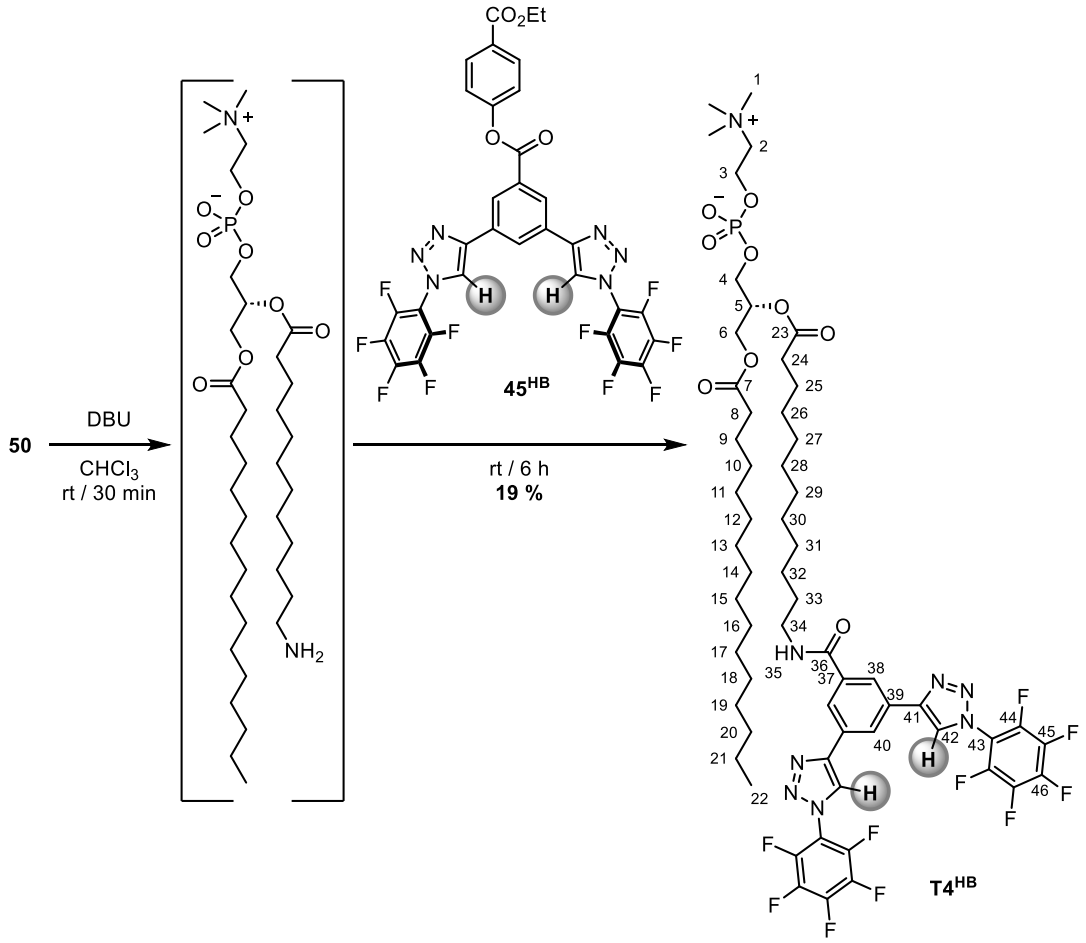

T4^{HB}. DBU (10 µL, 0.07 mmol, 2 Equiv.) was added to a stirred solution of Fmoc-protected lipid **50** (30 mg, 0.03 mmol, 1 Equiv.) in anhydrous $CHCl_3$ (0.25 mL) under N_2. After stirring the reaction mixture overnight, **45^{HB}** (50 mg, 0.07 mmol, 2 Equiv.) was added and left to stir for 6 h. The reaction mixture was concentrated and loaded onto a short plug of DOWEX (2 g) and washed with $CHCl_3$:MeOH (1:1, 50 mL) and then flushed off with $CHCl_3$:MeOH:H_2O (65:25:4,

50 mL). This crude product was then purified by prep TLC (1% H_2O / 25% MeOH / $CHCl_3$) to afford the title compound as a white solid (8 mg, 6 µmol, 19%).

^{1}H NMR (500 MHz, $CDCl_3$:CD_3OD (2:1)) δ 8.44 (s, 2H, H_{42}), 8.43 (s, 1H, H_{40}), 8.18 (s, 2H, H_{38}), 7.91 (t, *J* = 5.1 Hz, 1H, H_{35}), 5.04 – 4.95 (m, 1H, H_5), 4.06 – 4.00 (m, 2H, H_3), 3.93 (dd, *J* = 11.9, 6.9 Hz, 1H, H_6), 3.80 – 3.74 (m, 2H, H_4), 3.41 – 3.36 (m, 2H, H_2), 3.28 – 3.22 (m, 2H, H_{34}), 3.00 (s, 9H, H_1), 2.13 – 2.05 (m, 4H, $H_{8\ \&\ 24}$), 1.50 – 1.43 (m, 2H, H_{33}), 1.42 – 1.34 (m, 4H, $H_{9\ \&\ 25}$), 1.24 – 1.17 (m, 2H, H_{32}), 1.13 – 1.01 (m, 36H, $H_{10\text{-}21\ \&\ 26\text{-}31}$), 0.65 (t, *J* = 6.8 Hz, 3H, H_{22}). One proton environment for H_6 is obscured by the H_2O peak.

^{13}C NMR (126 MHz, $CDCl_3$:CD_3OD (2:1)) δ 173.8, 173.4, 167.1, 146.9, 143.5 – 141.2 (dm, $J_{C\text{-}F}$ = 258 Hz), 139.1 – 136.9 (dm, $J_{C\text{-}F}$ = 257 Hz), 136.1, 130.4, 125.6, 124.7, 123.6, 112.7 – 112.6 (m), 70.2 (d, $J_{C\text{-}P}$ = 7.4 Hz) (C_5), 66.3 (C_2), 63.4 (d, $J_{C\text{-}P}$ = 4.5 Hz) (C_4), 62.4 (C_6), 58.8 (d, $J_{C\text{-}P}$ = 4.3 Hz) (C_3), 53.9 (t, $J_{C\text{-}N}$ = 3.6 Hz) (C_1), 40.1 (C_{34}), 33.9, 33.8, 31.6, 29.4, 29.4, 29.4, 29.4, 29.4, 29.4, 29.3, 29.3, 29.2, 29.2, 29.2, 29.1, 29.1, 29.0, 29.0, 28.9, 28.8, 26.8, 24.6, 24.6, 22.4, 13.6 (C_{22}).

^{19}F NMR (470 MHz, $CDCl_3$:CD_3OD (2:1)) δ -146.29 – -146.43 (m, 2F, F_{44}), -150.49 (t, *J* = 21.2 Hz, 1F, F_{46}), -160.20 – -160.35 (m, 2F, F_{45}).

HRMS-ESI (m/z) Calculated for $C_{59}H_{88}F_{10}O_9N_8P$ $[M+H]^+$, 1263.5464; found 1263.5490.

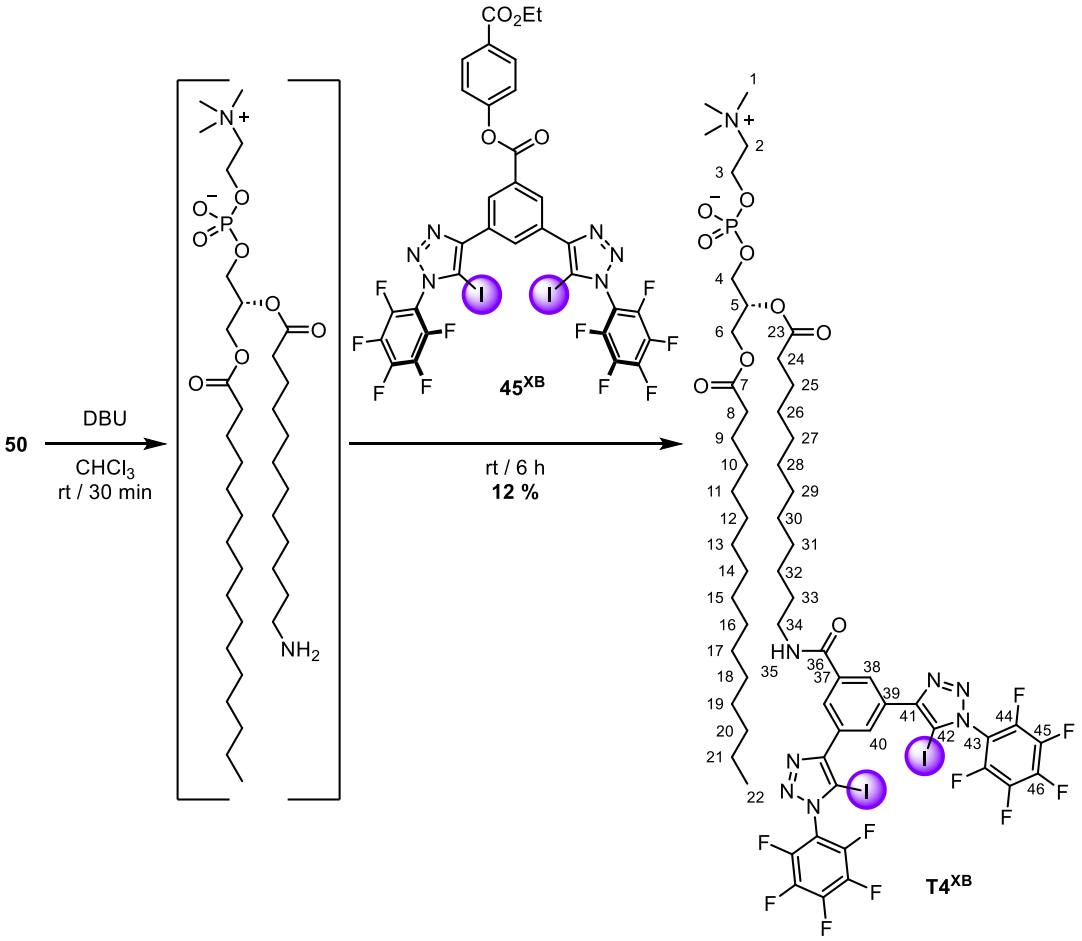

T4^{XB}. DBU (10 µL, 0.07 mmol, 2 Equiv.) was added to a stirred solution of Fmoc-protected lipid **50** (30 mg, 0.03 mmol, 1 Equiv.) in anhydrous $CHCl_3$ (0.25 mL) under N_2. After stirring the reaction mixture overnight, **45^{XB}** (65 mg, 0.07 mmol, 2 Equiv.) was added and left to stir for 6 h. The reaction mixture was concentrated and loaded onto a short plug of DOWEX (2 g) and washed with $CHCl_3$:MeOH (1:1, 50 mL) and then flushed off with $CHCl_3$:MeOH:H_2O (65:25:4, 50 mL). This crude product was then purified by prep TLC (1% H_2O / 25% MeOH / $CHCl_3$) to afford the title compound as a white solid (6 mg, 4 µmol, 12%).

^{1}H NMR (600 MHz, $CDCl_3$:CD_3OD (2:1)) δ 8.64 (t, *J* = 1.4 Hz, 1H, H_{40}), 8.36 (d, *J* = 1.5 Hz, 2H, H_{38}), 5.05 – 4.97 (m, 1H, H_5), 4.05 – 3.99 (m, 2H, H_3), 3.93 (dd, *J* = 12.0, 6.9 Hz, 1H, H_6), 3.79 – 3.76 (m, 2H, H_4), 3.40 – 3.37 (m, 2H, H_2), 3.27 – 3.23 (m, 2H, H_{34}), 3.00 (s, 9H, H_1), 2.13 – 2.06 (m, 4H, $H_{8\ \&\ 24}$), 1.49 – 1.43 (m, 2H, H_{33}), 1.41 – 1.34 (m, 4H, $H_{9\ \&\ 25}$), 1.23 – 1.18 (m, 2H, H_{32}),

1.12 – 1.01 (m, 36H, $H_{10\text{-}21\ \&\ 26\text{-}31}$), 0.65 (t, *J* = 6.9 Hz, 3H, H_{22}). One proton environment for H_6 is obscured by the H_2O peak.

^{13}C NMR (151 MHz, $CDCl_3$:CD_3OD (2:1)) δ 173.8, 173.4, 167.2, 149.4, 144.7 – 142.3 (dm, $J_{C\text{-}F}$ = 263 Hz), 138.9 – 136.7 (dm, $J_{C\text{-}F}$ = 248 Hz), 136.0, 130.2, 128.1, 126.5, 112.3 – 111.9 (m), 83.2, 70.2 (d, $J_{C\text{-}P}$ = 7.8 Hz) (C_5), 66.3 (C_2), 63.4 (d, $J_{C\text{-}P}$ = 5.0 Hz) (C_4), 62.4 (C_6), 58.8 (d, $J_{C\text{-}P}$ = 4.9 Hz) (C_3), 53.9 (t, $J_{C\text{-}N}$ = 3.7 Hz) (C_1), 40.1, 34.0, 33.8, 31.7, 29.4, 29.4, 29.4, 29.4, 29.4, 29.4, 29.3, 29.3, 29.2, 29.2, 29.2, 29.1, 29.1, 29.0, 29.0, 28.9, 28.8, 26.8, 24.6, 24.6, 22.4, 13.6 (C_{22}).

^{19}F NMR (470 MHz, $CDCl_3$:CD_3OD (2:1)) δ -143.20 – -143.38 (m, 2F, F_{44}), -147.88 (t, *J* = 21.3 Hz, 1F, F_{46}), -159.77 – -159.93 (m, 2F, F_{45}).

HRMS-ESI (m/z) Calculated for $C_{59}H_{76}F_{10}O_9N_8I_2P$ $[M\text{-}H]^-$, 1515.3397; found 1515.3371.

5.4.2 Chapter 2 ^{1}H NMR Titration Experiments

Binding constants were determined through analysis of ^{1}H NMR chemical shift perturbations upon the addition of an analyte, measured with a Bruker AVIII 500 spectrometer (500 MHz, 298 K). The host was dissolved in deuterated solvent (1 mM concentration, 0.5 mL) and added to an NMR tube. Known volumes of guest ([TBACl] = 50 mM) in the same deuterated solvent were added, and the spectra were recorded after each addition. The chemical shifts of the host spectra were referenced to the residual solvent peak and monitored as a function of [G]. The chemical shift perturbations were analysed using a global fit procedure in the Dynafit software program,[219] using non-linear least squares analysis to obtain the best fit between observed and calculated chemical shifts. In all experiments the association of guest and host was fast on the ^{1}H NMR timescale.

Chloride binding to **T3** was determined by ^{1}H NMR titration analysis in acetone-d_6:D_2O, (v/v 97.5/2.5) performed by Dr Andrew Docker as described above, fitting excellently to a 1:1 binding model with a high association constant (K_a(Cl^-): 4660 (72) M^{-1}):

$$\mathbf{T3} + Cl^- \overset{K_a(Cl^-)}{\longleftrightarrow} \mathbf{T3} \cdot Cl^-$$

Binding of a second equivalent of chloride, to form a 1:2 host:guest complex was not observed, inferred from the failure of the data to fit to a 1:2 binding model, presumably due to inter-anion repulsion in the 1:2 complex, leading to negligible association of the second anion.

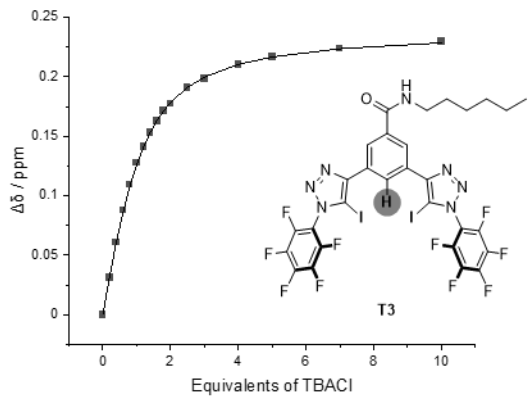

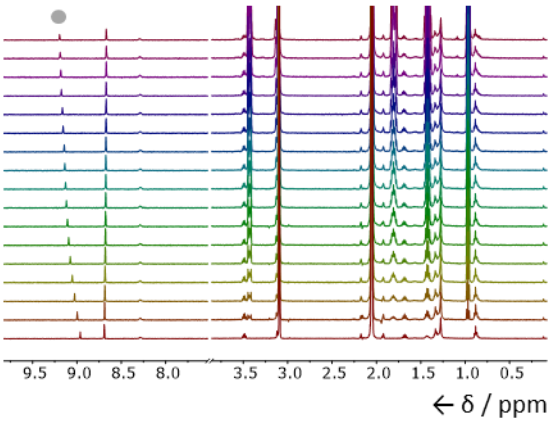

5.4.2 Chapter 2 UV-vis Characterisation

UV-vis spectrum of **T4^{XB}** was measured in DMSO solution at 15 µM.

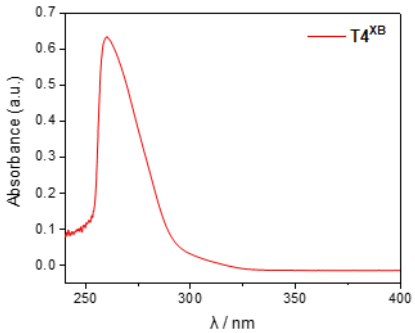

5.5.1 Chapter 3 Synthetic Procedures

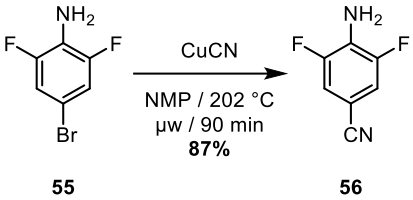

55 **56**

56. Prepared according to the literature procedure.[220] Data consistent with that given in the literature.

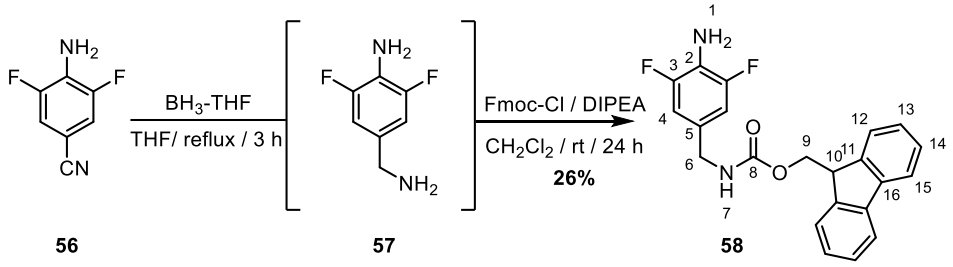

56 **57** **58**

58. To a solution of 4-amino-3,5-difluorobenzonitrile **56** (1.45 g, 9.41 mmol, 1 equiv.) in anhydrous degassed THF (20 mL) at 0°C was added dropwise 1M BH_3-THF solution (38.4 mL, 38.4 mmol, 4 equiv.). The reaction was stirred at reflux for 3 hours. MeOH (5mL) was added dropwise at this temperature until effervescence stopped, and the resulting mixture was refluxed for 30 min. The solvent was removed *in vacuo*, redissolved in EtOAc (100 mL) and washed with water (3 × 50 mL). The off-white solid was redissolved in anhydrous CH_2Cl_2 (30 mL) and DIPEA (1.6 mL, 9.41 mmol, 1 equiv.) was added. Fmoc-Cl (2.43 g, 9.41 mmol, 1 equiv.) in anhydrous CH_2Cl_2 (5 mL) was added dropwise and the reaction was stirred overnight at rt under N_2. The solution was concentrated *in vacuo* and the residue was purified by column chromatography (Buchi Pure C-815 Flash, 24 g SiO_2, hexane:acetone 0 – 20%) to give the title compound as a white solid (0.93 g, 2.4 mmol, 26%).

^{1}H NMR (400 MHz, $CDCl_3$) δ 7.76 (d, *J* = 7.6 Hz, 2H, H_{15}), 7.59 (d, *J* = 7.5 Hz, 2H, H_{12}), 7.40 (t, *J* = 7.5 Hz, 2H, H_{13}), 7.31 (t, *J* = 7.5 Hz, 2H, H_{14}), 6.75 (d, *J* = 7.4 Hz, 2H, H_4), 5.02 (s, 1H, H_7), 4.47 (d, *J* = 6.8 Hz, 2H, H_9), 4.30 – 4.01 (m, 3H, H_6 & H_{10}), 3.70 (s, 2H, H_1).

^{13}C NMR (126 MHz, $CDCl_3$) δ 156.5 (C_8), 152.1 (dd, $J_{C\text{-}F}$ = 241.2, 8.2 Hz) (C_3), 144.0, 141.5, 127.9 (C_{13}), 127.8 (C_5), 127.2 (C_{14}), 125.1 (C_{12}), 123.2 (t, $J_{C\text{-}F}$ = 16.2 Hz) (C_2), 120.1 (C_{15}), 110.3 (dd, $J_{C\text{-}F}$ = 15.7, 6.7 Hz) (C_4), 66.9 (C_9), 47.4, 44.3.

^{19}F NMR (377 MHz, $CDCl_3$) δ -131.69 (d, *J* = 7.4 Hz) (F_3).

HRMS-ESI (m/z) Calculated for $C_{22}H_{18}F_2N_2O_2$ $[M+H]^+$, 381.1409; found 381.1408.

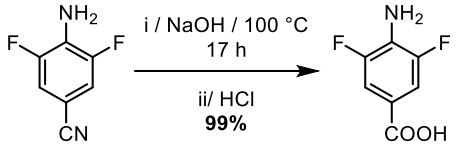

56 **59**

59. Prepared according to the literature procedure.[221] Data consistent with that given in the literature.

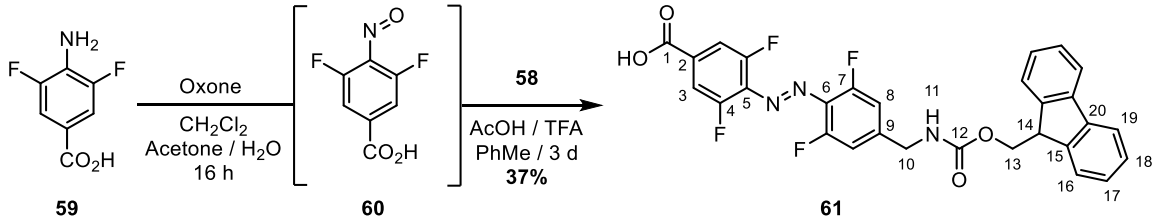

59 **60** **61**

61. 4-Amino-3,5-difluorobenzoic acid **59** (510 mg, 3.0 mmol, 1.7 equiv.) was dissolved in CH_2Cl_2:acetone ((5:1), 12 mL). Oxone (3 g, 9.8 mmol, 5.5 eq) in water (6 mL) was added and the biphasic solution was stirred overnight, after which the organic layer turned green. The reaction mixture was diluted with water (50 mL) and extracted with EtOAc (3 × 50 mL), the organic layers were combined and concentrated. The residue was redissolved in

AcOH:toluene:TFA ((6:6:1), 18 mL) and 9-fluorenylmethyl (4-amino-3,5-difluorobenzyl)carbamate **58** (675 mg, 1.8 mmol, 1 equiv.) was added to the stirred reaction mixture which was left stirring at rt under N_2 for 3 days. The mixture was concentrated and the residue was purified by silica gel flash chromatography (1 – 8% MeOH / CH_2Cl_2) to give the title compound as an orange solid (358 mg, 0.65 mmol, 37%).

^{1}H NMR (600 MHz, acetone-d_6) δ 7.86 (d, *J* = 7.5 Hz, 2H, H_{19}), 7.80 (d, *J* = 9.4 Hz, 2H, H_3), 7.71 (d, *J* = 7.4 Hz, 2H, H_{16}), 7.41 (t, *J* = 7.4 Hz, 2H, H_{18}), 7.33 (t, *J* = 7.4 Hz, 2H, H_{17}), 7.21 (d, *J* = 10.8 Hz, 2H, H_8), 4.49 – 4.45 (m, 4H, $H_{10\ \&\ 13}$), 4.27 (t, *J* = 6.7 Hz, 1H, H_{14}).

^{13}C NMR (151 MHz, acetone-d_6) δ 165.0 (C_{12}), 157.5 (d, $J_{C\text{-}F}$ = 7.8 Hz) (C_1), 156.9 (dd, $J_{C\text{-}F}$ = 135.0, 4.0 Hz), 155.2 (dd, $J_{C\text{-}F}$ = 132.6, 4.1 Hz), 148.5 (t, $J_{C\text{-}F}$ = 9.1 Hz) (C_2), 145.2, 142.2, 135.1 (t, $J_{C\text{-}F}$ = 10.8 Hz), 134.7 (t, $J_{C\text{-}F}$ = 8.6 Hz), 130.7 (t, $J_{C\text{-}F}$ = 9.9 Hz) (C_9), 128.6 (C_{18}), 127.9 (C_{17}), 126.0 (C_{16}), 120.8 (C_{19}), 114.8 (dd, $J_{C\text{-}F}$ = 21.4, 3.9 Hz) (C_3), 112.2 (dd, $J_{C\text{-}F}$ = 21.4, 1.8 Hz) (C_8), 67.0 (C_{14}), 48.2 (C_{13}), 44.5 (d, $J_{C\text{-}F}$ = 18.0 Hz) (C_{10}).

^{19}F NMR (377 MHz, acetone-d_6) δ -120.76 ($F_{4\ or\ 7}$), -122.02 ($F_{4\ or\ 7}$).

HRMS-ESI (m/z) Calculated for $C_{29}H_{20}N_3O_4F_4$ $[M+H]^+$, 550.1384; found 550.1381.

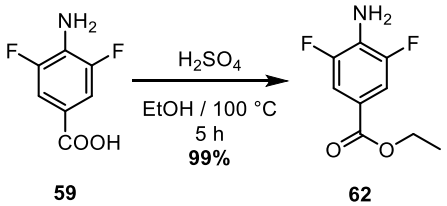

59 **62**

62. Prepared according to the literature procedure.[221] Data consistent with that given in the literature.

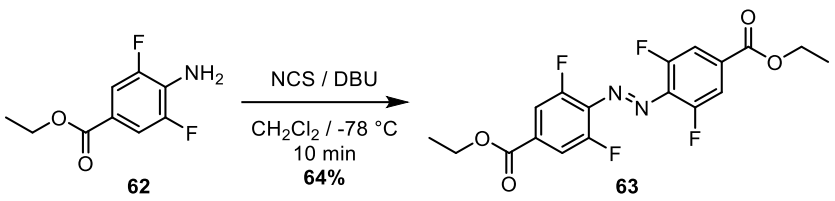

62 63

63. Prepared according to the literature procedure.[222] Data consistent with that given in the literature.

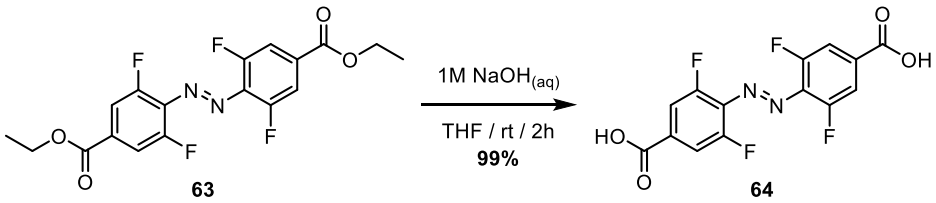

63 64

64. Prepared according to the literature procedure.[219] Data consistent with that given in the literature.

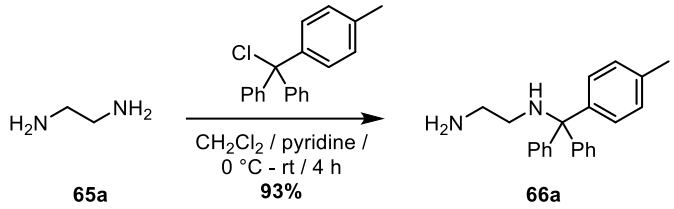

65a 66a

66a. Prepared according to the literature procedure.[221] Data consistent with that given in the literature.

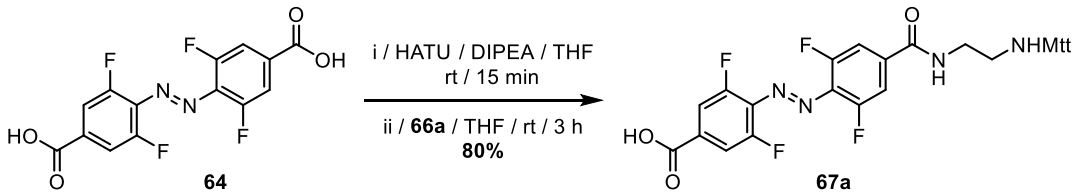

64 67a

67a. Prepared according to the literature procedure.[221] Data consistent with that given in the literature.

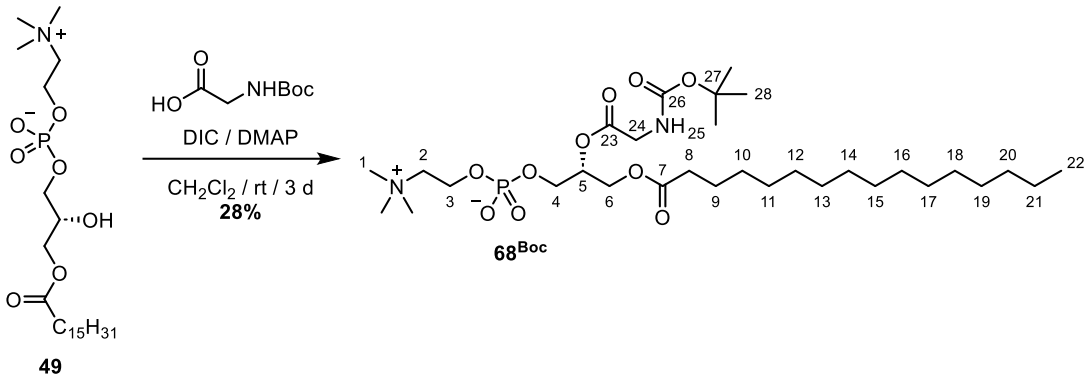

68^{Boc}. This known compound[219] was prepared *via* a novel procedure: Boc-glycine (1.24 g, 7.1 mmol, 5 Equiv.), DIC (1.8 mL, 11.5 mmol, 8 Equiv.) and DMAP (250 mg, 2.1 mmol, 1.5 Equiv.) were added to a solution of 16:0 lyso PC **49** (700 mg, 1.4 mmol, 1 Equiv.) in anhydrous CH_2Cl_2 (100 mL) under N_2. After stirring the reaction mixture for 3 days, DOWEX 50 WX2-400 ion exchange resin was added to remove DMAP. The solution was allowed to stir for 45 min. The reaction mixture was filtered, washed with $CHCl_3$:MeOH (1:1, 100 mL) and concentrated. The crude material was purified by silica gel flash chromatography (0 - 4% H_2O / 25% MeOH / $CHCl_3$) to give the title compound as a white solid (260 mg, 0.40 mmol, 28%). The characterisation matches that reported in the literature.[219]

^{1}H NMR (400 MHz, $CDCl_3$:CD_3OD (2:1)) δ 5.30 – 5.17 (m, 1H, H_5), 4.37 – 4.31 (m, 1H, H_6), 4.26 – 4.19 (m, 2H, H_3), 4.15 (dd, *J* = 12.1, 6.6 Hz, 1H, H_6), 4.07 – 3.92 (m, 2H, H_4), 3.84 (s, 2H, H_{24}), 3.62 – 3.55 (m, 2H, H_2), 3.19 (s, 9H, H_1), 2.29 (t, *J* = 7.6 Hz, 2H, H_8), 1.60 – 1.52 (m, 2H, H_9), 1.42 (s, 9H, H_{28}), 1.29 – 1.19 (m, 24H, H_{10-21}), 0.84 (t, *J* = 6.8 Hz, 3H, H_{22}).

^{13}C NMR (101 MHz, $CDCl_3$:CD_3OD (2:1)) δ 174.4, 170.7, 157.1, 80.2, 72.1 (d, J_{C-P} = 7.2 Hz), 66.9 – 66.7 (m), 64.1 (d, J_{C-P} = 5.2 Hz), 62.7, 59.5 (d, J_{C-P} = 5.0 Hz), 54.5 (t, J_{C-N} = 3.5 Hz), 42.5, 34.3, 32.3, 30.0, 30.0, 30.0, 30.0, 30.0, 29.8, 29.8, 29.7, 29.6, 29.5, 28.5, 25.2, 23.0, 14.3.

LRMS-ESI (m/z) Calculated for $C_{31}H_{62}N_2O_{10}P$ $[M+H]^+$, 653.41; found 653.34.

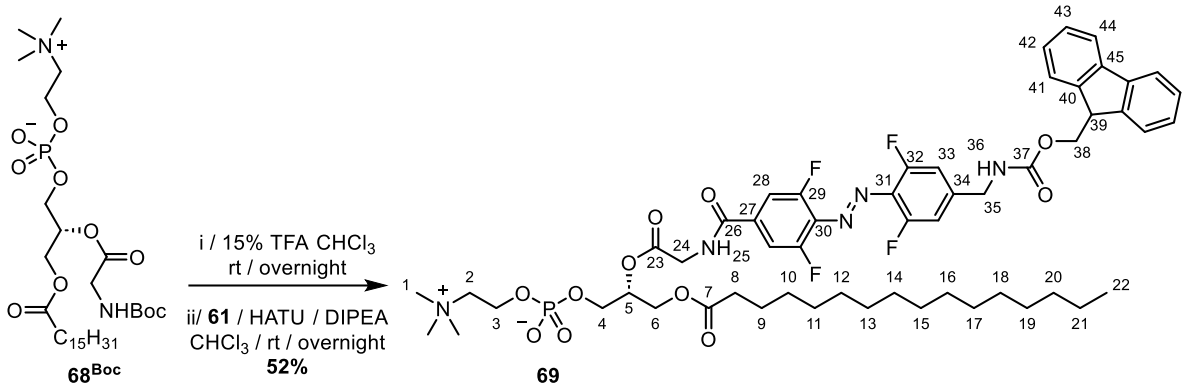

69. TFA (450 µL) was added to a stirred solution of (*R*)-1-palmitoyl-2-(*N*-boc-glycyl)-*sn*-glycero-3-phosphocholine **68^{Boc}** (100 mg, 0.15 mmol, 1 Equiv.) in anhydrous $CHCl_3$ (3 mL) under N_2 at rt. ^{1}H NMR confirmed complete deprotection after leaving the reaction overnight. The reaction mixture was concentrated and redissolved in anhydrous $CHCl_3$ (1 mL) and DIPEA (25 uL, 0.2 mmol, 1.3 Equiv.). Azobenzene **61** (126 mg, 0.23 mmol, 1.5 Equiv.), HATU (117 mg, 0.31 mmol, 2 Equiv.) and DIPEA (50 uL, 0.4 mmol, 2.6 Equiv.) were dissolved in anhydrous $CHCl_3$ (2 mL) and left to stir under N_2 for 10 min before being added to the lipid solution. The reaction mixture was then left to stir overnight. A drop of H_2O was added to the reaction mixture to quench the reaction and then the solvent was removed *in vacuo.* This crude material was purified by silica gel flash chromatography (0 - 2% H_2O / 25% MeOH / $CHCl_3$) to give the title compound as a red solid (87 mg, 0.8 mmol, 52%).

^{1}H NMR (500 MHz, $CDCl_3$:CD_3OD (2:1)) δ 7.74 (d, *J* = 7.3 Hz, 2H, H_{44}), 7.70 – 7.55 (m, 4H, $H_{41\ \&\ 28}$), 7.37 (t, *J* = 7.3 Hz, 2H, H_{43}), 7.29 (t, *J* = 7.2 Hz, 2H, H_{42}), 6.98 (d, *J* = 10.3 Hz, 2H, H_{33}), 5.30 – 5.24 (m, 1H, H_5), 4.45 (d, *J* = 6.6 Hz, 2H, H_{38}), 4.42 – 4.33 (m, 2H, H_6), 4.31 (s, 2H, H_{35}), 4.23 (s, 2H, H_3), 4.22 – 4.15 (m, 3H, $H_{24\ \&\ 39}$), 4.13 – 3.97 (m, 2H, H_4), 3.59 (s, 2H, H_2), 3.19 (s, 9H, H_1), 2.28 (q, *J* = 9.2 Hz, 2H, H_8), 1.61 – 1.51 (m, 2H, H_9), 1.34 – 1.17 (m, 24H, $H_{10\ -\ 21}$), 0.84 (t, *J* = 6.9 Hz, 3H, H_{22}).

^{13}C {^{19}F} NMR (126 MHz, $CDCl_3$:CD_3OD (2:1)) δ 174.5 (C_7), 169.8 (C_{23}), 165.8 (C_{26}), 157.9 (C_{37}), 156.3, 155.5, 146.5 (C_{34}), 144.2, 141.8, 136.8 (C_{27}), 134.0, 130.6, 128.2 (C_{43}), 127.5 (C_{42}), 125.4 (C_{41}), 120.3 (C_{44}), 112.4 (C_{28}), 111.5 (C_{33}), 72.4 (d, $J_{C\text{-}P}$ = 6.4 Hz) (C_5), 67.1 (C_{38}), 66.9 – 66.8 (m) (C_2), 64.2 (d, $J_{C\text{-}P}$ = 4.6 Hz) (C_4), 62.6 (d, $J_{C\text{-}P}$ = 5.8 Hz) (C_6), 59.6 (d, $J_{C\text{-}P}$ = 4.6 Hz) (C_3), 54.6 – 54.2 (m) (C_1), 47.7 (C_{39}), 44.2 (C_{35}), 42.1 (C_{24}), 34.3 (C_8), 32.3, 30.1, 30.0, 30.0, 30.0, 30.0, 29.7, 29.7, 29.7, 29.7, 29.5, 25.2, 23.0, 14.3.

^{19}F NMR (471 MHz, $CDCl_3$:CD_3OD (2:1)) δ -116.05 ($F_{29\text{ or }32}$), -116.73 ($F_{29\text{ or }32}$).

HRMS-ESI (m/z) Calculated for $C_{55}H_{71}N_5O_{11}F_4$ $[M+H]^+$, 1084.4818; found 1084.4816.

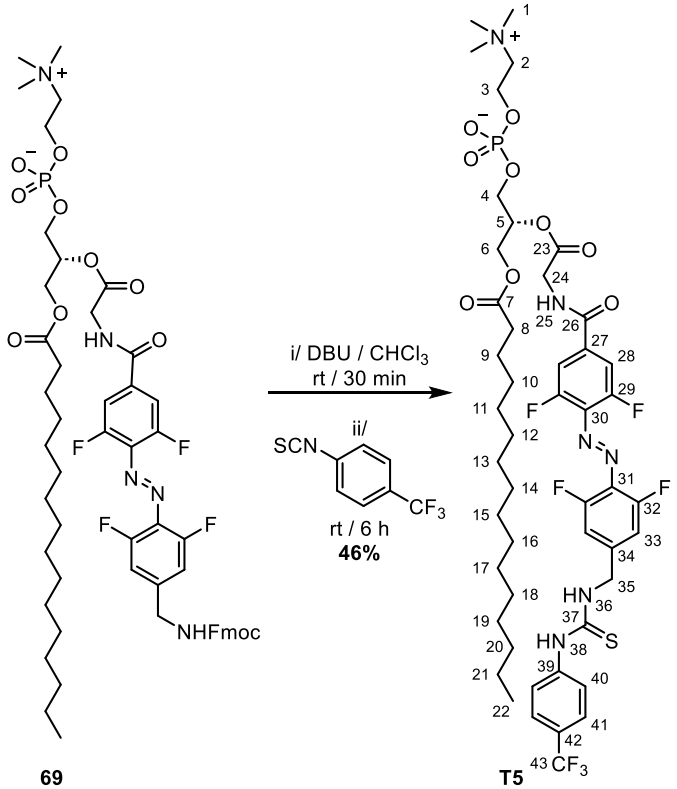

T5. DBU (5.5 µL, 0.037 mmol, 2 Equiv.) was added to a stirred solution of Fmoc-protected azobenzene lipid **69** (20 mg, 0.019 mmol, 1 Equiv.) in anhydrous $CHCl_3$ (2 mL) and left to stir for 1 h under N_2. After complete deprotection of the Fmoc group, 4-(trifluoromethyl)phenyl isothiocyanate (5 mg, 0.025 mmol, 1.3 Equiv.) was added and left to stir for 6 h. The reaction

mixture was concentrated and purified by silica gel flash chromatography (0 - 2% H_2O / 25% MeOH / $CHCl_3$) to give the title compound as a red solid (9 mg, 0.008 mmol, 46%).

^{1}H NMR (400 MHz, $CDCl_3$:CD_3OD (2:1)) δ 7.66 (d, *J* = 8.5 Hz, 2H, $H_{40\ or\ 41}$), 7.62 (d, *J* = 9.1 Hz, 2H, H_{28}), 7.57 (d, *J* = 8.5 Hz, 2H, $H_{40\ or\ 41}$), 7.10 (d, *J* = 10.2 Hz, 2H, H_{33}), 5.32 – 5.27 (m, 1H, H_5), 4.90 (s, 2H, H_{35}), 4.40 – 4.30 (m, 4H, $H_{3\ \&\ 6}$), 4.26 – 4.07 (m, 4H, $H_{4\ \&\ 24}$), 3.67 – 3.64 (m, 2H, H_2), 3.20 (s, 9H, H_1), 2.30 (t, *J* = 7.6 Hz, 2H, H_8), 1.59 – 1.53 (m, 2H, H_9), 1.32 – 1.17 (m, 24H, $H_{10\text{-}21}$), 0.88 – 0.80 (t, *J* = 6.7 Hz, 3H, H_{22}).

^{13}C NMR (151 MHz, $CDCl_3$:CD_3OD (2:1)) δ 182.7 (C_{37}), 174.5 (C_7), 169.8 (C_{23}), 166.0 (C_{26}), 157.5 – 156.3 (m), 155.1 (dd, $J_{C\text{-}F}$ = 122.6, 4.5 Hz), 146.0 (C_{34}), 142.6, 136.8 (C_{27}), 134.2, 130.7, 127.1 (d, $J_{C\text{-}F}$ = 32.9 Hz) (C_{43}), 126.4, 125.6, 112.4 (C_{28}), 111.9 (d, $J_{C\text{-}F}$ = 21.2 Hz) (C_{33}), 72.0 (d, $J_{C\text{-}P}$ = 6.6 Hz) (C_5), 66.7 – 66.5 (m) (C_2), 65.1 (d, $J_{C\text{-}P}$ = 4.8 Hz) (C_4), 62.4 (C_6), 60.4 (d, $J_{C\text{-}P}$ = 5.4 Hz) (C_3), 54.5 (C_1), 47.5 (C_{35}), 42.2 (C_{24}), 34.5 (C_8), 32.4, 30.1, 30.0, 30.0, 29.9, 29.9, 29.8, 29.7, 29.7, 29.6, 29.5, 25.2 (C_9), 23.1, 14.3 (C_{22}).

^{19}F NMR (377 MHz, $CDCl_3$:CD_3OD (2:1)) δ -62.75 (F_{43}), -120.01 ($F_{29\ or\ 32}$), -120.63 ($F_{29\ or\ 32}$).

HRMS-ESI (m/z) Calculated for $C_{48}H_{63}N_6O_9F_7PS$ $[M\text{-}H]^-$, 1063.4009; found 1063.3982.

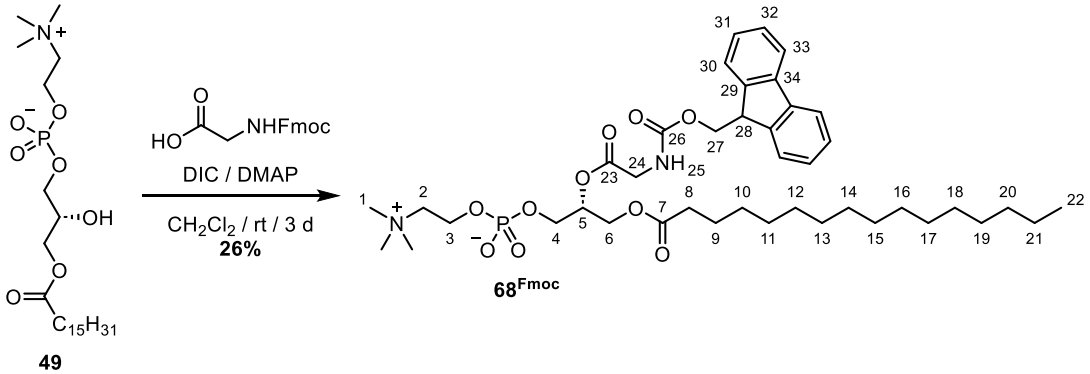

68^{Fmoc}. Fmoc-glycine (2.1 g, 7.1 mmol, 5 Equiv.), DIC (1.8 mL, 11.5 mmol, 8 Equiv.) and DMAP (250 mg, 2.1 mmol, 1.5 Equiv.) were added to a solution of 16:0 lyso PC **49** (700 mg, 1.4 mmol,

1 Equiv.) in anhydrous CH_2Cl_2 (100 mL) under N_2. After stirring the reaction mixture for 3 days, DOWEX 50 WX2-400 was added to remove DMAP. The solution was allowed to stir for 45 minutes. The reaction mixture was filtered, washed with $CHCl_3$:MeOH (1:1, 100 mL) and concentrated. The crude material was purified by silica gel flash chromatography (0 - 2% H_2O / 25% MeOH / $CHCl_3$) to afford the title compound as a white solid (240 mg, 0.37 mmol, 26%).

^{1}H NMR (400 MHz, $CDCl_3$:CD_3OD (2:1)) δ 7.74 (d, *J* = 7.5 Hz, 2H, H_{33}), 7.61 (t, *J* = 6.6 Hz, 2H, H_{30}), 7.37 (t, *J* = 7.4 Hz, 2H, H_{32}), 7.28 (t, *J* = 7.3 Hz, 2H, H_{31}), 5.28 – 5.22 (m, 1H, H_5), 4.33 – 4.30 (m, 3H, $H_{6\ \&\ 27}$), 4.23 – 4.12 (m, 4H, $H_{3,\ 6\ \&\ 28}$), 4.05 – 3.96 (m, 2H, H_4), 3.93 (d, *J* = 3.7 Hz, 2H, H_{24}), 3.57 – 3.49 (m, 2H, H_2), 3.13 (s, 9H, H_1), 2.27 (t, *J* = 7.6 Hz, 2H, H_8), 1.59 – 1.49 (m, 2H, H_9), 1.29 – 1.17 (m, 24H, $H_{10\text{-}21}$), 0.84 (t, *J* = 6.8 Hz, 3H, H_{22}).

^{13}C NMR (101 MHz, $CDCl_3$:CD_3OD (2:1)) δ 174.5 (C_7), 170.5 (C_{23}), 157.8 (C_{26}), 144.2 (two s, *Fmoc rotamers*), 141.7, 128.1 (C_{32}), 127.5 (C_{31}), 125.5 (two s, *Fmoc rotamers*) (C_{30}), 120.3 (C_{33}), 72.2 (d, $J_{C\text{-}P}$ = 7.0 Hz) (C_5), 67.5 (C_{27}), 66.9 – 66.6 (m) (C_2), 64.2 (d, $J_{C\text{-}P}$ = 4.8 Hz) (C_4), 62.7 (C_6), 59.5 (d, $J_{C\text{-}P}$ = 5.1 Hz) (C_3), 54.5 – 54.3 (m) (C_1), 47.5 (C_{28}), 42.8 (C_{24}), 34.3 (C_8), 32.3, 30.0, 30.0, 30.0, 30.0, 30.0, 29.8, 29.7, 29.6, 29.5, 25.1 (C_9), 23.0, 14.3 (C_{22}).

HRMS-ESI (m/z) Calculated for $C_{41}H_{64}O_{10}N_2P$ $[M+H]^+$, 775.4293; found 775.4291.

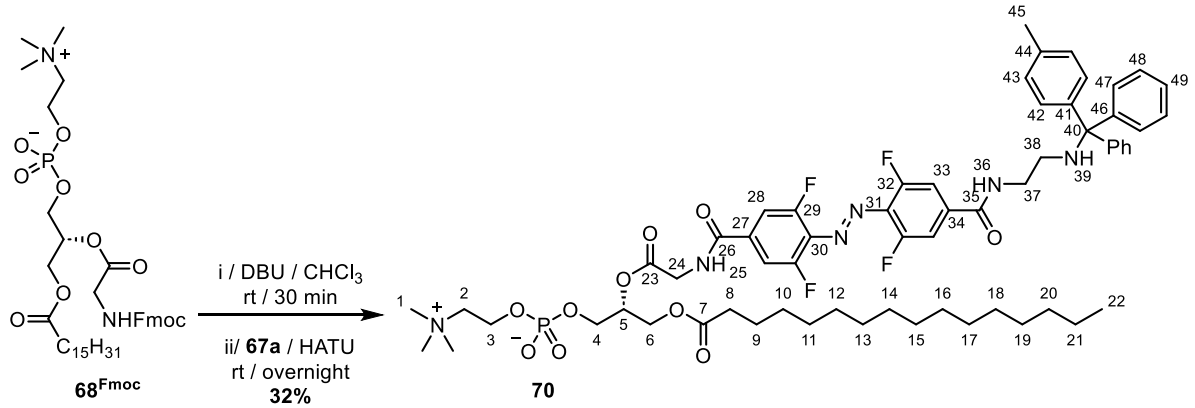

70. DBU (25 µL, 0.17 mmol, 2 Equiv.) was added to a stirred solution of **68^{Fmoc}** (65 mg, 0.84 mmol, 1 Equiv.) in anhydrous $CHCl_3$ (1 mL) and left to stir for 1 h under N_2. Compound **67a** (100 mg, 0.13 mmol, 1.6 Equiv.) and HATU (64 mg, 0.17 mmol, 2 Equiv.) were dissolved in anhydrous $CHCl_3$ (1 mL) and left to stir for 10 min before being added to the reaction mixture, which was left to stir overnight under N_2. The reaction mixture was concentrated and purified by silica gel flash chromatography (0 - 2% H_2O / 25% MeOH / $CHCl_3$) to afford the title compound as a red solid (32 mg, 0.027 mmol, 32%).

^{1}H NMR (400 MHz, $CDCl_3$:CD_3OD (2:1)) δ 7.66 (d, *J* = 9.2 Hz, 2H, $H_{28\ or\ 33}$), 7.58 (d, *J* = 9.2 Hz, 2H $H_{28\ or\ 33}$), 7.44 – 7.36 (m, 4H, H_{47}), 7.29 (d, *J* = 8.3 Hz, 2H, H_{42}), 7.27 – 7.20 (m, 4H, H_{48}), 7.16 (q, *J* = 6.2 Hz, 2H, H_{49}), 7.05 (d, *J* = 8.1 Hz, 2H, H_{43}), 5.34 – 5.19 (m, 1H, H_5), 4.37 – 4.28 (m, 1H, H_6), 4.26 – 4.15 (m, 4H, $H_{3,\ 6\ \&\ 24}$), 4.14 – 3.96 (m, 3H, $H_{3\ \&\ 4}$), 3.58 (s, 2H, H_2), 3.51 (t, *J* = 6.0 Hz, 2H, H_{37}), 3.18 (s, 9H, H_1), 2.45 (t, *J* = 5.8 Hz, 2H, H_{38}), 2.33 – 2.27 (m, 2H, H_8), 2.27 (s, 3H, H_{45}), 1.59 – 1.52 (m, 2H, H_9), 1.29 – 1.78 (m, 24H, $H_{10\ -\ 21}$), 0.83 (t, *J* = 6.8 Hz, 3H, H_{22}).

^{13}C {^{19}F} NMR (126 MHz, $CDCl_3$:CD_3OD (2:1)) δ 174.4 (C_7), 169.7 (C_{23}), 165.5 (C_{26}), 165.5 (C_{35}), 155.6, 155. 6, 151.8, 151.7, 138.3, 137.6, 136.7, 133.6, 133.4, 129.0, 128.9, 128.3, 128.1, 127.0, 112.4 ($C_{28\ or\ 33}$), 112.2 ($C_{28\ or\ 33}$), 72.3(C_{40}), 72.3 (d, $J_{C\text{-}P}$ = 6.5 Hz) (C_5), 66.9 – 66.7 (m) (C_2), 64.2 (d, $J_{C\text{-}P}$ = 4.6 Hz) (C_4), 62.5 (C_6), 59.5 (d, $J_{C\text{-}P}$ = 4.5 Hz) (C_3), 54.5 – 54.4 (m) (C_1), 44.0 (C_{38}), 42.1 (C_{24}), 40.9 (C_{37}), 34.3 (C_8), 32.2, 30.0, 30.0, 30.0, 30.0, 29.8, 29.8, 29.8, 29.7, 29.6, 29.5, 25.1 (C_9), 23.0, 21.0 (C_{45}), 14.2 (C_{22}).

^{19}F NMR (471 MHz, $CDCl_3$:CD_3OD (2:1)) δ -115.73 ($F_{29\ or\ 32}$), -115.81 ($F_{29\ or\ 32}$).

HRMS-ESI (m/z) Calculated for $C_{62}H_{80}O_{10}N_6F_4P$ $[M+H]^+$, 1175.5604; found 1175.5562.

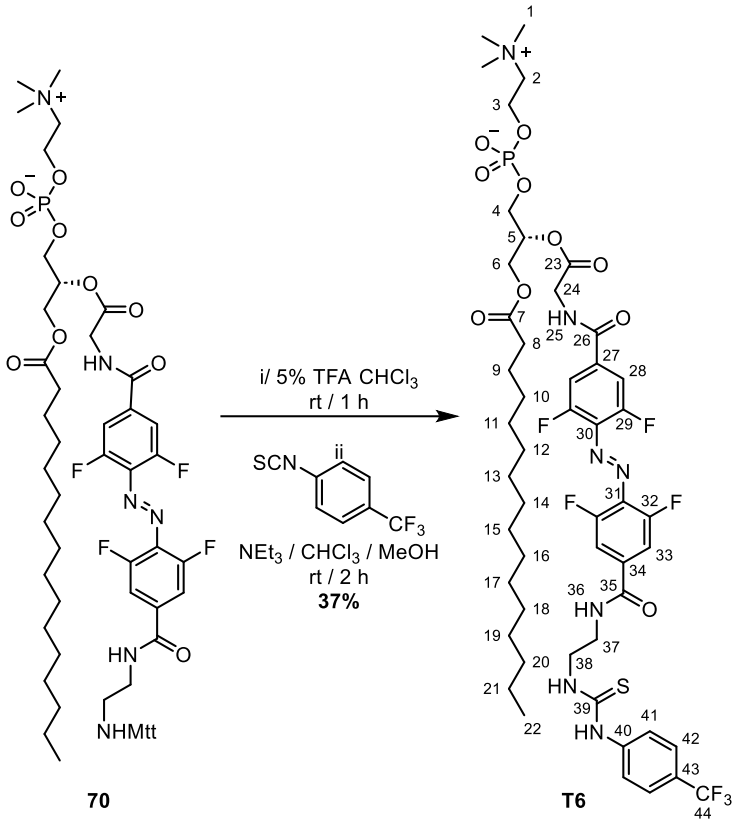

T6. Mtt-protected medium azobenzene lipid **70** (17 mg, 0.015 mmol, 1 Equiv.) was dissolved in anhydrous $CHCl_3$ (1 mL) and TFA (50 µL, 5% v/v) and left to stir at rt for 1 h under N_2. After complete deprotection, MeOH (1 mL) was added and the reaction mixture was concentrated. The residue was dissolved in anhydrous $CHCl_3$:MeOH (1:1, 2 mL) and NEt_3 (50 µL). 4-(Trifluoromethyl)phenyl isothiocyanate (6 mg, 0.03 mmol, 2 Equiv.) was added to the reaction mixture and left to stir at rt for 4 h under N_2. The reaction mixture was then concentrated and purified by silica gel flash chromatography (0 - 3% H_2O / 25% MeOH / $CHCl_3$) to afford the title compound as a red solid (6 mg, 0.005 mmol, 37%).

^{1}H NMR (400 MHz, $CDCl_3$:CD_3OD (2:1)) δ 7.68 – 7.60 (m, 4H, $H_{28\ \&\ 33}$), 7.56 (s, 4H, $H_{41\ \&\ 42}$), 5.32 – 5.28 (m, 1H, H_5), 4.40 – 4.27 (m, 4H, $H_{3\ \&\ 6}$), 4.26 – 4.08 (m, 4H, $H_{4\ \&\ 24}$), 3.91 – 3.86 (m, 2H, H_{38}), 3.70 – 3.58 (m, 4H, $H_{2\ \&\ 37}$), 3.21 (s, 9H, H_1), 2.31 (t, *J* = 7.4 Hz, 2H, H_8), 1.62 – 1.53 (m, 2H, H_9), 1.30 – 1.84 (m, 24H, $H_{10\ -\ 21}$), 0.91 – 0.76 (m, 3H, H_{22}).

^{13}C NMR (151 MHz, $CDCl_3$:CD_3OD (2:1)) δ 175.7, 174.5 (C_7), 170.9, 169.8, 166.1 (C_{39}), 156.6, 154.9, 142.3, 138.2, 137.6, 133.9, 133.6, 127.2, 126.5 ($C_{41\text{ or }42}$), 125.5, 124.0 ($C_{41\text{ or }42}$), 112.5, 112.4, 72.0 (C_5), 66.6 (C_2), 65.2 (C_4), 62.4 (C_6), 60.6 (C_3), 54.5 (C_1), 44.2 (C_{38}), 42.2 (C_{24}), 40.9 (C_{37}), 34.5 (C_8), 32.4, 30.1, 30.1, 30.0, 29.9, 29.9, 29.8, 29.7, 29.7, 29.6, 29.6, 25.4 (C_9), 23.1, 14.3 (C_{22}).

^{19}F NMR (377 MHz, $CDCl_3$:CD_3OD (2:1)) δ -62.79 (C_{44}), -119.73 ($C_{28\text{ or }33}$), -119.78 ($C_{28\text{ or }33}$).

HRMS-ESI (m/z) Calculated for $C_{50}H_{68}O_{10}N_7F_7PS$ $[M+H]^+$, 1122.4369; found 1122.4349.

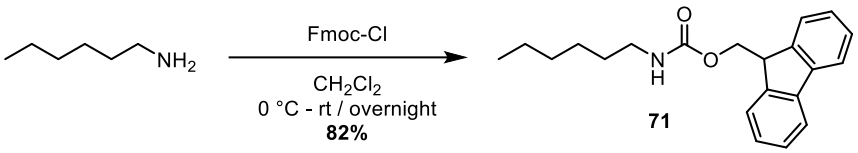

71. Prepared according to the literature procedure.[219] Data consistent with that given in the literature.

5.5.2 Chapter 3 UV-vis Characterisation

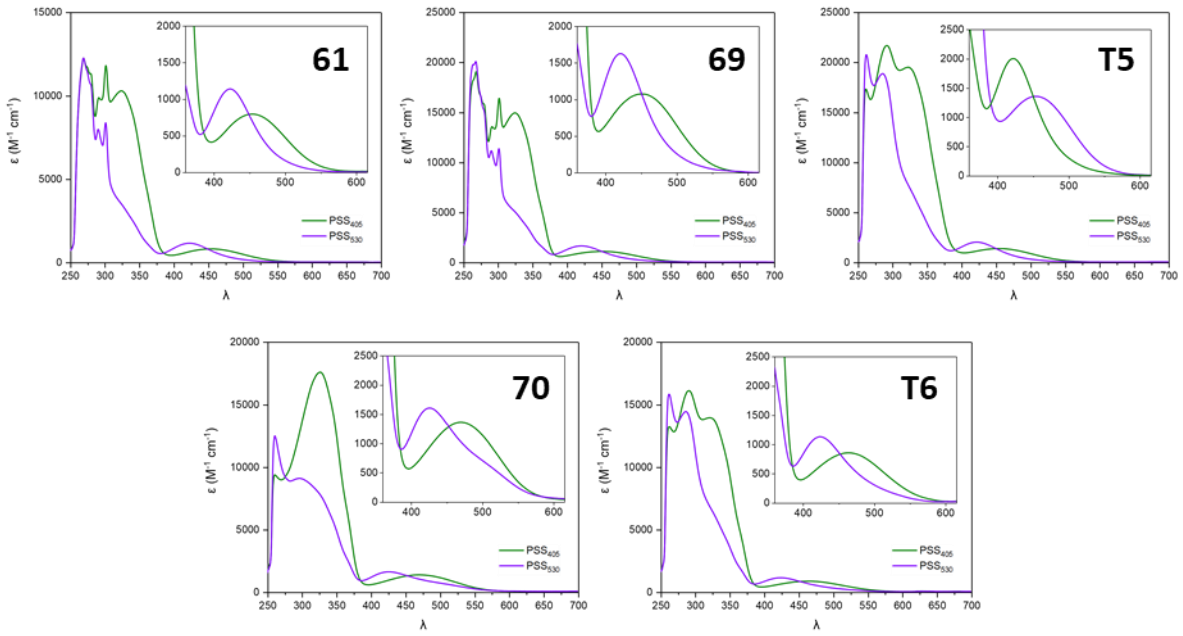

Figure 5.2 UV-vis spectra of azobenzene derivatives in DMSO, measured after irradiation with 405/530 nm for 3 mins to reach PSS.

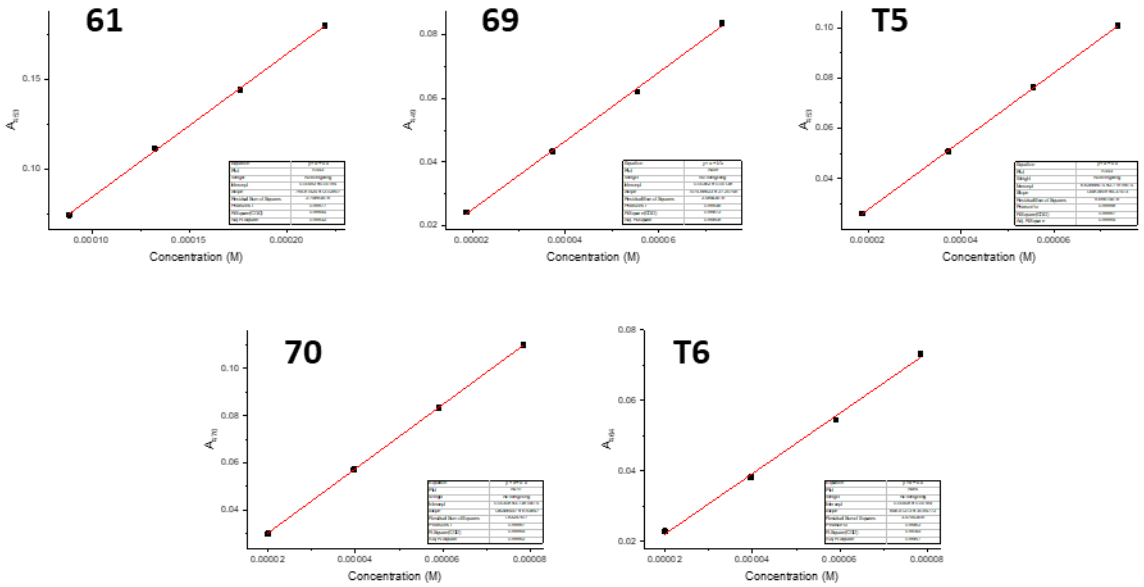

*Figure 5.3 Beer-Lambert plots for azobenzene derivatives **61**, **69**, **70**, **T5**, **T6**.*

5.5.3 Chapter 3 Photo-stationary State Determination

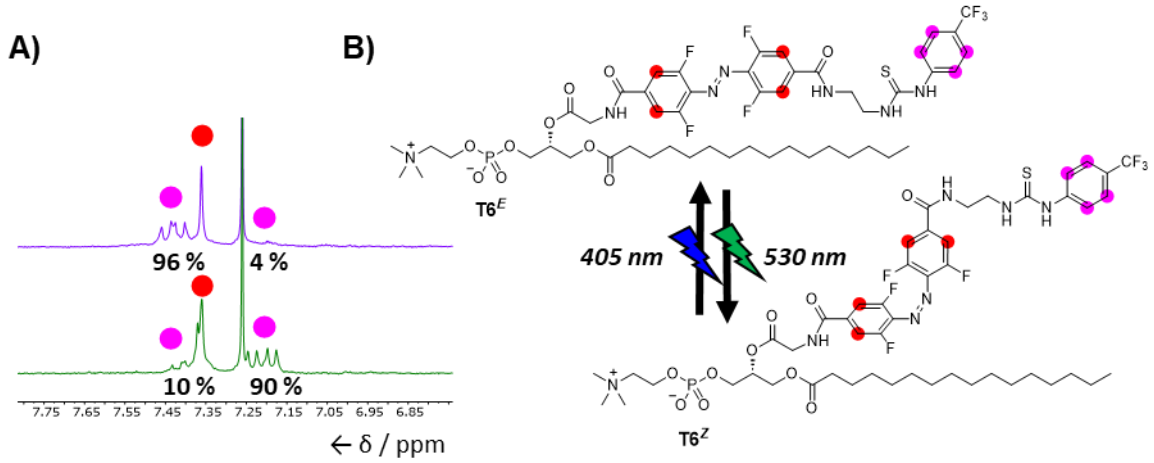

Figure 5.4 PSS distribution determination in $CDCl_3$:CD_3OD (2:1) at 298K by ^{1}H NMR. *A) Partial ^{1}H NMR spectra of **$T6^E$**/**$T6^Z$** ($CDCl_3$:CD_3OD (2:1), 400 MHz, 298 K) showing the PSS achieved by irradiation with blue 405 nm (top blue line, 96% E) and green 530 nm (bottom green line, 90% Z) light. B) Structure of the two configurations of the photo-switchable lipid **T6**.*

5.5.4 Chapter 3 ^{1}H NMR Titration Experiments

^{1}H NMR titration experiments were performed as previously described in **Section 5.4.2**.

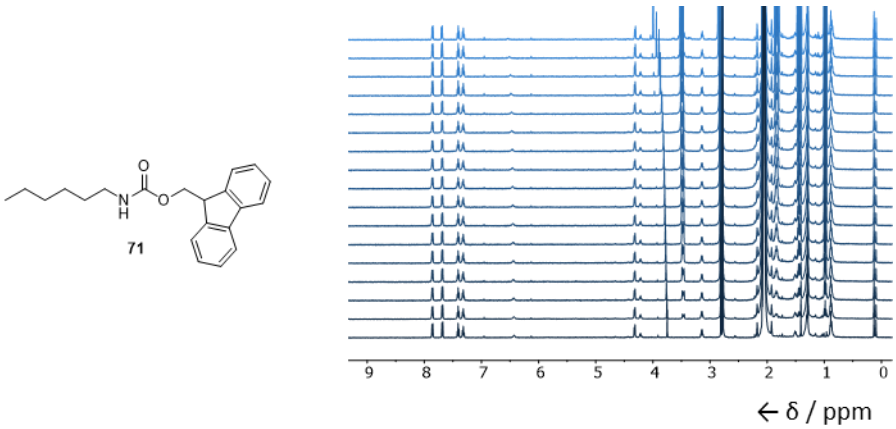

Figure 5.5 Stacked ^{1}H NMR of hexyl Fmoc derivative 71 (1 mM, acetone-d_6, 500 MHz, 298 K) titrated with TBACl (no binding observed in this solvent).

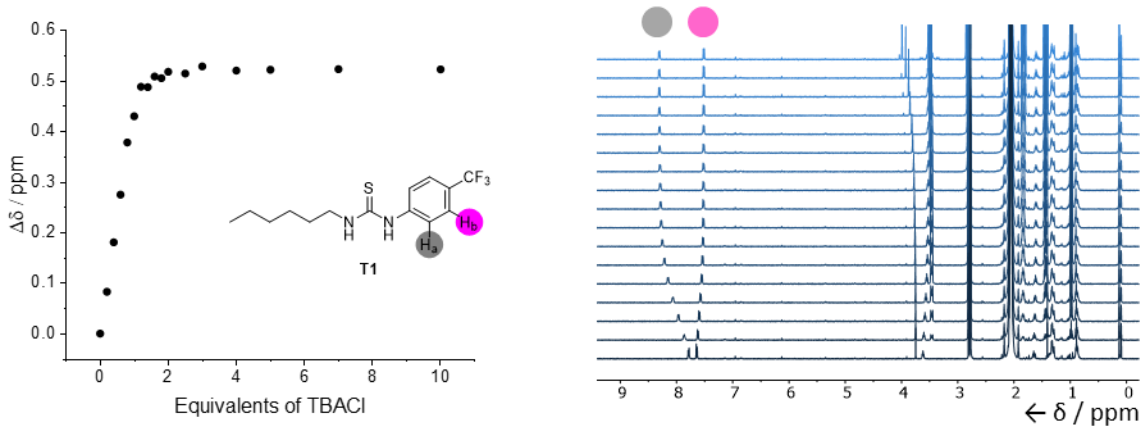

*Figure 5.6 Left, Binding isotherm for ^{1}H NMR TBACl titrations with **T1** (acetone-d_6), where circles represent experimental chemical shift perturbation of proton H_a upon chloride binding. Binding constant too high to be determined (>10^4 M^{-1}). Right, Stacked ^{1}H NMR of hexyl thiourea **T1**(1 mM, acetone-d_6, 500 MHz, 298 K) titrated with TBACl.*

5.5.5 Chapter 3 Photo-switchable Relay Anion Transport Data

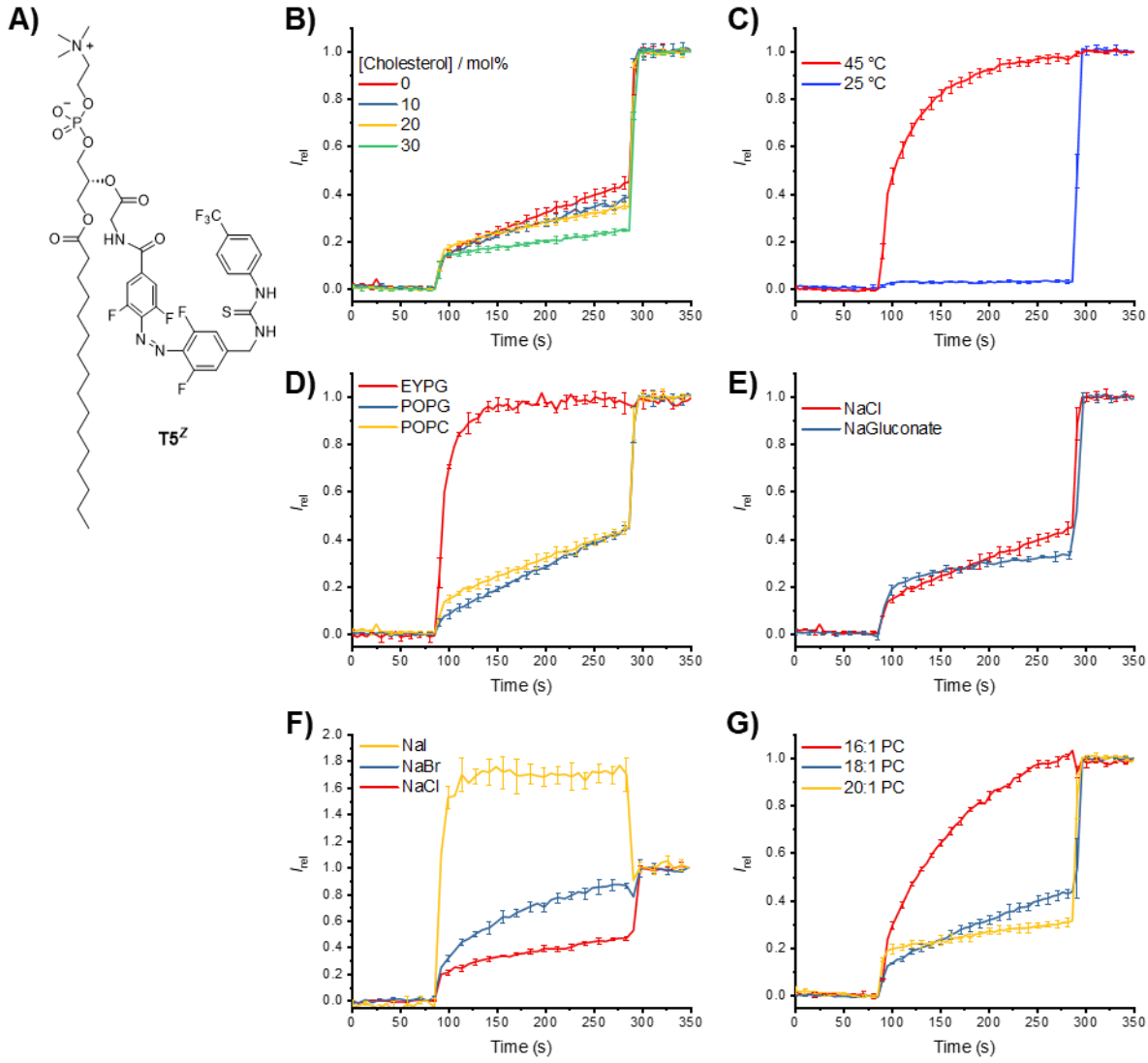

Figure 5.7 HPTS transport data for T5^Z (5 mol%, pre-incorporated) in LUVs. *A) Structure of* ***T5^Z****. B) POPC LUVs with varying concentration of cholesterol (0-30 mol% to POPC). C) DPPC LUVs at 25 °C (gel phase) and 45 °C (fluid phase). D) LUVs composed of lipids with different headgroups (POPC, POPG or EYPG). E) and F) POPC LUVs with different salt (NaCl, NaGluconate, NaBr or NaI) in the internal and external buffer. G) LUVs composed of lipids with different alkyl chain lengths (16:1 PC, 18:1 PC or 20:1 PC).*

5.6.1 Chapter 4 Synthetic Procedures

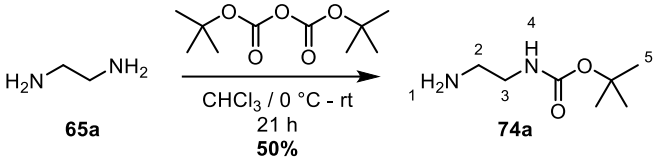

74a. Prepared according to the literature procedure.[199] Data consistent with that given in the literature.

^{1}H NMR (400 MHz, $CDCl_3$) δ 4.86 (s, 1H, H_4), 3.16 (q, *J* = 6.0 Hz, 2H, H_3), 2.79 (t, *J* = 5.9 Hz, 2H, H_2), 1.44 (s, 9H, H_5), 1.33 (s, 2H, H_1).

^{13}C NMR (126 MHz, $CDCl_3$) δ 156.5, 79.4, 77.4, 77.2, 76.9, 42.6, 41.5, 28.5.

LRMS-ESI (m/z) Calculated for $C_7H_{17}N_2O_2$ $[M+H]^+$, 161.13; found 161.150.

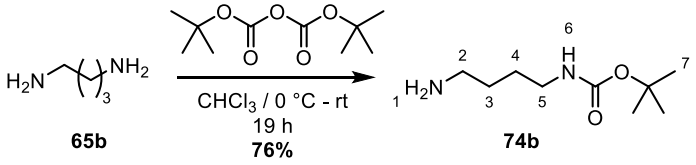

74b. Prepared according to the literature procedure.[199] Data consistent with that given in the literature.

^{1}H NMR (400 MHz, $CDCl_3$) δ 4.81 (brs, 1H, H_6), 3.06 (q, *J* = 6.4 Hz, 2H, H_5), 2.66 (t, *J* = 6.6 Hz, 2H, H_2), 1.54 – 1.40 (m, 4H, $H_{3\text{-}4}$), 1.38 (s, 9H, H_7).

LRMS-ESI (m/z) Calculated for $C_9H_{21}N_2O_2$ $[M+H]^+$, 189.28; found 189.20.

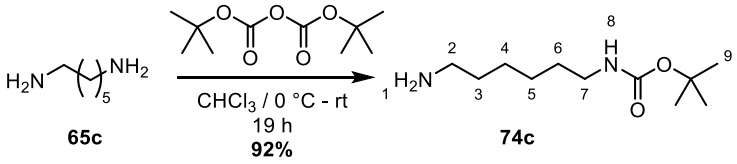

74c. Prepared according to the literature procedure.[199] Data consistent with that given in the literature.

^{1}H NMR (400 MHz, $CDCl_3$) δ 4.70 (brs, 1H, H_8), 3.02 (q, *J* = 6.7 Hz, 2H, H_7), 2.77 – 2.44 (m, 2H, H_2), 1.38-1.31 (m, 13H, $H_{3,6,9}$), 1.27-1.22 (m, 4H, $H_{4\text{-}5}$), 1.07 (s, 2H, H_1).

LRMS-ESI (m/z) Calculated for $C_{11}H_{25}N_2O_2$ $[M+H]^+$, 217.33; found 217.20.

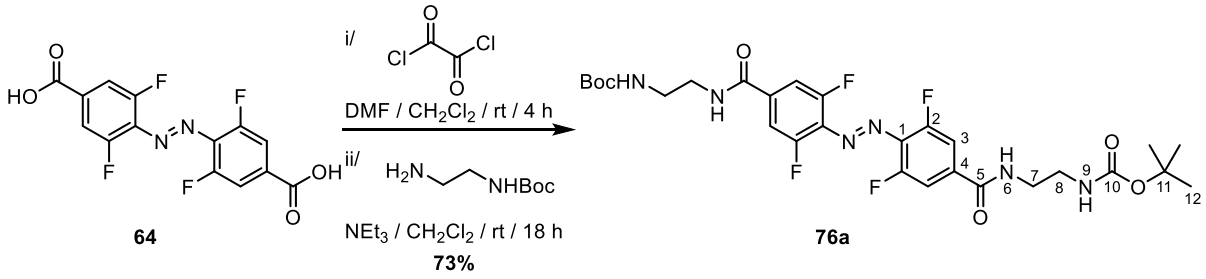

Bis-Boc-ethyl-amide-tetrafluoroazobenzene 76a. 4,4'-(diazene-1,2-diyl)bis(3,5-difluorobenzoic acid) **64** (50 mg, 0.15 mmol, 1 equiv.) was suspended in anhydrous CH_2Cl_2 (2 mL) under an inert atmosphere. Oxalyl chloride (0.05 mL, 0.6 mmol, 4 equiv.) and catalytic DMF (1 drop) were added to the reaction mixture which was left to stir for 4 h. Upon completion of reaction the solvent was removed *in vacuo* to give the acid chloride intermediate which was dissolved in anhydrous CH_2Cl_2 (2 mL) and added dropwise to a stirred solution of *tert*-butyl *N*-(2-aminoethyl)carbamate **74a** (52 mg, 0.32 mmol, 2.2 equiv.) and NEt_3 (0.08 mL, 0.6 mmol, 4 equiv.) in anhydrous CH_2Cl_2 (8 mL) at 0 °C. The reaction mixture was left to stir at 0 °C for 1 h, and then left to warm to rt and left to stir overnight. The reaction mixture was then diluted with CH_2Cl_2 (50 mL) and washed with water (3 x 25 mL). The aqueous layers were combined and back extracted with CH_2Cl_2 (1 x 50 mL) and the organic layers were combined and solvent removed *in vacuo* to give a crude product. This material was passed through a silica plug eluted with 10% MeOH/CH_2Cl_2 to afford the title compound as a rusty coloured solid (67 mg, 0.11 mmol, 73%).

^{1}H NMR (500 MHz, DMSO-d_6) δ 8.81 (t, *J* = 5.7 Hz, 2H, H_6), 7.79 (d, *J* = 10.7 Hz, 4H, H_3), 6.96 (t, *J* = 6.0 Hz, 2H, H_9), 3.33 (q, *J* = 6.0 Hz, 4H, H_7), 3.13 (q, *J* = 6.2 Hz, 4H, H_8), 1.38 (s, 18H, H_{12}).

^{13}C {^{19}F} NMR (126 MHz, DMSO-d_6) δ 163.1, 155.8, 154.4, 138.7, 131.8, 112.2 (C_3), 77.7, 40.1 (C_7), 39.6 (C_8), 28.2(C_{12}).

^{19}F NMR (471 MHz, DMSO-d_6) δ -120.32 (d, *J* = 11.3 Hz).

HRMS-ESI (m/z) Calculated for $C_{28}H_{34}O_6N_6F_4Na$ $[M+Na]^+$, 649.2368; found 649.2365.

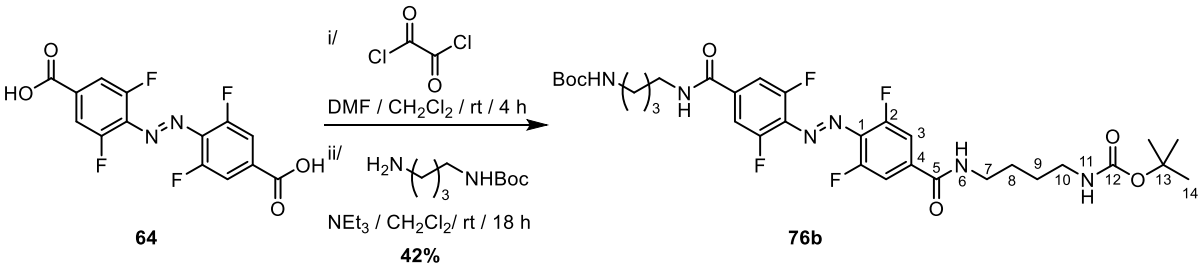

Bis-Boc-butyl-amide-tetrafluoroazobenzene **76b**. 4,4'-(diazene-1,2-diyl)bis(3,5-difluorobenzoic acid) **64** (50 mg, 0.15 mmol, 1 equiv.) was suspended in anhydrous CH_2Cl_2 (2 mL) under an inert atmosphere. Oxalyl chloride (0.05 mL, 0.6 mmol, 4 equiv.) and catalytic DMF (1 drop) were added to the reaction mixture which was left to stir for 4 h. Upon completion of reaction the solvent was removed *in vacuo* to give the acid chloride intermediate which was dissolved in anhydrous CH_2Cl_2 (2 mL) and added dropwise to a stirred solution of *tert*-butyl *N*-(4-aminobutyl)carbamate **74b** (61 mg, 0.32 mmol, 2.2 equiv.) and NEt_3 (0.08 mL, 0.6 mmol, 4 equiv.) in anhydrous CH_2Cl_2 (8 mL) at 0 °C. The reaction mixture was left to stir at 0 °C for 1 h, and then left to warm to rt and left to stir overnight. The reaction mixture was then diluted with CH_2Cl_2 (50 mL) and washed with water (3 x 25 mL). The aqueous layers were combined and back extracted with CH_2Cl_2 (1 x 25 mL) and the organic layers were combined and solvent removed *in vacuo* to give the title compound as a rusty coloured solid (43 mg, 0.06 mmol, 42%).

^{1}H NMR (400 MHz, DMSO-d_6) δ 8.78 (t, *J* = 5.6 Hz, 2H, H_5), 8.04 – 7.69 (m, 4H, H_3), 6.81 (t, *J* = 5.7 Hz, 2H, H_{11}), 3.28 (q, *J* = 6.9 Hz, 4H, H_7), 2.94 (q, *J* = 6.6 Hz, 4H, H_{10}), 1.51 (m, 4H, H_8), 1.43 (m, 4H, H_9), 1.37 (s, 18H, H_{14}).

^{19}F NMR (376 MHz, DMSO-d_6) δ -120.23.

HRMS-ESI (m/z) Calculated for $C_{32}H_{42}O_6N_6F_4Na$ $[M+Na]^+$, 705.2994; found 705.2988.

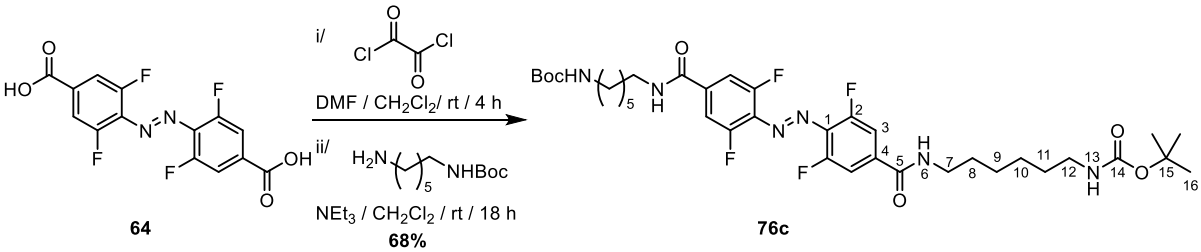

Bis-Boc-hexyl-amide-tetrafluoroazobenzene **76c**. 4,4'-(diazene-1,2-diyl)bis(3,5-difluorobenzoic acid) **64** (50 mg, 0.15 mmol, 1 equiv.) was suspended in anhydrous CH_2Cl_2 (2

mL) under an inert atmosphere. Oxalyl chloride (0.05 mL, 0.6 mmol, 4 equiv.) and catalytic DMF (1 drop) were added to the reaction mixture which was left to stir for 4 h. Upon completion of reaction the solvent was removed *in vacuo* to give the acid chloride intermediate which was dissolved in anhydrous CH_2Cl_2 (2 mL) and added dropwise to a stirred solution of tert-butyl *N*-(6-aminohexyl)carbamate **74c** (70 mg, 0.32 mmol, 2.2 equiv.) and NEt_3 (0.08 mL, 0.6 mmol, 4 equiv.) in anhydrous CH_2Cl_2 (8 mL) at 0 °C. The reaction mixture was left to stir at 0 °C for 1 h, and then left to warm to rt and left to stir overnight. The reaction mixture was then diluted with CH_2Cl_2 (50 mL) and washed with water (3 x 25 mL). The aqueous layers were combined and back extracted with CH_2Cl_2 (1 x 50 mL) and the organic layers were combined and solvent removed *in vacuo* to give the title compound as a rusty coloured solid (75 mg, 0.1 mmol, 68%).

^{1}H NMR (400 MHz, DMSO-d_6) δ 8.77 (t, *J* = 5.6 Hz, 2H, H_6), 7.81 (m, 4H, H_3), 6.77 (t, *J* = 5.2 Hz, 2H, H_{13}), 3.28 (q, *J* = 6.6 Hz, 4H, H_7), 2.90 (q, *J* = 9.4, 8.1 Hz, 4H, H_{12}), 1.52 (q, *J* = 7.2 Hz, 4H, H_8), 1.36 (s, 18H, H_{16}), 1.35 – 1.18 (m, 12H, $H_{9, 10, 11}$).

^{13}C {^{19}F} NMR (126 MHz, DMSO-d_6) δ 162.7, 155.6, 154.4, 138.7, 131.9, 112.1, 77.3, 40.0, 39.8, 29.5, 28.9, 28.3, 26.2, 26.0.

^{19}F NMR (471 MHz, DMSO-d_6) δ -120.20.

HRMS-ESI (m/z) Calculated for $C_{36}H_{50}O_6N_6F_4Na$ $[M+Na]^+$, 761.3620; found 761.3614.

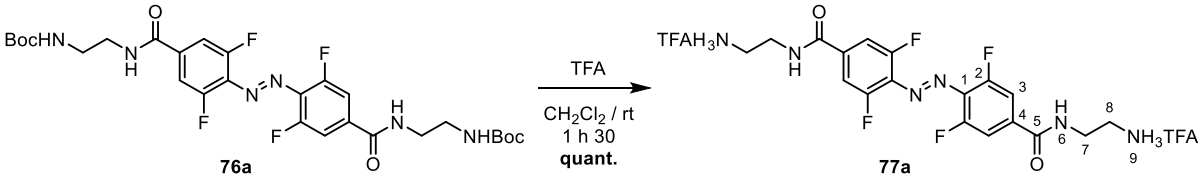

Diamino-ethyl-amide-tetrafluoroazobenzene TFA salt 77a. Boc-protected azobenzene **76a** (57 mg, 0.09 mmol, 1 equiv.) was dissolved in CH_2Cl_2 (1 mL) and trifluoroacetic acid (100 µL) and left to stir for 1 h 30 at rt. The solvent was removed *in vacuo* and the residue was redissolved in MeOH and solvent removed *in vacuo* to give the title compound as red tacky solid (69 mg, quant.).

^{1}H NMR (400 MHz, CD_3OD) δ 8.06 – 7.42 (m, 4H, H_3), 3.70 (t, *J* = 5.9 Hz, 4H, H_7), 3.20 (t, *J* = 5.9 Hz, 4H, H_8).

^{13}C {^{19}F} NMR (126 MHz, CD_3OD) δ 167.4, 163.1, 156.4, 138.9, 134.4, 113.2, 112.8, 40.8, 38.9.

^{19}F NMR (376 MHz, CD_3OD) δ -77.11 (TFA, C*F*$_3$), -120.44.

HRMS-ESI (m/z) Calculated for $C_{18}H_{19}O_2N_6F_4$ $[M+H]^+$, 427.15001; found 427.14984.

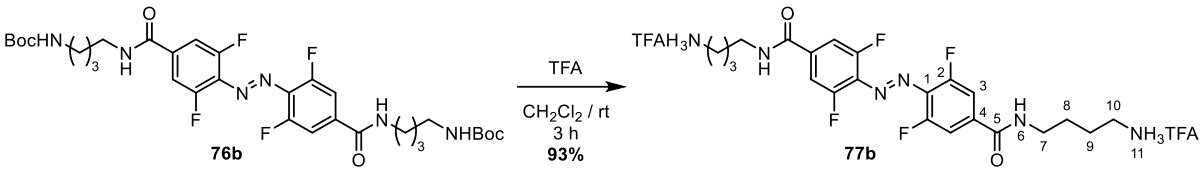

Diamino-butyl-amide-tetrafluoroazobenzene TFA salt 77b. Boc-protected azobenzene **76b** (50.8 mg, 0.075 mmol, 1 equiv.) was dissolved in CH_2Cl_2 (2 mL) and trifluoroacetic acid (150 µL) and left to stir for 3 h at rt. The solvent was removed *in vacuo* and the residue was redissolved in MeOH and Et_2O was added until a precipitate formed which was collected and washed with Et_2O to give the title compound as a red solid (49 mg, 93%).

^{1}H NMR (400 MHz, CD_3OD) δ 7.75 – 7.62 (m, 4H, H_3), 3.52 – 3.41 (m, 4H, H_7), 3.08 – 2.94 (m, 4H, H_{10}), 1.76 – 1.71 (m, 8H, $H_{8,9}$).

^{13}C {^{19}F} NMR (126 MHz, CD_3OD) δ 166.5, 163.1, 156.4, 139.5, 134.2, 113.0, 112.6, 40.4, 40.4, 27.4, 26.0.

^{19}F NMR (376 MHz, CD_3OD) δ -76.93 (TFA, C*F*$_3$), -121.54.

HRMS-ESI (m/z) Calculated for $C_{22}H_{27}O_2N_6F_4$ $[M+H]^+$, 483.2126; found 483.2125.

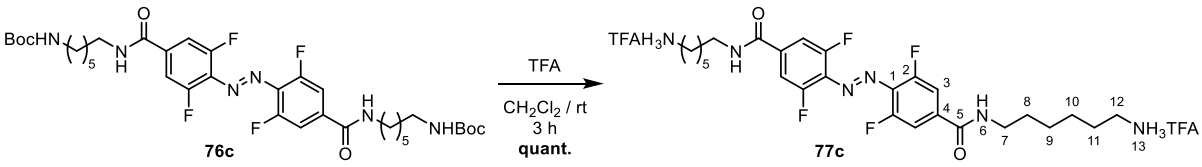

Di-amino-hexyl-amide-tetrafluoroazobenzene TFA salt 77c. Boc-protected azobenzene **76c** (50.8 mg, 0.069 mmol, 1 equiv.) was dissolved in CH_2Cl_2 (2 mL) and trifluoroacetic acid (150 µL) and left to stir for 3 h at rt. The solvent was removed *in vacuo* and the residue was redissolved in MeOH and Et_2O was added until a precipitate formed which was collected and washed with Et_2O to give the title compound as a red solid (53 mg, 100%).

^{1}H NMR (400 MHz, CD_3OD) δ 7.70 – 7.63 (m, 4H_3), 3.42 (t, *J* = 7.1 Hz, 4H_7), 2.94 (t, *J* = 7.5 Hz, 4H_{12}), 1.69 (m, 8$H_{8,11}$), 1.46 (m, 8$H_{9,10}$).

^{13}C NMR (126 MHz, CD_3OD) δ 166.3, 163.1, 156.4, 139.7, 134.2, 112.9, 112.5, 41.0, 40.6, 30.1, 28.5, 27.4, 27.0.

^{19}F NMR (471 MHz, CD_3OD) δ -76.91 (TFA, C*F*$_3$), -121.57.

HRMS-ESI (m/z) Calculated for $C_{26}H_{35}O_2N_6F_4$ $[M+H]^+$, 539.2752; found 539.2753.

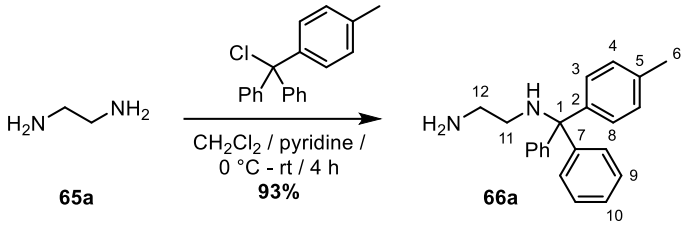

***N*-(diphenyl(p-tolyl)methyl)-1,2-ethanediamine 66a.** Prepared according to the literature procedure.[221] Data consistent with that given in the literature.

^{1}H NMR (400 MHz, $CDCl_3$) δ 7.52 – 7.46 (m, 4H, H_8), 7.37 (d, *J* = 8.3 Hz, 2H, H_3), 7.27 (dd, *J* = 8.4, 6.9 Hz, 4H, H_9), 7.21 – 7.14 (m, 2H, H_{10}), 7.09 (d, *J* = 8.1 Hz, 2H, H_4), 2.81 (t, *J* = 6.0 Hz, 2H, H_{12}), 2.31 (s, 3H, H_6), 2.24 (t, *J* = 5.9 Hz, 2H, H_{11}), 1.88 (brs, 2H, NH_2).

^{13}C NMR (126 MHz, $CDCl_3$) δ 146.4, 143.2, 135.9, 128.7, 128.7, 128.6, 127.9, 126.3, 70.6, 46.3, 42.8, 21.1.

LRMS-ESI (m/z) Calculated for $C_{22}H_{25}N_2$ $[M+H]^+$, 317.20; found 317.231.

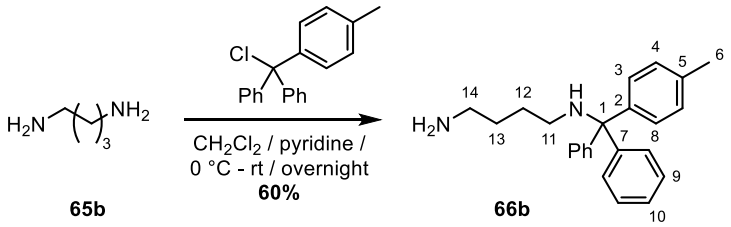

***N*-(diphenyl(p-tolyl)methyl)-1,4-butanediamine 66b.** 1,4-Diaminobutane **65b** (1.5 mL, 1.3 g, 15 mmol, 9 equiv.) was dissolved in anhydrous CH_2Cl_2 (3.5 mL) and pyridine (2.5 mL) was added portionwise. Methyltrityl chloride (500 mg, 1.7 mmol, 1 equiv.) was added at 0 °C and the solution was allowed to warm to rt and left to stir for 18 h under an inert atmosphere of N_2. The reaction was quenched by adding MeOH (0.5 mL) and the solvent was evaporated. The crude was dissolved in CH_2Cl_2 (1% NEt_3) / H_2O (1:1; 25 mL) and the product was extracted with CH_2Cl_2 (2 x 10 mL). The combined organic layers were washed with H_2O (25 mL) and the solvent was removed *in vacuo* to give a crude product. This material was purified by flash chromatography on silica (CH_2Cl_2 / 2% MeOH / 3% NEt_3) to give the title compound as a colourless oil (350 mg, 1.0 mmol, 60%).

^{1}H NMR (400 MHz, $CDCl_3$) δ 7.50 – 7.44 (m, 4H, H_8), 7.38 – 7.32 (m, 2H, H_3), 7.31 – 7.23 (m, 4H, H_9), 7.20 – 7.14 (m, 2H, H_{10}), 7.08 (d, *J* = 8.1 Hz, 2H, H_4), 2.71 – 2.66 (m, 2H, H_{14}), 2.31 (s, 3H, H_6), 2.18 – 2.11 (m, 2H, H_{11}), 1.53 – 1.49 (m, 4H, $H_{12\ \&\ 13}$).

^{13}C NMR (101 MHz, $CDCl_3$) δ 146.5, 143.4, 135.8, 128.7, 128.7, 128.6, 127.8, 126.2, 70.7, 43.5, 42.0, 30.8, 28.3, 21.1.

HRMS-ESI (m/z) Calculated for $C_{24}H_{29}N_2$ $[M+H]^+$, 345.2325; found 345.2322.

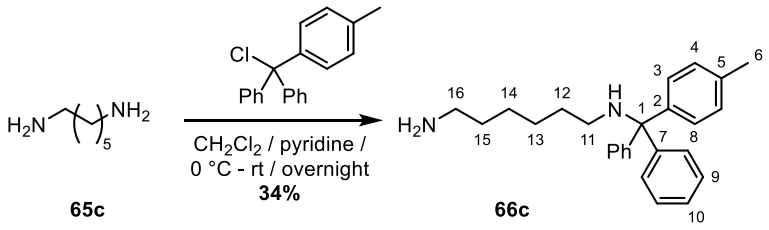

***N*-(diphenyl(p-tolyl)methyl)-1,6-hexanediamine 66c.** 1,6-Diaminohexane **65c** (1.7 g, 15 mmol, 9 equiv.) was dissolved in anhydrous CH_2Cl_2 (3.5 mL) and pyridine (2.5 mL) was added portionwise. Methyltrityl chloride (500 mg, 1.7 mmol, 1 equiv.) was added at 0 °C and the solution was allowed to warm to rt and left to stir for 18 h under an inert atmosphere of N_2. The reaction was quenched by adding MeOH (0.5 mL) and the solvent was evaporated. The crude was dissolved in CH_2Cl_2 (1% NEt_3) / H_2O (1:1; 25 mL) and the product was extracted with CH_2Cl_2 (2 x 10 mL). The combined organic layers were washed with H_2O (25 mL) and the solvent was removed *in vacuo* to give a crude product. This material was purified by flash chromatography on silica (CH_2Cl_2 / 2% MeOH / 3% NEt_3) to give the title compound as a colourless oil (213 mg, 0.6 mmol, 34%).

^{1}H NMR (400 MHz, $CDCl_3$) δ 7.47 (dt, *J* = 8.2, 1.7 Hz, 4H, H_8), 7.34 (d, *J* = 8.2 Hz, 2H, H_3), 7.26 (td, *J* = 7.7, 3.6 Hz, 4H, H_9), 7.20 – 7.14 (m, 2H, H_{10}), 7.08 (d, *J* = 8.2 Hz, 2H, H_4), 2.71 (t, *J* = 7.2 Hz, 2H, H_{16}), 2.31 (s, 3H, H_6), 2.18 – 2.07 (m, 2H, H_{11}), 1.53 – 1.43 (m, 4H, $H_{12\ \&\ 15}$), 1.34 – 1.24 (m, 4H, $H_{13\ \&\ 14}$).

^{13}C NMR (101 MHz, $CDCl_3$) δ 146.6, 143.5, 135.8, 128.8, 128.7, 128.6, 127.8, 126.2, 70.7, 43.6, 41.8, 32.5, 31.0, 27.3, 26.9, 21.1.

HRMS-ESI (m/z) Calculated for $C_{26}H_{32}N_2Na$ $[M+Na]^+$, 395.2458; found 395.2458.

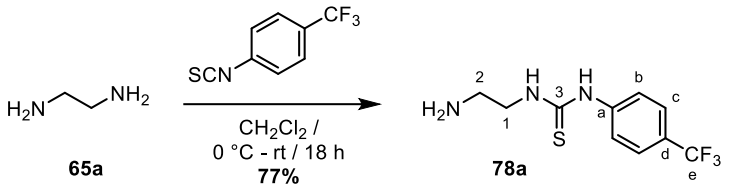

1-Ethylamine-3-(4-trifluoromethyl-phenyl)thiourea 78a. 4-(Trifluoromethyl)phenyl isothiocyanate (200 mg, 1.0 mmol, 1 equiv.) in anhydrous CH_2Cl_2 (2 mL) was added dropwise to a stirred solution of ethylene diamine **65a** (0.46 mL, 414 mg, 6.9 mmol, 7 equiv.) dissolved in anhydrous CH_2Cl_2 (4 mL) cooled with an ice bath. The reaction mixture was left to stir at 0 °C for 1h before allowing it to warm to rt and leaving to stir overnight under an inert atmosphere of N_2. The reaction mixture was diluted with CH_2Cl_2 (25 mL) and extracted with sat. $NH_4Cl_{(aq)}$ (3 × 25 mL). The combined aqueous layers were neutralised with $NaOH_{(aq)}$ and extracted with CH_2Cl_2 (12 × 25 mL). To give a crude material which was purified by flash chromatography on silica ($CHCl_3$ / MeOH / H_2O; 65:25:4) to give the title compound as a colourless oil (200 mg, 0.76 mmol, 77%).

^{1}H NMR (400 MHz, CD_3OD) δ 7.73 (d, *J* = 8.5 Hz, 2H, $H_{b\ or\ c}$), 7.58 (d, *J* = 8.5 Hz, 2H, $H_{b\ or\ c}$), 3.83 (t, *J* = 5.8 Hz, 2H, H_1), 3.08 (t, *J* = 6.0 Hz, 2H, H_2).

^{13}C NMR (101 MHz, CD_3OD) δ 183.3 (C_3), 144.2, 127.0 (q, $J_{C\text{-}F}$ = 15.5 Hz), 126.7 (q, $J_{C\text{-}F}$ = 3.7 Hz), 124.4, 124.2, 44.7, 40.9.

^{19}F NMR (377 MHz, CD_3OD) δ -63.58.

HRMS-ESI (m/z) Calculated for $C_{10}H_{13}F_3N_3S$ $[M+H]^+$, 264.0777; found 264.0775.

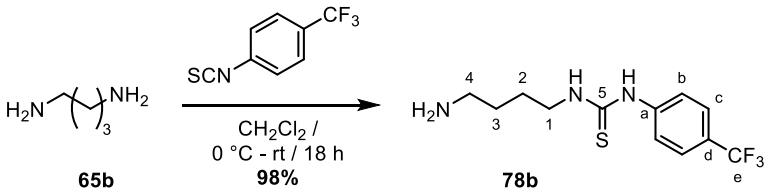

1-Butylamine-3-(4-trifluoromethyl-phenyl)thiourea 78b. 4-(Trifluoromethyl)phenyl isothiocyanate (100 mg, 0.5 mmol, 1 equiv.) in anhydrous CH_2Cl_2 (1 mL) was added dropwise to a stirred solution of 1,4-diaminobutane **65b** (310 mg, 3.5 mmol, 7 equiv.) dissolved in anhydrous CH_2Cl_2 (2 mL) cooled with an ice bath. The reaction mixture was left to stir at 0 °C for 1h before allowing it to warm to rt and leaving to stir overnight under an inert atmosphere of N_2. Afterwards, the solvent was removed *in vacuo* and the crude product was purified by

flash chromatography on silica ($CHCl_3$ / MeOH / H_2O; 65:25:4) to give the product as a colourless oil (140 mg, 0.48 mmol, 98%).

^{1}H NMR (400 MHz, CD_3OD) δ 7.70 (d, *J* = 8.5 Hz, 2H, $H_{b\ or\ c}$), 7.58 (d, *J* = 8.6 Hz, 2H, $H_{b\ or\ c}$), 3.63 (t, *J* = 6.3 Hz, 2H, H_1), 2.95 – 2.89 (m, 2H, H_4), 1.74 – 1.68 (m, 4H, $H_{2\ and\ 3}$).

^{13}C NMR (101 MHz, CD_3OD) δ 182.5 (C_5), 144.3, 127.1 (m), 126.8 (q, $J_{C\text{-}F}$ = 3.7 Hz), 124.4, 123.9, 44.5 (C_1), 40.8 (C_4), 26.9, 26.9.

^{19}F NMR (377 MHz, CD_3OD) δ -63.54.

HRMS-ESI (m/z) Calculated for $C_{12}H_{17}F_3N_3S$ $[M+H]^+$, 292.1090; found 292.1087.

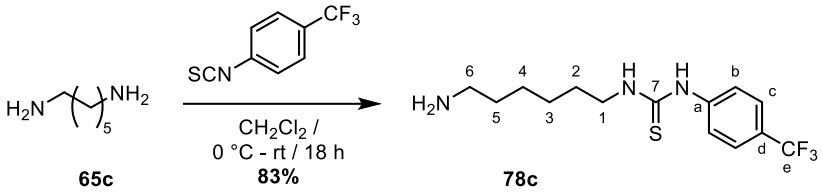

1-Hexylamine-3-(4-trifluoromethyl-phenyl)thiourea 78c. 4-(Trifluoromethyl)phenyl isothiocyanate (200 mg, 1.0 mmol, 1 equiv.) in anhydrous CH_2Cl_2 (2 mL) was added dropwise to a stirred solution of 1,6-diaminohexane **65c** (800 mg, 6.9 mmol, 7 equiv.) dissolved in anhydrous CH_2Cl_2 (2 mL) cooled with an ice bath. The reaction mixture was left to stir at 0 °C for 1h before allowing it to warm to rt and leaving to stir overnight under an inert atmosphere of N_2. The reaction mixture was diluted with CH_2Cl_2 (25 mL) and washed with H_2O (8 × 25 mL) to give the product as a colourless oil (260 mg, 0.81 mmol, 83%).

^{1}H NMR (400 MHz, CD_3OD) δ 7.67 (d, *J* = 8.5 Hz, 2H, $H_{b\ or\ c}$), 7.59 (d, *J* = 8.6 Hz, 2H, $H_{b\ or\ c}$), 3.59 (t, *J* = 7.5 Hz, 2H, H_1), 2.97 – 2.59 (m, 2H, H_6), 1.83 – 1.62 (m, 2H, H_2), 1.62 – 1.53 (m, 2H, H_5), 1.47 – 1.35 (m, 4H, $H_{3\ and\ 4}$).

^{13}C NMR (101 MHz, CD_3OD) δ 182.3 (C_7), 144.3, 127.1 (m), 126.8 (m), 124.4, 123.9, 45.4, 41.8, 31.8, 29.8, 27.6, 27.5.

^{19}F NMR (377 MHz, CD_3OD) δ -63.58.

HRMS-ESI (m/z) Calculated for $C_{14}H_{21}F_3N_3S$ $[M+H]^+$, 320.1403; found 320.1401.

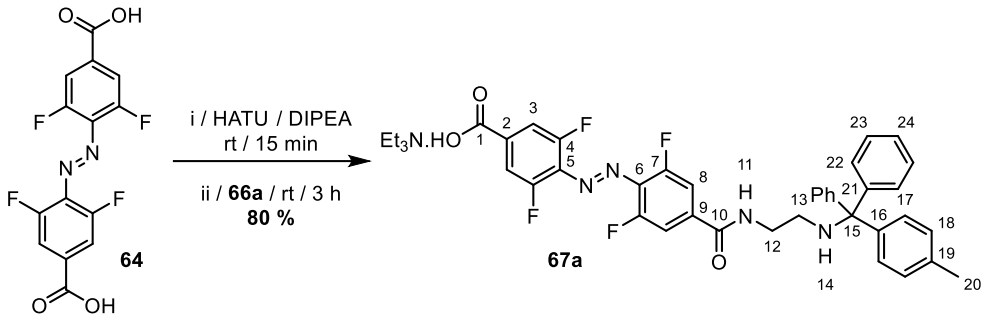

Methyltrityl protected ethyl monoamide tetra-fluoroazobenzene triethylamine salt 67a. Prepared according to the literature procedure.[221] Data consistent with that given in the literature.

^{1}H NMR (400 MHz, $CDCl_3$) δ 7.75 – 7.69 (m, 2H), 7.55 – 7.49 (m, 2H), 7.47 – 7.42 (m, 4H), 7.34 – 7.30 (m, 2H), 7.29 – 7.21 (m, 4H), 7.20 – 7.15 (m, 2H), 7.09 – 7.05 (m, 2H), 6.94 (t, *J* = 5.5 Hz, $1H_{11}$), 3.56 – 3.50 (m, 2H, H_{12}), 3.10 (q, *J* = 7.3 Hz, 6H), 2.46 (t, *J* = 5.9 Hz, 2H, H_{13}), 2.29 (s, 3H), 1.41 (t, *J* = 7.3 Hz, 2H), 1.35 (t, *J* = 7.3 Hz, 9H).

^{13}C {^{19}F} NMR (126 MHz, $CDCl_3$) δ 169.5, 164.5, 155.3, 155.3, 145.9, 142.7, 142.6, 137.5, 136.2, 133.6, 132.4, 128.8, 128.6, 128.6, 128.1, 126.6, 113.5, 111.7, 70.7, 45.5, 43.3, 41.0, 21.0, 8.7.

HRMS-ESI (m/z) Calculated for $C_{36}H_{28}O_3N_4F_4Na$ $[M+Na^{23}]^+$, 663.1990; found 663.1988.

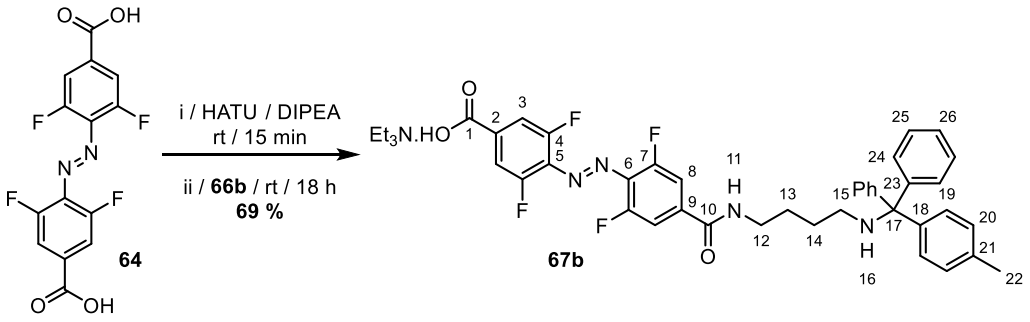

Methyltrityl protected butyl monoamide tetra-fluoroazobenzene triethylamine salt 67b. *Ortho*-tetrafluoroazobenzene-4,4'-dicarboxylic acid **64** (45 mg, 0.13 mmol, 1.2 equiv.) was suspended in anhydrous THF (4.0 mL). HATU (41 mg, 0.11 mmol, 1 equiv.) and DIPEA (37 µL, 0.21 mmol, 2 equiv.) were added and the resulting solution was stirred at rt. After 15 min, *N*-(diphenyl(p-tolyl)methyl)-1,4-butanediamine **66b** (45 mg, 0.13 mmol, 1.2 equiv.) in anhydrous THF (1.4 mL) was added and the solution was stirred overnight at rt. Afterwards, the solvent was removed *in vacuo* and the crude product was purified by flash

chromatography on silica (CH_2Cl_2 / 2% MeOH / 3 % NEt_3) to give the title compound as a red solid triethylamine salt (57 mg, 0.07 mmol, 69%).

HRMS-ESI (m/z) Calculated for $C_{38}H_{32}O_3N_4F_4Na$ $[M+Na]^+$, 691.2303; found 691.2300.

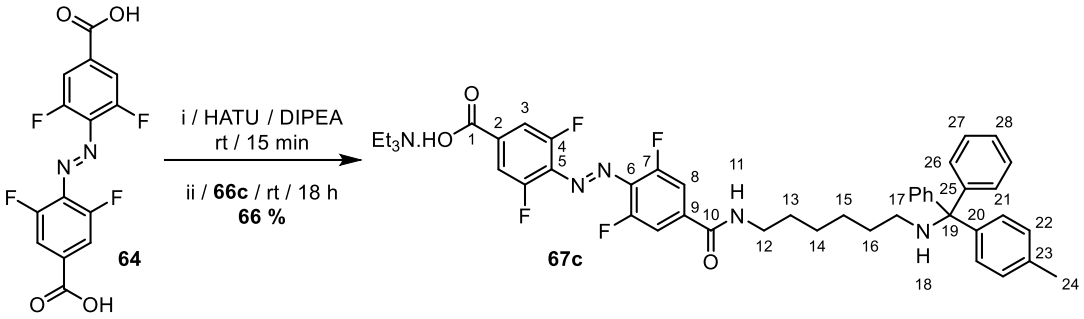

Methyltrityl protected hexyl monoamide tetra-fluoroazobenzene triethylamine salt 67c. *Ortho*-tetrafluoroazobenzene-4,4'-dicarboxylic acid **64** (45 mg, 0.13 mmol, 1.2 equiv.) was suspended in anhydrous THF (4.0 mL). HATU (41 mg, 0.11 mmol, 1 equiv.) and DIPEA (37 µL, 0.21 mmol, 2 equiv.) were added and the resulting solution was stirred at rt. After 15 min, *N*-(diphenyl(p-tolyl)methyl)-1,6-hexanediamine **66c** (48 mg, 0.13 mmol, 1.2 equiv.) in anhydrous THF (1.4 mL) was added and the solution was stirred overnight at rt. Afterwards, the solvent was removed *in vacuo* and the crude product was purified by flash chromatography on silica (CH_2Cl_2 / 2% MeOH / 3 % NEt_3) to give the product as the triethylamine salt as a red solid (57 mg, 0.07 mmol, 66%).

HRMS-ESI (m/z) Calculated for $C_{40}H_{36}O_3N_4F_4Na$ $[M+Na^{23}]^+$, 719.2616; found 719.2615.

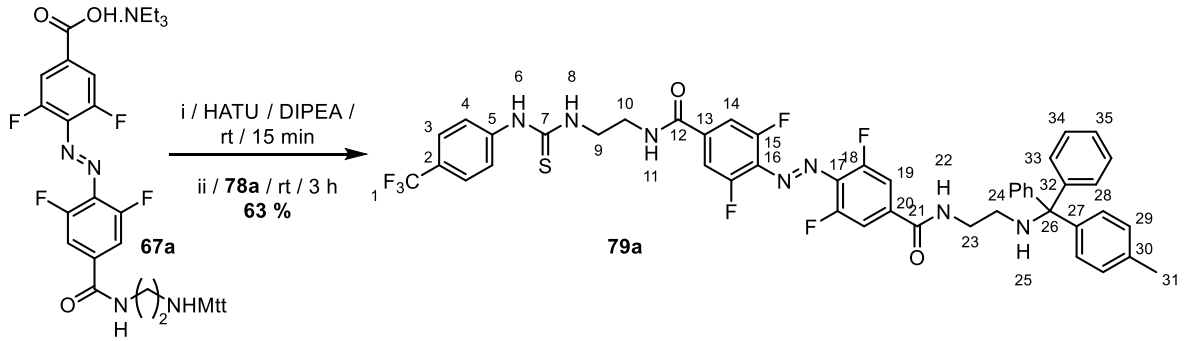

Methyltrityl protected thiourea ethyl tetra-fluoroazobenzene 79a. Methyltrityl protected 2-carbon monoamide azobenzene **67a** (40 mg, 0.054 mmol, 1 equiv.) was suspended in anhydrous THF (4.0 mL). HATU (27 mg, 0.07 mmol, 1.3 equiv.) and DIPEA (24 µL, 0.14 mmol, 2.6 equiv.) were added and the resulting solution was stirred at rt. After 15 min, 1-ethylamine-3-(4-trifluoromethyl-phenyl)thiourea **78a** (19 mg, 0.07 mmol, 1.3 equiv.) in anhydrous THF

(1.5 mL) was added and the solution was stirred overnight at rt. Afterwards, the solvent was removed *in vacuo* and the crude product was purified by flash chromatography on silica (CH_2Cl_2 / 20% Me_2CO) to give the title compound as a red solid (30 mg, 0.034 mmol, 63%).

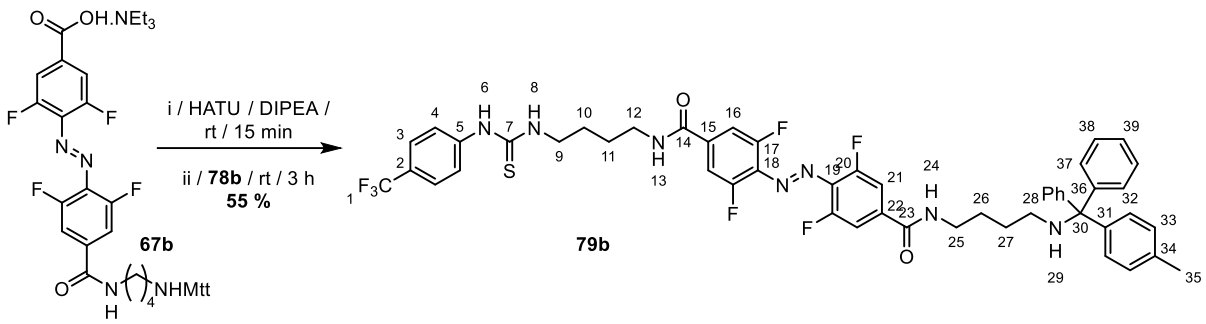

Methyltrityl protected thiourea butyl tetra-fluoroazobenzene 79b. Methyltrityl protected 4-carbon monoamide azobenzene **67b** (40 mg, 0.052 mmol, 1 equiv.) was suspended in anhydrous THF (4.0 mL). HATU (25.7 mg, 0.07 mmol, 1.3 equiv.) and DIPEA (23.5 µL, 0.14 mmol, 2.6 equiv.) were added and the resulting solution was stirred at rt. After 15 min, 1-butylamine-3-(4-trifluoromethyl-phenyl)thiourea **78b** (20 mg, 0.07 mmol, 1.3 equiv.) in anhydrous THF (1.5 mL) was added and the solution was stirred overnight at rt. Afterwards, the solvent was removed *in vacuo* and the crude product was purified by flash chromatography on silica (CH_2Cl_2 / 20% Me_2CO) to give the product as a red solid (27 mg, 0.029 mmol, 55%).

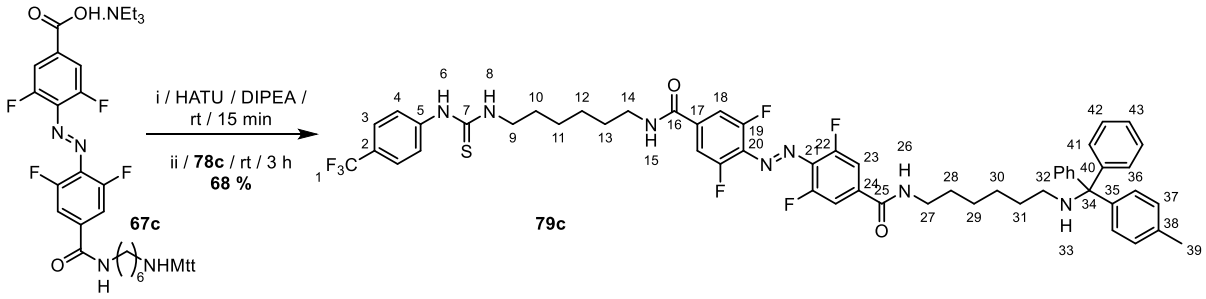

Methyltrityl protected thiourea hexyl tetra-fluoroazobenzene 79c. Methyltrityl protected 6-carbon monoamide azobenzene **67c** (40 mg, 0.05 mmol, 1 equiv.) was suspended in anhydrous THF (4.0 mL). HATU (24.8 mg, 0.07 mmol, 1.3 equiv.) and DIPEA (22.7 µL, 0.14 mmol, 2.6 equiv.) were added and the resulting solution was stirred at rt. After 15 min, 1-hexylamine-3-(4-trifluoromethyl-phenyl)thiourea **78c** (21 mg, 0.07 mmol, 1.3 equiv.) in anhydrous THF (1.5 mL) was added and the solution was stirred overnight at rt. Afterwards, the solvent was removed *in vacuo* and the crude product was purified by flash

chromatography on silica (CH_2Cl_2 / 20% Me_2CO) to give the title compound as a red solid (34 mg, 0.034 mmol, 68%).

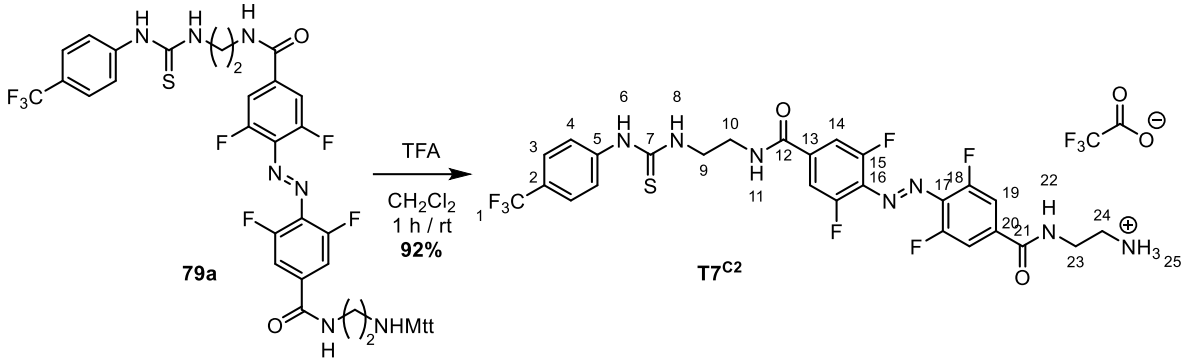

Amino thiourea ethyl tetra-fluoroazobenzene TFA salt T7^{C2}. Methyltrityl protected 2-carbon thiourea azobenzene **79a** (8 mg, 0.009 mmol, 1 equiv.) was dissolved in a solution of TFA (20 µL, 0.26 mmol) in CH_2Cl_2 (1 mL) and left to stir at rt for 1 h. MeOH (1 mL) was added to quench the reaction and solvent was removed *in vacuo* to give a crude red solid. The crude material was triturated with CH_2Cl_2 to give the title compound as a red solid (6.2 mg, 0.008 mmol, 92%).

^{1}H NMR (400 MHz, CD_3OD) δ 7.75 – 7.66 (m, 4H, $H_{14,19}$), 7.62 (s, 4H, $H_{3,4}$), 3.93 – 3.89 (m, 2H, H_{24}), 3.74 – 3.61 (m, 4H, $H_{10,23}$), 3.20 (t, *J* = 5.9 Hz, 2H, H_9).

^{13}C {^{19}F} NMR (126 MHz, CD_3OD) δ 183.1, 167.4, 167.2, 166.8, 166.5, 163.1, 157.6, 153.6, 151.7, 143.7, 138.8, 137.7, 127.5, 127.1, 125.7, 124.5, 113.2, 112.8, 44.7, 40.9, 40.8, 38.8.

^{19}F NMR (377 MHz, CD_3OD) δ -63.67, -76.94, -121.55.

HRMS-ESI (m/z) Calculated for $C_{26}H_{23}O_2N_7F_7S$ $[M+H]^+$, 630.1517; found 630.1505.

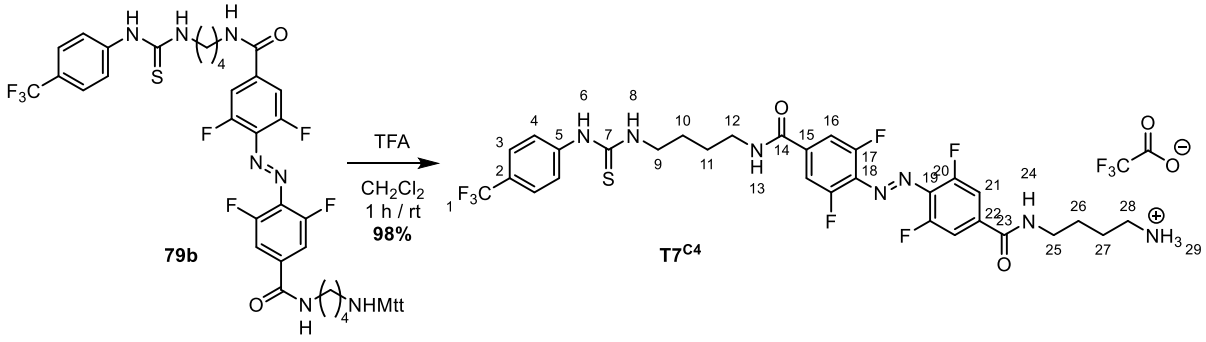

Amino thiourea butyl tetra-fluoroazobenzene TFA salt T7^{C4}. Methyltrityl protected 4-carbon thiourea azobenzene **79b** (12 mg, 0.013 mmol, 1 equiv.) was dissolved in a solution of TFA (20

µL, 0.26 mmol) in CH_2Cl_2 (1 mL) and left to stir at rt for 1 h. MeOH (1 mL) was added to quench the reaction and solvent was removed *in vacuo* to give a crude red solid. The crude material was triturated with CH_2Cl_2 to give the title compound as a red solid (10 mg, 0.013 mmol, 98%).

^{1}H NMR (400 MHz, CD_3OD) δ 7.70 – 7.65 (m, 4H, $H_{16,21}$), 7.63 – 7.60 (m, 4H, $H_{3,4}$), 3.68 – 3.63 (m, 2H, H_{28}), 3.53 – 3.43 (m, 4H, $H_{12,25}$), 3.06 – 2.96 (m, 2H, H_9), 1.78 – 1.69 (m, 8H, $H_{10,11,26,27}$).

^{13}C {^{19}F} NMR (126 MHz, CD_3OD) δ 182.5, 166.5, 166.4, 166.3, 166.2, 163.0, 157.5, 155.3, 153.6, 151.7, 144.1, 139.4, 138.3, 127.0, 125.7, 124.0, 113.0, 112.7, 45.2, 40.4, 40.3, 40.2, 27.6, 27.4, 27.3, 26.0.

^{19}F NMR (377 MHz, CD_3OD) δ -63.51, -76.83, -121.44.

HRMS-ESI (m/z) Calculated for $C_{30}H_{31}O_2N_7F_7S$ $[M+H]^+$, 686.2143; found 686.2126.

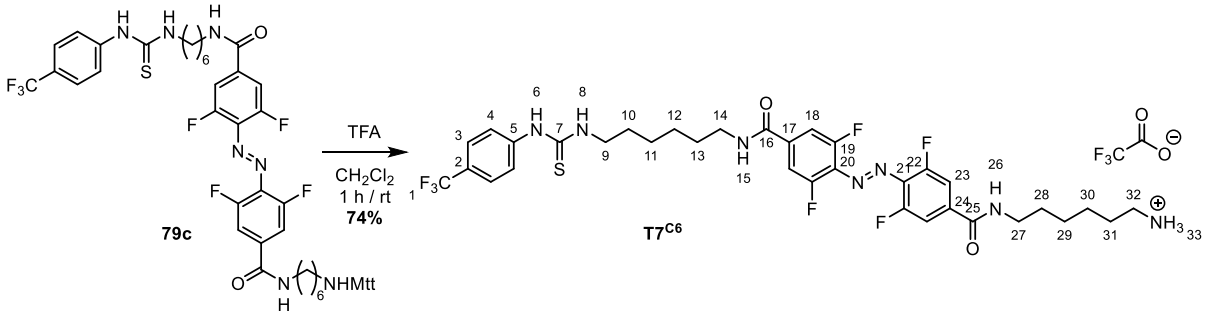

Amino thiourea hexyl tetra-fluoroazobenzene TFA salt T7^{C6}. Methyltrityl protected 6-carbon thiourea azobenzene **79c** (11 mg, 0.011 mmol, 1 equiv.) was dissolved in a solution of TFA (20 µL, 0.26 mmol) in CH_2Cl_2 (1 mL) and left to stir at rt for 1 h. MeOH (1 mL) was added to quench the reaction and solvent was removed *in vacuo* to give a crude red solid. The crude material was triturated with CH_2Cl_2 to give the title compound as a red solid (7 mg, 0.008 mmol, 74%).

^{1}H NMR (400 MHz, CD_3OD) δ 7.70 – 7.64 (m, 4H, $H_{18,23}$), 7.64 – 7.58 (m, 4H, $H_{3,4}$), 3.62 – 3.57 (m, 2H, H_{32}), 3.49 – 3.37 (m, 4H, $H_{14,27}$), 3.01 – 2.87 (m, 2H, H_9), 1.76 – 1.63 (m, 8H, $H_{10,13,28,31}$), 1.54 – 1.42 (m, 8H, $H_{11,12,29,30}$).

^{13}C {^{19}F} NMR (126 MHz, CD_3OD) δ 182.4, 166.4, 166.3, 166.2, 166.1, 163.0, 157.6, 155.3, 153.6, 151.7, 144.2, 139.6, 138.5, 126.9, 125.8, 123. 9, 112.9, 112.6, 45.4, 41.1, 40.9, 40.6, 30.2, 30.1, 29.8, 28.5, 27.6, 27.5, 27.4, 27.0.

^{19}F NMR (377 MHz, CD_3OD) δ -63.59, -76.92, -121.57.

HRMS-ESI (m/z) Calculated for $C_{34}H_{39}O_2N_7F_7S$ $[M+H]^+$, 742.2769; found 742.2759.

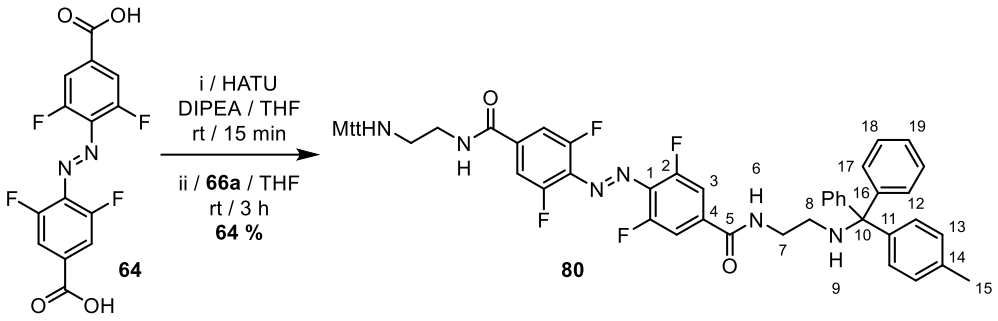

80. Dicarboxylic acid azobenzene **64** (40 mg, 0.12 mmol, 1 equiv.) was suspended in anhydrous THF (4.0 mL). HATU (98 mg, 0.26 mmol, 2.2 equiv.) and DIPEA (90 µL, 0.51 mmol, 4.4 equiv.) were added and the resulting solution was stirred at rt. After 15 min, *N*-(diphenyl(*p*-tolyl)methyl)-1,2-ethanediamine **66a** (82 mg, 0.26 mmol, 2.2 equiv.) in anhydrous THF (2 mL) was added and the solution was stirred overnight at rt. Afterwards, the solvent was removed *in vacuo* and the crude product was purified by flash chromatography on silica (CH_2Cl_2 / 0 - 15% EtOAc) to give the title compound as a red solid (57 mg, 0.07 mmol, 64%).

^{1}H NMR (400 MHz, $CDCl_3$) δ 7.48 – 7.40 (m, 12H, $H_{3,17}$), 7.32 – 7.28 (m, 4H, H_{12}), 7.25 – 7.22 (m, 8H, H_{18}), 7.19 – 7.15 (m, 4H, H_{19}), 7.08 – 7.04 (m, 4H, H_{13}), 6.71 (brs, 2H, H_6), 3.56 – 3.47 (m, 4H, H_7), 2.71 – 2.41 (m, 4H, H_8), 2.27 (s, 6H, H_{15}).

^{13}C NMR (101 MHz, $CDCl_3$) δ 164.4, 156.8 (m), 154.2 (m), 145.6, 142.5, 136.4, 133.3, 128.9, 128.6, 128.2, 128.0, 126.8, 111.7 (d, $J_{C\text{-}F}$ = 22 Hz), 70.9, 43.4, 40.9, 21.1.

^{19}F NMR (377 MHz, $CDCl_3$) δ -118.45.

HRMS-ESI (m/z) Calculated for $C_{58}H_{51}O_2N_6F_4$ $[M+H]^+$, 939.4004; found 939.4003.

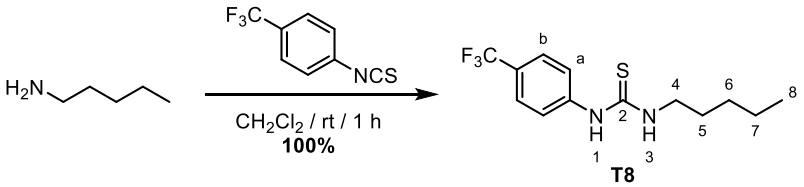

1-Pentyl-3-(4-trifluoromethyl-phenyl)thiourea T8. 4-(Trifluoromethyl)phenyl isothiocyanate (40 mg, 0.2 mmol, 1 equiv.) in anhydrous CH_2Cl_2 (0.5 mL) was added dropwise to a stirred solution of *n*-pentylamine (21 mg, 0.24 mmol, 1.2 equiv.) dissolved in anhydrous CH_2Cl_2 (1 mL). The reaction mixture was left to stir for 1h under an inert atmosphere of N_2. Afterwards, the solvent was removed *in vacuo* to give the title compound as a white solid (57 mg, 0.20 mmol, 100%).

^{1}H NMR (500 MHz, $CDCl_3$) δ 8.05 (brs, 1H, H_1), 7.68 (d, *J* = 8.3 Hz, 2H, $H_{a\ or\ b}$), 7.33 (d, *J* = 8.1 Hz, 2H, $H_{a\ or\ b}$), 6.12 (brs, 1H, H_3), 3.67 – 3.59 (m, 2H, H_4), 1.66 – 1.56 (m, 2H, H_5), 1.40 – 1.26 (m, 4H, $H_{6,7}$), 0.90 (t, *J* = 7.0 Hz, 3H, H_8).

^{13}C {^{19}F} NMR (126 MHz, $CDCl_3$) δ 180.5, 139.9, 128.6, 127.5, 124.2, 123.8, 45.9, 29.2, 28.7, 22.4, 14.1.

^{19}F NMR (471 MHz, $CDCl_3$) δ -62.49.

HRMS-ESI (m/z) Calculated for $C_{13}H_{18}F_3N_2S$ $[M+H]^+$, 291.1137; found 291.1137.

5.6.2 Chapter 4 Transport Activity Data

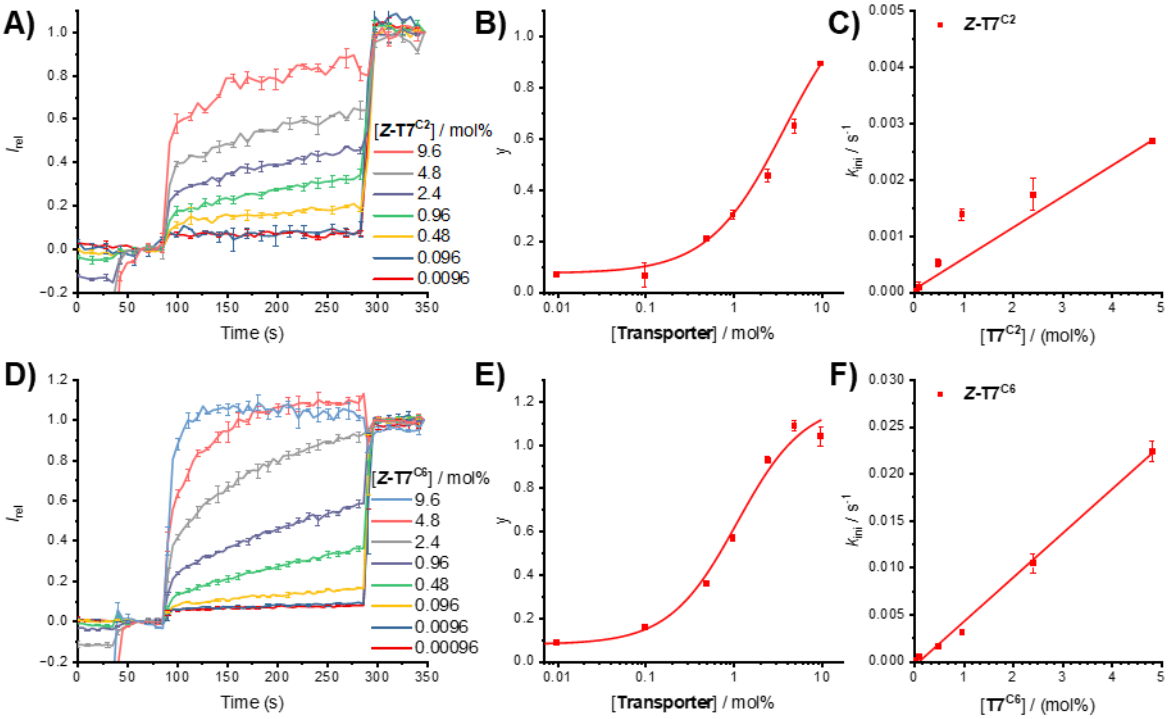

Figure 5.8 Ammonium anchored mobile carrier transport activity of Z-T7^{C2} and Z-T7^{C6}. *A) HPTS transport data for **Z-T7^{C2}** (0.0096 – 9.6 mol% to lipid, PSS$_{530}$ = 8:92 E:Z) added externally in DMSO to POPC LUVs. B) Concentration dependent activity of **Z-T7^{C2}** fit to the Hill equation. C) Dependence of k_{ini} on [**T7^{C2}**] for the E-rich PSS generated by ex situ photo-isomerisation with 530 nm light fit to a straight line. D) HPTS transport data for **Z-T7^{C6}** (0.00096 – 9.6 mol% to lipid, PSS$_{530}$ = 8:92 E:Z) added externally in DMSO to POPC LUVs. B) Concentration dependent activity of **Z-T7^{C6}** fit to the Hill equation. C) Dependence of k_{ini} on [**T7^{C6}**] for the E-rich PSS generated by ex situ photo-isomerisation with 530 nm light fit to a straight line. Error bars denote the standard deviations from two runs.*

References

1 R. M. Vaden, K. P. Guillen, J. M. Salvant, C. B. Santiago, J. B. Gibbons, S. S. Pathi, S. Arunachalam, M. S. Sigman, R. E. Looper and B. E. Welm, *ACS Chem. Biol.*, 2019, **14**, 106–117.

2 M. Mayer and J. Yang, *Acc. Chem. Res.*, 2013, **46**, 2998–3008.

3 Y. Elani, R. V. Law and O. Ces, *Nat. Commun.*, 2014, **5**, 1–5.

4 J. N. Israelachvili, D. J. Mitchell and B. W. Ninham, *BBA - Biomembranes*, 1977, **470**, 185–201.

5 S. J. Singer and G. L. Nicolson, *Science*, 1972, **175**, 720–731.

6 P. Läuger, *Angew. Chem. Int. Ed.*, 1985, **24**, 905–923.

7 R. Benz, G. Stark, K. Janko and P. Läuger, *J. Membr. Biol.*, 1973, **14**, 339–364.

8 E. Sato, K. Hirata, J. M. Lisy, S. I. Ishiuchi and M. Fujii, *J. Phys. Chem. Lett.*, 2021, **12**, 1754–1758.

9 M. M. Shemyakin, Y. A. Ovchinnikov, V. T. Ivanov, V. K. Antonov, E. I. Vinogradova, A. M. Shkrob, G. G. Malenkov, A. V. Evstratov, I. A. Laine, E. I. Melnik and I. D. Ryabova, *J. Membr. Biol.*, 1969, **1**, 402–430.

10 S. Huang, Y. Liu, W. Liu, P. Neubauer and J. Li, *Microorganisms*, 2021, **9**, 780.

11 A. Fürstner, *Angew. Chem. Int. Ed.*, 2003, **42**, 3582–3603.

12 S. Cheung, D. Wu, H. C. Daly, D. Scholz, P. A. Gale, D. F. O'Shea, N. Busschaert, M. Morgunova and J. C. Simpson, *Chem*, 2018, **4**, 879–895.

13 J. L. Seganish and J. T. Davis, *Chem. Commun.*, 2005, 5781–5783.

14 K. Neupert-Laves and M. Dobler, *Helv. Chim. Acta.*, 1975, **58**, 432–442.

15 H. Li, C. Y. Huang, E. G. Govorunova, C. T. Schafer, O. A. Sineshchekov, M. Wang, L. Zheng and J. L. Spudich, *Elife*, 2019, **8**, 1–21.

16 Y. S. Kim, H. E. Kato, K. Yamashita, S. Ito, K. Inoue, C. Ramakrishnan, L. E. Fenno, K. E. Evans, J. M. Paggi, R. O. Dror, H. Kandori, B. K. Kobilka and K. Deisseroth, *Nature*, 2018, **561**, 343–348.

17 H. E. Kato, Y. S. Kim, J. M. Paggi, K. E. Evans, W. E. Allen, C. Richardson, K. Inoue, S. Ito, C. Ramakrishnan, L. E. Fenno, K. Yamashita, D. Hilger, S. Y. Lee, A. Berndt, K. Shen, H. Kandori, R. O. Dror, B. K. Kobilka and K. Deisseroth, *Nature*, 2018, **561**, 349–371.

18 A. Zhou, A. Rohou, D. G. Schep, J. V. Bason, M. G. Montgomery, J. E. Walker, N. Grigorieffniko and J. L. Rubinstein, *Elife*, 2015, **4**, e10180.

19 S. Nath, *Biophys. Chem.*, 2018, **241**, 20–26.

20 A. Barba-Bon, M. Nilam and A. Hennig, *ChemBioChem*, 2020, **21**, 886–910.

21 L. E. Bickerton, T. G. Johnson, A. Kerckhoffs and M. J. Langton, *Chem. Sci.*, 2021, **12**, 11252–11274.

22 W. L. Huang, X. D. Wang, Y. F. Ao, Q. Q. Wang and D. X. Wang, *J. Am. Chem. Soc.*, 2020, **142**, 13273–13277.

23 W. L. Huang, X. D. Wang, Y. F. Ao, Q. Q. Wang and D. X. Wang, *Angew. Chem. Int. Ed.*, 2023, **62**, e202302198.

24 R. Dutzler, E. B. Campbell, M. Cadene, B. T. Chait and R. MacKinnon, *Nature*, 2002, **415**, 287–294.

25 P. Xin, L. Xu, W. Dong, L. Mao, J. Guo, J. Bi, S. Zhang, Y. Pei and C.-P. Chen, *Angew. Chem. Int. Ed.*, 2023, **62**, e202217859.

26 Y. Zhou, J. H. Morais-Cabral, A. Kaufman and R. Mackinnon, *Nature*, 2001, **414**, 43–48.

27 N. Sakai and S. Matile, *Langmuir*, 2013, 29, 9031–9040.
28 A. Gilles and M. Barboiu, *J. Am. Chem. Soc.*, 2016, **138**, 426–432.
29 T. Saha, A. Gautam, A. Mukherjee, M. Lahiri and P. Talukdar, *J. Am. Chem. Soc.*, 2016, **138**, 16443–16451.
30 F. C. Cossarizza A., Baccaranicontri M., Kalashnikova G., *Biochem. Biophys. Res. Commun.*, 1993, **197**, 40–45.
31 G. Picci, S. Marchesan and C. Caltagirone, *Biomedicines*, 2022, 10, 885.
32 P. A. Gale, R. Pérez-Tomás and R. Quesada, *Acc. Chem. Res.*, 2013, **46**, 2801–2813.
33 X. Wu, P. Wang, W. Lewis, Y. B. Jiang and P. A. Gale, *Nat. Commun.*, 2022, **13**, 1–7.
34 T. G. Johnson, A. Docker, A. Sadeghi-Kelishadi and M. J. Langton, *Chem. Sci.*, 2023, **14**, 5006–5013.
35 M. J. Spooner and P. A. Gale, *Chem. Commun.*, 2015, **51**, 4883–4886.
36 V. Saggiomo, S. Otto, I. Marques, V. Félix, T. Torroba and R. Quesada, *Chem. Commun.*, 2012, **48**, 5274–5276.
37 N. J. Knight, E. Hernando, C. J. E. Haynes, N. Busschaert, H. J. Clarke, K. Takimoto, M. García-Valverde, J. G. Frey, R. Quesada and P. A. Gale, *Chem. Sci.*, 2016, **7**, 1600–1608.
38 B. Testa, P. Crivori, M. Reist and P.-A. Carrupt, *Perspect. Drug Discov. Des.*, 2000, **19**, 179–211.
39 H. Valkenier, C. J. E. Haynes, J. Herniman, P. A. Gale and A. P. Davis, *Chem. Sci.*, 2014, **5**, 1128–1134.
40 C. M. Dias, H. Valkenier and A. P. Davis, *Chem. Eur. J.*, 2018, **24**, 6262–6268.
41 N. Busschaert, N. Busschaert, M. Wenzel, C. J. E. Haynes, J. R. Hiscock, I. L. Kirby, L. E. Karagiannidis, S. J. Moore, N. J. Wells, J. Herniman, G. J. Langley, P. N. Horton, M. E. Light, I. Marques, P. J. Costa, V. Félix, J. G. Frey and P. A. Gale, *Chem. Sci.*, 2013, **4**, 3036–3045.
42 S. Hussain, P. R. Brotherhood, L. W. Judd and A. P. Davis, *J. Am. Chem. Soc.*, 2011, **133**, 1614–1617.
43 H. Valkenier, L. W. Judd, H. Li, S. Hussain, D. N. Sheppard and A. P. Davis, *J. Am. Chem. Soc.*, 2014, **136**, 12507–12512.
44 N. Busschaert, I. L. Kirby, S. Young, S. J. Coles, P. N. Horton, M. E. Light and P. A. Gale, *Angew. Chem. Int. Ed.*, 2012, **51**, 4426–4430.
45 N. Busschaert, R. B. P. Elmes, D. D. Czech, X. Wu, I. L. Kirby, E. M. Peck, K. D. Hendzel, S. K. Shaw, B. Chan, B. D. Smith, K. A. Jolliffe and P. A. Gale, *Chem. Sci.*, 2014, **5**, 3617–3626.
46 L. Nie, Z. Li, J. Han, X. Zhang, R. Yang, W. X. Liu, F. Y. Wu, J. W. Xie, Y. F. Zhao and Y. B. Jiang, *J. Org. Chem.*, 2004, **69**, 6449–6454.
47 J. Yang, G. Yu, J. L. Sessler, I. Shin, P. A. Gale and F. Huang, *Chem*, 2021, **7**, 3256–3291.
48 P. A. Gale, J. T. Davis and R. Quesada, *Chem. Soc. Rev.*, 2017, **46**, 2497–2519.
49 J. T. Davis, P. A. Gale and R. Quesada, *Chem. Soc. Rev.*, 2020, **49**, 6056–6086.
50 H. Li, H. Valkenier, L. W. Judd, P. R. Brotherhood, S. Hussain, J. A. Cooper, O. Jurček, H. A. Sparkes, D. N. Sheppard and A. P. Davis, *Nat. Chem.*, 2016, **8**, 24–32.
51 S. K. Ko, S. K. Kim, A. Share, V. M. Lynch, J. Park, W. Namkung, W. Van Rossom, N. Busschaert, P. A. Gale, J. L. Sessler and I. Shin, *Nat. Chem.*, 2014, **6**, 885–892.
52 H. Li, H. Valkenier, A. G. Thorne, C. M. Dias, J. A. Cooper, M. Kieffer, N. Busschaert, P. A. Gale, D. N. Sheppard and A. P. Davis, *Chem. Sci.*, 2019, **10**, 9663–9672.
53 J. L. Sessler, L. R. Eller, W. S. Cho, S. Nicolaou, A. Aguilar, J. T. Lee, V. M. Lynch and D. J. Magda, *Angew. Chem. Int. Ed.*, 2005, **44**, 5989–5992.

54 G. Cavallo, P. Metrangolo, R. Milani, T. Pilati, A. Priimagi, G. Resnati and G. Terraneo, *Chem. Rev.*, 2016, **116**, 2478–2601.
55 P. Politzer, J. S. Murray and T. Clark, *Phys. Chem. Chem. Phys.*, 2013, **15**, 11178–11189.
56 J. Y. C. Lim and P. D. Beer, *Chem*, 2018, **4**, 731–783.
57 A. Docker and M. J. Langton, *Trends Chem.*, 2023, **5**, 792–794.
58 C. C. Robertson, R. N. Perutz, L. Brammer and C. A. Hunter, *Chem. Sci.*, 2014, **5**, 4179–4183.
59 A. Vargas Jentzsch, D. Emery, J. Mareda, P. Metrangolo, G. Resnati and S. Matile, *Angew. Chem. Int. Ed.*, 2011, **50**, 11675–11678.
60 A. V. Jentzsch, D. Emery, J. Mareda, S. K. Nayak, P. Metrangolo, G. Resnati, N. Sakai and S. Matile, *Nat. Commun.*, 2012, **3**, 1–8.
61 L. E. Bickerton, A. J. Sterling, P. D. Beer, F. Duarte and M. J. Langton, *Chem. Sci.*, 2020, **11**, 4722–4729.
62 S. Benz, M. Macchione, Q. Verolet, J. Mareda, N. Sakai and S. Matile, *J. Am. Chem. Soc.*, 2016, **138**, 9093–9096.
63 B. Zhou and F. P. Gabbaï, *Chem. Sci.*, 2020, **11**, 7495–7500.
64 B. L. Murphy and F. P. Gabbaï, *J. Am. Chem. Soc.*, 2023, **145**, 19458–19477.
65 L. M. Lee, M. Tsemperouli, A. I. Poblador-Bahamonde, S. Benz, N. Sakai, K. Sugihara and S. Matile, *J. Am. Chem. Soc.*, 2019, **141**, 810–814.
66 G. Park, D. J. Brock, J.-P. Pellois and F. P. Gabbaï, *Chem*, 2019, **5**, 2215–2227.
67 V. M. Gonzalez, G. Park, M. Yang and F. P. Gabbaï, *Dalton Trans.*, 2021, **50**, 17897–17900.
68 K. Yang, H. A. Kotak and C. J. E. Haynes, *Coord. Chem. Rev.*, 2022, **470**, 214705.
69 D. Milano, B. Benedetti, M. Boccalon, A. Brugnara, E. Iengo and P. Tecilla, *Chem. Commun.*, 2014, **50**, 9157–9160.
70 A. Vidal, M. Tosolini, G. Balducci and P. Tecilla, *Eur. J. Org. Chem.*, 2022, e202201121.
71 X. X. Peng, H. Zhang, R. Zhang, Z. H. Li, Z. S. Yang, J. Zhang, S. Gao and J. L. Zhang, *Angew. Chem. Int. Ed.*, 2023, **62**, e202307838.
72 X. X. Peng, H. Zhang, R. Zhang, Z. H. Li, Z. S. Yang, J. Zhang, S. Gao and J. L. Zhang, *Angew. Chem. Int. Ed.*, 2023, **62**, e202307838.
73 M. J. Langton, *Nat. Rev. Chem.*, 2021, **5**, 46–61.
74 N. Kumar and N. Madhavan, *Org. Biomol. Chem.*, 2023, **21**, 5892–5905.
75 J. de Jong, J. E. Bos and S. J. Wezenberg, *Chem. Rev.*, 2023, **123**, 8530–8574.
76 A. Mondal, M. Ahmad, D. Mondal and P. Talukdar, *Chem. Commun.*, 2023, **59**, 1917–1938.
77 Y. R. Choi, B. Lee, J. Park, W. Namkung and K. S. Jeong, *J. Am. Chem. Soc.*, 2016, **138**, 15319–15322.
78 Y. R. Choi, M. K. Chae, D. Kim, M. S. Lah and K. S. Jeong, *Chem. Commun.*, 2012, **48**, 10346–10348.
79 N. J. Roy, S. N. Save, V. K. Sharma, B. Abraham, A. Kuttanamkuzhi, S. Sharma, M. Lahiri and P. Talukdar, *Chem. Eur. J.*, 2023, **29**, e202301412.
80 M. Ahmad, S. A. Gartland and M. J. Langton, *Angew. Chem. Int. Ed.*, 2023, **62** e202308842.
81 C. Lang, X. Zhang, Z. Dong, Q. Luo, S. Qiao, Z. Huang, X. Fan, J. Xu and J. Liu, *Nanoscale*, 2016, **8**, 2960–2966.
82 G. Park and F. P. Gabbaï, *Chem. Sci.*, 2020, **11**, 10107–10112.
83 M. Fares, X. Wu, D. Ramesh, W. Lewis, P. A. Keller, E. N. W. Howe, R. Pérez-Tomás and P. A. Gale, *Angew. Chem. Int. Ed.*, 2020, **59**, 17614–17621.

84 A. Docker, T. G. Johnson, H. Kuhn, Z. Zhang and M. J. Langton, *J. Am. Chem. Soc.*, 2023, **145**, 2661–2668.

85 S. A. Gartland, T. G. Johnson, E. Walkley and M. J. Langton, *Angew. Chem. Int. Ed.*, 2023, **62**, e202309080.

86 S. B. Salunke, J. A. Malla and P. Talukdar, *Angew. Chem. Int. Ed.*, 2019, **58**, 5354–5358.

87 M. Ahmad, N. J. Roy, A. Singh, D. Mondal, A. Mondal, T. Vijayakanth, M. Lahiri and P. Talukdar, *Chem. Sci.*, 2023, **14**, 8897–8904.

88 L. E. Bickerton and M. J. Langton, *Chem. Sci.*, 2022, **13**, 9531–9536.

89 J. D. Harris, M. J. Moran and I. Aprahamian, *Proc. Natl. Acad. Sci. U.S.A.*, 2018, **115**, 9414–9422.

90 M. Ahmad, S. Metya, A. Das and P. Talukdar, *Chem. Eur. J.*, 2020, **26**, 8703–8708.

91 T. Jin, *Mater Lett*, 2007, **61**, 805–808.

92 A. Kerckhoffs, Z. Bo, S. E. Penty, F. Duarte and M. J. Langton, *Org. Biomol. Chem.*, 2021, **19**, 9058–9067.

93 A. Kerckhoffs and M. J. Langton, *Chem. Sci.*, 2020, **11**, 6325–6331.

94 S. Shinkai, T. Nakaji, T. Ogawa, K. Shigematsu and O. Manabe, *J. Am. Chem. Soc.*, 1981, **103**, 111–115.

95 R. F. Khairutdinov and J. K. Hurst, *Langmuir*, 2004, **20**, 1781–1785.

96 T. Jin, *Chem. Commun.*, 2000, **0**, 1379–1380.

97 Y. R. Choi, G. C. Kim, H. G. Jeon, J. Park, W. Namkung and K. S. Jeong, *Chem. Commun.*, 2014, **50**, 15305–15308.

98 S. J. Wezenberg, L. J. Chen, J. E. Bos, B. L. Feringa, E. N. W. Howe, X. Wu, M. A. Siegler and P. A. Gale, *J. Am. Chem. Soc.*, 2022, **144**, 331–338.

99 T. Fehrentz, M. Schönberger and D. Trauner, *Angew. Chem. Int. Ed.*, 2011, **50**, 12156–12182.

100 J. Volarić, W. Szymanski, N. A. Simeth and B. L. Feringa, *Chem. Soc. Rev.*, 2021, **50**, 12377–12449.

101 T. K. Mukhopadhyay, J. Morstein and D. Trauner, *Curr. Opin. Pharmacol.*, 2022, **63**, 102202.

102 Q. Xiao, W. W. Haoyang, T. Lin, Z. T. Li, D. W. Zhang and J. L. Hou, *Chem. Commun.*, 2021, **57**, 863–866.

103 T. Muraoka, K. Umetsu, K. V. Tabata, T. Hamada, H. Noji, T. Yamashita and K. Kinbara, *J. Am. Chem. Soc.*, 2017, **139**, 18016–18023.

104 T. Yan, S. Liu, C. Li, J. Xu, S. Yu, T. Wang, H. Sun and J. Liu, *Angew. Chem. Int. Ed.*, 2022, **61**, e202210214.

105 P. V. Jog and M. S. Gin, *Org. Lett.*, 2008, **10**, 3693–3696.

106 R. Y. Yang, C. Y. Bao, Q. N. Lin and L. Y. Zhu, *Chin. Chem. Lett.*, 2015, **26**, 851–856.

107 T. Liu, C. Bao, H. Wang, Y. Lin, H. Jia and L. Zhu, *Chem. Commun.*, 2013, **49**, 10311.

108 Y. Zhou, Y. Chen, P. P. Zhu, W. Si, J. L. Hou and Y. Liu, *Chem. Commun.*, 2017, **53**, 3681–3684.

109 W.-Z. Z. Wang, L.-B. B. Huang, S.-P. P. Zheng, E. Moulin, O. Gavat, M. Barboiu and N. Giuseppone, *J. Am. Chem. Soc.*, 2021, **143**, 15653–15660.

110 H. Yang, J. Yi, S. Pang, K. Ye, Z. Ye, Q. Duan, Z. Yan, C. Lian, Y. Yang, L. Zhu, D. H. Qu and C. Bao, *Angew. Chem. Int. Ed.*, 2022, **61**, e202204605.

111 J. Chen, J. C. M. Kistemaker, J. Robertus and B. L. Feringa, *J. Am. Chem. Soc.*, 2014, **136**, 14924–14932.

112 M. A. Watson and S. L. Cockroft, *Chem. Soc. Rev.*, 2016, **45**, 6118–6129.

113 J. Shen, C. Ren and H. Zeng, *Acc. Chem. Res.*, 2022, **55**, 1148–1159.

114 R. Ye, C. Ren, J. Shen, N. Li, F. Chen, A. Roy and H. Zeng, *J. Am. Chem. Soc.*, 2019, **141**, 9788–9792.

115 J. Shen, J. J. Y. Han, R. Ye and H. Zeng, *Sci. China Chem.*, 2021, **64**, 2154–2160.

116 C. Ren, F. Chen, R. Ye, Y. S. Ong, H. Lu, S. S. Lee, J. Y. Ying and H. Zeng, *Angew. Chem. Int. Ed.*, 2019, **58**, 8034–8038.

117 M. Miao, X. Shao and W. Cai, *J. Phys. Chem. B*, 2022, **126**, 1520–1528.

118 N. Li, J. Shen, G. K. Ang, R. Ye and H. Zeng, *CCS Chem.*, 2021, **3**, 2269–2279.

119 S. Chen, Y. Wang, T. Nie, C. Bao, C. Wang, T. Xu, Q. Lin, D. H. Qu, X. Gong, Y. Yang, L. Zhu and H. Tian, *J. Am. Chem. Soc.*, 2018, **140**, 17992–17998.

120 H. Zhang, Y. Guo, C. Chipot, W. Cai and X. Shao, *J. Phys. Chem. Lett.*, 2021, **12**, 3281–3287.

121 S. Pang, X. Sun, Z. Yan, C. Wang, K. Ye, S. Ma, L. Zhu and C. Bao, *Chem. Commun.*, 2023, **59**, 3866–3869.

122 K. Ye, Z. Zhang, Z. Yan, S. Pang, H. Yang, X. Sun, C. Liu, L. Zhu, C. Lian and C. Bao, *Sci. China Chem.*, 2023, **66**, 2300–2308.

123 B. A. McNally, E. J. O'Neil, A. Nguyen and B. D. Smith, *J. Am. Chem. Soc.*, 2008, **130**, 17274–17275.

124 M. E. Weber, P. H. Schlesinger and G. W. Gokel, *J. Am. Chem. Soc.*, 2005, **127**, 636–642.

125 R. Benz, O. Fröhlich and P. Läuger, *BBA - Biomembranes*, 1977, **464**, 465–481.

126 N. Busschaert, S. H. Park, K. H. Baek, Y. P. Choi, J. Park, E. N. W. Howe, J. R. Hiscock, L. E. Karagiannidis, I. Marques, V. Félix, W. Namkung, J. L. Sessler, P. A. Gale and I. Shin, *Nat. Chem.*, 2017, **9**, 667–675.

127 S. H. Park, S. H. Park, E. N. W. Howe, J. Y. Hyun, L. J. Chen, I. Hwang, G. Vargas-Zuñiga, N. Busschaert, P. A. Gale, J. L. Sessler and I. Shin, *Chem*, 2019, **5**, 2079–2098.

128 A. Singh, A. Torres-Huerta, T. Vanderlinden, N. Renier, L. Martínez-Crespo, N. Tumanov, J. Wouters, K. Bartik, I. Jabin and H. Valkenier, *Chem. Commun.*, 2022, **58**, 6255–6258.

129 P. A. Gale, R. Pérez-Tomás and R. Quesada, *Acc. Chem. Res.*, 2013, **46**, 2801–2813.

130 X. Wu, L. W. Judd, E. N. W. Howe, A. M. Withecombe, V. Soto-Cerrato, H. Li, N. Busschaert, H. Valkenier, R. Pérez-Tomás, D. N. Sheppard, Y. B. Jiang, A. P. Davis and P. A. Gale, *Chem*, 2016, **1**, 127–146.

131 A. E. Hess and P. D. Beer, *Org. Biomol. Chem.*, 2016, **14**, 10193–10200.

132 B. R. Mullaney, A. L. Thompson and P. D. Beer, *Angew. Chem. Int. Ed.*, 2014, **53**, 11458–11462.

133 L. E. Bickerton, A. Docker, A. J. Sterling, H. Kuhn, F. Duarte, P. D. Beer and M. J. Langton, *Chem. Eur. J.*, 2021, **27**, 11738–11745.

134 S. J. Moore, M. Wenzel, M. E. Light, R. Morley, S. J. Bradberry, P. Gómez-Iglesias, V. Soto-Cerrato, R. Pérez-Tomás and P. A. Gale, *Chem. Sci.*, 2012, **3**, 2501–2509.

135 A. Docker, J. G. Stevens and P. D. Beer, *Chem. Eur. J.*, 2021, **27**, 14600–14604.

136 S. S. Tatevosyan, Y. N. Kotovshchikov, G. V. Latyshev, D. A. Erzunov, D. V. Sokolova, I. P. Beletskaya and N. V. Lukashev, *J. Org. Chem.*, 2020, **85**, 7863–7876.

137 Y. N. Kotovshchikov, G. V. Latyshev, M. A. Navasardyan, D. A. Erzunov, I. P. Beletskaya and N. V. Lukashev, *Org. Lett.*, 2018, **20**, 4467–4470.

138 D. L. Daleke, K. Hong and D. Papahadjopoulos, *BBA - Biomembranes*, 1990, **1024**, 352–366.

139 A. M. Gilchrist, P. Wang, I. Carreira-Barral, D. Alonso-Carrillo, X. Wu, R. Quesada and P. A. Gale, *Supramol. Chem.*, 2021, **33**, 325–344.

140 B. A. McNally, A. V. Koulov, B. D. Smith, J. B. Joos and A. P. Davis, *Chem. Commun.*, 2005, 1087–1089.

141 L. A. Jowett and P. A. Gale, *Supramol. Chem.*, 2019, **31**, 297–312.

142 J. Frallicciardi, J. Melcr, P. Siginou, S. J. Marrink and B. Poolman, *Nat. Commun.*, 2022, **13**, 1–12.

143 S. Bhosale and S. Matile, *Chirality*, 2006, **18**, 849–856.

144 G. Van Den Bogaart, J. V. Guzmán, J. T. Mika and B. Poolman, *J. Bio. Chem.*, 2008, **283**, 33854–33857.

145 S. J. Moore, M. Wenzel, M. E. Light, R. Morley, S. J. Bradberry, P. Gómez-Iglesias, V. Soto-Cerrato, R. Pérez-Tomás and P. A. Gale, *Chem. Sci.*, 2012, **3**, 2501–2509.

146 L. A. Jowett, E. N. W. Howe, X. Wu, N. Busschaert and P. A. Gale, *Chem. Eur. J.*, 2018, **24**, 10475–10487.

147 S. G. A. McLaughlin and J. P. Dilger, *Physiol. Rev.*, 1980, 60, 825–863.

148 C. Hansch, A. Leo and R. W. Taft, *Chem. Rev.*, 1991, **91**, 165–195.

149 H. Valkenier, C. J. E. Haynes, J. Herniman, P. A. Gale and A. P. Davis, *Chem. Sci.*, 2014, **5**, 1128–1134.

150 V. Saggiomo, S. Otto, I. Marques, V. Félix, T. Torroba and R. Quesada, *Chem. Commun.*, 2012, **48**, 5274–5276.

151 B. A. McNally, A. V. Koulov, T. N. Lambert, B. D. Smith, J. B. Joos, A. L. Sisson, J. P. Clare, V. Sgarlata, L. W. Judd, G. Magro and A. P. Davis, *Chem. Eur. J.*, 2008, **14**, 9599–9606.

152 N. Busschaert, M. Wenzel, M. E. Light, P. Iglesias-Hernández, R. Pérez-Tomás and P. A. Gale, *J. Am. Chem. Soc.*, 2011, **133**, 14136–14148.

153 R. Benz, O. Fröhlich and P. Läuger, *BBA - Biomembranes*, 1977, **464**, 465–481.

154 X. Wu, L. W. Judd, E. N. W. Howe, A. M. Withecombe, V. Soto-Cerrato, H. Li, N. Busschaert, H. Valkenier, R. Pérez-Tomás, D. N. Sheppard, Y. B. Jiang, A. P. Davis and P. A. Gale, *Chem*, 2016, **1**, 127–146.

155 T. G. Johnson, A. Docker, A. Sadeghi-Kelishadi and M. J. Langton, *Chem. Sci.*, 2023, **14**, 5006–5013.

156 H. Valkenier, L. W. Judd, H. Li, S. Hussain, D. N. Sheppard and A. P. Davis, *J. Am. Chem. Soc.*, 2014, **136**, 12507–12512.

157 R. Rosseto and J. Hajdu, *Tet. Lett.*, 2005, **46**, 2941–2944.

158 W. Huang and D. G. Levitt, *Biophys. J.*, 1977, **17**, 111–128.

159 G. Gramse, A. Dols-Perez, M. A. Edwards, L. Fumagalli and G. Gomila, *Biophys. J.*, 2013, **104**, 1257–1262.

160 W. L. Huang, X. D. Wang, Y. F. Ao, Q. Q. Wang and D. X. Wang, *J. Am. Chem. Soc.*, 2020, **142**, 13273–13277.

161 J. L. M. Abboud, C. Foces-Foces, R. Notario, R. E. Trifonov, A. P. Volovodenko, V. A. Ostrovskii, I. Alkorta and J. Elguero, *Eur. J. Org. Chem.*, 2001, 3013–3024.

162 A. Singh, A. Torres-Huerta, T. Vanderlinden, N. Renier, L. Martínez-Crespo, N. Tumanov, J. Wouters, K. Bartik, I. Jabin and H. Valkenier, *Chem. Commun.*, 2022, **58**, 6255–6258.

163 A. Mondal, M. Ahmad, D. Mondal and P. Talukdar, *Chem. Commun.*, 2023, **59**, 1917–1938.

164 E. N. W. Howe, N. Busschaert, X. Wu, S. N. Berry, J. Ho, M. E. Light, D. D. Czech, H. A. Klein, J. A. Kitchen and P. A. Gale, *J. Am. Chem. Soc.*, 2016, **138**, 8301–8308.

165 M. Ahmad, S. Metya, A. Das and P. Talukdar, *Chem. Eur. J.*, 2020, **26**, 8703–8708.

166 S. J. Wezenberg, L. J. Chen, J. E. Bos, B. L. Feringa, E. N. W. Howe, X. Wu, M. A. Siegler and P. A. Gale, *J. Am. Chem. Soc.*, 2022, **144**, 331–338.

167 D. Villarón, J. E. Bos, F. Kohl, S. Mommer, J. de Jong and S. J. Wezenberg, *J. Org. Chem.*, 2023, **88**, 11328–11334.

168 M. Ahmad, S. Chattopadhayay, D. Mondal, T. Vijayakanth and P. Talukdar, *Org. Lett.*, 2021, **23**, 7319–7324.

169 C. Wang, S. Wang, H. Yang, Y. Xiang, X. Wang, C. Bao, L. Zhu, H. Tian and D. H. Qu, *Angew. Chem. Int. Ed.*, 2021, **60**, 14836–14840.

170 D. Bléger, J. Schwarz, A. M. Brouwer and S. Hecht, *J. Am. Chem. Soc.*, 2012, **134**, 20597–20600.

171 C. Knie, M. Utecht, F. Zhao, H. Kulla, S. Kovalenko, A. M. Brouwer, P. Saalfrank, S. Hecht and D. Bléger, *Chem. Eur. J.*, 2014, **20**, 16492–16501.

172 C. Liangzhen, L. Xin, X. Tao and D. Shen, *Synth. Commun.*, 2004, **34**, 1215–1221.

173 B. Priewisch and K. Rück-Braun, *J. Org. Chem.*, 2005, **70**, 2350–2352.

174 A. Antoine John and Q. Lin, *J. Org. Chem.*, 2017, **82**, 9873–9876.

175 L. Albert, A. Peñalver, N. Djokovic, L. Werel, M. Hoffarth, D. Ruzic, J. Xu, L. O. Essen, K. Nikolic, Y. Dou and O. Vázquez, *Chem. Bio. Chem.*, 2019, **20**, 1417–1429.

176 J. Volarić, J. Buter, A. M. Schulte, K. O. Van Den Berg, E. Santamaría-Aranda, W. Szymanski and B. L. Feringa, *J. Org. Chem.*, 2022, **87**, 14319–14333.

177 A. Kerckhoffs, K. E. Christensen and M. J. Langton, *Chem. Sci.*, 2022, **13**, 11551–11559.

178 N. Chander, J. Morstein, J. S. Bolten, A. Shemet, P. R. Cullis, D. Trauner, D. Witzigmann, N. Chander, P. R. Cullis, D. Witzigmann, J. Morstein, A. Shemet, D. Trauner and J. S. Bolten, *Small*, 2021, **17**, 2008198.

179 T. Róg, M. Pasenkiewicz-Gierula, I. Vattulainen and M. Karttunen, *BBA - Biomembranes*, 2009, **1788**, 97–121.

180 M. A. Barrett, S. Zheng, L. A. Toppozini, R. J. Alsop, H. Dies, A. Wang, N. Jago, M. Moore and M. C. Rheinstädter, *Soft Matter*, 2013, **9**, 9342–9351.

181 Y. Liu, A. Sengupta, K. Raghavachari and A. H. Flood, *Chem*, 2017, **3**, 411–427.

182 B. A. McNally, A. V. Koulov, T. N. Lambert, B. D. Smith, J. B. Joos, A. L. Sisson, J. P. Clare, V. Sgarlata, L. W. Judd, G. Magro and A. P. Davis, *Chem. Eur. J.*, 2008, **14**, 9599–9606.

183 M. J. Spooner and P. A. Gale, *Chem. Commun.*, 2015, **51**, 4883–4886.

184 G. Gramse, A. Dols-Perez, M. A. Edwards, L. Fumagalli and G. Gomila, *Biophys. J.*, 2013, **104**, 1257–1262.

185 F. Otis, C. Racine-Berthiaume and N. Voyer, *J. Am. Chem. Soc.*, 2011, **133**, 6481–6483.

186 C. E. Weston, R. D. Richardson, P. R. Haycock, A. J. P. White and M. J. Fuchter, *J. Am. Chem. Soc.*, 2014, **136**, 11878–11881.

187 P. Läuger, *Angew. Chem. Int. Ed.*, 1985, **24**, 905–923.

188 D. C. Gadsby, *Nat. Rev. Mol. Cell Biol.*, 2009, **10**, 344–352.

189 L. Martínez-Crespo, L. Halgreen, M. Soares, I. Marques, V. Félix and H. Valkenier, *Org. Biomol. Chem.*, 2021, **19**, 8324–8337.

190 M. Ahmad, S. A. Gartland and M. J. Langton, *Angew. Chem. Int. Ed.*, 2023, **62**, e202308842.

191 A. Kerckhoffs and M. J. Langton, *Chem. Sci.*, 2020, **11**, 6325–6331.

192 D. Villarón, J. E. Bos, F. Kohl, S. Mommer, J. de Jong and S. J. Wezenberg, *J. Org. Chem.*, 2023, **88**, 11328–11334.

193 S. J. Edwards, I. Marques, C. M. Dias, R. A. Tromans, N. R. Lees, V. Félix, H. Valkenier and A. P. Davis, *Chem. Eur. J.*, 2016, **22**, 2004–2011.

194 H. Valkenier, L. W. Judd, H. Li, S. Hussain, D. N. Sheppard and A. P. Davis, *J. Am. Chem. Soc.*, 2014, **136**, 12507–12512.

195 T. G. Johnson, A. Sadeghi-Kelishadi and M. J. Langton, *J. Am. Chem. Soc.*, 2022, **144**, 10455–10461.

196 K. Maslowska-Jarzyna, K. M. Bąk, B. Zawada and M. J. Chmielewski, *Chem. Sci.*, 2022, **13**, 12374–12381.

197 V. Blažek Bregović, N. Basarić and K. Mlinarić-Majerski, *Coord. Chem. Rev.*, 2015, 295, 80–124.

198 R. Weissleder and V. Ntziachristos, *Nat. Med.*, 2003, 9, 123–128.

199 D. Muller, I. Zeltser, G. Bitan and C. Gilon, *J. Org. Chem.*, 1997, **62**, 411–416.

200 L. Albert, A. Peñalver, N. Djokovic, L. Werel, M. Hoffarth, D. Ruzic, J. Xu, L. Essen, K. Nikolic, Y. Dou and O. Vázquez, *Chem. Bio. Chem.*, 2019, **20**, 1417–1429.

201 M. Hirschmann, O. Soltwedel, P. Ritzert, R. Von Klitzing and C. M. Thiele, *J. Am. Chem. Soc.*, 2023, **145**, 3615–3623.

202 D. Hermann, H. A. Schwartz, M. Werker, D. Schaniel and U. Ruschewitz, *Chem. Eur. J.*, 2019, **25**, 3606–3616.

203 S. Jia and E. M. Sletten, *ACS Chem. Biol.*, 2022, **17**, 3255–3269.

204 C. Knie, M. Utecht, F. Zhao, H. Kulla, S. Kovalenko, A. M. Brouwer, P. Saalfrank, S. Hecht and D. Bléger, *Chem. Eur. J.*, 2014, **20**, 16492–16501.

205 J. Moreno, M. Gerecke, A. L. Dobryakov, I. N. Ioffe, A. A. Granovsky, D. Bléger, S. Hecht and S. A. Kovalenko, *J. Phys. Chem. B*, 2015, **119**, 12281–12288.

206 R. J. Mart and R. K. Allemann, *Chem. Commun.*, 2016, **52**, 12262–12277.

207 A. V Rayer, K. Z. Sumon, L. Jaffari and A. Henni, *J. Chem. Eng. Data*, 2014, **59**, 3805–3813.

208 E. N. W. Howe and P. A. Gale, *J. Am. Chem. Soc.*, 2019, **141**, 10654–10660.

209 A. Guesdon-Vennerie, P. Couvreur, F. Ali, F. Pouzoulet, C. Roulin, I. Martínez-Rovira, G. Bernadat, F. X. Legrand, C. Bourgaux, C. L. Mazars, S. Marco, S. Trépout, S. Mura, S. Mériaux and G. Bort, *Nat. Commun.*, 2022, **13**, 1–12.

210 T. M. Fyles and B. Zeng, *J. Org. Chem.*, 1998, **63**, 8337–8345.

211 M. J. Spooner and P. A. Gale, *Chem. Commun.* , 2015, **51**, 4883–4886.

212 J. N. Martins, B. Raimundo, A. Rioboo, Y. Folgar-Cameán, J. Montenegro and N. Basílio, *J. Am. Chem. Soc.*, 2023, **145**, 13126–13133.

213 N. L. Mora, A. Bahreman, H. Valkenier, H. Li, T. H. Sharp, D. N. Sheppard, A. P. Davis and A. Kros, *Chem. Sci.*, 2016, **7**, 1768–1772.

214 D. A. Mcnaughton, T. Y. T. To, B. A. Hawkins, D. E. Hibbs and P. A. Gale, *Org. Biomol. Chem.*, 2021, **19**, 9624–9628.

215 L. E. Bickerton, A. Docker, A. J. Sterling, H. Kuhn, F. Duarte, P. D. Beer and M. J. Langton, *Chem. Eur. J*, 2021, **27**, 11738–11745.

216 L. Perlin, S. MacNeil and S. Rimmer, *Chem. Commun.*, 2008, 5951–5953.

217 E. Fasoli, A. Arnone, A. Caligiuri, P. D'Arrigo, L. De Ferra and S. Servi, *Org. Biomol. Chem.*, 2006, **4**, 2974–2978.

218 R. Rosseto and J. Hajdu, *Tet. Lett.*, 2005, **46**, 2941–2944.

219 L. Zhang, H. Zhang, F. Gao, H. Peng, Y. Ruan, Y. Xu and W. Weng, *RSC Adv.*, 2015, **5**, 12007–12014.

220 A. Kerckhoffs, Z. Bo, S. E. Penty, F. Duarte and M. J. Langton, *Org. Biomol. Chem.*, 2021, **19**, 9058–9067.

221 L. Albert, A. Peñalver, N. Djokovic, L. Werel, M. Hoffarth, D. Ruzic, J. Xu, L. Essen, K. Nikolic, Y. Dou and O. Vázquez, *Chem. Bio. Chem.*, 2019, **20**, 1417–1429.

222 A. Antoine John and Q. Lin, *J. Org. Chem.*, 2017, **82**, 9873–9876.